UNIVERSITY OF LIVERPOOL

Synthesis and simulation of porous organic cages

Shan Jiang

Department of Chemistry, University of Liverpool

Thesis submitted in accordance with the requirements of the University of Liverpool for the degree of Doctor of Philosophy

October 2012

Supervisor: Prof. Andy Cooper

Co-supervisor: Dr. Abbie Trewin

Abstract

The design of porous organic molecules in the solid state where packing is dictated by weak van der Waals forces is attracting considerable attention. Most organic molecules pack in such a way to minimize free volume, which suggests molecules with permanent porosity in the solid state is rare. In this thesis, an experimental and molecular modeling study of porous organic cages is presented. These porous cage molecules are of interest for a wide range of applications in gas storage, separation and molecular recognition. Compared with other classes of porous materials such as porous frameworks or porous polymers, porous organic molecules possess potential advantages in solubility, molecular mobility and synthetic diversity.

A series of tetrahedral imine linked cage molecules can be synthesized by [4+6] cycloimination condensation reaction. The crystalline packing motifs of them can be directed by the vertex functionality giving control over the pore connectivity. The synthesis and characterization of one such cage molecule **(CC2)** is introduced in Chapter 2. The packing of the **CC2** molecules is frustrated by six vertex methyl groups, leading to 1D extrinsic pore channels and isolated intrinsic voids. **CC2** adsorbs a number of gases such as N_2, H_2, CO_2 and CH_4. The H_2 adsorption capacity of this material exceeds reports for other porous organic molecules. In addition, a 'propeller' shaped crystalline porous organic cage molecule, **CC6**, is prepared by [2+3] cycloimination reaction (Chapter 3). The cage molecule has a compact structure with a little void inside the cage. A narrow 1D channel is formed by molecular ineffective packing. The material demonstrates selective adsorption of H_2 and CO_2 over N_2.

We have found these cage molecules can inefficiently pack, creating permanent porosity in the amorphous solid state. These scrambled cage molecules are synthesized by either dynamic exchange reactions or co-reactions (Chapter 5). They show a high level of porosity and H_2/N_2 gas selectivity can be tuned by varying the cage functionality. The BET surface area of up to 898 m^2 g^{-1} exceeds comparable

amorphous molecular solids. A methodology is designed to generate amorphous cage structural models and gas diffusion simulations are also performed for these materials in Chapter 6. The simulations provide detailed information of the microscopic structures in these amorphous materials, including gas hopping, accumulative cage occupancy by gas molecules, residential times, and diffusion pathways, which cannot be achieved by experimental techniques.

Acknowledgements

First of all I would like to say a great big thank you to my supervisor Prof. Andy Cooper for giving me the opportunity to work on this fascinating project in his research group. Without his support, advices and encouragement, I definitely would not have gone this far. He gave me lots of confidence and all the help that I needed which I greatly appreciate.

A big thanks also goes to Dr. Abbie Trewin who is a wonderful supervisor for my simulation work. Her enormous contribution to my PhD studies has been invaluable to me. I would also like to gratefully thank Dr Dave Adams for his valuable suggestions and help in the lab. I have learned a lot from him and really enjoyed working with him.

Many thanks also goes to people who have contributed to my work and aided me: Dr John Bacsa for his help on single crystal X-ray diffraction, Dr James T .A. Jones for gas sorption and Le Bail refinement of PXRD, Dr Tom Hasell for measuring SEM, Dan Holden for designing cage force fields, Dr Kim Jelfs for writing scripts for gas diffusion analysis, Dr Xiaofeng Wu for synthesis of the strating monomer, Charlotte Blythe for designing the HPLC methodology to determine the scrambled cage molecules, Dr Rob Dawson for gas sorption analysis.

Also a big big thanks goes to my thesis committee for reading and correcting my thesis: Dr Dave Adam, Dr Abbie Trewin, Dr Rob Dawson, Dr Kim Jelfs, Dr Tom Hasell, Dr Jelena Jordanovic, Dr Tim Cooper and Prof. Andy Cooper. Without their inputs, the thesis would not be perfect.

I would like to thank all the people in the Cooper group, both past and present, particularly Shashi, James, Rob, Kim, Tom, Dan, Jamie, Shijie, Ming, Jiaxing, Xiaofeng, Sam , Marc, Jelena and Mark from Abbie's group for all your help and assistant. Many thanks to my lab & office mates: Jamie Culshaw, Dan Holden and Hilary Shepherd for your companies and help.

I would like to give my sincere thanks to my parents for their support and love. I am also thankful to my aunt, uncle and my lovely cousin (Wei) for sticking with me throughout the years in Liverpool. Finally, I would to thank my boyfriend, Lingjian, as he has always encouraged me towards excellence.

List of publications

1. T. Tozawa, J. T. A. Jones, S. I. Swamy, **S. Jiang**, D. J. Adams, S. Shakespeare, R. Clowes, D. Bradshaw, T. Hasell, S. Y. Chong, C. Tang, S. Thompson, J. Parker, A. Trewin, J. Bacsa, A. M. Z. Slawin, A. Steiner, A. I. Cooper, *Nat. Mater.* **2009**, *8*, 973-978.

2. **S. Jiang**, J. T. A. Jones, T. Hasell, C. E. Blythe, D. J. Adams, A. Trewin, A. I. Cooper, *Nat. Commun.* **2011**, *2*, 207.

3. **S. Jiang**, J. Bacsa, X. Wu, J.T.A. Jones, R. Dawson, A. Trewin, D.J. Adams and A.I. Cooper，*Chem. Commun*., **2011**, *47*, 8919-8921

4. **S. Jiang**, K. E. Jelfs, D. Holden, T. Hasell, A. I. Cooper and A. Trewin, Simulation of gas diffusion in amorphous porous organic cages. In preparation.

5. **S. Jiang**, J.Bacsa, D.J.Adams, A. Trewin and A. I. Cooper, Porous asymmetrical cage molecules. In preparation.

List of Abbreviations

MOF	Metal Organic Framework
COF	Covalent Organic Framework
CMP	Conjugated Microporous Polymer
PIM	Polymers of Intrinsic Microporosity
EOF	Element Organic Framework
PAF	Porous Aromatic Framework
PPN	Porous Polymer Networks
BET	Brunauer Emmett Teller
PXRD	Powder X-ray Diffraction
SA	Surface Area
TGA	Thermogravimetric Analysis
FTIR	Fourier Transform Infrared Spectroscopy
SEM	Scanning Electron Microscope
NMR	Nuclear Magnetic Resonance
HPLC	High Performance Liquid Chromatography
MS	Mass Spectrometry
MD	Molecular Dynamics
DFT	Density Functional Theory
LDA	Local Density Approximation
GGA	Generalized Gradient Approximation
MC	Monte Carlo

Contents

Chapter 3-Crystalline porous organic cage-CC2

Chapter 4-Selective gas sorption in a [2+3] 'propeller' cage crystal

Chapter 5-Amorphous porous scrambled organic molecular solids

Chapter 6-Simulation of gas diffusion in amorphous porous organic cages

Chapter 7-Conclusions and future work

Chapter 1

Introduction

1.1 Porous materials

Porous materials are important in a wide range of applications such as catalysis, separations, and energy storage.[1] They can be divided into the following groups according to their pore size: macroporous materials with pore sizes larger than 50 nm; mesoporous materials with pore sizes between 2 and 50 nm; microporous materials with pore sizes less than 2 nm.[2] The main focus of this thesis is to evaluate new materials for H_2, N_2, CH_4, and CO_2 storage and the associated gas selectivity. The target set by the US Department of Energy (DOE) for H_2 storage is not less than 45 mmol g^{-1} (9 wt %) by 2015 at room temperature.[3] Unfortunately, as yet, porous materials have not achieved this target. The DOE defines the CH_4 storage target as 180 v/v under 35 bar and ambient temperature.[4] Some activated carbons have achieved CH_4 storage values of up to 200 v/v.[5] CO_2 emissions from fossil fuel combustion and power plants are a global environmental problem. Thus CO_2 capture and storage (CCS) is a key issue and challenge. Potential materials for CCS need not only to adsorb a large amount of CO_2, but also to separate CO_2 from a mixture of other gases.[1a]

The main classes of porous materials are crystalline and amorphous materials. Crystalline porous materials are in general better understood because the structures of the materials can be determined by X-ray diffractions. In contrast, amorphous porous materials are difficult to characterize due to lack of periodic structure.[1b] There are several well-known classes of microporous materials including zeolites,[6] activated carbons,[7] covalent organic frameworks (COFs),[8] metal-organic frameworks (MOFs),[9] polymers of intrinsic microporosity (PIMs),[10] conjugated microporous polymers (CMPs),[11] and porous organic molecules.[12] This thesis will focus on the design the synthesis of porous organic molecules in either a crystalline or amorphous solid state.

1.2 Porous frameworks

1.2.1 Metal organic frameworks (MOFs)

Metal-organic frameworks (MOFs) have received considerable attention over the last decade due to their interesting pore structures, chemical diversity, and potential applications in various fields such as gas storage, separation, shape/size selectivity, catalysis, sensors and drug delivery.[13] MOFs have extended crystalline structures, containing metal clusters and organic ligands. One-, two- and three- dimensional structures (1D, 2D and 3D, respectively) are formed by linking metal sites and organic ligands, where the dimensionality can be controlled by the connectivity and geometry of the secondary building blocks. More importantly, due to the large number of choices of both metal clusters and organic linkers, the number of potential structures of MOFs is vast. The concept of 'reticular chemistry' was proposed by Yaghi and O'Keeffe to design and construct porous MOFs materials by using secondary building units (SBUs).[14] A large number of topologies results from linking various molecular ligands and metal clusters. By choosing appropriate building blocks and synthetic methods, MOFs with well-defined pore sizes, shapes and functionalities can be formed that result in desired properties. One of most well-known 3D MOFs is MOF-5, consisting of zinc clusters and 1,4 benzenedicarboxylate (BDC) that generate a cubic extended porous structure reported by the Yaghi group that can be used for hydrogen storage.[15] MOF-5 adsorbs 22.5 mmol g^{-1} (4.5 wt %) H_2 at 78 K and 20 bar. A number of analogues of MOF-5, IRMOFs (IsoReticular MOFs), have been investigated using different organic linkers as shown in Figure 1.[9] To date, MOFs have demonstrated high porosity, for example, MOF-201 has Brunauer−Emmet−Teller (BET) and Langmuir surface areas of 6240 and 10400 m^2/g, respectively.[16] High values of H_2 storage have been achieved within MOFs such as MOF-177 (37.5 mmol g^{-1} which corresponds to 7.5 wt% at 70 bar, 77 K) [17] and NOTT-112 (50 mmol g^{-1} which corresponds to 10 wt% at 77 bar, 77 K).[18] For CH_4 storage, IRMOF-6 has a CH_4 uptake of 10.7 mmol g^{-1} (155 v/v) at 298 K and 36 atm.[19] MOF-177 has a CO_2 storage capacity of up to 33.5 mmol g^{-1} at room

temperature and pressures up to 42 bar.[20] The uptake of CO_2 in MIL-101 has reached a capacity of 40 mmol g^{-1} at 5 MPa and 303 K.[21] MOFs also selectively adsorb and separate H_2 over other gases, CO_2 over N_2, CO_2 over CH_4, xylene and alkane isomers.[13, 22] Although MOFs possesses flexible structures, high surface areas and large pore volumes, some of them show low thermal or hydrolytic stabilities, and pore structures can collapse after desolvation. [22-23]

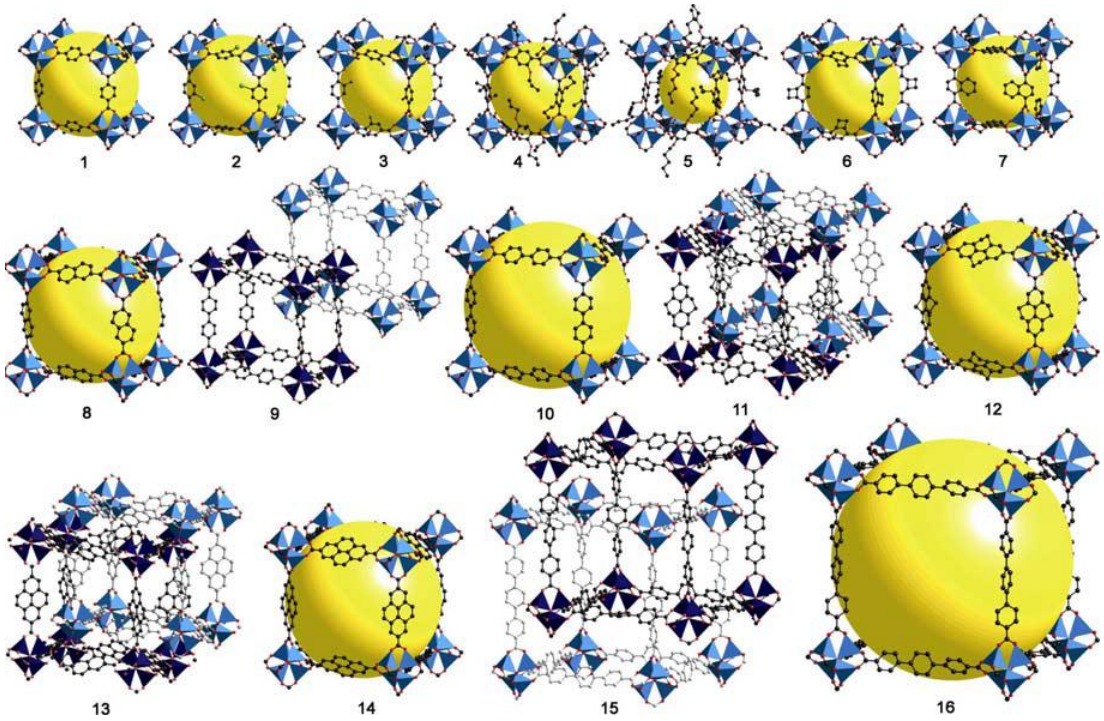

Figure 1. A series of IRMOFs with different functional organic linkers. The yellow spheres represent the internal voids. The extended organic linker increases the internal void and it also allows the formation of catenated structure. (Figure taken from the Ref.[9])

1.2.2 Covalent organic frameworks (COFs)

Covalent Organic Frameworks (COFs) are a class of purely organic crystalline porous materials. 2D layered structures or 3D networks can be constructed by strong covalent bonds between B, C, O and Si atoms. COF-1 was synthesized by the self-condensation reaction of 1,4-benzenediboronic acid (BDBA) itself which produced a staggered layer framework linked by planar boroxine rings, B_3O_3 (Figure

2b).[8] COF-5 was synthesized by the condensation reaction of 1,4-benzenediboronic acid (BDBA) and hexahydroxy triphenylene (HHTP), giving an eclipsed framework structure (Figure 2b).[8] COF-1 and COF-5 show apparent surface areas of 711 and 1590 m^2/g, respectively.[8] These materials exhibit high thermal stability up to 600 °C, but rather low hydrolytic stability in some cases. Furthermore, a series of 3D COFs were reported by self-condensation and co-condensation reactions of the rigid molecular building blocks, tetrahedral (tetra(4-dihydroxyborylphenyl)methane, TBPM and its silicon analogue TBPS) and triangular (HHTP) monomers shown in Figure 2a.[24] The 3D COFs (Figure 2c) exhibit very low crystal densities (0.17 g/cm^3 for COF-108) and high porosities (BET surface area of 4210 m^2/g for COF-103).[24] COFs have lower densities than MOFs and the low densities coupled with large pore volumes in 3D COFs result in their higher gas uptakes. Some of the COFs have shown very high CH_4 storage capacities. The CH_4 sorption capacity of COF-1 is 2.5 mmol g^{-1} (195 v/v) at 298 K and 35 bar, which has exceeded the US CH_4 storage target.[25] Simulations of H_2 adsorption isotherms for COFs suggest that COF-105 and COF-108 reveal high H_2 storage capacities.[26] The predicted H_2 uptake is 50 mmol g^{-1} (10 wt %) at 77K and 80 bar for COF-105 and 50 mmol g^{-1} (10 wt %) at 77 K and 100 bar for COF-108.

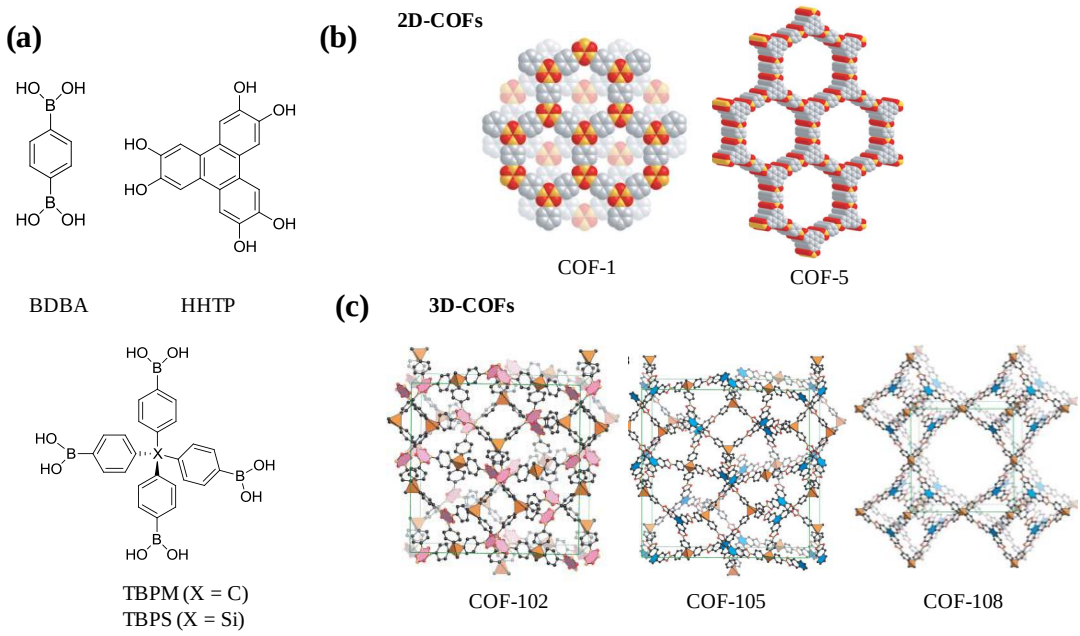

Figure 2. (a) Molecular structures of starting monomers. (b) Crystal structures of 1D COFs (COF-1 and COF-5). (c) Crystal structures of 3D COFs (COF-102, COF-105 and COF-108, respectively). Hydrogen atoms are omitted for clarity. Carbon, boron, oxygen and silicon atoms are represented as gray, orange, red and blue, respectively. (Figure adapted from the Refs.[8, 24])

1.3 Porous polymers

1.3.1 Polymers of intrinsic microporosity (PIMs)

Porous polymers can be constructed in the amorphous solid state using irreversible chemistry. The 'cost' of irreversible chemistry is that the materials are amorphous, not crystalline, but benefit is that these solids can show significantly better physical stability in some cases. Polymers of intrinsic microporosity (PIMs) have rigid, contorted structures and a large amount of interconnected free volume is created by the inefficient packing of polymer chains reported by McKeown and Budd.[27] PIMs can be prepared either as insoluble networks or, uniquely, as soluble linear polymers. Most PIMs are synthesized by a highly efficient dibenzodioxane-forming reaction using a spirobisindane monomer and an o-dihalide monomer. The first PIM networks were prepared based on porphyrins and phthalocyanines.[28,29] The porphyrin-based

PIMs exhibit large surface areas of 900-1000 $m^2 g^{-1}$.[29] PIMs containing Zn^{2+}, Cu^{2+}, Co^{2+} and $2H^+$ centers are synthesized by the phthalocyanie formation reaction which have surface areas of 450-950 $m^2 g^{-1}$.[28] Furthermore, the PIM networks were synthesized containing hexaazatrinaphthalyene (HATN) for catalyst support,[30] with cyclotricatechylene (CTC) for hydrogen storage,[31] and with 9,10-diethyl-2,3,6,7,12,13-hexahydroxytriptycene (Trip), showing a high surface area of 1065 m^2/g. [32] The molecular repeated units for PIMs are shown in Figure 3.

Soluble linear PIMs have a BET surface area of up to 850 $m^2 g^{-1}$.[10] The structures of soluble PIM-1 and PIM-7 are shown in Figure 3. A significant advantage of these materials is their solution processability. PIM-1 film can be cast from solution and PIM membranes have shown high permeability and gas separation such as for O_2/N_2.[27, 33] It is noted that soluble liner PIMs with low molecular weight chains have low surface areas and the porosity increases with increasing chain length. For example, PIM-4 with molecular weight of 5.0×10^3 g mol^{-1} shows a BET surface area of 440 $m^2 g^{-1}$, while PIM-1 with molecular weight of 2.7×10^5 g mol^{-1} shows a BET surface area of 750 $m^2 g^{-1}$.[10, 27]

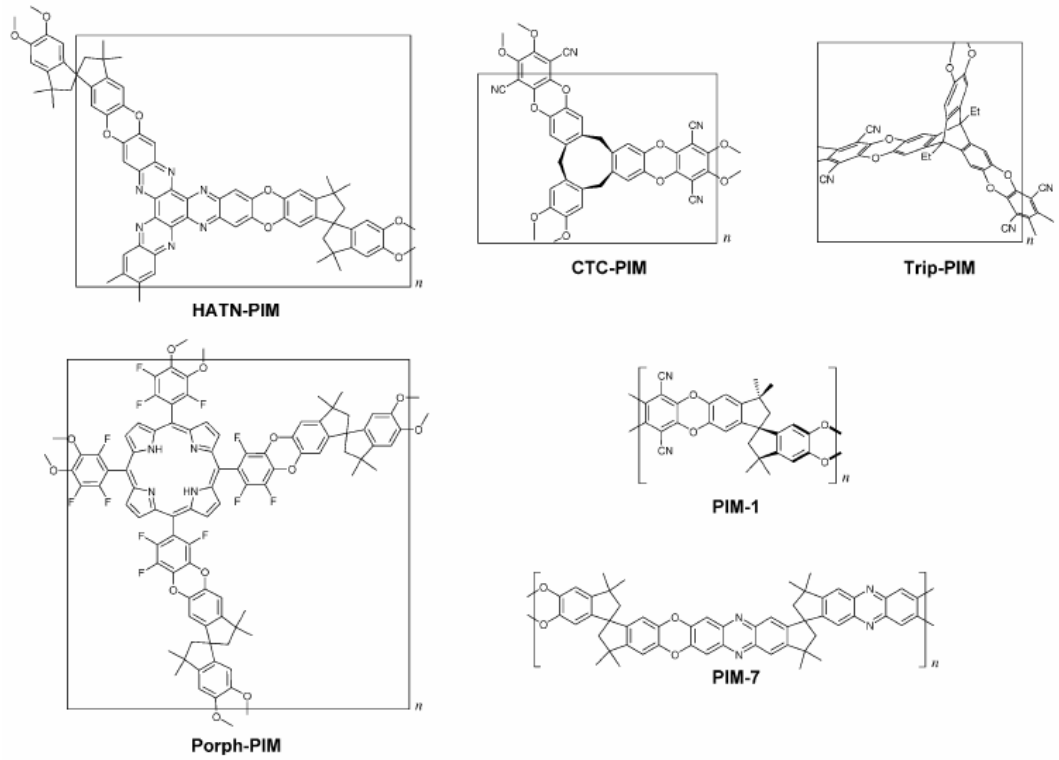

Figure 3. Molecular repeated units for linear and network PIMs. PIM-1 and PIM-7 are linear and soluble. HATN-PIM, CTC-PIM, Trip-PIM, Porph-PIM are insoluble networks.(Figure taken from Ref. [34])

1.3.2 Conjugated microporous polymers (CMPs)

The first generation of CMPs, conjugated poly(aryleneethynylene) networks, were reported in 2007 by our group using the palladium-catalyzed Sonogashira-Hagihara coupling reaction of aromatic halides and aromatic alkynes.[11] These polymers exhibit microporosity in the amorphous solid state and the series of CMPs (from CMP-0 to CMP-5) have BET surface areas of between 512 and 1018 $m^2 g^{-1}$.[11, 35] The molecular repeat units and structural models of CMPs are shown in Figure 4. The micropore size distributions and surface areas of these materials can be tuned by varying the length of the organic linkers, even though the materials are amorphous.[11, 35] Gas sorption analysis reveals that the shortest strut length gives rise to the smallest pore size and highest micropore volume and surface area (such as CMP-0). In contrast, the largest strut length results in the largest pore size, but the lowest micropore volume

and surface area (such as CMP-5). Atomistic simulations suggest that short rigid struts have low flexibility between the struts and adjacent connected benzene nodes.[35] The lower interpenetration in CMP-0 gives rise to a higher porosity.[35] CMP-5 has the longest struts and hence there is more geometric interpenetration.[35] The flexibility of the network makes the packing closer that reduces the porosity.[35]

Many applications using CMPs have been investigated in the last few years. For example, metal-CMPs containing rhenium, rhodium and iridium have been designed for heterogeneous catalysis.[36] Moreover, metalloporphyrin CMP possesses a surface area of 1270 m^2 g^{-1} and can be used as a heterogeneous catalyst for the oxidation of various sulfides with up to 99 % selectivity and 98 % conversion.[37] CMPs based on pyrene building blocks have shown high luminescence and emission colour.[38] Polyphenylene CMPs (PP-CMPs) has been reported for light harvesting. The materials have a pore size of 15.6 Å and a surface area of 1083 m^2 g^{-1}.[39] The material is able to contain energy accepting coumarin 6 in the pores, with energy transfer observed from the network to the coumarin 6 molecules.[39]

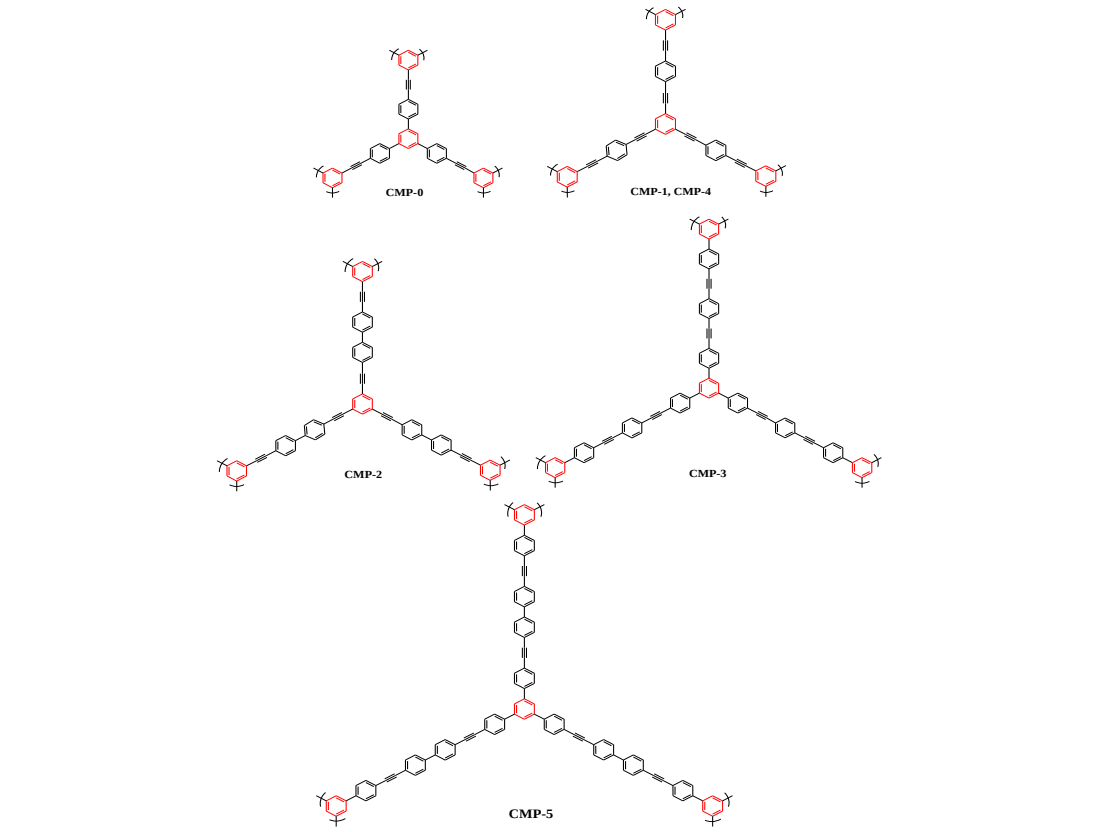

CMP-0 CMP-1/4 CMP-2 CMP-3 CMP-5

Figure 4. (a) Molecular repeated units for CMPs (b) Structural models to represent CMP-0, CMP-1, CMP-2, CMP-3 and CMP-5. (Figure taken from ref.[34])

1.3.3 Porous organic networks

Element organic frameworks (EOFs), for example, poly(1,4-phenylene)silane (EOF-1) and poly(4,4'-biphenylene)silane (EOF-2), are prepared by the tetrakis(4-bromophenyl)silane and 4,4'-dibromobiphenylene building block, respectively, reported by Kaskel and coworkers.[23b] These organic frameworks demonstrate high thermal stabilities and BET surface areas of 780 m^2 g^{-1} (EOF-1) and 1046 m^2 g^{-1}(EOF-2), respectively. Moreover, a series of EOFs was synthesized by using different tetrahedral monomers and orangic linkers, resulting in organic frameworks with BET surface areas of up to 1380 m^2 g^{-1}.[40]

The microporous polyphenylene framework, PAF-1 was synthesized by highly efficient Yamamoto reaction and showed an exceptionally high BET surface area of 5600 m^2 g^{-1} and Langmuir surface area of 7100 m^2 g^{-1}.[41] The PAF-1 synthesis is shown in Figure 5. PAF-1 has a diamond-like framework topology which is constructed by tetrahedral building blocks. The material has high thermal and chemical stability. PXRD of PAF-1 shows broad peaks indicating a disordered structure.[25b] The material adsorbs 7.0 wt % H_2 at 77 K and 48 bar. The CO_2 uptake of PAF-1 is 29.5 mmol g^{-1} at 40 bar and room temperature. PAF-1 also shows adsorption capabilities for organic vapors such as benzene (16.7 mmol g^{-1}) and toluene (14.8 mg g^{-1}) at room temperature and saturated vapor pressures.

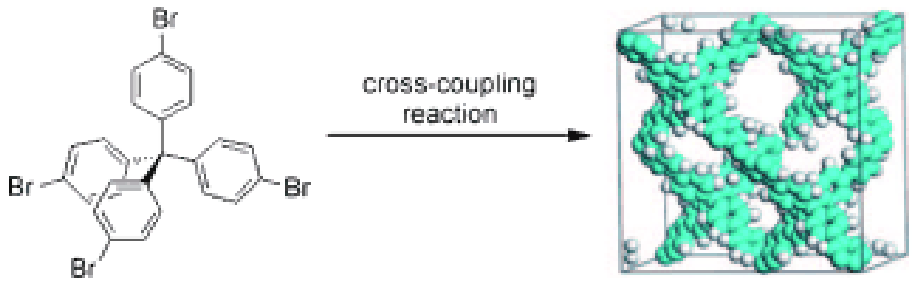

Figure 5. Synthesis of PAF-1 by a Yamamoto cross-coupling reaction. (The Figure is taken from the Ref.[41])

Highly stable porous polymer networks (PPNs) have been synthesized using tetrahedral monomers with different central elements (adamantine center for PPN3,

silicon center for PPN4 and germanium center for PPN5) by the Yamamoto coupling (Figure 6).[42] PPN-4 shows exceptionally high Langmuir surface area of 10063 $m^2 g^{-1}$ (BET surface area of 6461 $m^2 g^{-1}$) which currently exceeds those of all other porous materials. The H_2 storage capacity of PPN-4 is 45.5 mmol g^{-1} at 77 K and 55 bar. It adsorbs 48.2 mmol g^{-1} CO_2 at 50 bar and 295 K.

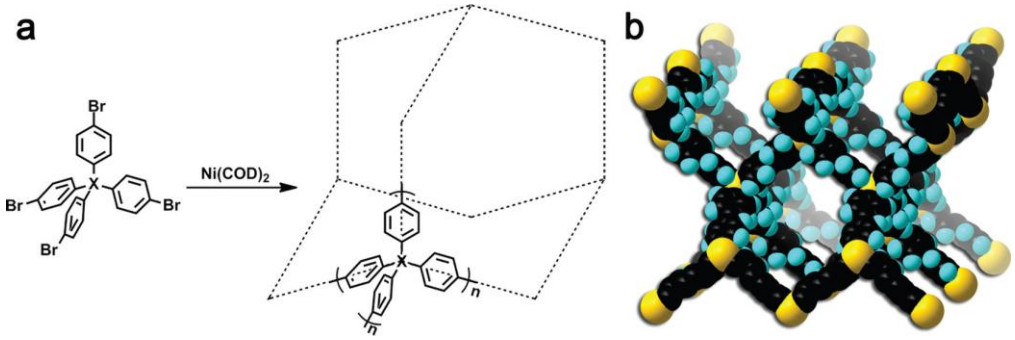

Figure 6. (a) Synthesis of PPNs using tetrahedral monomers. PPN-3 (X is adamantine), PPN-4 (X is silicon) and PPN-5 (X is germanium). (b) Structural model for PPN-4.Carbon silicon and hydrogen atoms are represented as black, yellow and blue. (Figure taken from the Ref.[42])

1.4 Porous molecules

The design and synthesis of porous organic molecules stems originally from work in the 1960's on macrocycles and has developed recently into an exciting and prosperous field.[12, 43] It has become an alternative strategy for assembly and construction of porous materials. In brief, the approach is to pack discrete molecules with the packing dictated by weak van der Waals forces, so that porosity can be generated in either the amorphous or the crystalline solid state. However, most organic molecules pack efficiently with minimal void volume and are generally nonporous.[12] Solvated organic molecular solids may have cavities or channels where solvents molecules are situated. Upon desolvation, however, these voids usually collapse and hence permanently porous organic molecules are comparatively rare with respect to porous networks or frameworks.[12]

It is worth defining of the term 'porosity' for porous molecules. In general, porosity

can be divided into intrinsic and extrinsic porosity.[44] Intrinsic pores arise from the intrinsic voids in a molecule, whereas extrinsic pores result from inefficient molecular packing.[44] Some porous molecules exhibit both intrinsic and extrinsic porosity. A review by Barbour described three distinct categories of porosity: conventional porosity, porosity 'without pores', and virtual porosity.[44] Conventional porosity is generated by permanent voids or channels in the materials. The conventional porosity of a material can be measured either experimentally by gas adsorption analysis or computationally by rolling a probe around the surface of the pores, which is dependent on the radius of the probe. The typical probe radii are 1.82 Å for N_2 probe, 1.72 Å for CO_2 probe and 1.42 Å for H_2 probe.[45] Porosity 'without pores' is used to describe materials without channels or voids in the structures which, however, are still accessible to a guest molecule.[44] For example, *p-tert*-butylcalix[4]arene does not have connected channels in the static crystal structure, but guest molecules can nonetheless diffuse in the lattice voids by a dynamic process.[46] Virtual porosity is not a class of porosity, but rather the result of visualizing the structure using the capped-stick or ball-and-stick display style. This kind of 'porosity' disappears when using a space-filling display style.[44] Virtual porosity also can be created by artificially deleting solvents in the structure, but this assumes that the structure will not rearrange upon desolvation, which is not typically the case.[44]

There have been a number of reports of organic molecules that pack inefficiently in the solid state and which are stable to desolvation, thus forming permanently porous molecular crystals such as calixarenes,[47] cucurbit[6]uril,[48] some dipeptides,[49] 3,3',4,4'-tetra(trimethylsilylethynyl) biphenyl,[50] and imine-based organic cages.[43a] In comparison to many conventional microporous materials, porous organic molecules have potential advantages due to their good solution processability and functional group modification.[12, 43a] These porous organic molecules have desirable properties for gas storage, molecular separations and catalysis. In the following section, the various classes of porous molecules will be introduced in more detail.

1.4.1 Calixarenes

Calix[n]arenes are a class of macrocyclic compounds that are useful building blocks in supramolecular chemistry.[51] The molecules possess a bowl-shaped conformation with defined upper and lower rims (Figure 7) and the cavity of calixarenes can be used to accommodate guest molecules.[51] Calixarenes are generally formed via a phenol-formaldehyde condensation reaction.[52] Various calix[n]arenes derivatives have been synthesized by modifying functionality either at the upper or lower rim. [53] The simplest representative of calix[n]arenes is calix[4]arene (Figure 7).[47] Calix[4]arene is observed to incorporate methane and freon molecules in the interstitial voids forming highly stable host-guest systems.[47]

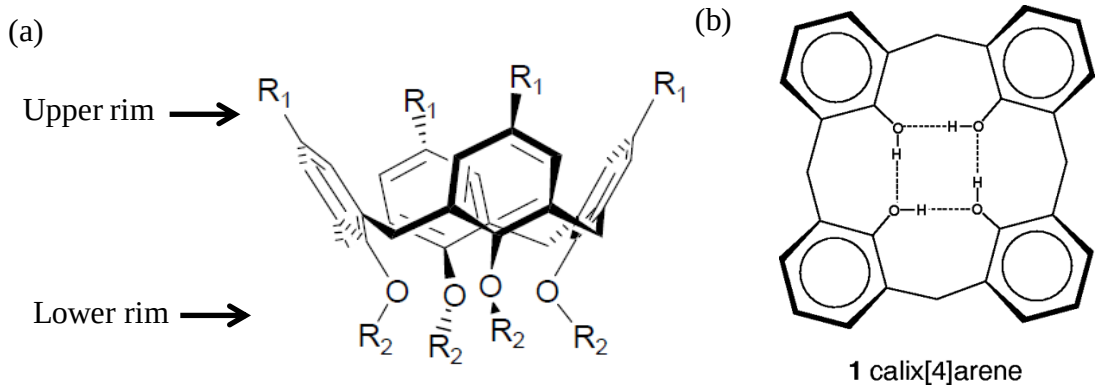

Figure 7. (a) The conformation of calixarenes. (b) The molecular structure of calix[4]arene.

In addition, a well-known host molecule *p-tert*-butylcalix[4]arene was prepared by sublimation to form a low density polymorph shown in Figure 8.[46] The crystal structure shows an up-down bilayer packing with isolated pore cavities. The crystal structures can undergo single crystal to single crystal phase transitions with the uptake of organic vapors such as vinyl bromide as shown in Figure 8.[46] Upon incorporation of vinyl bromide into *p-tert*-butylcalix[4]arene, the vinyl bromide is situated in the cavity of the *p-tert*-butylcalix[4]arene resulting in a 1:1 guest-host complex. The mechanism of guest molecule transport in the *p-tert*-butylcalix[4]arene involves a diffusion cooperative process. The shift of bilayers allows the vinyl

bromide to diffuse.

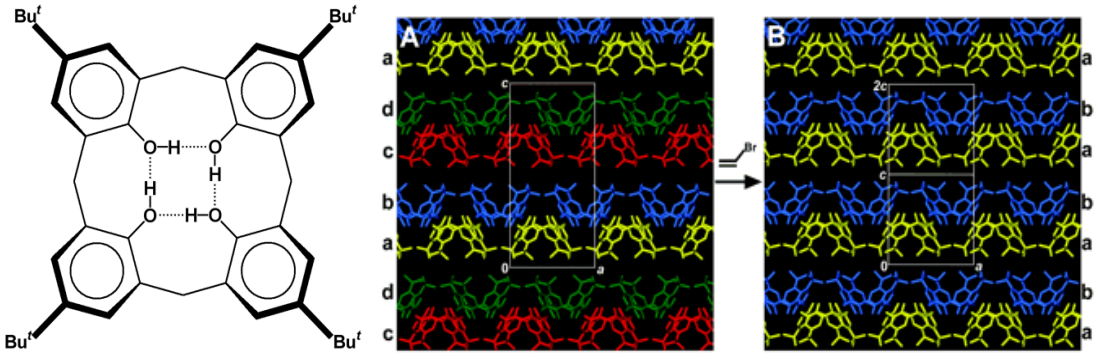

Figure 8. The molecular structure of *p-tert*-butylcalix[4]arene. The crystal packing change upon incorporation of vinyl bromide molecule in the *p-tert*-butylcalix[4]arene lattice. (The images are taken from Ref.[46])

Furthermore, the low density polymorph of *p-tert*-butylcalix[4]arene also revealed absorption of O_2, N_2 and CO_2 under ambient conditions.[54] The CO_2 occupancy in the cavities of the calixarene is 80 % at 1 atm and 100 % at 3 atm. In contrast, H_2 adsorption is not observed up to 7 atm. Hence, this material can be used to separate H_2 and CO_2 from a mixture of these gases.

The porous organic molecule, 1, 2-dimethoxy-*p-tert*-butylcalix[4]dihydroquinone (Figure 9), has a type I N_2 isotherm with a BET surface area of 230 m^2 g^{-1}.[55] The crystal packing shows open channels with a free volume of 988 $Å^3$. This material has a high selectivity for CO_2 over H_2.

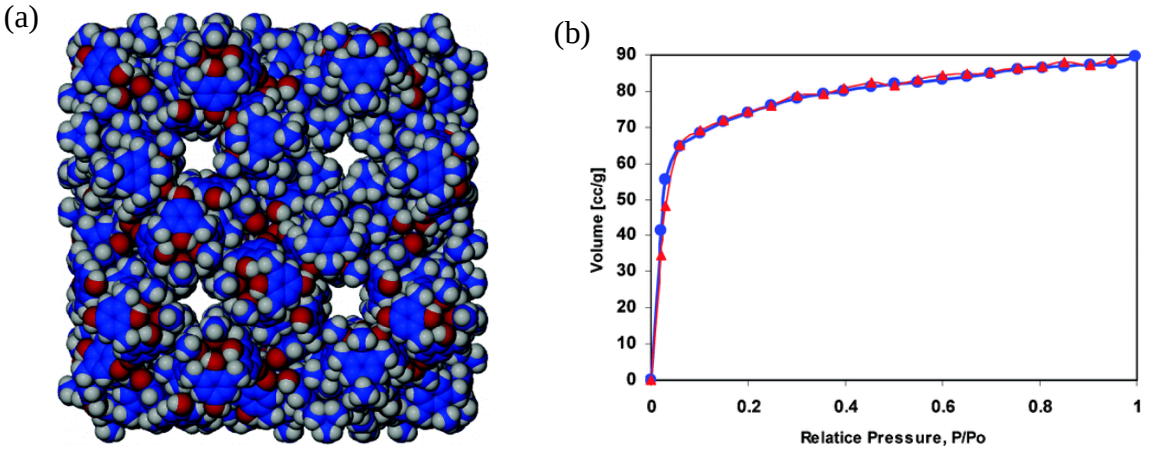

Figure 9. (a) The crystal packing of 1, 2-dimethoxy-*p-tert*-butylcalix

[4]dihydroquinone. (b) Nitrogen isotherm at 77 K. Blue circles indicate absorption and red triangles represent desorption. (Figure taken from the Ref.[55])

In order to enhance the internal cavities of the calix[n]arenes, *para*-hexanoyl and *para*-octanoyl-calix[4]arenes with long flexible chains on the upper rim were synthesized.[53a] Unlike *para*-hexanoyl-calix[4]arenes, *para*-octanoyl-calix[4]arenes shows permanent porosity after solvent removal. The adsorption isotherms were measured volumetrically at room temperature for linear C_1-C_4 alkane, ethylene, nitrogen, oxygen, and carbon dioxide. The material is able to adsorb all of these gases except N_2 and O_2. This material shows a preference for the adsorption of hydrocarbons, indicating the feature of hydrophobic channels.

1.4.2 Cucurbit[n]urils

Cucurbit[n]urils (CB[n]) are macrocyclic molecules composed of *n* glycoluril repeat units where *n* can be 5, 6, 7, 8 and 10 (Figure 10).[56] Cucurbit[n]urils are 'pumpkin' shaped molecules that can be synthesized by condensing glycoluril with formaldehyde.[56] The cavity of the cucurbiturils is nonpolar and is widely used for binding of hydrophobic guests.[57]

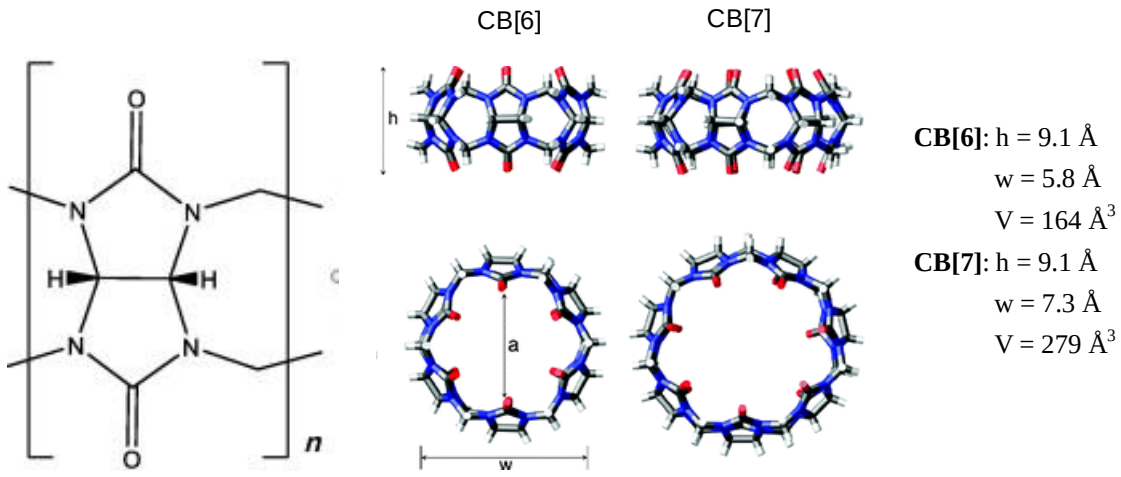

Figure 10. The general chemical structure of cucurbit[n]uril, where n=5, 6, 7, 8 or 10 and the molecular structures of CB[6] and CB[7] demonstrating the cavity. (Figure adapted from Ref.[57])

Kim and co-workers reported a porous organic molecule CB[6]. The crystal structure demonstrates an accessible 1D channel. CB[6] has a BET surface area of $210\,m^2\,g^{-1}$ and a pore volume of $0.13\,cm^3\,g^{-1}$ (Figure 11a-b).[48] CB[6] also shows high adsorption capacity of acetylene. The C_2H_2 uptake is 4.2 mol of C_2H_2 per mole of CB[6] at 196 K and 1 atm. The high uptake can be ascribed to a high enthalpy of acetylene and CB[6]. The single crystal X-ray data reveals that two acetylene molecules per CB[6] are found in the 1D channels (Figure 11d).[48] The acetylene molecules at specific adsorption sites can form hydrogen bonds with CB[6] resulting in high adsorption enthalpy. CB[6] obtained by recrystallization shows a high CO_2 adsorption capacity at 298 K and 1 bar also due to the high enthalpy of CO_2 absorption by the same research group (Figure 11e).[58] Structural analysis indicates that the CO_2 molecules are not only located in the 1D channels but also in the cavities of CB[6]. The material shows the highest selectivity of CO_2 over CO among those of any known porous materials. Recently, Atwood and coworkers described a porous amorphous organic CB[7].[59] The material showed a high CO_2 capacity and selectivity of CO_2 over N_2 and CH_4.

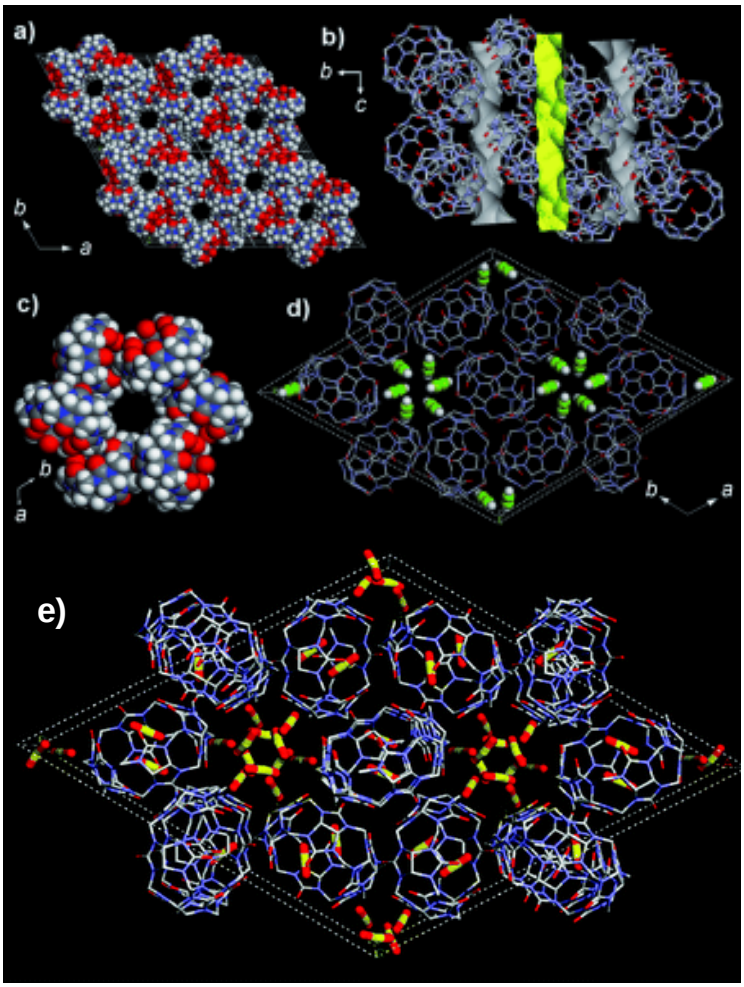

Figure 11. (a) The crystal structure of CB[6]. (b) 1D channels represented in yellow. (c) The hexagonal arrangement of CB[6]. (d) X-ray crystal structure of CB[6] with acetylene molecules adsorbed in the channels. (e) X-ray crystal structure of CO_2 absorbed in CB[6]. (The Figure is adapted from the Refs.[48, 58])

1.4.3 Tris-*o*-phenylenedioxycyclotriphosphazene (TPP)

Tris-*o*-phenylenedioxycyclotriphosphazene (TPP) has a 'paddle-wheel' molecular structure (Figure 12a). The TPP molecules can form a hexagonal packing and create channels with a diameter of ~ 5 Å (Figure 12b-c).[60] TPP has been widely used to form stable inclusion compounds with various guest molecules such as benzene derivatives and iodine.[60-61] Sozzani and coworkers reported that the desovlated crystal structure of TPP had 25 % free volume accessible for guest molecules.[62] The gas sorption capacity of TPP crystal was measured for several gases, including Ar, N_2,

O_2, H_2, CH_4 and CO_2. The material was found to selectively adsorb CH_4 and CO_2. The CH_4 uptake was 1.5 mmol g^{-1} at 195 K and 1 atm, and the CO_2 adsorption capacity was 2.7 mmol g^{-1} under the same conditions. The sorption of N_2 at 77 K and xenon (Xe) at 298 K by TPP was investigated by Hulliger and coworkers.[63] The total N_2 uptake was 1.13 mol of N_2 per mol TPP (corresponding to 2.46 mmol g^{-1} of TPP) and the Langmuir surface area calculated from the N_2 isotherm was 240 m^2 g^{-1}. Xe molecules showed a high affinity to the channels of TPP. The uptake was 0.77 mol of Xe per mol of TPP at 298 K and 100 kPa, corresponding to 90 % channel occupancy.[63]

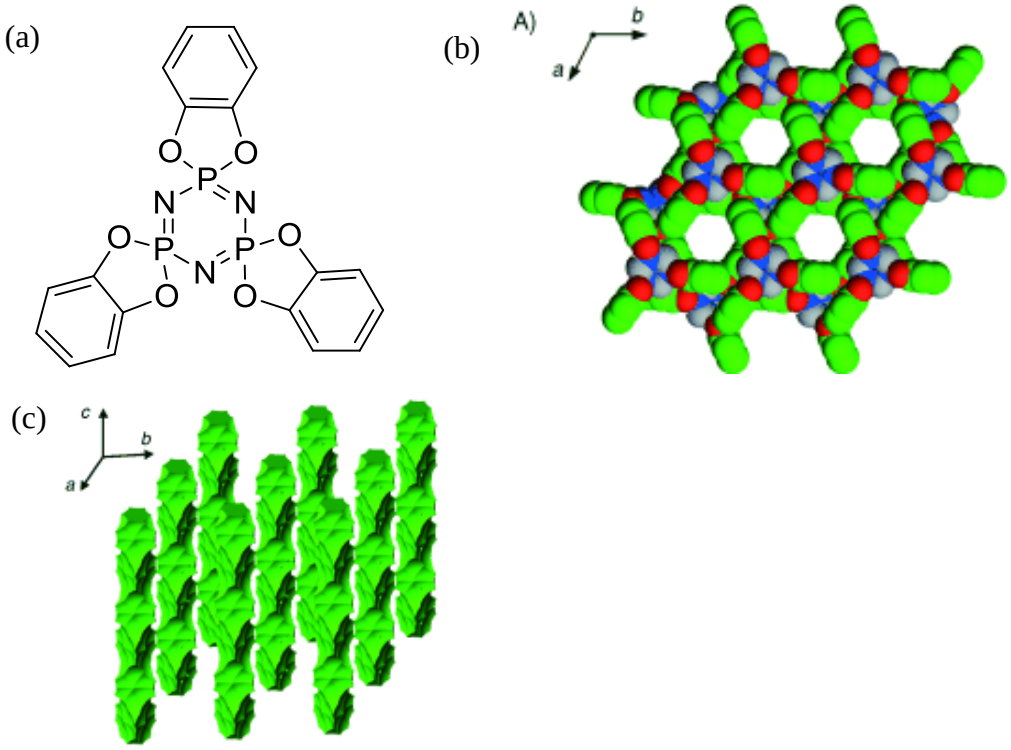

Figure 12. (a) TPP molecular structure. (b) Crystal structure of TPP showing a hexagonal packing. (c) 1D pore channels with 5 Å diameter. (Figure from the Ref.[62])

1.4.4 3,3′,4,4′-Tetra(trimethylsilylethynyl)biphenyl (4TMSEBP)

The organic porous crystal of 3,3',4,4′-tetra(trimethylsilylethynyl)biphenyl (4TMSEBP) (Figure 13a) was discovered by McKeown and coworkers by searching through many crystal structures in Cambridge Structural Database (CSD) using a set of well-defined search criteria to find crystals with low densities and, hence, the possibility of permanent porosity.[50] The crystal structure of 4TMSEBP shows 3D interconnectivity of pore voids and channels (Figure 13b). The size of the pore voids is 11 Å and 4TMSEBP has narrow channels between these voids with a diameter of 4 Å. N_2 sorption measurements show a type I isotherm at 77 K, from which a BET surface area of 278 m^2 g^{-1} and a micropore volume of 0.16 mL g^{-1} are calculated. The total amount of N_2 absorption is 4.4 mmol g^{-1} at $P/P_o = 1$. The material also absorbs a large amount of H_2 at 77 K, with 3.9 mmol g^{-1} absorbed at 10 bar. Database searching of this kind is an interesting strategy to find porous molecular materials that have not been recognized.

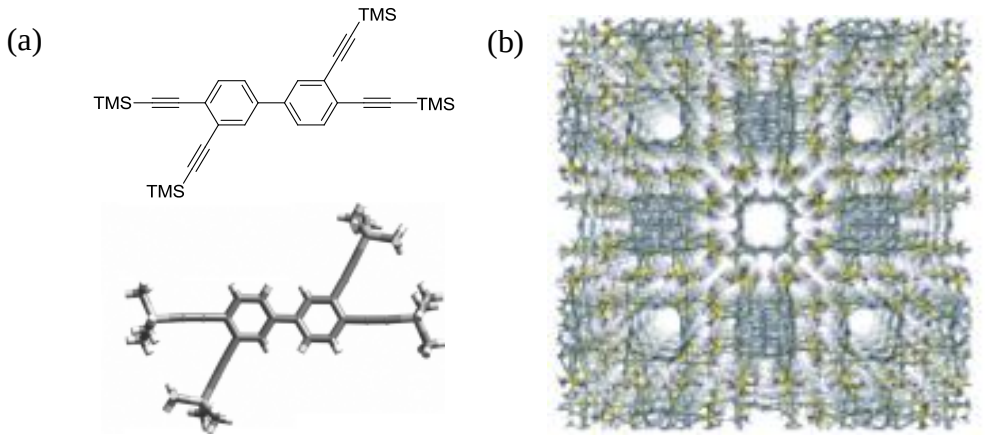

Figure 13. (a) The molecular structure of 4TMSEBP and its structure derived from the single crystal X-ray. (b) Crystal structure packing of 4TMSEBP.(Figure taken from Ref.[50])

1.4.5 Phthalocyanine metal nanoporous crystals (PNCs)

Phthalocyanine metal nanoporous crystals (PNCs)[64] show permanent microporosity in the solid sates (Figure 14). A series of substituted metal phthalocyanine complexes

form molecular crystals which result in various pore sizes and shapes. In order to prevent structural collapse during solvents removal, the axial ligands are replaced by exchange reactions and ditopic bipyridyl acts as molecular wall ties, bridging adjacent phthalocyanine molecules to stabilize cavities in the structures. The materials exhibit type I N_2 isotherms with high surface areas in the range from 850 to 1000 m^2 g^{-1} and pore volumes in the range of 0.40 to 0.46 mL g^{-1}.

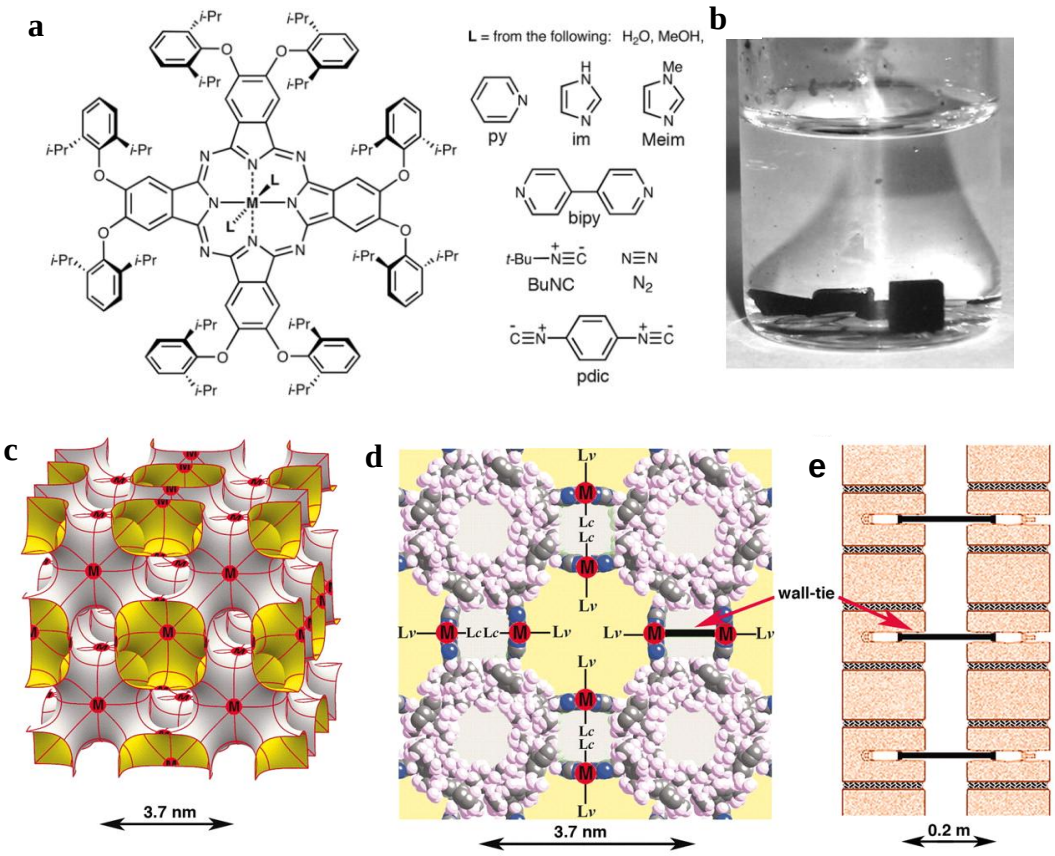

Figure 14. (a) The molecular structures of the metal phtalocyanine complexes and a series of axial ligands (L) are chosen. (b) The large and cubic crystals are grown by ligands exchange reactions. (c) The pore structure of a PNC is represented by triply periodic minimal surface. (d) The crystal structure of PNC shows pore voids. Lv is the ligand in the void and Lc is the ligand in the cavity. The intrinsic porosity is represented as yellow, and the extrinsic porosity is represented as gray. (e) Lc acts as molecular wall ties, bridging adjacent phthalocyanine molecules to stabilize cavities in the structures. (Figure taken from the Ref.[64])

1.4.6 Dipeptides

The four crystalline dipeptides, L-alanyl-L-valine (AV), L-valyl-L-alanine (VA), L-isoleucyl-L-valine (IV) and L-valyl-L-isoleucine (VI), assemble in a hexagonal packing to form 1D channels by hydrogen bonds (Figure 15).[65] The dipetides have hydrophobic channels and diameters of 5.0, 4.7, 3.9, 3.7 Å for AV, VA, IV and VI, respectively.[49] The gas sorption analysis of dipeptides was investigated by Sozzani and coworkers.[49] The CO_2 storage capacity of VA and AV was 4.1 mmol g^{-1} and 3.5 mmol g^{-1} at 195 K and 1 atm, respectively. The methane uptakes were 2.2 mmol g^{-1} and 1.6 mmol g^{-1} at 195 K and 1 atm for VA and AV. The CO_2/CH_4 selectivity was calculated to be 2-2.5 for VA and AV at 195 K and 1 atm.[49] The small channel diameter of IV shows a higher level of selectivity for CO_2 over CH_4 at mild conditions, due to the high affinity for the adsorption of CO_2.[49] The IV and VI molecular crystal also can adsorb 2.3 and 1.8 mmol g^{-1} of H_2, respectively, at 77 K and 10 bar, indicating the narrow channels are suitable for H_2 accommodation. Moreover, AV and VA are observed to have a high affinity for the adsorption of Xe.[66]

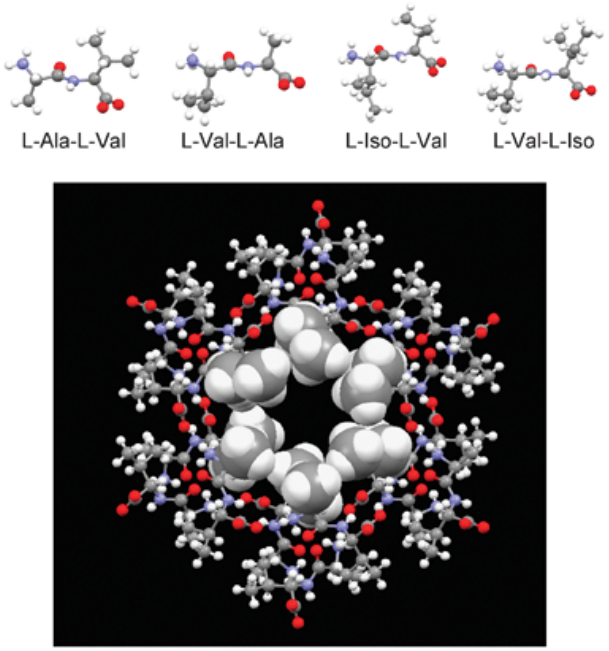

Figure 15. The molecular structures of L-alanyl-L-valine (AV), L-valyl-L-alanine (VA), L-isoleucyl-L-valine (IV) and L-valyl-L-isoleucine (VI). Crystal structure of

L-alanyl-L-valine (AV) with the open hydrophobic channel. The methyl groups point towards the channels.(Figure taken from the Ref.[49])

1.4.7 'Noria'

The 'Noria' molecule shows a 'waterwheel' structure with a large hydrophobic cavity and its gas sorption properties in the amorphous state have been reported by Atwood and coworkers(Figure 16).[67] It has a low N_2 and H_2 uptake, with a BET surface area of 40 m^2 g^{-1} calculated from the N_2 isotherm at 77 K. However, it displays a high absorption capacity for CO_2. The amorphous Noria material exhibits a type I CO_2 isotherm from which the surface area was calculated to be in the range of 280-350 m^2 g^{-1} and the pore volume of 0.13 cm^3 g^{-1}. The Noria molecule was the first amorphous porous organic molecule and showed selective uptake of CO_2 over H_2 and N_2. This study is particularly relevant to my own work on amorphous porous cages (See Chapters 5 and 6).

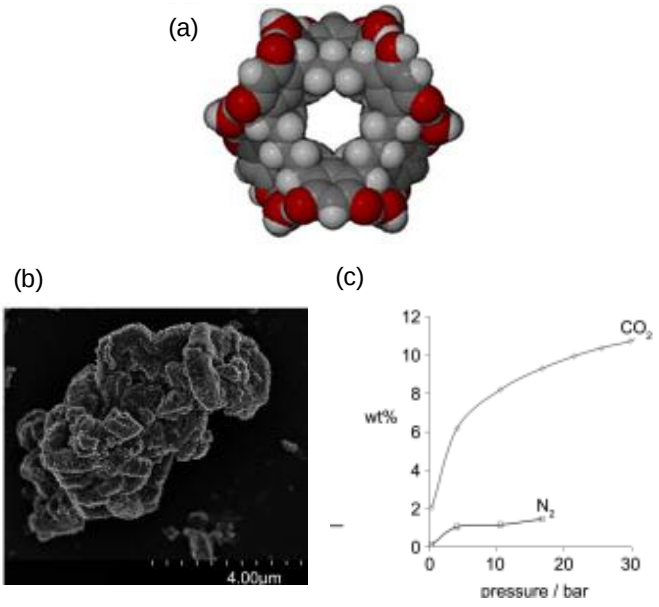

Figure 16. (a) Space-filling representation of the Noria molecule. (b) SEM image of amorphous Noria material. (c) Gravimetric CO_2 and N_2 capacity for amorphous Noria material at room temperature and 30 bar. (Figure taken from Ref.[67])

1.4.8 Triptycene trisbenzimidazolone (TTBI)

Very recently, Mastalerz and coworkers reported self-assembly of the rigid triptycene trisbenzimidazolone (TTBI) by hydrogen bonds to give the porous crystal in Figure 17a.[68] The molecules form 1D cylindrical channel (Pore A in Figure 17b) with an average diameter of 14.5 Å. In addition, slit-like pores (Pore B in Figure 17b) are generated between the cylindrical channels. The material absorbs a significant amount of N_2 (33.7 mmol g^{-1}) at 77 K and P/P_0 = 0.95. The measured BET surface area is 2796 m^2 g^{-1} and the Langmuir surface area is 3020 m^2 g^{-1}. The material adsorbs CO_2 (3.6 mmol g^{-1}) over CH_4 (0.9 mmol g^{-1}) at 273 K and 1 bar. The H_2 uptake is 11 mmol g^{-1} at 77 K and 1 bar. These values exceed all other porous organic molecules and are comparable to some MOFs, and this study represents a remarkable achievement in terms of crystal engineering for porous organic solids.[68]

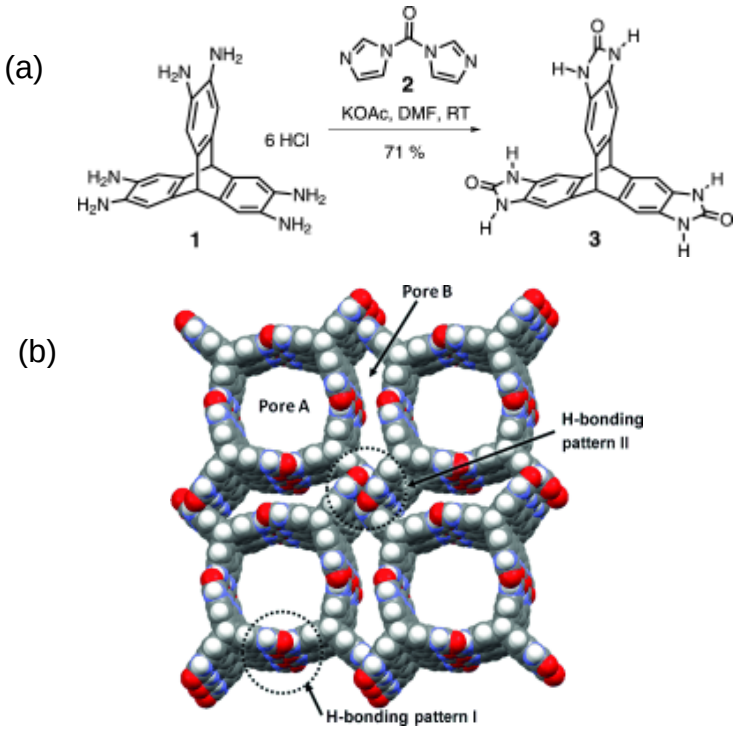

Figure 17. (a) Synthesis of triptycene trisbenzimidazolone molecule. (b) Crystal structure of molecules in 2 x 2 x 2 unit cell.(Figures taken from Ref.[68]) This material is currently the most porous molecular organic solid known.

1.5 Imine cage molecules

1.5.1 Warmuth research group

Warmuth and coworkers developed a number of molecular nanocages by a dynamic covalent chemistry approach.[69] The nanocage molecules were synthesized by the condensation reactions between tetraformylcavitand and a series of diamines. The [6+12] octahedral nanocage **1** consisted of six cavitands connecting by twelve 1,2-ethylenediamine linkers which was synthesized by the trifluoroacetic acid catalyzed cycloimination reaction. The reactions of tetraformylcavitand with 1,3-diaminopropane or 1,4-diaminobutane gave [2+4] cages.[69b] Furthermore, the tetrahedral, octahedral and square nanocages can be controlled by the solvent used for the reaction of cavitand and 1,2-ethylenediamine as illustrated in Figure 18.[69c] The rhombicuboctahedral nanocage was synthesized by six cavitands and eight triangular-shaped triamines.[70] These imine cage molecules possess large cavity volumes which can be used to encapsulate guest molecules. However, so far none of these materials has been reported to be porous, and there are no crystal structures for these molecules.

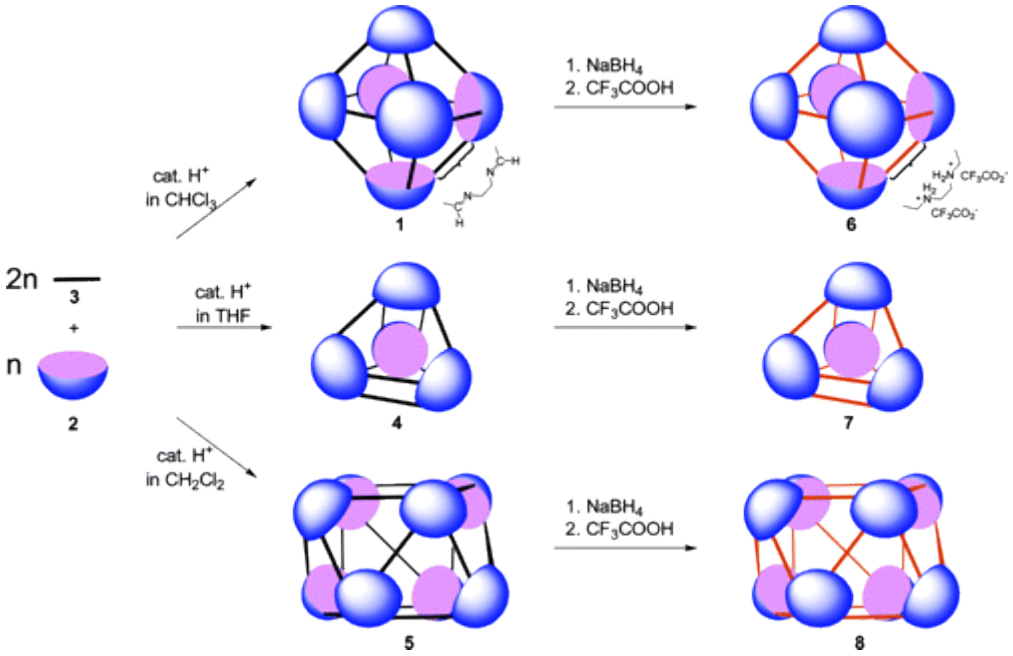

Figure 18. Three different nanocage molecules (octahedral, tetrahedral,

square-antiprismatic) are produced in different solvents ($CHCl_3$, THF, and CH_2Cl_2, respectively). (Figure taken from Ref.[69c])

1.5.2 Mastalerz research group

Mastalerz and coworkers reported salicylbisimine cage molecule with a large internal pore volume (Figure 19).[71] The packing of these cage molecules creates an interconnected 3D pore network which is dictated by π-π stacking interactions. The material has high thermal stability. To evaluate its permanent porosity, gas sorption isotherms (N_2, CH_4 and CO_2) were measured.[71c] The calculated surface areas based on the N_2 isotherm are 1566 $m^2\ g^{-1}$ (Langmuir) and 1375 $m^2\ g^{-1}$ (BET). The material is able to adsorb 2.1 mmol g^{-1} CO_2 and 0.6 mmol g^{-1} CH_4 at 273 K and 1 bar. The porous cage molecule shows good selectivity for CO_2 over CH_4 (10/1 (mmol/mmol)).

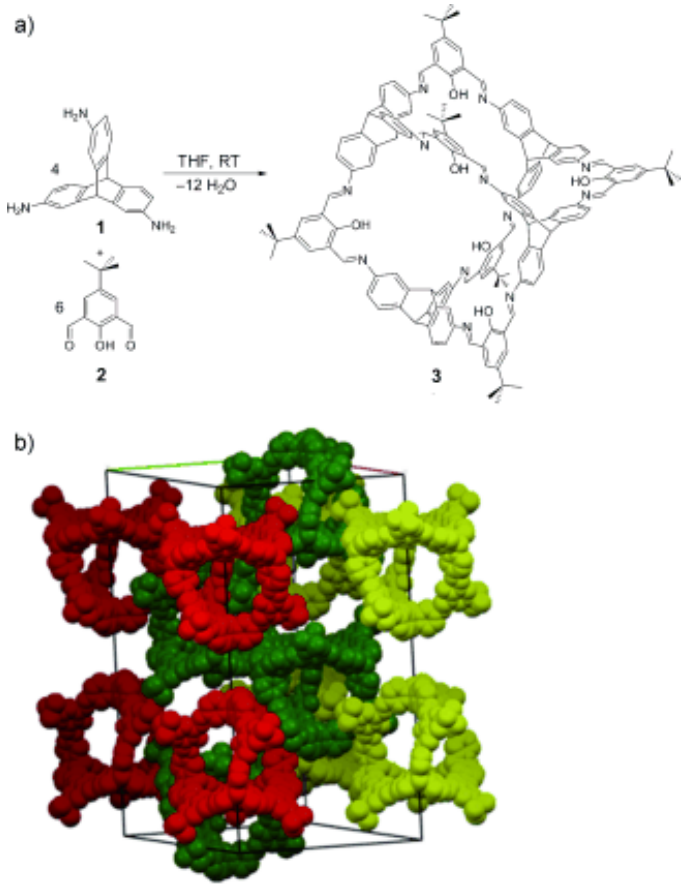

Figure 19. (a) Synthesis of the salicylbisimine cage by triamine and salicylic

dialdehyde in a [4+6] cycloimination reaction. (b) Crystal packing of the molecules in the unit cell. (Figure taken from Ref.[71c])

In addition, a series of periphery-substituted shape-persistent cage compounds were synthesized by Mastalerz and coworkers[72] The cage compounds showed permanent porosity in both crystalline and amorphous solid states. The amorphous cages with various functionalities have surface areas in a range 690 to 727 $m^2 g^{-1}$. The bulkiness of the peripheral groups has a significant effect on the surface areas of the crystalline cage materials. The cage compound with methyl groups at the periphery has a BET surface area of 1291 $m^2 g^{-1}$, while the value is 309 $m^2 g^{-1}$ for the cage with 3-ethylpentyl groups, and 22 $m^2 g^{-1}$ for the cage with trityl groups. One crystalline polymorph of the cage compound with *tert*-butyl groups at the periphery displays a remarkably high BET surface area of 2071 $m^2 g^{-1}$. Mastalerz and coworkers used a synthetic approach to control the morphology and size of the materials particles for periphery-substituted shape-persistent cage compounds. The amorphous cage materials have a BET surface area of approximately 700 $m^2 g^{-1}$, When the cage compounds are crystalline or nanospheres, the surface areas are lower.[73]

A study has been carried out to investigate the influence of the rigidity of the molecular structure of [2+3] cage compounds synthesized by an imine condensation of triptycene triamine and bissalicylaldehyde.[74] The cage compound with a short organic linker (3a shown in Figure 20) adsorbs 12.8 mmol g^{-1} of N_2 at 77 K and P/P_o = 0.95 and the calculated BET surface area is 744 $m^2 g^{-1}$. In contrast, the [2+3] cage with a long organic linker (3b in Figure 20) shows a low level of porosity with a BET surface area of 30 $m^2 g^{-1}$. Interestingly, 3b exhibits a high uptake of CO_2 at 298 K and 1 bar and results in a high selectivity of 10 (mmol/mmol) for CO_2 over CH_4.

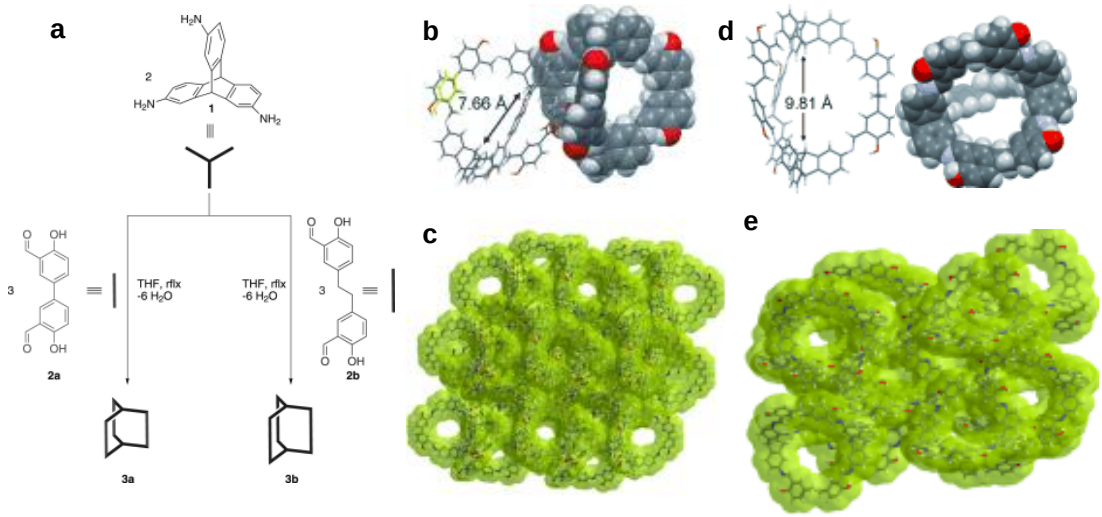

Figure 20. (a) Synthesis of [2+3] cage compounds 3a and 3b. (b) The cage molecule 3a depicted using both a capped-stick and space-filling models. (c) Crystal packing of 2 x 2 x 2 super cell of 3a. (d) The cage molecule 3b depicted with both capped-stick and space-filling models. (e) Crystal packing of 2 x 2 x 2 super cell of 3b. (Figure taken from the Ref.[74])

1.5.3 Cooper research group

A series of imine cage molecules has been synthesized in the Cooper research group and the molecular structures are shown in Figure 21.[23a, 75] The cage molecules can be desolvated to generate permanent porosity to gas molecules such as nitrogen, hydrogen, methane, and carbon dioxide. The crystal porosity of these materials is a result of both of the intrinsic molecular voids and extrinsic voids from the inefficient packing of cage molecules. Pore structure and connectivity is strongly directed by functional groups attached to the cage vertices such that it is possible to connect or disconnect the void volume in the organic crystals. These porous organic cages have high surface areas and gas uptakes compared to other porous organic molecules.[12, 67]

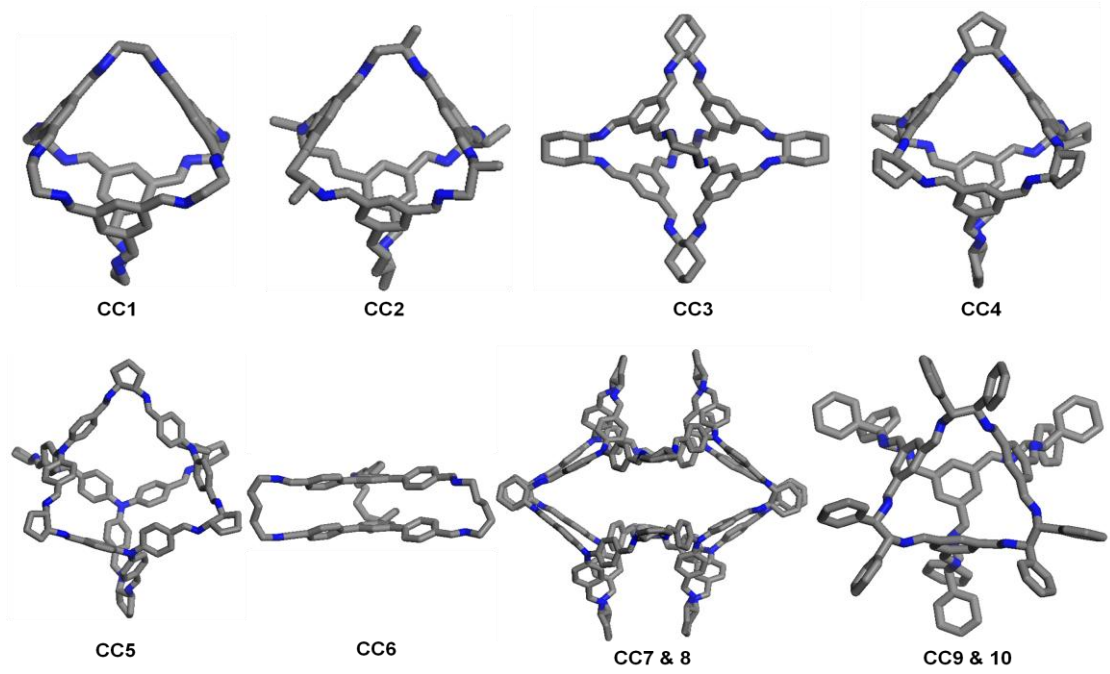

Figure 21. The cage structures synthesized in the Cooper group obtained from single crystal X-ray diffraction. (Figures taken from Refs [23a, 75], molecules not all shown on the same scale).

Initially, **CC1**-**CC3** were synthesized by the condensation reaction of 1,3,5-triformylbenzene with 1,2-ethylenediamine, 1,2-propylenediamine, and (*R*,*R*)-1,2-diaminocyclohexane, respectively, in a simple one-step [4 + 6] cycloimination.[75a] Products were isolated directly as crystals which were characterized by single crystal X-ray diffraction. The molecular structures show that **CC1** has un-functionalized ethylene linkers on the six vertices. **CC2** has one methyl group on each vertex. The synthesis and characterization of **CC2** will be discussed in details in Chapter 3. **CC3** has relatively bulky cyclohexyl groups on the vertices.

The **CC1** crystal packing shows isolated cage voids from the Connolly surfaces generated using a N_2 probe of 1.82 Å (Figure 22a). **CC2** gives 1D pore channels running between the cages which are coloured by yellow Connolly surfaces (Figure 22b) and also shows cage void volumes (orange coloured by Connolly surfaces in Figure 22b). However, the cage void volumes are lack of connection with 1D pore channels due to no cage windows facing to the cage channels. The bulkier cyclohexyl

groups in **CC3** direct the cages to pack window-to-window, leading to the interconnected diamondoid pore channel structure in Figure 22c.

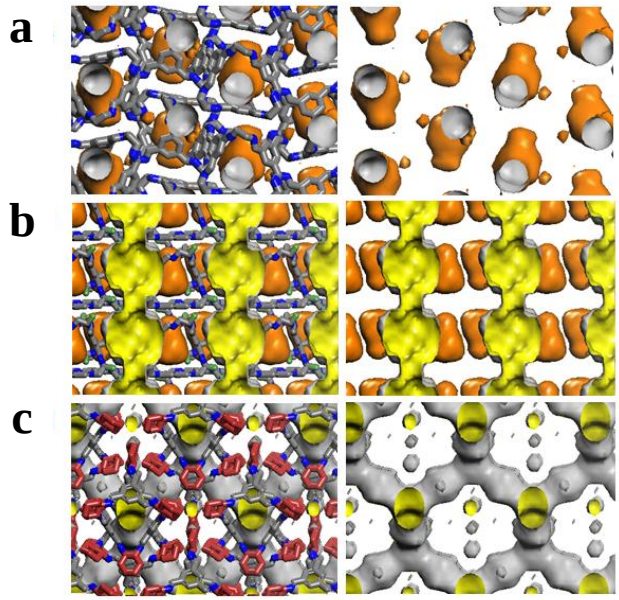

Figure 22. Varying the vertex functionality for CC1-3. The Connolly surface areas are generated for each cage structures using a N_2 probe of 1.82 Å. Pore structure and connectivity of (a) **CC1**, (b) **CC2** and (c) **CC3**. (Figure taken from the Ref.[75a])

Gas sorption studies were used to investigate the porosity of these materials. **CC1** adsorbs little N_2 or H_2 compared with **CC2** and **CC3** at 77 K. This is consistent with the disconnected void structure in **CC1.** The apparent BET surface area for **CC1** is 23 m^2g^{-1}. **CC1** can form three polymorphs in the solid state by recrystallization in different organic solvents and the gas porosity and selectivity in these polymorphs can be interconverted reversibly.[76] **CC1α** is non-porous to N_2 and H_2. **CC1β** is selectively porous to H_2 only. **CC1γ** is porous to both N_2 and H_2.

CC2 exhibits a Type I N_2 sorption isotherm and adsorbs a total of 7.52 mmol g^{-1} N_2 at 77.3 K and 1 bar. The BET surface area is 533 m^2 g^{-1}. **CC2** adsorbs 8.88 mmol g^{-1} H_2 (1.75 wt. %) at 77.3 K and 7 bar. The CO_2 isotherm for **CC2** reveals a gas uptake (3.0 mmol/g) at 275K, 1 bar. The gas uptake for CH_4 is 0.95 mmol g^{-1} at 289 K, 1 bar.

CC3 also shows a Type I N_2 sorption isotherm with a BET surface area of 624 $m^2 g^{-1}$. The material can adsorb 8.17 mmol g^{-1} N_2 at 77.3 K and 1 bar. The CH_4 uptake is 1.15 mmol g^{-1} at 289 K, 1bar and the CO_2 uptake is 2.47 mmol g^{-1} at 275 K, 1bar.

CC4 is obtained from the reaction of (*R*,*R*)-1,2-diaminocyclopentane with 1,3,5-triformylbenzene.[75e] The cage packing shows a complex pore structure with a close intermolecular interaction. The N_2 sorption shows a four steps isotherm with a large degree of hysteresis at 77 K. The sorption behavior is dictated by the molecular packing and flexibility of cages.

CC5 is synthesized by the [4+6] cycloimination reaction between tri(4-formylphenyl)amine and the diamine (*R*,*R*)-1,2-cyclopentanediamine. The material exhibits a higher BET surface area of 1333 $m^2 g^{-1}$ and a larger pore volume.[75d]

It has been shown that co-crystals can be produced by mixing different organic cage molecules (**CC1**, **CC3** and **CC4**) (Figure 23).[75d] Due to conformer inter-conversion, **CC1** exists as equal amounts of its *R* and *S* enantiomers in solution.[77] The co-crystallization of a mixture of **CC1** and homochiral **CC3-R** results in a heterochiral co-crystal of **CC1-S** and **CC3-R** with a BET surface area of 437 $m^2 g^{-1}$. The enantiomers **CC3-S** and **CC3-R** also strongly assemble in a **CC3-S** / **CC3-R** racemic co-crystal with a BET surface area of 873 $m^2 g^{-1}$. A racemic co-crystal of **CC4-S** / **CC3-R** can be formed with a BET surface area of 980 $m^2 g^{-1}$. The crystal packing arrangements of mixtures of cages are predicted by molecular simulations. The co-crystal of **CC5** was not observed in the experiments, as homochiral crystals with window to window packing are strongly energetically preferred compared to the racemic crystals from calculations.[75d]

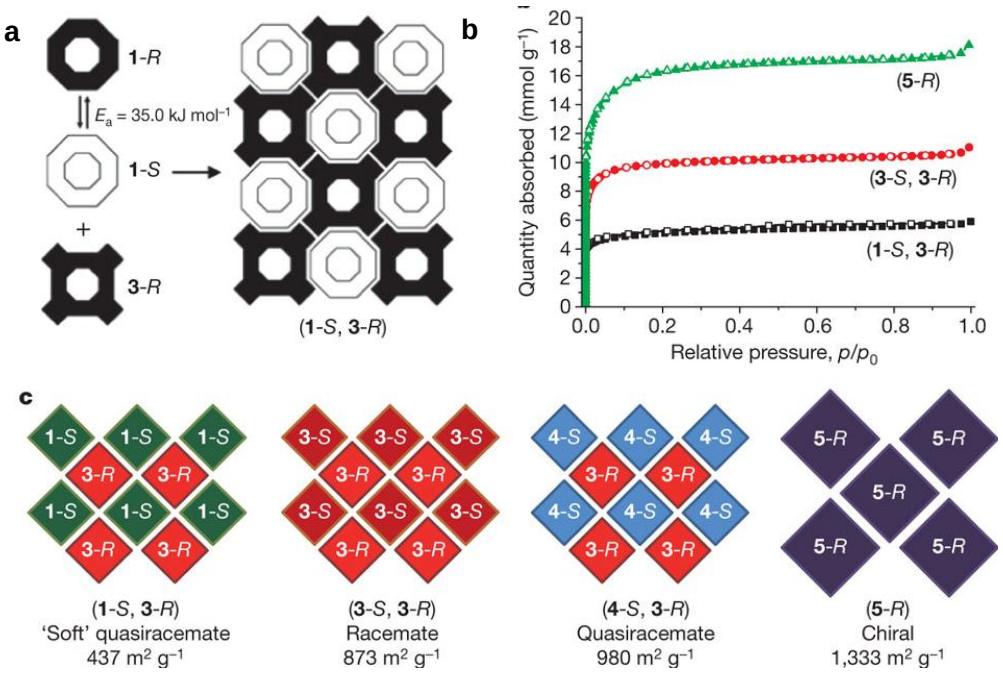

Figure 23. (a) The co-crystallization of **CC1** and homochiral **CC3-R**. (b) Nitrogen gas sorption isotherms for co-crystals and **CC5-R**. (c) The packing diagram for various crsytals and co-crystals. (Figure taken from Ref.[75d])

CC6 is synthesized from the condensation reaction of 1,3,5-tri-(4-formylphenyl)benzene with 1,5-pentanediamine. The cage molecule possesses a [2+3] topology with little cage void. A narrow 1D channel is generated by molecular packing. **CC6** shows selective adsorption of H_2 and CO_2 over N_2. More details will be described in Chapter 4.

Two [8+12] large self-assembled cage molecules **CC7** and **CC8** were reported by the imine condensation reactions of tris(4-formylphenyl)amine and the chiral diamines (*R*,*R*)-1,2-cyclohexanediamine and (*R*,*R*)-1,2-cyclohex-4-enediamine, respectively.[75c] The cage molecules have void diameters of 1.2 nm, and solvent (dichloromethane) is observed to occupy more than 70 % of the available solvent accessible volume which is equal to 80 and 75 DCM molecules per cage molecule for **CC7** and **CC8**, respectively, from the X-ray diffraction data. The topology is similar to that of the [8+12] chiral nanocube structure proposed by Warmuth.[78] Upon desolvation, the materials become amorphous, and they were not found to adsorb N_2 at 77 K.

Molecular dynamics simulations suggest that the large voids in the solvated phase collapse upon solvent removal (Figure 24).

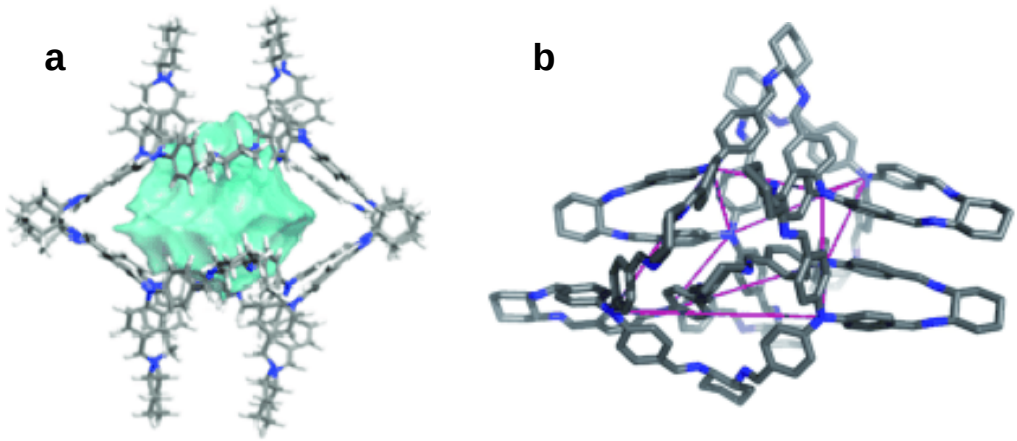

Figure 24. (a) **CC7** molecular structure obtained from single crystal X-ray structure of solvated **CC7**. (b) A representative collapsed cage obtained from the final configuration of a 10 ns NPT MD simulation of a desolvated **CC7** cell. (Figure adapted from Ref.[75c])

CC9 and **CC10** cage molecules with bulky aryl groups attached to the vertices have been reported (Figure 25).[75b] The vertex functionality enhanced the extrinsic porosity, and a polymorph study was carried out for these cage molecules. These materials have high gas uptakes.

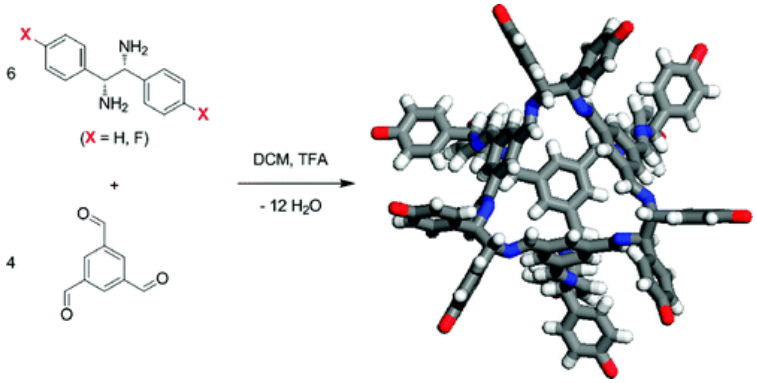

Figure 25. Imine reaction for the [4 + 6] Schiff-base condensation yielding **CC9** (X = H) and **CC10** (X = F) cage molecules. (Figure taken from the Ref.[75b])

A series of amorphous scrambled cage molecules has also been synthesized. These amorphous cage molecules show high level of porosities (BET surface areas up to

898 m^2 g^{-1}) and gas selectivity can be tuned by the cage functionality. Chapters 5 and 6 describe an experimental and molecular dynamic study on these amorphous cage materials.

1.5.4 Zhang research group

Zhang and his co-workers have synthesized a shape-persistent organic cage molecule in a [2+3] cycloimination reaction.[79] This cage molecule has a very small internal void and the packing diagram shows that the molecules close pack to each other in a layered structure form (Figure 26). The crystalline [2+3] cage material showed a low gas uptake of CO_2 and H_2 at 1 bar and 20 ºC. The gas uptake of CO_2 was 0.19 mmol g^{-1}, whereas the material hardly adsorbed N_2 (0.0027 cm^3 g^{-1}). However, the material displayed a high ideal CO_2/N_2 (CO_2/N_2 = 73/1 (mmol/mmol)) adsorption selectivity at 1 bar and 20 ºC. In addition, the imine reduction reaction for the cage molecule was carried out. The CO_2/N_2 adsorption selectivity for the amine cage material at 1 bar and 20 ºC decreased to 39/1(mmol/mmol). The authors suggested that the good gas selectivity can be attributed to the well-defined pore structure and the strong interaction of CO_2 with the imine groups of the cage molecules, although in reality the selectivity must be considered in the context of the capacity, as pointed out in a publication arising from my own work.[23a]

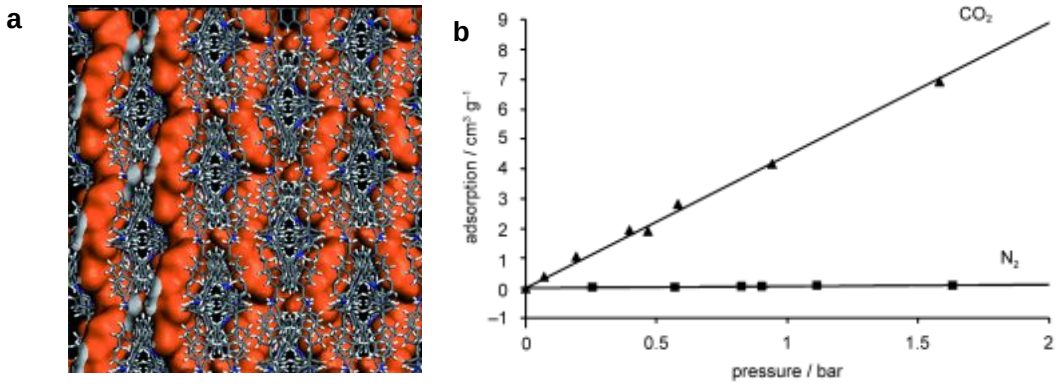

Figure 26. (a) Crystal packing of [2+3] cage molecules. The 1D channels are shown using an orange Connolly surface (probe radius of 1.82 Å). (b) CO_2 and N_2 adsorption isotherms at 20 °C and 2 bar. (Figure taken from the Ref.[79])

The same research group also reported a series of related [2+3] cage compounds with different sizes of internal cavities that exhibited ideal CO_2/N_2 selectivity in the range from 36/1 (mmol/mmol) to 138/1 (mmol/mmol) at 20 ºC and 1 bar.[80] Although the actual CO_2 adsorption capacity of these [2+3] cage molecules at 1 bar and 20 ºC is much lower than other organic molecules published, the selectivity is extraordinarily high, although errors may be substantial when gas capacities become this low. Moreover, a series of organic cage frameworks were reported by Zhang and coworkers with ideal gas selectivities for CO_2/N_2 of up to 213/1 (mmol/mmol) at 1 bar and 20 ºC.

1.6 Aims of this PhD project

My PhD project aims to synthesize and simulate crystalline and amorphous porous organic cages for potential applications in gas storage and separation. The cage molecules are synthesized in a simple one-step cycloimination reaction by various trialdehyde and diamine monomers. The molecules pack in the solid state by weak wan der Waals interactions. The porosity in these materials is due to both the intrinsic molecular voids and extrinsic voids from inefficient packing. First, I aim to investigate that the effect of functional groups on the cage vertices on the porosity of the crystalline cage materials. Next I will attempt to design crystalline cage molecules that are capable of selective guest binding for gas separation. Furthermore, amorphous cage molecules will be also investigated. I will study the gas selectivity in these materials and how to tune the properties by modifying reaction conditions or introducing functionality in the cages.

On the basis of the materials obtained by synthesis, molecular simulations will be used to rationalize the properties and understand molecular packing. In particular with respect to gas selectivity, molecular dynamics are carried out to simulate gas diffusion properties. For the amorphous cage materials, a simulation methodology is used to generate amorphous cage models. This method will be applicable to structure generation of other classes of amorphous molecules. In the future, I hope it can be

used to predict properties of other amorphous cage molecules and related molecular materials.

1.7 References

1. (a) Dawson, R.; Cooper, A. I.; Adams, D. J., Nanoporous organic polymer networks. *Prog.Polym.Sci.* **2012,** *37* (4), 530-563; (b) Jiang, J.-X.; Cooper, A., Microporous Organic Polymers: Design, Synthesis, and Function Functional Metal-Organic Frameworks: Gas Storage, Separation and Catalysis. Schröder, M., Ed. Springer Berlin / Heidelberg: 2010; Vol. 293, pp 1-33; (c) Li, J.-R.; Kuppler, R. J.; Zhou, H.-C., Selective gas adsorption and separation in metal-organic frameworks. *Chem. Soc. Rev.* **2009,** *38* (5), 1477-1504.
2. Sing, K. S. W.; Everett, D. H.; Haul, R. A.; Moscou, W. L.; Pierotti, R. A.; Rouquérol, J.; Siemieniewska, T., Reporting physisorption data for gas/solid systems with special reference to the determination of surface area and porosity (Recommendations 1984). *Pure Appl. Chem.* **1985,** *57*, 603-619.
3. Hydrogen storage. http://www.hydrogen.energy.gov/storage.html.July 2012
4. Burchell, T. R., M., *SAE Tech. Pap. Ser.* **2000,** (2000-01-2205).
5. Wegrzyn, J.; Gurevich, M., Adsorbent storage of natural gas. *Appl. Energ.* **1996,** *55* (2), 71-83.
6. Nishi, K.; Thompson, R. W., Synthesis of Classical Zeolites. In *Handbook of Porous Solids*, Wiley-VCH Verlag GmbH: 2008; pp 736-814.
7. Rodríguez-Reinoso, F., Production and applications of activated carbons. *Handbook of Porous Solids* **2002**, 1786-1827.
8. Côté, A. P.; Benin, A. I.; Ockwig, N. W.; O'Keeffe, M.; Matzger, A. J.; Yaghi, O. M., Porous, Crystalline, Covalent Organic Frameworks. *Science* **2005,** *310* (5751), 1166-1170.
9. Rowsell, J. L. C.; Yaghi, O. M., Metal–organic frameworks: a new class of porous materials. *Microporous Mesoporous Mater*. **2004,** *73* (1–2), 3-14.
10. Budd, P. M.; Ghanem, B. S.; Makhseed, S.; McKeown, N. B.; Msayib, K. J.; Tattershall, C. E., Polymers of intrinsic microporosity (PIMs): robust, solution-processable, organic nanoporous materials. *Chem. Commun.* **2004,** (2), 230-231.
11. Jiang, J.-X.; Su, F.; Trewin, A.; Wood, C. D.; Campbell, N. L.; Niu, H.; Dickinson, C.; Ganin, A. Y.; Rosseinsky, M. J.; Khimyak, Y. Z.; Cooper, A. I., Conjugated Microporous Poly(aryleneethynylene) Networks. *Angew. Chem. Int. Ed.* **2007,** *46* (45), 8574-8578.
12. Holst, J. R.; Trewin, A.; Cooper, A. I., Porous organic molecules. *Nat. Chem.* **2010,** *2* (11), 915-920.
13. (a) Kuppler, R. J.; Timmons, D. J.; Fang, Q.-R.; Li, J.-R.; Makal, T. A.; Young, M. D.; Yuan, D.; Zhao, D.; Zhuang, W.; Zhou, H.-C., Potential applications of metal-organic frameworks. *Coord. Chem. Rev.* **2009,** *253* (23–24), 3042-3066; (b)

Gu, Z.-Y.; Jiang, D.-Q.; Wang, H.-F.; Cui, X.-Y.; Yan, X.-P., Adsorption and Separation of Xylene Isomers and Ethylbenzene on Two Zn−Terephthalate Metal−Organic Frameworks. *J. Phys. Chem. C* **2009,** *114* (1), 311-316.
14. Yaghi, O. M.; O'Keeffe, M.; Ockwig, N. W.; Chae, H. K.; Eddaoudi, M.; Kim, J., Reticular synthesis and the design of new materials. *Nature* **2003,** *423* (6941), 705-714.
15. Rosi, N. L.; Eckert, J.; Eddaoudi, M.; Vodak, D. T.; Kim, J.; O'Keeffe, M.; Yaghi, O. M., Hydrogen Storage in Microporous Metal-Organic Frameworks. *Science* **2003,** *300* (5622), 1127-1129.
16. Furukawa, H.; Ko, N.; Go, Y. B.; Aratani, N.; Choi, S. B.; Choi, E.; Yazaydin, A. Ö.; Snurr, R. Q.; O'Keeffe, M.; Kim, J.; Yaghi, O. M., Ultrahigh Porosity in Metal-Organic Frameworks. *Science* **2010,** *329* (5990), 424-428.
17. Furukawa, H.; Miller, M. A.; Yaghi, O. M., Independent verification of the saturation hydrogen uptake in MOF-177 and establishment of a benchmark for hydrogen adsorption in metal-organic frameworks. *J. Mater. Chem.* **2007,** *17* (30), 3197-3204.
18. Yan, Y.; Lin, X.; Yang, S.; Blake, A. J.; Dailly, A.; Champness, N. R.; Hubberstey, P.; Schroder, M., Exceptionally high H_2 storage by a metal-organic polyhedral framework. *Chem. Commun.* **2009,** (9), 1025-1027.
19. Eddaoudi, M.; Kim, J.; Rosi, N.; Vodak, D.; Wachter, J.; O'Keeffe, M.; Yaghi, O. M., Systematic Design of Pore Size and Functionality in Isoreticular MOFs and Their Application in Methane Storage. *Science* **2002,** *295* (5554), 469-472.
20. Millward, A. R.; Yaghi, O. M., Metal−Organic Frameworks with Exceptionally High Capacity for Storage of Carbon Dioxide at Room Temperature. *J. Am. Chem. Soc.* **2005,** *127* (51), 17998-17999.
21. Llewellyn, P. L.; Bourrelly, S.; Serre, C.; Vimont, A.; Daturi, M.; Hamon, L.; De Weireld, G.; Chang, J.-S.; Hong, D.-Y.; Kyu Hwang, Y.; Hwa Jhung, S.; Férey, G. r., High Uptakes of CO_2 and CH_4 in Mesoporous Metal Organic Frameworks MIL-100 and MIL-101. *Langmuir* **2008,** *24* (14), 7245-7250.
22. Alaerts, L.; Kirschhock, C. E. A.; Maes, M.; van der Veen, M. A.; Finsy, V.; Depla, A.; Martens, J. A.; Baron, G. V.; Jacobs, P. A.; Denayer, J. F. M.; De Vos, D. E., Selective Adsorption and Separation of Xylene Isomers and Ethylbenzene with the Microporous Vanadium(IV) Terephthalate MIL-47. *Angew. Chem. Int. Ed.* **2007,** *46* (23), 4293-4297.
23. (a) Jiang, S.; Bacsa, J.; Wu, X.; Jones, J. T. A.; Dawson, R.; Trewin, A.; Adams, D. J.; Cooper, A. I., Selective gas sorption in a [2+3] 'propeller' cage crystal. *Chem. Commun.* **2011,** *47* (31), 8919-8921; (b) Rose, M.; Bohlmann, W.; Sabo, M.; Kaskel, S., Element-organic frameworks with high permanent porosity. *Chem. Commun.* **2008,** (21), 2462-2464.
24. El-Kaderi, H. M.; Hunt, J. R.; Mendoza-Cortés, J. L.; Côté, A. P.; Taylor, R. E.; O'Keeffe, M.; Yaghi, O. M., Designed Synthesis of 3D Covalent Organic Frameworks. *Science* **2007,** *316* (5822), 268-272.
25. (a) Mendoza-Cortés, J. L.; Han, S. S.; Furukawa, H.; Yaghi, O. M.; Goddard, W. A., Adsorption Mechanism and Uptake of Methane in Covalent Organic Frameworks:

Theory and Experiment. *J. Phys. Chem. A* **2010,** *114* (40), 10824-10833; (b) Furukawa, H.; Yaghi, O. M., Storage of Hydrogen, Methane, and Carbon Dioxide in Highly Porous Covalent Organic Frameworks for Clean Energy Applications. *J. Am. Chem. Soc.* **2009,** *131* (25), 8875-8883.
26. Han, S. S.; Furukawa, H.; Yaghi, O. M.; Goddard, W. A., Covalent Organic Frameworks as Exceptional Hydrogen Storage Materials. *J. Am. Chem. Soc.* **2008,** *130* (35), 11580-11581.
27. McKeown, N. B.; Budd, P. M., Polymers of intrinsic microporosity (PIMs): organic materials for membrane separations, heterogeneous catalysis and hydrogen storage. *Chem. Soc. Rev.* **2006,** *35* (8), 675-683.
28. McKeown, N. B.; Makhseed, S.; Budd, P. M., Phthalocyanine-based nanoporous network polymers. *Chem. Commun.* **2002,** (23), 2780-2781.
29. McKeown, N. B.; Hanif, S.; Msayib, K.; Tattershall, C. E.; Budd, P. M., Porphyrin-based nanoporous network polymers. *Chem. Commun.* **2002,** (23), 2782-2783.
30. Budd, P. M.; Ghanem, B.; Msayib, K.; McKeown, N. B.; Tattershall, C., A nanoporous network polymer derived from hexaazatrinaphthylene with potential as an adsorbent and catalyst support. *J. Mater. Chem.* **2003,** *13* (11), 2721-2726.
31. McKeown, N. B.; Gahnem, B.; Msayib, K. J.; Budd, P. M.; Tattershall, C. E.; Mahmood, K.; Tan, S.; Book, D.; Langmi, H. W.; Walton, A., Towards Polymer-Based Hydrogen Storage Materials: Engineering Ultramicroporous Cavities within Polymers of Intrinsic Microporosity. *Angew. Chem. Int. Ed.* **2006,** *45* (11), 1804-1807.
32. Ghanem, B. S.; Msayib, K. J.; McKeown, N. B.; Harris, K. D. M.; Pan, Z.; Budd, P. M.; Butler, A.; Selbie, J.; Book, D.; Walton, A., A triptycene-based polymer of intrinsic microposity that displays enhanced surface area and hydrogen adsorption. *Chem. Commun.* **2007,** (1), 67-69.
33. Peter M. Budd, N. B. M., Detlev Fritsch, Polymers of Intrinsic Microporosity (PIMs): High Free Volume Polymers for Membrane Applications. *Macromol. Symp. 245-246* (1).
34. J-X. Jiang, a. A. I. C., Microporous organic polymers: design, synthesis and function. *Topics Curr. Chem.* **2101,** *293*, 33.
35. Jiang, J.-X.; Su, F.; Trewin, A.; Wood, C. D.; Niu, H.; Jones, J. T. A.; Khimyak, Y. Z.; Cooper, A. I., Synthetic Control of the Pore Dimension and Surface Area in Conjugated Microporous Polymer and Copolymer Networks. *J. Am. Chem. Soc.* **2008,** *130* (24), 7710-7720.
36. Jiang, J.-X.; Wang, C.; Laybourn, A.; Hasell, T.; Clowes, R.; Khimyak, Y. Z.; Xiao, J.; Higgins, S. J.; Adams, D. J.; Cooper, A. I., Metal–Organic Conjugated Microporous Polymers. *Angew. Chem. Int. Ed.* **2011,** *50* (5), 1072-1075.
37. Chen, L.; Yang, Y.; Jiang, D., CMPs as Scaffolds for Constructing Porous Catalytic Frameworks: A Built-in Heterogeneous Catalyst with High Activity and Selectivity Based on Nanoporous Metalloporphyrin Polymers. *J. Am. Chem. Soc.* **2010,** *132* (26), 9138-9143.
38. Jiang, J.-X.; Trewin, A.; Adams, D. J.; Cooper, A. I., Band gap engineering in

fluorescent conjugated microporous polymers. *Chem. Sci.* **2011,** *2* (9), 1777-1781.
39. Chen, L.; Honsho, Y.; Seki, S.; Jiang, D., Light-Harvesting Conjugated Microporous Polymers: Rapid and Highly Efficient Flow of Light Energy with a Porous Polyphenylene Framework as Antenna. *J. Am. Chem. Soc.* **2010,** *132* (19), 6742-6748.
40. Rose, M.; Klein, N.; Bohlmann, W.; Bohringer, B.; Fichtner, S.; Kaskel, S., New element organic frameworks viaSuzuki coupling with high adsorption capacity for hydrophobic molecules. *Soft Matter* **2010,** *6* (16), 3918-3923.
41. Ben, T.; Ren, H.; Ma, S.; Cao, D.; Lan, J.; Jing, X.; Wang, W.; Xu, J.; Deng, F.; Simmons, J. M.; Qiu, S.; Zhu, G., Targeted Synthesis of a Porous Aromatic Framework with High Stability and Exceptionally High Surface Area. *Angew. Chem. Int. Ed.* **2009,** *48* (50), 9457-9460.
42. Yuan, D.; Lu, W.; Zhao, D.; Zhou, H.-C., Highly Stable Porous Polymer Networks with Exceptionally High Gas-Uptake Capacities. *Adv. Mater.* **2011,** *23* (32), 3723-3725.
43. (a) Tian, J.; Thallapally, P. K.; McGrail, B. P., Porous organic molecular materials. *CrystEngComm*, **2012,** *14* (6), 1909-1919; (b) McKeown, N. B., Nanoporous molecular crystals. *J. Mater. Chem.* **2010,** *20* (47), 10588-10597.
44. Barbour, L. J., Crystal porosity and the burden of proof. *Chem. Commun.* **2006,** (11), 1163-1168.
45. Sircar, S., Basic Research Needs for Design of Adsorptive Gas Separation Processes. *Ind. Eng. Chem. Res.* **2006,** *45* (16), 5435-5448.
46. Atwood, J. L.; Barbour, L. J.; Jerga, A.; Schottel, B. L., Guest Transport in a Nonporous Organic Solid via Dynamic van der Waals Cooperativity. *Science* **2002,** *298* (5595), 1000-1002.
47. Atwood, J. L.; Barbour, L. J.; Jerga, A., Storage of Methane and Freon by Interstitial van der Waals Confinement. *Science* **2002,** *296* (5577), 2367-2369.
48. Lim, S.; Kim, H.; Selvapalam, N.; Kim, K.-J.; Cho, S. J.; Seo, G.; Kim, K., Cucurbit[6]uril: Organic Molecular Porous Material with Permanent Porosity, Exceptional Stability, and Acetylene Sorption Properties. *Angew. Chem. Int. Ed.* **2008,** *47* (18), 3352-3355.
49. Comotti, A.; Bracco, S.; Distefano, G.; Sozzani, P., Methane, carbon dioxide and hydrogen storage in nanoporous dipeptide-based materials. *Chem. Commun.* **2009,** (3), 284-286.
50. Msayib, K. J.; Book, D.; Budd, P. M.; Chaukura, N.; Harris, K. D. M.; Helliwell, M.; Tedds, S.; Walton, A.; Warren, J. E.; Xu, M.; McKeown, N. B., Nitrogen and Hydrogen Adsorption by an Organic Microporous Crystal. *Angew. Chem. Int. Ed.* **2009,** *48* (18), 3273-3277.
51. Gutsche, C. D., Calixarenes: An Introduction (Monographs in Supramolecular Chemistry). Stoddart, J. F., Ed. RSC publishing: 2008.
52. Gutsche, C. D.; Dhawan, B.; No, K. H.; Muthukrishnan, R., Calixarenes. 4. The synthesis, characterization, and properties of the calixarenes from p-tert-butylphenol. *J. Am. Chem. Soc.* **1981,** *103* (13), 3782-3792.
53. (a) Ananchenko, G. S.; Moudrakovski, I. L.; Coleman, A. W.; Ripmeester, J. A.,

A Channel-Free Soft-Walled Capsular Calixarene Solid for Gas Adsorption. *Angew. Chem. Int. Ed.* **2008,** *47* (30), 5616-5618; (b) Ananchenko, G. S.; Udachin, K. A.; Dubes, A.; Ripmeester, J. A.; Perrier, T.; Coleman, A. W., Guest Exchange in Single Crystals of van der Waals Nanocapsules. *Angew. Chem. Int. Ed.* **2006,** *45* (10), 1585-1588.

54. Atwood, J. L.; Barbour, L. J.; Jerga, A., A New Type of Material for the Recovery of Hydrogen from Gas Mixtures. *Angew. Chem. Int. Ed.* **2004,** *43* (22), 2948-2950.

55. Thallapally, P. K.; McGrail, B. P.; Atwood, J. L.; Gaeta, C.; Tedesco, C.; Neri, P., Carbon Dioxide Capture in a Self-Assembled Organic Nanochannels. *Chem. Mater.* **2007,** *19* (14), 3355-3357.

56. Lagona, J.; Mukhopadhyay, P.; Chakrabarti, S.; Isaacs, L., The Cucurbit[n]uril Family. *Angew. Chem. Int. Ed.* **2005,** *44* (31), 4844-4870.

57. Isaacs, L., Cucurbit[n]urils: from mechanism to structure and function. *Chem. Commun.* **2009,** (6), 619-629.

58. Kim, H.; Kim, Y.; Yoon, M.; Lim, S.; Park, S. M.; Seo, G.; Kim, K., Highly Selective Carbon Dioxide Sorption in an Organic Molecular Porous Material. *J. Am. Chem. Soc.* **2010,** *132* (35), 12200-12202.

59. Tian, J.; Ma, S.; Thallapally, P. K.; Fowler, D.; McGrail, B. P.; Atwood, J. L., Cucurbit[7]uril: an amorphous molecular material for highly selective carbon dioxide uptake. *Chem. Commun.* **2011,** *47* (27), 7626-7628.

60. Sozzani, P.; Comotti, A.; Bracco, S.; Simonutti, R., A Family of Supramolecular Frameworks of Polyconjugated Molecules Hosted in Aromatic Nanochannels. *Angew. Chem. Int. Ed.***2004,** *43* (21), 2792-2797.

61. (a) Lee, D. K. Y.; Jackson, A.-M. S.; Fushimi, T.; Yennawar, H.; Allcock, H. R., Synthesis and inclusion behavior of cyclotriphosphazene molecules with asymmetric spiro rings. *Dalton Trans.* **2010,** *39* (22), 5341-5348; (b) Hertzsch, T.; Budde, F.; Weber, E.; Hulliger, J., Supramolecular-Wire Confinement of I_2 Molecules in Channels of the Organic Zeolite Tris(o-phenylenedioxy)cyclotriphosphazene. *Angew. Chem. Int. Ed.* **2002,** *41* (13), 2281-2284.

62. Sozzani, P.; Bracco, S.; Comotti, A.; Ferretti, L.; Simonutti, R., Methane and Carbon Dioxide Storage in a Porous van der Waals Crystal. *Angew. Chem. Int. Ed.* **2005,** *44* (12), 1816-1820.

63. Couderc, G.; Hertzsch, T.; Behrnd, N. R.; Krämer, K.; Hulliger, J., Reversible sorption of nitrogen and xenon gas by the guest-free zeolite tris(o-phenylenedioxy)cyclotriphosphazene (TPP). *Microporous Mesoporous Mater.* **2006,** *88* (1–3), 170-175.

64. Bezzu, C. G.; Helliwell, M.; Warren, J. E.; Allan, D. R.; McKeown, N. B., Heme-Like Coordination Chemistry Within Nanoporous Molecular Crystals. *Science* **2010,** *327* (5973), 1627-1630.

65. (a) Gorbitz, C. H.; Gundersen, E., l-Valyl-l-alanine. *Acta Crystallogr., Sect. C* **1996,** *52* (7), 1764-1767; (b) Gorbitz, C., An exceptionally stable peptide nanotube system with flexible pores. *Acta Crystallogr., Sect. B* **2002,** *58* (5), 849-854.

66. Soldatov, D. V.; Moudrakovski, I. L.; Ripmeester, J. A., Dipeptides as

Microporous Materials. *Angew. Chem. Int. Ed.* **2004,** *43* (46), 6308-6311.
67. Tian, J.; Thallapally, P. K.; Dalgarno, S. J.; McGrail, P. B.; Atwood, J. L., Amorphous Molecular Organic Solids for Gas Adsorption. *Angew. Chem. Int. Ed.* **2009,** *48* (30), 5492-5495.
68. Mastalerz, M.; Oppel, I. M., Rational Construction of an Extrinsic Porous Molecular Crystal with an Extraordinary High Specific Surface Area. *Angew. Chem. Int. Ed.* **2012,** *51* (21), 5252-5255.
69. (a) Liu, X.; Liu, Y.; Warmuth, R., Multi-Component Synthesis of Tetracavitand Nanocapsules. *Supramolecular Chemistry* **2008,** *20* (1-2), 41-50; (b) Liu, X.; Liu, Y.; Li, G.; Warmuth, R., One-Pot, 18-Component Synthesis of an Octahedral Nanocontainer Molecule. *Angew. Chem. Int. Ed.* **2006,** *45* (6), 901-904; (c) Liu, X.; Warmuth, R., Solvent Effects in Thermodynamically Controlled Multicomponent Nanocage Syntheses. *J. Am. Chem. Soc.* **2006,** *128* (43), 14120-14127.
70. Liu, Y.; Liu, X.; Warmuth, R., Multicomponent Dynamic Covalent Assembly of a Rhombicuboctahedral Nanocapsule. *Chem. Eur. J.* **2007,** *13* (32), 8953-8959.
71. (a) Mastalerz, M., One-pot synthesis of a shape-persistent endo-functionalised nano-sized adamantoid compound. *Chem. Commun.* **2008,** (39), 4756-4758; (b) Cooper, A. I., Nanoporous Organics Enter the Cage Age. *Angew. Chem. Int. Ed.* **2011,** *50* (5), 996-998; (c) Mastalerz, M.; Schneider, M. W.; Oppel, I. M.; Presly, O., A Salicylbisimine Cage Compound with High Surface Area and Selective CO_2/CH_4 Adsorption. *Angew. Chem. Int. Ed.* **2011,** *50* (5), 1046-1051.
72. Schneider, M. W.; Oppel, I. M.; Ott, H.; Lechner, L. G.; Hauswald, H.-J. S.; Stoll, R.; Mastalerz, M., Periphery-Substituted [4+6] Salicylbisimine Cage Compounds with Exceptionally High Surface Areas: Influence of the Molecular Structure on Nitrogen Sorption Properties. *Chem. Eur. J.* **2012,** *18* (3), 836-847.
73. Schneider, M. W.; Lechner, L. G.; Mastalerz, M., Uniform porous nanospheres of discrete shape-persistent organic cage compounds. *J. Mater. Chem.* **2012,** *22* (15), 7113-7116.
74. Schneider, M. W.; Oppel, I. M.; Mastalerz, M., Exo-Functionalized Shape-Persistent [2+3] Cage Compounds: Influence of Molecular Rigidity on Formation and Permanent Porosity. *Chem. Eur. J.* **2012,** *18* (14), 4156-4160.
75. (a) Tozawa, T.; Jones, J. T. A.; Swamy, S. I.; Jiang, S.; Adams, D. J.; Shakespeare, S.; Clowes, R.; Bradshaw, D.; Hasell, T.; Chong, S. Y.; Tang, C.; Thompson, S.; Parker, J.; Trewin, A.; Bacsa, J.; Slawin, A. M. Z.; Steiner, A.; Cooper, A. I., Porous organic cages. *Nat. Mater.* **2009,** *8* (12), 973-978; (b) Bojdys, M. J.; Briggs, M. E.; Jones, J. T. A.; Adams, D. J.; Chong, S. Y.; Schmidtmann, M.; Cooper, A. I., Supramolecular Engineering of Intrinsic and Extrinsic Porosity in Covalent Organic Cages. *J. Am. Chem. Soc.* **2011,** *133* (41), 16566-16571; (c) Jelfs, K. E.; Wu, X.; Schmidtmann, M.; Jones, J. T. A.; Warren, J. E.; Adams, D. J.; Cooper, A. I., Large Self-Assembled Chiral Organic Cages: Synthesis, Structure, and Shape Persistence. *Angew. Chem. Int. Ed.* **2011,** *50* (45), 10653-10656; (d) Jones, J. T. A.; Hasell, T.; Wu, X.; Bacsa, J.; Jelfs, K. E.; Schmidtmann, M.; Chong, S. Y.; Adams, D. J.; Trewin, A.; Schiffman, F.; Cora, F.; Slater, B.; Steiner, A.; Day, G. M.; Cooper, A. I., Modular and predictable assembly of porous organic molecular crystals. *Nature*

2011, *474* (7351), 367-371; (e) Mitra, T.; Wu, X.; Clowes, R.; Jones, J. T. A.; Jelfs, K. E.; Adams, D. J.; Trewin, A.; Bacsa, J.; Steiner, A.; Cooper, A. I., A Soft Porous Organic Cage Crystal with Complex Gas Sorption Behavior. *Chem. Eur. J.* **2011,** *17* (37), 10235-10240.

76. Jones, J. T. A.; Holden, D.; Mitra, T.; Hasell, T.; Adams, D. J.; Jelfs, K. E.; Trewin, A.; Willock, D. J.; Day, G. M.; Bacsa, J.; Steiner, A.; Cooper, A. I., On–Off Porosity Switching in a Molecular Organic Solid. *Angew. Chem. Int. Ed.* **2011,** *50* (3), 749-753.

77. Jelfs, K. E.; Schiffmann, F.; Jones, J. T. A.; Slater, B.; Cora, F.; Cooper, A. I., Conformer interconversion in a switchable porous organic cage. *Phys. Chem. Chem. Phys.* **2011,** *13* (45), 20081-20085.

78. Xu, D.; Warmuth, R., Edge-Directed Dynamic Covalent Synthesis of a Chiral Nanocube. *J. Am. Chem. Soc.* **2008,** *130* (24), 7520-7521.

79. Jin, Y.; Voss, B. A.; Noble, R. D.; Zhang, W., A Shape-Persistent Organic Molecular Cage with High Selectivity for the Adsorption of CO_2 over N_2. *Angew. Chem. Int. Ed.* **2010,** *49* (36), 6348-6351.

80. Jin, Y.; Voss, B. A.; Jin, A.; Long, H.; Noble, R. D.; Zhang, W., Highly CO_2-Selective Organic Molecular Cages: What Determines the CO_2 Selectivity. *J. Am. Chem. Soc.* **2011,** *133* (17), 6650-6658.

Chapter 2

Experimental and computational methods

2.1 Introduction

In this Chapter, the experimental and computational methods for characterizing and simulating porous organic molecules, respectively, will be introduced. The main experimental characterization techniques used in this thesis are gas sorption, X-ray diffraction (XRD), thermogravimetric analysis (TGA), Fourier transform infrared spectroscopy (FTIR), scanning electron microscope (SEM), high performance liquid chromatography (HPLC), mass spectrometry (MS), and nuclear magnetic resonance spectroscopy (NMR). Generally, gas sorption analysis is used to measure gas uptake, surface area, pore size distribution, and pore volume of porous solids. XRD has been performed to determine the crystal structure and phase purity of materials. TGA provides information about the decomposition temperature and solvent loss of materials. The morphology of materials can be observed by SEM. MS is an analytical technique to measure the accurate molecular weight of a compound. HPLC is used to indentify molecular mass distributions for mixtures of compounds and to purify each component in the mixture. NMR and IR techniques are important tools for determining molecular structures.

Molecular simulation is an alternative approach to characterize porous materials in microscopically scope. It has been widely used to rationalize materials properties and, less often, to design new materials with particular properties. Calculation techniques used in the thesis include density functional theory (DFT), molecular dynamics (MD), force fields, and energy minimization. Some basic theoretical backgrounds will be discussed in detail here.

2.2 Gas adsorption

Gas adsorption is used to describe a surface phenomenon where gas molecules are introduced and bound to a solid surface.[1] As shown in Figure 1, the solid is called the adsorbent and the gas is referred to as the adsorbate. Porous materials are often used practically as adsorbents. The analysis is widely used to estimate the surface area, pore size, and pore volume of porous materials. The adsorption process can be classified into two categories: physical adsorption (physisorption) and chemical adsorption (chemisorption), depending on the strength of the interaction between the adsorbate and the adsorbent.[2] Some features have been used to distinguish between physisorption and chemisorption. For chemisorption, a chemical bond is formed

between adsorbate and adsorbent which leads to a non-reversible process. The adsorption process is limited to a single layer (monolayer) formation of adsorbates on the surface.

Physisorption involves a weak van der Waals interaction between the adsorbate and the adsorbent surface. Therefore, the adsorption heat of physisorption is typically low. Unlike chemisorption, physisorption is a totally reversible process and desorption can occur without dissociation of adsorbed molecules. Multiple layers (multilayers) of adsorbates can also be formed during the physisorption process, if the pores in the material are large enough to permit this.

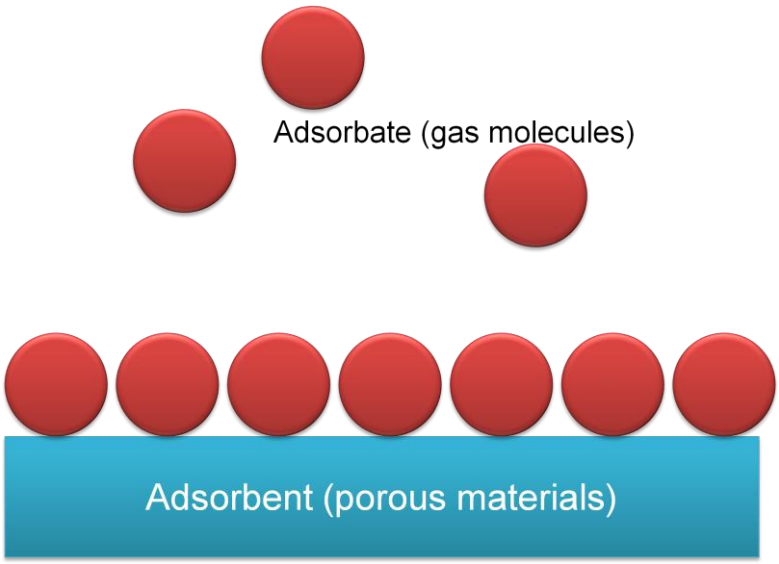

Figure 1. The illustration of gas adsorption.(Figure adapted from Ref.[1])

2. 2.1 Gas adsorption isotherms

Gas adsorption isotherms can be obtained by measuring the amount of gas adsorbed as function of a pressure at a given temperature (typically N_2 isotherm at 77 K and up to 1 bar).[2c, 3] A desorption isotherm is measured by reducing the pressure. The N_2 sorption isotherms are classified into six different types (Type I – VI) shown in Figure 2.

Type I is a typical adsorption isotherm for microporous materials. The amount of gas adsorbed increases rapidly at low relative pressures where micropores are filled by gas molecules. The gas uptake reaches saturation at high relative pressures where pores are completely filled. Type II isotherm is observed for macroporous solids. The

point **a** in Figure 2II indicates a transition stage for adsorbates from monolayer to multilayer formation. Type III isotherm shows a very low gas uptake at low relative pressures indicating a weak adsorbate-adsorbent interaction. Type IV isotherm is observed for many mesoporous solids. The monolayer gas sorption is formed at low relative pressures (the point from **a** to **b** in Figure 2IV) which is similar to the Type II isotherm. After the point **b**, the multilayer formation is followed. The high gas uptake occurs after the point **c** due to gas condensation in the mesopores. Hysteresis is observed in Type IV isotherm. Type V isotherm has a low gas uptake at low relative pressures that is similar to type III isotherm and a hysteresis loop exists. Type VI isotherm represents a stepwise adsorption process.

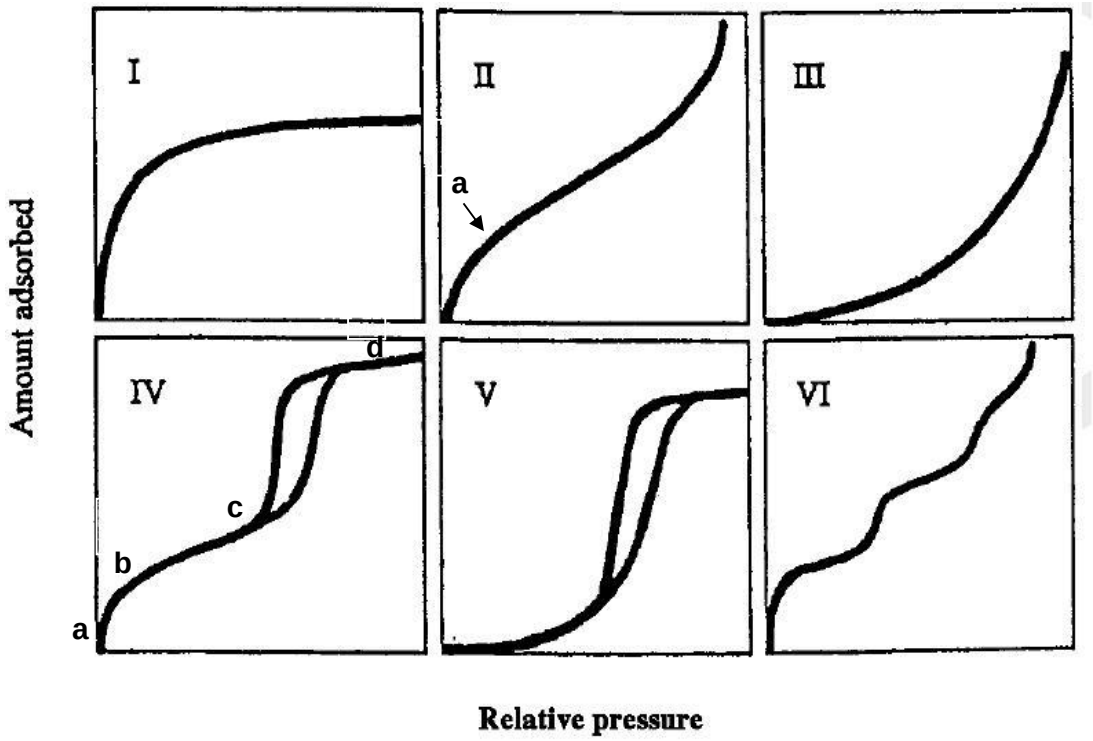

Figure 2. The IUPAC classifications of adsorption isotherms. I – VI are type I – VI isotherms, respectively. (Figure taken form Ref.[3])

Hysteresis can be observed in the adsorption isotherms for a number of gas-solid systems. The hysteresis loops are usually due to capillary condensation. Four types of hysteresis loops are classified by IUPAC.[3] They are illustrated in Figure 3. Type H1 has a steep adsorption and desorption curve at high relative pressures. Type H1 is a normally observed by porous solids with uniform pore size distribution. Type H2 is given by porous solids with irregular sizes or shapes. Type H3 and H4 is seen by porous solids with slit-shapes pore sizes. Type H4 is normally observed by

micoporous solids with Type I adsorption isotherm.

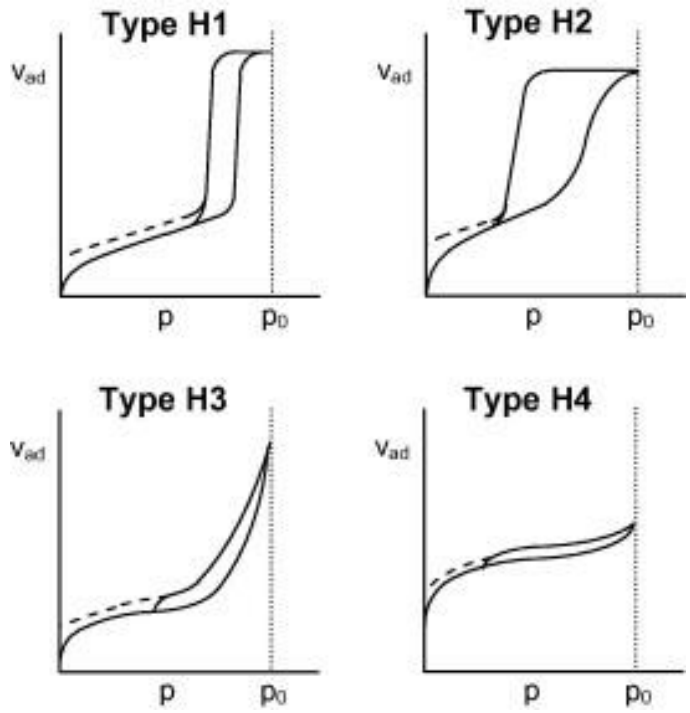

Figure 3. The IUPAC classifications of hysteresis loops. (Figure from Ref.[4c])

2.2.2 Langmuir adsorption model

One widely-used model for describing gas adsorption processes was proposed first by Langmuir. The assumptions of the Langmuir model are based on[2c, 4]:

1. Adsorption process occurs on the monolayer coverage.
2. All adsorbent surface sites are equivalent and each site can only accommodate one adsorbate molecule.
3. The interactions between adsorbate molecules on adjacent sites are not considered.

The processes of adsorption and desorption are dynamic. The rate of adsorption depends on the pressure of adsorbate, P, and the fractional coverage of a surface, θ, is defined as:

$$\theta = \frac{number\ of\ occupied\ adsorption\ sites}{total\ number\ of\ possible\ sites} \quad (2.\ 1)$$

The rate of adsorption is:

$$Rate\ of\ adsorption = k_a P(1-\theta) \quad (2.\ 2)$$

(k_a is the rate constant for adsorption step)

And the rate of desorption is:

$$Rate\ of\ desorption = k_d\theta \exp(-\frac{E_d}{RT}) \qquad (2.3)$$

(k_d is the rate constant for desorption, E_d is activation energy of desorption)

At equilibrium, the rate of adsorption and desorption are equal. Therefore, the equation can be written as follows:

$$k_a P(1-\theta) = k_d\theta \exp(-\frac{E_d}{RT}) \quad (2.4)$$

$$\frac{\theta}{1-\theta} = \frac{k_a P}{k_d\,(exp-\frac{E_d}{RT})} \quad (2.5)$$

where the overall rate constant *K* can be defined by:

$$K = \frac{k_a}{k_d\,(\exp-\frac{E_d}{RT})} \quad (2.6)$$

If *n* is the number of sites occupied and n_m is the monolayer capacity, the fractional coverage of a surface, θ can be written as:

$$\theta = \frac{n}{n_m} \quad (2.7)$$

Langmuir equation can be written as follow:

$$\frac{n}{n_m} = \frac{KP}{1-KP} \quad (2.8)$$

where *P* is the equilibrium pressure (mbar). *n* is the amount adsorbed (mmol/g). n_m is the amount adsorbed in the monolayer (mmol/g). *K* is an adsorption coefficient.

Experimentally, θ can be expressed as the volume of gas adsorbed (V_{ads}) divided by the volume of gas on the monolayer (V_{mono}):

$$\theta = \frac{V_{ads}}{V_{mono}} \quad (2.9)$$

The Langmuir equation can be rewritten in the linear form as:

$$P/n = (1/K\,n_m) + (P/n_m) \qquad (2.10)$$

The plot of P/n against P will give a straight line with the slope of $1/n_m$.

The specific surface area can then be calculated via:

$$SA_{lang} = n_m L a_m \qquad (2.\ 11)$$

where a_m is the molecular cross sectional area (nm^2) and L is the Avogadro constant(6.023×10^{23} mol^{-1}).

2.2.3 Brunauer-Emmett-Teller model (BET model)

The Brunauer-Emmett-Teller (BET) model is most widely used to determine the adsorption isotherms and surface areas of porous solids for the multilayer adsorption.[2c, 5] The BET theory assumes that there is no interaction between adsorption layers. The first monolayer of adsorbate has a fixed heat of adsorption, whereas the second and subsequent layers have heats of adsorption equal to the latent heat of evaporation. The Langmuir model is applied to each adsorption layer. Therefore, the BET equation can be expressed as:

$$\frac{P}{V\,(P_0-P)} = \frac{1}{V_m C} + \frac{(C-1)}{V_m\,C}\,\frac{P}{P_0} \quad (2.\ 12)$$

where, P is the equilibrium pressure. P_o is the saturated gas pressure at 77 K. V is the total gas adsorbed volume. V_m is the volume of gas adsorbed on monolayer. C is a constant.

A plot of $\frac{P}{V\,(P_0-P)}$ against $\frac{P}{P_0}$ gives a linear graph.The gradient $\frac{(C-1)}{V_m\,C}$ and intercept $\frac{1}{V_m C}$ can be obtained from the plot. The BET equation is widely used for N_2 adsorption at 77 K and is applied to estimate the BET surface area. From both values of the slope and the intercept, the value of V_m can be calculated and used to calculate the surface area (SA), as follows:

$$SA = \sigma V_m L / V_o \quad (2.\ 13)$$

where, L is the Avogadro number (6.023×10^{23} mol^{-1}) and V_o is the molar volume of N_2 (22,414 dm^3/mol at the standard temperature and pressure) and σ is the area occupied by each adsorbate molecule (16.2 $Å^2$ for a nitrogen molecule). The BET equation has shown it to be linear only in the pressure range $0.05 < P/P_0 < 0.35$ for open surfaces.

2.3 Gas diffusion

Gas diffusion properties in porous materials play an important role in various applications such as gas separation, catalytic process. The typical approach to characterize diffusion is Fick's laws.[1] The first law by Fick describes a linear relationship between the matter flux, $\bar{J}$ and the concentration gradient $\bar{\nabla} C$:

$$\bar{J} = -D\,\bar{\nabla}\,C = -D\left[\frac{\partial C}{\partial a}\right] \quad (2.14)$$

where: D is the diffusion coefficient, the proportionality constant. C is the concentration and a is diffusion distance.

The transport diffusion can be calculated from the matter flux and the concentration gradient (from high concentration to low concentration). The illustration of transport diffusion is shown in Figure 4 (left). The transport diffusivity can be defined as the equation below in terms of the corrected diffusivity, D_0:

$$D_t(C) = D_0(C)\left(\frac{\partial \ln f}{\partial \ln c}\right)_T \quad (2.15)$$

Here, the partial derivative involves the adsorbate concentration C, and the bulk phase fugacity, f.

The self-diffusion describes a movement of a molecule when the system is equilibrated as shown in Figure 4 (right). In the three dimensional materials, the self-diffusivity can be determined by the mean square displacement (MSD) of molecular trajectories after t time by the Einstein relation:

$$D_s(C) = lim_{t\to\infty}\frac{1}{6t}\left\langle\left|\underset{r}{\rightarrow}(t) - \underset{r}{\rightarrow}(0)\right|^2\right\rangle \quad (2.16)$$

where, $\underset{r}{\rightarrow}(t)$ is the position of a molecular at time t, $\underset{r}{\rightarrow}(t) - \underset{r}{\rightarrow}(0)$ is the vector distance travelled by a diffusing molecule over time interval of the length t and the angular brackets indicate an ensemble average.

Molecular Dynamic (MD) simulations can be performed to study self-diffusivities of gas molecules in porous solids based on the Einstein expression.[6] The self-diffusivities can be calculated from MSD plots. At extremely short times of the MSD plot, the motion of the gas molecule is ballistic and the equation can be written as

$\langle \left| \underset{r}{\rightarrow}(t) - \underset{r}{\rightarrow}(0) \right|^2 \rangle \sim t^2$, therefore the slope of logarithmic plot of MSD is 2. There is an intermediate region after the ballistic motion on the MSD plot and the slope of logarithmic plot is 0.5. The motion of gas molecule in this region is single file diffusion. Normal diffusion occurs when the slope of logarithmic plot is 1. For the normal diffusion, the MSDs should increase linearly with the time. The self-diffusivities for gas molecules in this thesis were determined from the data of normal diffusion region. More MD simulation details will be discussed in Chapter 6.

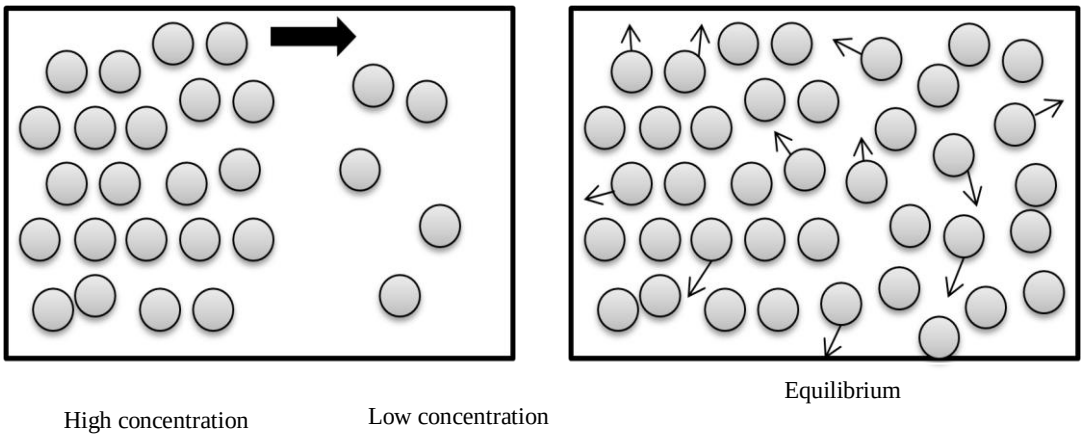

Figure 4. Illustration of transport diffusion (left) and self-diffusion (right). (Figure taken from Ref.[1])

2.4 X-ray diffraction techniques

2.4.1 X-ray diffraction

X-ray diffraction is a very useful technique for characterizing structures (cell parameters, space groups, full atomic positions), and phase purity of crystalline materials.[7] Crystalline solids consist of parallel rows of atoms with a characteristic interatomic distance. Diffraction can occur when the wavelength of the X-ray has a similar value of the interatomic distance of crystals. It can be expressed by Bragg's law.

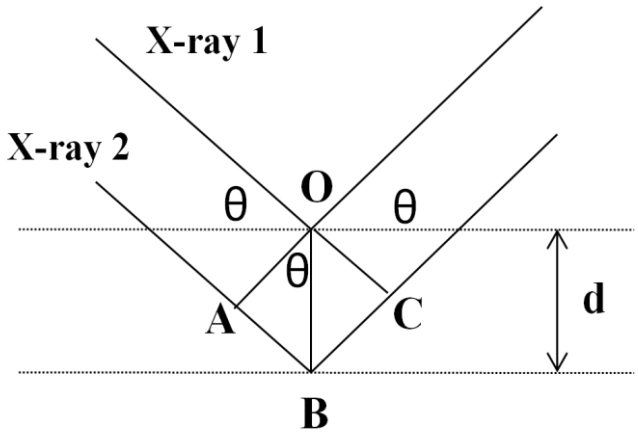

Figure 5. Bragg diffraction with two X-rays entering a crystal planes with a spacing, d. (Figure taken from Ref.[7b])

As shown in Figure 5, two X-rays are shown here and the spacing between the atomic planes is labelled as *d*. The X-rays reflect off the atomic planes at the same angle as the angle of incidence θ.

$$\text{The difference in path length} = AB + BC = 2\,d\sin\theta \quad (2.\,17)$$

This must be equal to an integral number, *n*, of wavelengths. And the wavelength of X-rays is λ, then,

$$n\,\lambda = 2\,d\,\sin\theta \quad (2.\,18)$$

n - An integer determined by the order given

λ - Wavelength of x-rays

d - Spacing between the planes in the atomic lattice

This is Bragg's law for X-ray diffraction. When these X-rays are incident on the sample they are diffracted by the atomic structure of the sample. The resulting diffraction patterns of X-rays at certain angles are then interpreted using Bragg's law to show structural information about the sample.

2.4.2 Powder X-ray diffraction (PXRD)

A powder sample consists of many thousands of small crystallites in random orientations. Each small crystallites can give a diffraction pattern when a beam of X-rays is scattered at specific angles upon the sample.[8] The diffracted beam produces a

cone, and these cones will form circles on a flat plane which are Debye-Scherrer rings shown in Figure 6.[8] The signal generated from Debye-Scherrer rings is recorded as peaks in the diffraction pattern. The diffraction pattern shows that the intensity of diffracted beams is measured as a function of *2θ*. X-ray powder diffraction can be used for phase identification of crystalline materials, such as determination of unit cell dimensions, measurement of sample purity, and determination of crystal structures using Rietveld refinement, particularly when it is not possible to grow diffractable crystals for single crystal XRD below.[9]

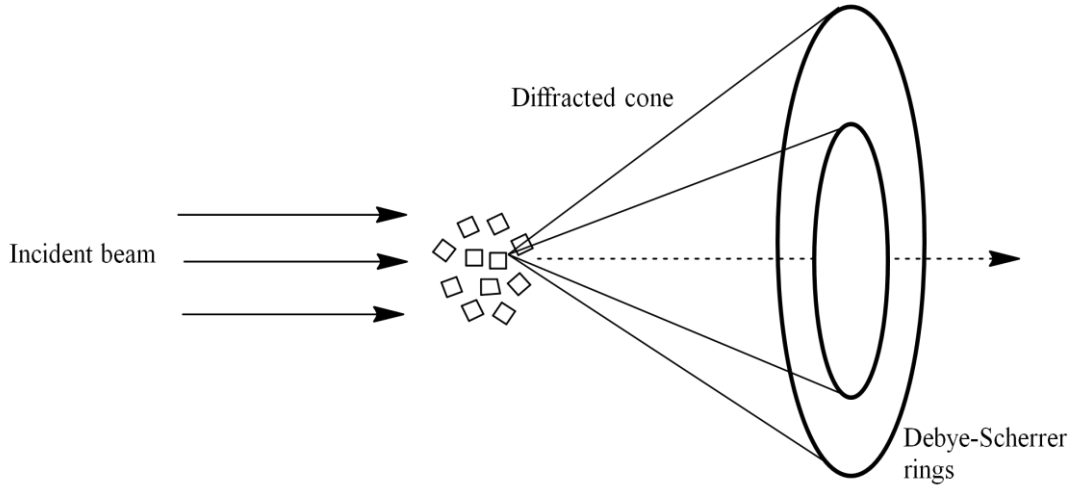

Figure 6. The diffraction from a powder sample. Cones and Debye-Scherrer rings produced by powder diffraction. (Figure taken from Ref.[8b])

2.4.3 Single crystal X-ray diffraction

Single crystal X-ray diffraction is the technique of choice for determining crystal structure, including unit cell dimensions and the positions of the atoms and chemical bonds in the lattice.[7b] The crystals for this analysis must be single and sufficiently large. The diffraction pattern generated from a single crystal is an array of spots in reciprocal space. Each spot represents the direction of the *hkl* reflection in the unit cell and is corresponded to a structure factor, F_{hkl}. The crystal structure is calculated from the diffraction patterns by applying a three dimensional Fourier Transform. The atom positions will be calculated from the electron density distribution. The structures of cage molecules are determined by single crystal X-ray diffraction in this thesis. The data in this thesis is collected and refined by Dr John Bacsa, our departmental crystallographer at the time of this work.

2.5 Thermogravimetric analysis (TGA)

TGA is used to characterize the thermal stability and solvent losses of the materials. It measures gravimetric weight loss from a sample as a function of increasing temperature. This is carried out under a flow of gas (in air or in an inert atmosphere such as N_2).[7b]

2.6 Fourier transform infrared spectroscopy (FTIR)

The FTIR spectrum represents the absorption of different IR frequencies by chemical compounds. It is used to identify the type of chemical bonds because different functional groups have characteristic vibrational frequencies. This thesis mainly uses FTIR to characterize imine organic cage molecules, which have a strong imine stretch at around 1640 cm^{-1} in the IR spectra.

2.7 Scanning electron microscope (SEM)

In SEM, high energy electrons are used to generate high magnification images of the surface of solids. SEM is also capable of performing analyses of morphology or topology, chemical composition, crystal orientations of porous solids.[7b] Here, I use it to characterize sample morphology.

2.8 Nuclear magnetic resonance (NMR) spectroscopy

NMR is a powerful technique to determine molecular structure of organic compounds. It can provide definitive information about the molecules and their environment based on the interactions of nuclear magnetic moments with electromagnetic radiation, in either liquid or the solid state. An NMR spectrum is composed of a number of peaks. The positions and intensities of the peaks can determine chemical environments of atoms. Due to good solubility of cage molecules, solution NMR is used in this thesis to characterize the molecular structures.

2.9 High performance liquid chromatography (HPLC)

HPLC is an analytical technique to separate a mixture of compounds. Moreover, each component can be identified and quantified when HPLC combines with mass spectrometry. HPLC utilizes the different interaction between the compounds, a column which contains a solid stationary phase and liquid mobile phase to separate a

mixture of compounds. By choosing the proper column or mobile phase, the compounds can separated based on hydrophobicity or size. Reversed phase chromatography which includes a non-polar stationary phase and polar mobile phase (solvents) are used to separate cage molecules in this thesis. The separation is based on molecular hydrophobicity properties. HPLC can also be used preparatively to separate samples on a larger scale (see e.g., Chapter 5, section 5.8).

2.10 Mass spectrometry (MS)

Mass spectrometry (MS) is a useful technique to measure the mass of a compound and to determine the elemental composition. The compound is ionized for the analysis. A range of different ionization methods have been used including electron ionization (EI), chemical ionization (CI), electrospray ionization (ESI) and matrix-assisted laser desorption ionization (MALDI). Here, we use MS to validate the identity of newly synthesized cages, and to ensure that catenanes are not formed.[10]

2.11 Equipment details

NMR. Solution ^{1}H NMR spectra were recorded at 400.13 MHz using a Bruker Avance 400 NMR spectrometer. ^{13}C NMR spectra were recorded at 100.6 MHz.

Thermogravimetric Analysis. TGA analysis was carried out using a Q5000IR analyzer (TA instruments) with an automated vertical overhead thermobalance. In a measurement, a sample was placed in a platinum pan and heated to 500-600 °C for cage materials with a heating rate of 5 °C / min under N_2 gas, and then cooled down to 25 °C with a rate of 50 °C / min.

Powder X-ray Diffraction. PXRD data were collected on a Panalytical X'pert pro multi-purpose diffractometer (MPD) in transmission Debye-Scherrer geometry operating with a Cu anode at 40 kV 40 mA. Samples were ground and mounted as loose powder onto a transparent film and spun at 2s/rotation. PXRD patterns were collected in 161 hour scans with a step size of 0.013 degrees 2θ and scan time of 115 s/step over 5 – 50 deg 2θ. The incident X-ray beam was conditioned with 0.04 rad Soller slits and an anti-scatter slit of 1/2 deg. The diffracted beam passed through an automatic antiscatter slit (5 mm), 0.04 rad Soller slits and Ni filter before processing by the PIXcel detector operating in scanning mode.

The data for **CC6** in Chapter 4 were also measured on a Bruker D8 advance diffractometer using monochromatic Cu $K\alpha_1$ radiation (λ = 1.54056 Å). Samples were mounted in 1.0 mm diameter special glass capillaries and recorded over 3 - 40 deg 2θ.

Gas Sorption Analysis. All samples were tested with gases of the following purities: hydrogen (99.9995% - BOC gases), carbon dioxide (SCF grade – BOC gases) and methane (ultrahigh purity -BOC). Surface areas and pore size distributions were measured by nitrogen adsorption and desorption at 77.3 K using either a Micromeritics ASAP 2420 or ASAP 2020 volumetric adsorption analyzer. Samples were degassed offline at 120 °C for 15 h under vacuum (10^{-5} bar) before analysis. Pore size distributions and pore volumes were derived from the adsorption branches of the isotherms using non-local density functional theory model (NL-DFT) within the Micrometritics ASAP software.

Hydrogen isotherms were measured using a Micrometrics ASAP 2420 volumetric adsorption analyzer at 77.3 K. High pressure hydrogen adsorption and desorption isotherms up to 10 bar were measured using Micrometritics ASAP 2050 sorption analyzer.

Carbon dioxide isotherms were measured at 273 and 293 K using a Micromeritics 2020 volumetric adsorption analyzer.

Methane isotherms were measured using either a Micromeritics ASAP 2420 at 298 K using a water bath, 273 K using an ice water mix and at 196 K using an acetone dry ice mixture, or a Micromeritics ASAP 2020 at 263, 273, 283 and 293 K using a chiller/circulator.

Fourier Transform Infrared Spectroscopy. IR spectra were collected on a Bruker Tensor 27 spectrometer. Samples were analyzed as KBr disks for 16 scans with a resolution of 4 cm^{-1}. Spectra were recorded in transmission mode.

Scanning Electron Microscopy. High resolution imaging of the crystal morphology was achieved using a Hitachi S-4800 cold Field Emission Scanning Electron Microscope (FE-SEM). The dry samples were prepared on 15 mm Hitachi M4 aluminium stubs using either silver dag or an adhesive high purity carbon tab. The samples were then coated with a 2 nm layer of gold using an Emitech K550X

automated sputter coater. The FE-SEM measurement scale bar was calibrated using certified SIRA calibration standards. Imaging was conducted at a working distance of 8 mm and a working voltage of 3 kV using a mix of upper and lower secondary electron detectors.

Single Crystal X-ray Diffraction. The single crystal data for **CC6** were collected on a Bruker Apex diffractometer and 1.5 kW graphite monochromated Mo radiation (λ = 0.71073 Å) using 0.3° ω scan steps spanning at least a hemisphere of reciprocal space for all structures. The frames were integrated with the SAINT v6.45a (Bruker, 2005). A semi-empirical absorption correction using multiple-reflections was carried out using the program SADABS V2008-1.

Single crystal X-ray diffraction data for **CC2** were performed at 173 K using a Rigaku MM007/Mercury diffractometer (confocal optics Mo-K∞ radiation). Intensity data were collected using ω steps accumulating area detector frames spanning at least a hemisphere of reciprocal space for all structures (data were integrated using CrystalClear). All data were corrected for Lorentz, polarisation and long-term intensity fluctuations (using CrystalClear). Absorption effects were corrected on the basis of multiple equivalent reflections.

Thermo Scientific Accela U-HPLC System: Analytical columns for coreaction samples and inter-cage exchange between **CC1** and **CC3** were Hypersil GOLD Phenyl, 150 x 4.6 mm, 5 µm (SN 0591330K, Lot 9193) linked to Hypersil GOLD, 150 x 4.6 mm, 5 µm, (SN 1284371N, Lot 9231). The mobile phase used for separation was ethanediol / MeOH, 5/95 (pre-mixed) at a flow rate was 0.5 mL/min. The injection volume was 10 µL and the sample concentration was 0.1 mg/mL in MeOH. The column oven temperature was set to 30 °C. Analytical columns of showing splitting of isomer peaks were Waters XBridge phenyl 4.6x150 mm, 5 µm and XBridge C18 4.6x100 mm, 5 µm. The mobile phase used was 80 to 95 % MeOH in 0.1 % NH_4OH.

2.12 Molecular simulations

2.12.1 *Ab initio* methods

Ab initio methods are referred to as 'first principles' methods which are used to calculate electronic structure and total energy of a system. First they attempt to solve the Schrödinger equation. The Schrödinger equation describes the movement of a particle of mass, *m*, in three dimensions with energy, *E*. The time independent Schrödinger equation is written as:

$$\left\{-\frac{\hbar^2}{2m}\nabla^2 + V\right\}\Psi = E\Psi \quad (2.\ 19)$$

where, *m* is the mass of the particle, ħ is Planck's constant, ∇^2 is relative to cartesian coordinates, x, y and z ($\nabla^2 = \frac{\partial^2}{\partial x^2} + \frac{\partial^2}{\partial y^2} + \frac{\partial^2}{\partial z^2}$), V is the potential energy, and Ψ is the wavefunction. It can be rewritten as:

$$\hat{H}\Psi = E\Psi \quad (2.\ 20)$$

where, $\hat{H}$ is the Hamiltonian operator of the system.

2.12.1.1 Wavefunction methods

A number of approximations and methods have been used to solve the Schrödinger equation.[11] In the Born-Oppenheimer (BO) approximation, electronic and nuclear motions are considered separately. The nuclei are assumed to be stationary and electrons are assumed to be in the ground state. The electronic time independent Schrödinger equation can be expressed for N electrons in the external field generated by nuclei. A further approximation related to wavefunction methods is the Linear Combination of Atomic Orbitals (LCAO). The method assumes the wavefunction as a series of functions of atomic orbitals.

The Hartree-Fock (HF) method is the basis of molecular orbital theory, which can be used to solve the Schrödinger equation for a many-body system.[11] This method treats many electron wavefunctions as a series of electron wavefunctions without considering electron correlation effects. A simple approximation for the many-body wavefunctions is given by a single Slater determination of N electrons. A self-consistent field (SCF) procedure is used to solve the equations.[11] The HF method is

widely used for energy calculations of small molecules. The disadvantages of the method are that electron correlation is not accounted and it is computationally expensive. Furthermore, post Hartree-Fock methods are used to improve the energy correlation effects in the calculations.

2.12.1.2 Density functional theory (DFT)

Density Functional Theory (DFT) is mainly concerned with the relationship between total electronic energy and overall electronic density rather than the wavefunction.[11-12] DFT calculations have been carried out in this thesis and more details will be described in the following sections.

The Hohenberg-Kohn theorems are considered as functional theorems of DFT.[13] For a system with a non-degenerate ground state, the first theorem means that the ground state electron density, ρ (r) of a many electron system can uniquely determine the external potential V_{ext}, with which it is sufficient to construct the full Hamiltonian operator and hence calculate any ground state property of the system. The total energy can be written as:

$$E[\rho] = E_{ext}[\rho] + F[\rho] \quad (2.21)$$

$$F[\rho] = T[\rho] + E_{ee}[\rho] \quad (2.22)$$

where, $E_{ext}[\rho]$ is the external energy. The Hohenberg-Kohn functional $F[\rho]$ is the sum of the kinetic energy $T[\rho]$ and the electron-electron repulsion operator$E_{ee}[\rho]$.

The second theorem proves that the ground state density is not only unique, but also the only one which minimizes the total energy.

The Kohn-Sham Approach

The electron-electron repulsion operator $E_{ee}[\rho]$ consists of the classical electron-electron interaction energy $J[\rho]$ and non-classical contribution to electron-electron interaction energy $E_{ncl}[\rho]$. Therefore, the total energy can be rewritten as follows:

$$E[\rho] = T[\rho] + J[\rho] + E_{ncl}[\rho] + E_{ext}[\rho] \quad (2.23)$$

In 1965, Kohn and Sham gave a solution to the unknown functional of the kinetic energy, where they formally split this functional into two parts[14]:

$$T[\rho] = T_s[\rho] + T_c[\rho] \quad (2.\ 24)$$

Here the first part, $T_s[\rho]$, is the kinetic energy of a model system of N non-interacting electrons. This can be expressed in a one particle approach similar to the Hartree-Fock method. While $T_c[\rho]$ is the residual part of the kinetic energy which is not covered by $T_s[\rho]$. $T_c[\rho]$ is still an unknown term. The exchange-correlation functional $E_{XC}[\rho]$ is used to contain everything that is unknown. The equation is shown as follows:

$$E_{XC}[\rho] = E_{ncl}[\rho] + T_c[\rho] \quad (2.\ 25)$$

Therefore, the expression for the energy can be rewritten:

$$E[\rho] = E_{XC}[\rho] + T_s[\rho] + J[\rho] + E_{ext}[\rho] \quad (2.\ 26)$$

The main point of the Kohn-Sham Approach is that for any interacting system, one can find a non-interacting model system, with some local effective potential $V_{eff}(r)$, with a ground state density which exactly equals the ground-state density of the interacting system. The difference in the kinetic energy between the interacting electron system and the model non-interacting system, as well as the many-particle effects, the exchange and correlation energy contribution are taken into account in the term $E_{XC}[\rho]$.

Self-consistent calculations

The minimization process corresponds to the determination of the solution of Kohn-Sham Equation:

$$\left[-\frac{\hbar^2}{2m}\nabla^2 + V_{ext}(r) + V_H(r) + V_{XC}(r)\right]\varphi_i(r) = \varepsilon_i\varphi_i(r) \quad (2.\ 27)$$

Here, $\varphi_i(r)$ is the wavefunction of electronic state, ε_i is the Kohn-Sham energy, and $V_H(r)$ is the Hartree potential of the electrons given by:

$$V_H(r) = e^2 \int \frac{\rho(r)}{|r-r'|}\, d^3 r' \quad (2.\ 28)$$

The exchange-correlation potential $V_{XC}(r)$ is given by the functional derivative:

$$V_{XC}(r) = \frac{\delta E_{XC}[\rho(r)]}{\delta\rho(r)} \quad (2.\ 29)$$

Which will lead to the Kohn-Sham energy, ε_i . Since the potentials in this equation depend on the electron density, which in turn depends on the one-particle wavefunction $\varphi_i(r)$, the Kohn-Sham equations must be solved self-consistently. The rough structure of an electronic self-consistent cycle is followed in Figure 7.

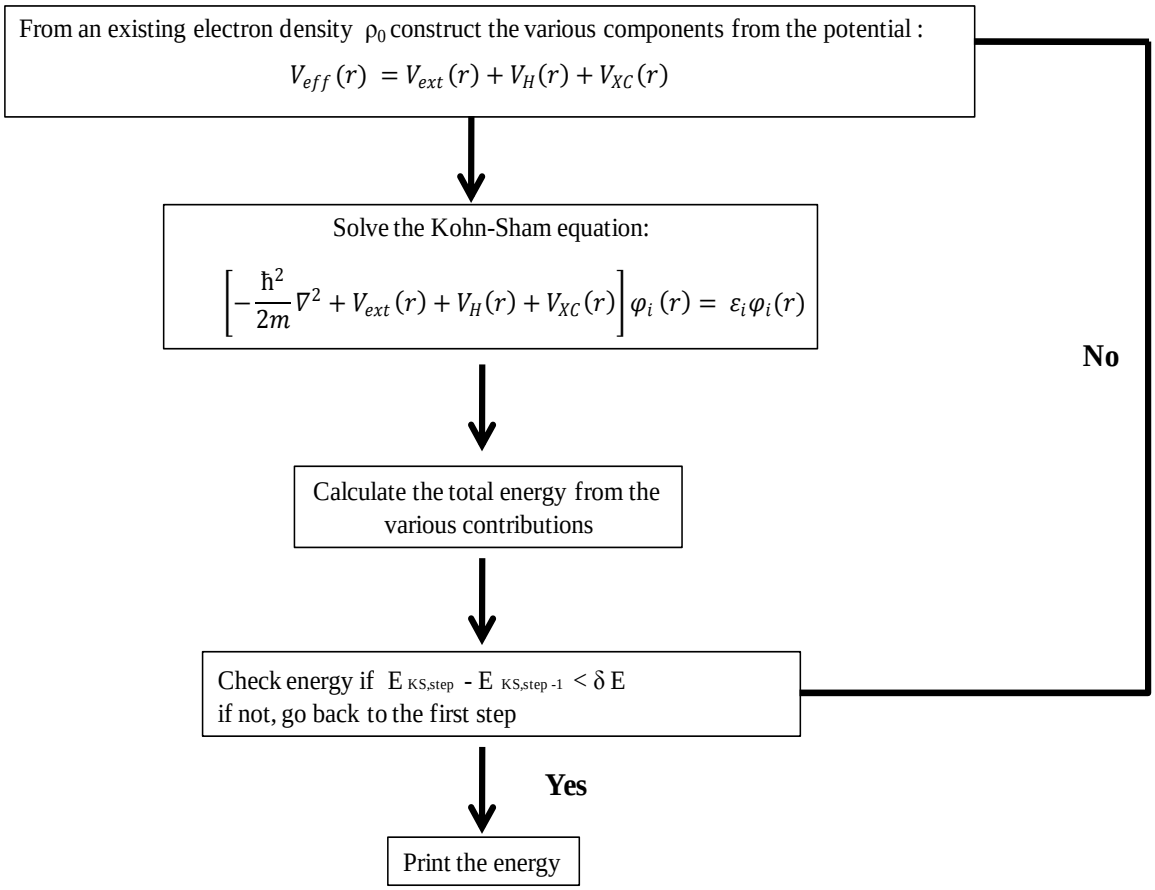

Figure 7. Illustration of the self-consistent field method to solve Kohn-Sham Equation.

2.12.1.3 Exchange correlation functionals

The Local Density Approximation (LDA)

The problem is that the exchange correlation term is not known. Some assumptions must be applied to solve the integrations. Within the local density approximation (LDA), the exchange correlation energy is the sum of the exchange correlation energy per electron. The density at each point is the same which is treated as homogeneous electron gas.[15] The LDA approximation works quite well for homogeneous and over binding systems such as metal systems. However, it can lead to a poor description of inhomogeneous and weakly bonded systems. This is mainly

due to the fact that the electron distribution within the molecule is far from being uniform. The approximation leads to underestimation of lattice parameters and band gaps, while overestimation of cohesive energies and phonon frequencies.[16]

Generalized Gradient Approximation (GGA)

GGA can be used to construct functionals which depend not only on the density but also on its gradient $\nabla\rho$.[17] GGA functionals typically improve the description of weak bonding (for example, hydrogen bonds) and is also suitable for magnetic systems. It gives a better description of bond angles, lengths and energies compared to LDA. The Becke exchange functional[18] combined with the Lee-Yang-Parr correlation functional[19] (BLYP) has been widely used. The PBE functional developed by Perdew, Burke and Ernzerhof in 1996 is a further improvement of the local spin density (LSD) approximation, giving a simple derivation and a good energy calculation accuracy.[20]

Hybrid functionals

One development in DFT was hybrid functionals where the exchange correlation energy functional incorporates a fraction of Hartree-Fock (HF) exchange.[12] A hybrid exchange correlation functional is expressed as a linear combination of the HF exchange functional E_x^{HF}. The exchange and correlation contributions are calculated using DFT, E_x^{DFT} and E_c^{DFT}. It is expressed as:

$$E_{xc}^{Hydrid} = \alpha E_x^{HF} + E_c^{DFT} + (1 - \alpha E_x^{DFT}) \quad (2.30)$$

where: α is chosen to satisfy certain criteria. B3LYP (Becke, three-parameter, Lee-Yang-Parr) function is one of hybrid methods.[21] The hybrid functional gives a high level of accuracy, but a less computational expense.

2.12.1.4 Dispersion correction for DFT calculations

DFT is a commonly used method for electronic structure calculations, which can provide reasonably accurate results for many properties of various molecules. However, a general disadvantage of all GGA, LDA and hybrid functionals is that they do not have a description of the long range electron correlation that is responsible for van der Waals interactions. Recently, a method of dispersion correction for standard DFT (DFT-D) has been proposed to calculate intermolecular interaction energies with higher accuracy.[22] When using the dispersion correction, the

total energy is the sum of the self-consistent Kohn-Sham energy (E_{KS-DFT}) and the empirical dispersion correction energy (E_{disp}). E_{disp} is an empirical dispersion correction which is given by [22]:

$$E_{disp} = -S_6 \sum_{i=1}^{N-1} \sum_{j=i+1}^{N} \frac{C_6^{ij}}{R_{ij}^6} f_{dmp}(R_{ij}) \quad (2.31)$$

Here, N is the number of atoms in the system, C_6^{ij} is the dispersion coefficient for the atom pair ij, S_6 is a global scaling factor and R_{ij} is the interatomic distance. The interatomic C_6^{ij} term is calculated as a geometric mean of the form:

$$C_6^{ij} = \sqrt{c_6^i c_6^j} \quad (2.32)$$

CP2K is a DFT code used in the thesis which includes a dispersion correction.[23]

2.12.1.5 Basis sets

Basis sets are sets of functions which are used to describe molecular orbitals. Increasing the size of the basis sets will typically improve the accuracy of the calculation. A minimal basis set describes each core or valence orbital by one function such as Slater Type Orbital (STO-*n*G), where *n* is an integer. One popular type of basis set is based on Gaussian functions. Here, the molecular orbital (MO) is described by a linear combination of atomic orbitals (AO). Gaussian type orbitals (GTOs) are generated from the equation:

$$\chi(\mathrm{x,y,z}) = N x^l y^m z^n e^{-\alpha r^2} \quad (2.33)$$

where, α determines the spread of the function, r is the distance from the nucleus, *x* ,*y* ,*z* are Cartesian variables and *l*, *m*, *n* are the order of the function. If the sum of *l*, *m*, *n* is equal to zero or one, the functions are equivalent to *s* orbitals or p_x, p_y and p_z orbitals.

The double-zeta (DZ), triple-zeta (TZ), quadruple-zeta (QZ) basis sets are used to describe each valence atomic orbital using multiple basis functions. In addition, the split valence DZ basis sets use two functions for describing the valence orbitals, for example, 3-21G and 6 -31G. Here, 3-21G means that 3 primitive Gaussian functions to describe each inner shell obitial and each valence orbital with two basis functions,

which combines 2 primitive and 1 primitive Gaussian functions for each valence orbital. Furthermore, polarization functions and diffuse functions are added as extra improvements, for example, 3-21G*(d polarization functions on heavy atoms, 3-21G** is 3-21G* and p polarization functions for hydrogen), 3-21+G (diffuse functions) and 3-21+G*(polarization and diffuse functions). Dunning developed correlation consistent polarized basis sets such as cc-pVDZ(double zeta) and cc-pVTZ(triple zeta).[24] The main advantage of Dunning basis sets is to reduce the number of primitive functions and take into account core-valence correlation effects. The Dunning basis sets can also add diffusion functions for better describing weakly interacting molecules. For a periodic system, the plane wave (PW) basis sets are widely used. PW basis sets combined with pseudopotential (effective core potential) can result in small wavefuctions and density gradients for core electrons which allow an efficient calculation of bulk materials. The CP2K, quickstep program used in the thesis uses a Gaussian and plane waves method (GPW) and its augmented extension (GAPW).[23] The GPW method uses a dual basis of atom centred Gaussian orbitals and plane waves. Therefore, the density is represented by an expansion of atom centred Gaussian functions and plane waves. The Goedecker, Teter and Hutter (GTH) pseudopotential is used to describe the effective core potential.[25]

2.12.2 Force fields

In contrast to quantum mechanics, force fields ignore electrons and use a set of parameters and functional forms to describe the potential energy surface (PES) of a system. These parameters and functional forms are fitted to experimental data or high-level quantum mechanical calculations. The advantage of force fields is that they are computationally less expensive than methods such as DFT, though the accuracy can suffer if they are not parameterized correctly.

Force fields for molecular systems can be expressed in terms of intermolecular and intramolecular forces. The total energy in the force field can be written as $E_{total} = E_{bonded} + E_{non-bonded}$ where the bonded and non-bonded contributions are given by the following equations[12]:

$$E_{bond} = E_{str} + E_{bend} + E_{tor} \qquad (2.34)$$

$$E_{non-bonded} = E_{elec} + E_{vdW} \qquad (2.35)$$

where E_{bond} is the intramolecular energy of the system, which consists of bond stretching (E_{str}), bending (E_{bend}) and torsions (E_{tor}). $E_{non-bonded}$ is the intermolecular energy which consists of electrostatic interactions (E_{elec}) and van der Waals interactions (E_{vdW})

The form of the intramolecular potentials used here are as follows[12]:

$$E_{str} = \frac{1}{2} k (l - l_o)^2 \quad (2.\ 36)$$

In the bond stretching energy term (E_{str}), the energy can be described as the square of the displacement from the reference bond length l_o. k is the bond stretching force constant.

$$E_{bend} = \frac{1}{2} k'(\theta - \theta_o)^2 \quad (2.\ 37)$$

The angle bending (E_{bend}) is expressed using Hooke's law.[12] k' is the angle bending force constant. θ_o is the equilibrium value for bond angle. And θ is the actual angle.

Bond stretching and angle bending are considered as hard degrees of freedom. More variations in the structure come from torsions and non bonding terms. The torsional term used here is[12]:

$$E_{tor} = \sum_{n=0}^{N} \frac{V_n}{2} \cos(nw - \gamma) \quad (2.\ 38)$$

The expression for the torsional term is a cosine series expansion. w is the torsion angle, V_n is the barrier height, n is the multiplicity, which gives the number of minimum points in the function as the bond is rotated through 360 °. γ is the phase factor which determines where the torsion angle passes through its minimum value.

The van der Waals potential functions usually use Lennard-Jones functions. Its 9-6 form is expressed as:

$$E_{vdW} = 4\varepsilon \left[\left(\frac{\sigma}{r_{ij}}\right)^9 - \left(\frac{\sigma}{r_{ij}}\right)^6 \right] \quad (2.\ 39)$$

ε is the well depth, r_{ij} is the separation between point charges, and σ is the collision diameter.

The Coulombic interaction is a long range force to deal with charged ions, with an

r_{ij}^{-1} inverse dependence on distance, as given by Coulomb's Law:

$$E_{elec} = \sum\sum \frac{q_i\ q_j}{4\pi\varepsilon_0\ r_{ij}} \qquad (2.\ 40)$$

where q_i and q_j are two point charge, r_{ij} is the separation between point charges. ε_0 is the electronic constant of vacuum.

There are several examples of generic force fields for molecular simulations, such as Universal force field (UFF),[26] COMPASS,[27] and PCFF.[28] In this thesis, due to the unique properties of cage molecules, generic force fields can not accurately describe the structure. A cage specific force field (CSFF) was developed in the Cooper research group by Daniel Holden.[29] CSFF was parameterized based on PCFF[28] and refitted for cage molecules. The force field (FF) parameters for the intra-molecular bonds, angles and dihedral potentials for the cage fragment were fitted using Density Functional Theory (DFT) with a B3LYP functional and 6-31G** basis set.[30] The energy curves from DFT have a good agreement with the optimized FF energy curves. Lennard-Jones (LJ) 9-6 potentials were refitted to describe the non-bonding interactions between cages. It has been shown that the CSFF minimized structures for crystalline cage **1**, cage **2** and cage **3** compare well to the structures obtained from single crystal XRD.[29]

2.12.3 Energy minimization

Energy minimization methods are used to find the global energy minimum which is a stable state of the system. Minimization algorithms can be divided into non-derivative minimization and derivative methods. Most minimization algorithms are used to find the local minimum which is the nearest minimum to the initial configuration. At the minimum point the first derivative of the function *f* with respect to each variable x_i is zero and the second derivatives are positive.

$$\frac{\partial f}{\partial x_i} = 0 \qquad \frac{\partial^2 f}{\partial x_i^2} > 0 \quad (2.\ 41)$$

The energy minimization calculations were performed using Forcite or Discover modules in Material studio 5.0 (Accelrys) with CSFF in this thesis. The steepest descent, conjugate gradient and quasi-Newton methods are included.[12]

Steepest descent method is a first-order minimization method. The method uses a

zig-zag like path to find the local minimum. The choice of direction is where a function *f* decreases most quickly and the gradient direction from the starting point is along the line search. The disadvantage of the method is a slow convergence and that the linear search may result in an estimate with a large error. The steepest descent method is often used for the initial configuration far from the minimum as a first and rough optimization process.

Conjugate gradient method is also a first-order derivative technique. For each minimization step, the gradient of the function for changing the direction vector is calculated. Combining this gradient and the information obtained from the previous interaction can produce a new direction vector of the minimization procedure. The method is a good choice for large scale systems as it has a less computational expense and higher level of accuracy than the steepest descent method.

Unlike computing the true Hessian matrix as in second order Newton methods, quasi-Newton methods use approximations to minimize the energy of a system, which is based on the change in gradient between interactions. DFP [31] and BFGS [32] (proposed by Broyden, Fletcher, Goldfarb and Shanno) algorithms are widely used. The quasi-Newton requires less memory and computational expense.

2.12.4 Molecular dynamics (MD)

2.12.4.1 General introduction

The objective of molecular dynamics (MD) is a computational method to simulate the time dependent behaviour of a molecular system. MD simulations can provide information on the kinetic and diffusive properties of the systems. The fluctuations and conformational change of molecular structure can then be observed. Successive configurations of the system are generated according to Newton's laws, which are used to describe the atomic trajectories and velocities. It can be expressed as:

$$F_i = m_i a_i \quad (2.42)$$

where F_i is the force of a particle i, a_i is the acceleration and m_i is the mass of a particle.

To calculate the trajectory of the particles this law is solved as

$$\frac{d^2x_i}{dt^2} = \frac{F_{x_i}}{m_i} \quad (2.\ 43)$$

where x_i is the position of the particle *i*, with mass m_i and *F* is the force of a particle. MD is a deterministic technique, when an initial set of positions and velocities are given, the subsequent positions and velocities will be determined.

2.12.4.2 Molecular dynamic algorithms

There are different algorithms for integrating the Newton's equations. Most integration algorithms are based on finite difference methods. First the total force of atoms is calculated and assumed to be constant, and then the accelerations can be determined. The positions and velocities at a time $t + \delta t$ can be calculated from the accelerations, positions and velocities at a time *t*. The position, velocity and acceleration can be approximated as expansions of the Taylor series [12]:

$$r\ (t + \ \delta t) = r(t) + \ \delta t\ v(t) + \frac{1}{2}\delta t^2 a(t) + \frac{1}{6}\ \delta t^3 b(t) + \ \ldots \quad (2.\ 44)$$

$$v(t + \delta t) = v(t) + \ \delta t a(t) + \frac{1}{2}\delta t^2 b(t) + \frac{1}{6}\ \delta t^3 c(t) + \ \ldots \quad (2.\ 45)$$

$$a\ (t + \delta t) = a(t) + \ \delta t b(t) + \frac{1}{2}\delta t^2 c(t) + \ \ldots \quad (2.\ 46)$$

where v is the velocity (the first derivative of the positions with respect to time), a is the acceleration (the second derivative), b is the third derivative.

The Verlet algorithm[33] uses the positions and accelerations at a time *t* and the positions and accelerations from the previous step *r (t - δt)* to calculate the new positions *r (t + δt)*.

The equations can be written down as follows:

$$r(t + \delta t) = r(t) + \ \delta t v(t) + \frac{1}{2}\delta t^2 a(t) + \ \ldots \quad (2.\ 47)$$

$$r(t - \delta t) = r(t) - \ \delta t v(t) + \frac{1}{2}\delta t^2 a(t) + \ \ldots \quad (2.\ 48)$$

Combining the two expressions gives:

$$r(t + \delta t) = 2r(t) - r(t - \delta t) + \ \delta t^2 a(t) \quad (2.\ 49)$$

The velocities can simply be calculated by the difference in the positions at time

$t + \delta t$ and $t - \delta t$:

$$v(t) = [r(t + \delta t) - r(t - \delta t)]/2\delta t \quad (2.\ 50)$$

The disadvantage of the Verlet algorithm is that it is a not self-starting algorithm. When t = 0, the previous positions $r\ (t - \delta t)$ can not be obtained. The velocities are not explicitly calculated.

There are several improvements upon the Verlet algorithm. They are the Leapfrog Verlet algorithm[34] and the Velocity Verlet algorithm.[35] The Leapfrog Verlet algorithm calculates the velocities at $v(t + \frac{1}{2}\delta t)$ from the velocities at $v(t - \frac{1}{2}\delta t)$ and the accelerations at t. The positions at $r(t + \delta t)$ can be obtained from velocities at $v(t + \frac{1}{2}\delta t)$ and the positions at $r(t)$.

$$r(t + \delta t) = r(t) + \delta t\, v(t + \tfrac{1}{2}\delta t) \quad (2.\ 51)$$

$$v\left(t + \tfrac{1}{2}\delta t\right) = v\left(t - \tfrac{1}{2}\delta t\right) + \delta t\, a(t) \quad (2.\ 52)$$

The velocities at time t can then be calculated from

$$v(t) = \tfrac{1}{2}\left[v\left(t + \tfrac{1}{2}\delta t\right) + v\left(t - \tfrac{1}{2}\delta t\right)\right] \quad (2.\ 53)$$

The velocities leap over the positions at t to calculate the values at $t + \frac{1}{2}\delta t$. The advantage of the Leapfrog Verlet algorithm is the precision of the velocities. The Velocity Verlet method gives positions, velocities and accelerations at the same time and it is more computationally expensive.

2.12.4.3 Molecular dynamic ensembles

MD simulations can be performed using an ensemble with a constant number of particles (N), volume (V) and total energy (E). The microcanonical ensemble (NVE) is obtained by solving Newton's equation with temperature and pressure exchanged. Different ensembles can be applied depending on the system and properties of simulations. Alternative ensembles include the constant number of particles, volume and temperature (NVT) and the constant number of particles, pressure and temperature (NPT) ensembles. The constant temperature is obtained by coupling to a heat bath that keeps the system at the average temperature. The thermostat methods

include Nosé-Hoover and Berendsen thermostat.[32a, 36] In the case of NPT, the number of particles, pressure and temperature are conserved where the volume and energy are allowed to fluctuate in order to equilibrate the system. Thermostat and barostat methods need to be used to keep constant temperature and pressure, respectively.

2.12.5 Monte carlo simulations (MC)

The Monte Carlo ((MC) method is used to generate a sequence of configurations of a system by randomly changing the positions and orientations of the molecule. The method accepts a new configuration (E_{new}) with a lower energy than the previous one (E_{old}). However, if $E_{new} > E_{old}$, the Boltzmann factor is used to compare with a random number (0-1). If the Boltzmann factor is bigger than the random number, the configuration is accepted. A basis MC algorithm consists of randomly selecting a particle and trial moves. It is a non-deterministic technique.

The Grand Canonical Monte Carlo (GCMC) is to simulate the system at constant chemical potential, μ, temperature, T, and volume, V, while the number of particles may change during the simulation. The simulation is performed in the following steps:

(1) Displacement of particles using the Metropolis method.[12]
(2) Creation and removal of particles.

GCMC simulations have been widely used for simulating adsorption isotherms or loading of molecules. In this thesis, the amorphous cage models are initially built using the Amorphous Cell module in the Materials Studio Modeling 5.0 software package (Accelrys), which is based on the GCMC method.

2.12.6 Calculated surface areas

Surface area is a very important property for the characterization of porous solids. Experimental surface areas are determined from nitrogen isotherms measured at 77 K by the BET model as discussed in section 2.2.4 above. The surface areas can also be calculated using a geometric method from the structural model. The calculated surface areas in this thesis are obtained by rolling a probe around the surface of the pores. The Connolly surface area (CSA) is defined as a probe molecule rolling across the interface between the probe and the pore surface. Whereas the solvent accessible

surface area (SASA) calculates the surface area from the center of a probe molecule rolling along the pore surface, as shown in Figure 8. The Connolly surface or solvent accessible surface is calculated using a probe radius of 1.82 Å for N_2, 1.72 Å for CO_2 and 1.42 for H_2 in this work.[37] CSA and SASA were calculated using Materials Studio 5.0 (Accelrys).

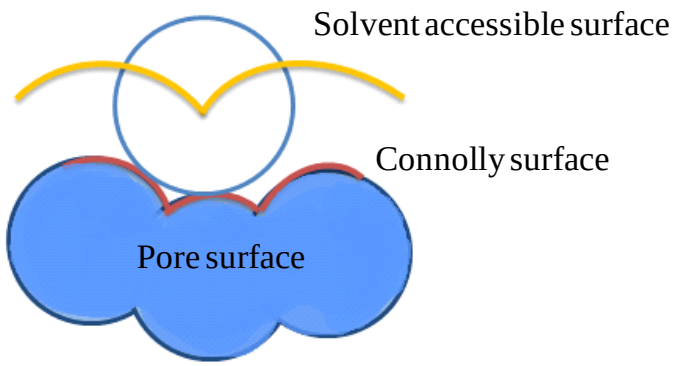

Figure 8. A representation of Connolly surface area (red line) and solvent accessible surface area (yellow line).(The Figure is adapted from the Ref.[38])

2.12.7 Computational techniques

DFT codes:

CP2K using a mixed Gaussian and plane waves approach[23] and Gaussian 09[30] are used to calculate the total energy and formation energy for cage molecules in this thesis.

MD code:

DL_POLY 2.20 is developed at Daresbury Laboratory by W. Smith, T.R. Forester and I.T. Todorov. [39] MD simulations in this thesis are carried out using DL_POLY.

Materials Studio 5.0 (Accelrys)

Forcite and Discover modules are used for energy minimization with CSFF. The Amorphous Cell module is used for generating initial amorphous cage structures. The calculated surface areas (CSA and SASA) in this thesis are measured using the Atom Volumes & Surfaces module.

2.13 Reference

1. Roque-Malherbe, R. M. A., *Adsorption and diffusion in nanoporous materials* CRC Press: 2007.
2. (a) Atkins, P. W., *Physical chemistry*. Oxford University Press: 1998; (b) Attard, G. B., C., *Surfaces*. Oxford University press: 2008; (c) S.Lowell, J. E. S., Martin A. Thomas and Matthias Thommes, *Characterization of porous solids and powders: surface area, pore size and density*. Springer: 2004.
3. Sing, K. S. W. E., D. H.; Haul, R. A. W.; Moscou, L.; Pierotti, R. A.; Rouquerol, J.; Siemieniewska, T., Reporting physisorption data for gas/solid systems with special reference to the determination of surface area and porosity (Recommendations 1984). *Pure Appl. Chem.* **1985,** *57* (4), 603-619.
4. Langmuir, I., The constitution and fundamental properties of solids and liquids. PART I. Solids. *J. Am. Chem. Soc.* **1916,** *38* (11), 2221-2295.
5. Brunauer, S.; Emmett, P. H.; Teller, E., Adsorption of Gases in Multimolecular Layers. *J. Am. Chem. Soc.* **1938,** *60* (2), 309-319.
6. (a) Skoulidas, A. I.; Sholl, D. S., Transport Diffusivities of CH_4, CF_4, He, Ne, Ar, Xe, and SF_6 in Silicalite from Atomistic Simulations. *J. Phys. Chem. B* **2002,** *106* (19), 5058-5067; (b) Skoulidas, A. I.; Sholl, D. S., Self-Diffusion and Transport Diffusion of Light Gases in Metal-Organic Framework Materials Assessed Using Molecular Dynamics Simulations. *J. Phys. Chem. B* **2005,** *109* (33), 15760-15768.
7. (a) Lesley E. Smart, E. A. M., *Solid state chemistry : an introduction*. CRC Press: 2005; (b) West., A. R., *Basic solid state chemistry*. 2nd edition; New York : John Wiley & Sons: 1999.
8. (a) R E Dinnebier, S. J. L. B., *Powder Diffraction ; Theory and Practice*. Cambridge, Royal Society of Chemistry: 2008; (b) Vitalij K. Pecharsky, P. Y. Z., *Fundamentals of Powder Diffraction and Structural Characterization of Materials*. Springer US: 2009.
9. Rietveld, H., A profile refinement method for nuclear and magnetic structures. *J. Appl. Crystallogr.* **1969,** *2* (2), 65-71.
10. Hasell, T.; Wu, X.; JonesJames, T. A.; Bacsa, J.; Steiner, A.; Mitra, T.; Trewin, A.; Adams, D. J.; Cooper, A. I., Triply interlocked covalent organic cages. *Nat. Chem.* **2010,** *2* (9), 750-755.
11. Wolfram Koch, M. C. H., *A chemist's Guide to Density Functional Theory*. Wiley-VCH: 2002.
12. Leach, A. R., *Molecular Modelling: Principles and applications*.2001
13. Hohenberg, P.; Kohn, W., Inhomogeneous Electron Gas. *Phys. Rev.* **1964,** *136* (3B), B864-B871.
14. Kohn, W.; Sham, L. J., Self-Consistent Equations Including Exchange and Correlation Effects. *Phys. Rev.* **1965,** *140* (4A), A1133-A1138.
15. Jones, R. O.; Gunnarsson, O., The density functional formalism, its applications and prospects. *Rev. Mod. Phys.* **1989,** *61* (3), 689-746.
16. van de Walle, A.; Ceder, G., Correcting overbinding in local-density-approximation calculations. *Phys. Rev. B* **1999,** *59* (23), 14992-15001.
17. Filippi, C.; Umrigar, C. J.; Taut, M., Comparison of exact and approximate density functionals for an exactly soluble model. *J. Chem. Phys.* **1994,** *100* (2), 1290-1296.
18. Becke, A. D., Density-functional exchange-energy approximation with correct asymptotic behavior. *Phys. Rev. A* **1988,** *38* (6), 3098-3100.
19. Lee, C.; Yang, W.; Parr, R. G., Development of the Colle-Salvetti correlation-

energy formula into a functional of the electron density. *Phys. Rev. B* **1988,** *37* (2), 785-789.
20. Perdew, J. P.; Burke, K.; Ernzerhof, M., Generalized Gradient Approximation Made Simple. *Phys. Rev. Lett.* **1996,** *77* (18), 3865-3868.
21. Becke, A. D., Density-functional thermochemistry. III. The role of exact exchange. *J. Chem. Phys.* **1993,** *98* (7), 5648-5652.
22. Grimme, S., Density functional theory with London dispersion corrections. *Wiley Interdisciplinary Reviews: Computational Molecular Science* **2011,** *1* (2), 211-228.
23. VandeVondele, J.; Krack, M.; Mohamed, F.; Parrinello, M.; Chassaing, T.; Hutter, J., Quickstep: Fast and accurate density functional calculations using a mixed Gaussian and plane waves approach. *Comput. Phys. Commun.* **2005,** *167* (2), 103-128.
24. Dunning, J. T. H., Gaussian basis sets for use in correlated molecular calculations. I. The atoms boron through neon and hydrogen. *J. Chem. Phys.* **1989,** *90* (2), 1007-1023.
25. Goedecker, S.; Teter, M.; Hutter, J., Separable dual-space Gaussian pseudopotentials. *Phys. Rev. B* **1996,** *54* (3), 1703-1710.
26. Rappe, A. K.; Casewit, C. J.; Colwell, K. S.; Goddard, W. A.; Skiff, W. M., UFF, a full periodic table force field for molecular mechanics and molecular dynamics simulations. *J. Am. Chem. Soc.* **1992,** *114* (25), 10024-10035.
27. Sun, H., COMPASS: An ab Initio Force-Field Optimized for Condensed-Phase ApplicationsOverview with Details on Alkane and Benzene Compounds. *J. Phys. Chem. B* **1998,** *102* (38), 7338-7364.
28. Sun, H., Ab initio calculations and force field development for computer simulation of polysilanes. *Macromolecules* **1995,** *28* (3), 701-712.
29. Daniel Holden, K. E. J., Andrew I. Cooper, Abbie Trewin, and David J. Willock, A Bespoke Force Field for Simulating the Molecular Dynamics of Porous Organic Cages. *J. Phys. Chem. C* **2012,** 116 (31), 16639-16651.
30. M. J. Frisch, G. W. T., H. B. Schlegel, G. E. Scuseria, M. A. Robb, J. R. Cheeseman, G. Scalmani, V. Barone, B. Mennucci, G. A. Petersson, H. Nakatsuji, M. Caricato, X. Li, H. P. Hratchian, A. F. Izmaylov, J. Bloino, G. Zheng, J. L. Sonnenberg, M. Hada, M. Ehara, K. Toyota, R. Fukuda, J. Hasegawa, M. Ishida, T. Nakajima, Y. Honda, O. Kitao, H. Nakai, T. Vreven, J. A. Montgomery, Jr., J. E. Peralta, F. Ogliaro, M. Bearpark, J. J. Heyd, E. Brothers, K. N. Kudin, V. N. Staroverov, R. Kobayashi, J. Normand, K. Raghavachari, A. Rendell, J. C. Burant, S. S. Iyengar, J. Tomasi, M. Cossi, N. Rega, J. M. Millam, M. Klene, J. E. Knox, J. B. Cross, V. Bakken, C. Adamo, J. Jaramillo, R. Gomperts, R. E. Stratmann, O. Yazyev, A. J. Austin, R. Cammi, C. Pomelli, J. W. Ochterski, R. L. Martin, K. Morokuma, V. G. Zakrzewski, G. A. Voth, P. Salvador, J. J. Dannenberg, S. Dapprich, A. D. Daniels, Ö. Farkas, J. B. Foresman, J. V. Ortiz, J. Cioslowski, and D. J. Fox, Gaussian, Inc., Wallingford CT, 2009.
31. (a) Davidon, W., Variable Metric Method for Minimization. *SIAM Journal on Optimization* **1991,** *1* (1), 1-17; (b) Fletcher, R., *Practical methods of optimization (2nd ed.)*. John Wiley & Sons: New York, 1987; (c) Nocedal, J. W., Stephen J., *Numerical Optimization*. Springer-Verlag: 1999.
32. (a) Berendsen, H. J. C.; Postma, J. P. M.; van Gunsteren, W. F.; DiNola, A.; Haak, J. R., Molecular dynamics with coupling to an external bath. *J. Chem. Phys.* **1984,** *81* (8), 3684-3690; (b) Fletcher, R., A new approach to variable metric algorithms. *The Computer Journal* **1970,** *13* (3), 317-322; (c) Goldfarb, D., A Family

of Variable-Metric Methods Derived by Variational Means. *Math. Comput.* **1970,** *24* (109), 23-26; (d) Shanno, D. F., Conditioning of Quasi-Newton Methods for Function Minimization. *Math. Comput.* **1970,** *24* (111), 647-656.
33. Verlet, L., Computer "Experiments" on Classical Fluids. I. Thermodynamical Properties of Lennard-Jones Molecules. *Phys. Rev.* **1967,** *159* (1), 98-103.
34. Hockney, R. W., Potential calculation and some applications. *Methods Comput. Phys.* **1970**.
35. Swope, W. C.; Andersen, H. C.; Berens, P. H.; Wilson, K. R., A computer simulation method for the calculation of equilibrium constants for the formation of physical clusters of molecules: Application to small water clusters. *J. Chem. Phys.* **1982,** *76* (1), 637-649.
36. Hoover, W. G., Canonical dynamics: Equilibrium phase-space distributions. *Phys. Rev. A* **1985,** *31* (3), 1695-1697.
37. Sircar, S., Basic Research Needs for Design of Adsorptive Gas Separation Processes. *Ind. Eng. Chem. Res.* **2006,** *45* (16), 5435-5448.
38. Düren, T.; Millange, F.; Férey, G.; Walton, K. S.; Snurr, R. Q., Calculating Geometric Surface Areas as a Characterization Tool for Metal−Organic Frameworks. *J. Phys. Chem. C* **2007,** *111* (42), 15350-15356.
39. Smith, W.; Yong, C. W.; Rodger, P. M., DL_POLY: Application to molecular simulation. *Mol. Simul.* **2002,** *28* (5), 385-471.

Chapter 3

Crystalline Porous Organic Cage – **CC2**

3.1 Introduction

This work forms part of a broader study, including other cage molecules, that was published in *Nat. Mater.* 2009.[1] Previously, the imine-linked organic cage molecule, **CC1**, was synthesised by a one-step [4+6] cycloimination condensation reaction between 1,3,5-triformylbenzene and 1,2-ethylenediamine.[1] The **CC1** molecule has tetrahedral symmetry and the structure is connected by six unfunctionalized ethylene vertices. The crystals exhibit monoclinic $P2_1/c$ symmetry after desolvation from ethyl acetate (EtOAc). The packing structure for **CC1** illustrates isolated lattice voids as represented by the orange Connolly surface in Figure 1. **CC1** is therefore formally non-porous due to a lack of interconnected cage voids. Gas sorption analysis has showed that **CC1** adsorbs very little N_2 or H_2 at 77.3 K with a BET surface area of 23 m^2/g calculated from the N_2 isotherm. This is consistent with the disconnected void structure. However, **CC1** is able to adsorb CH_4 and CO_2 at room temperature exhibiting porosity 'without pores' as observed for calix[4]arene. [2]

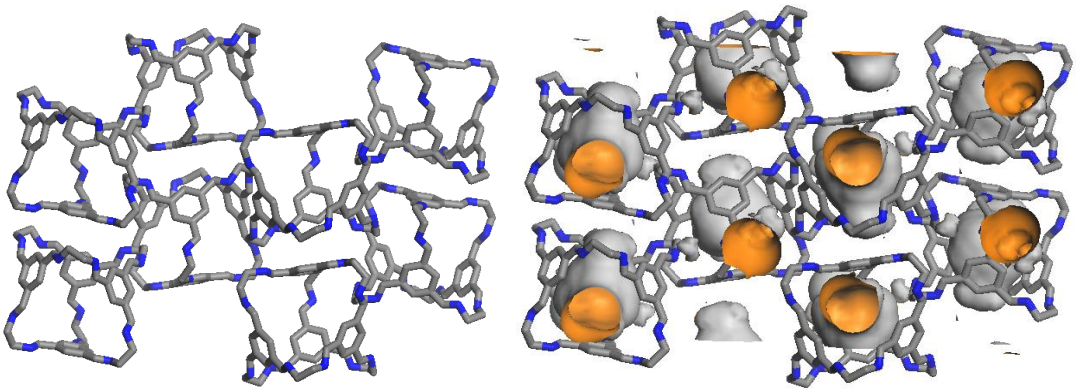

Figure 1. The crystal structure for **CC1** (hydrogen atoms are omitted for clarity. Carbon and nitrogen atoms are colored gray and blue, respectively). The molecular packing results in isolated void volume as illustrated by the orange Connolly surface.

CC1 was firstly synthesized by Dr Tomokazu Tozawa in the Cooper research group. The fascinating cage structure and molecular packing suggested that different trialdehyde and diamine monomers could be used to synthesize more porous organic cage systems. Commercially available trialdehydes with functional groups are limited, but there are a number of commercially available functionalized diamines. Initially, 1,2-propylenediamine and diaminomaleonitrile monomers were chosen to react with 1,3,5-triformylbenzene to form [4+6] imine cage molecules. The intention

was to investigate the effects of the functional groups (the methyl and cyano group) of the cage vertices on the crystal packing and porosity. Furthermore, post-synthetic modification could be carried out using the functionalities on the cage vertices.

3.2 Preliminary reactions to form cage molecules

The reaction procedure followed the **CC1** synthesis method. The reaction ratio of trialdehyde and diamine monomers of 2: 3 was used. The solvent (35 mL) was added to 1,3,5-triformylbenzene (50 mg, 0.31 mmol) in a sample vial. A solution of the corresponding amount of diamine (5 mL of solvent) was added. The resulting mixture was kept for 3-5 days without stirring at room temperature. In this study, chloroform ($CHCl_3$), dichloromethane (DCM), ethyl acetate (EtOAc), and acetonitrile (CH_3CN) solvents were included for testing reactions. It was found that solvents played an important role in the **CC1** synthesis.[1]

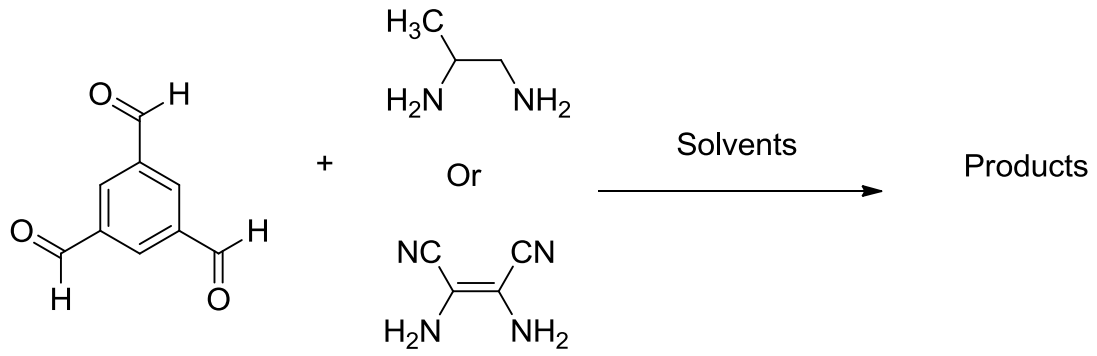

Scheme 1. Synthesis of imine cage molecules, analogous to **CC1**. The reactions were carried out using 1,3,5-triformylbenzene and 1, 2-propylenediamine or diaminomaleonitrile in a series of solvents.

The reactions of 1,3,5-triformylbenzene and diaminomaleonitrile in different solvents formed insoluble yellow solids which precipitated from the reaction solution. ^{1}H NMR was used to analyze the filtrate, showing unreacted trialdehyde. The preliminary reactions of 1,3,5-triformylbenzene and diaminomaleonitrile monomers did not proceed successfully to form cage molecules. This might be ascribed to electron withdrawing CN functional groups which reduce the reactivity of diamine.

In the case of 1,2-propylenediamine monomer, insoluble polymer was observed from the reaction in EtOAc. The products obtained from the reactions in $CHCl_3$ or DCM showed some evidence of cage formation based on NMR analysis, but some

impurities were also present, which could not be identified by NMR. Fortunately, single crystals were observed to grow after 3 days directly from the reaction in CH_3CN solvent. Single crystal X-ray analysis confirmed that the [4+6] cage molecule had formed.

In this Chapter, I will focus on introducing **CC2** which is synthesized by the reaction of 1,3,5-triformylbenzene with 1,2-propylenediamine in CH_3CN solvent. Products were isolated directly as crystals which were characterized by single crystal X-ray diffraction. The **CC2** molecule has a tetrahedral symmetry with one methyl group on each vertex. The methyl group directs molecular packing to give one-dimensional (1D) pore channels which run between the cages. Unlike **CC1**, the **CC2** material exhibits permanent porosity and adsorbs a significant amount of gas molecules, such as N_2, H_2, CH_4 and CO_2.

3.3 Synthesis of cage 2 (CC2)

CC2 was synthesized by a condensation reaction of 1,3,5-triformylbenzene with 1,2-propylenediamine in a [4+6] cycloimination reaction in the absence of any added catalyst or template shown in Scheme 2. Acetonitrile (35 mL) was added to 1, 3, 5-triformylbenzene (50 mg, 0.31 mmol) in a sample vial at room temperature. After 5 minutes, a solution of 1, 2-diaminopropane (34 mg, 0.47 mmol) in CH_3CN (5 mL) was added. The resulting mixture was left covered for 3 days without stirring. A turbid solution was observed to form within 5 minutes after 1,2-diaminopropane was added to the partially dissolved trialdehyde. This was followed by precipitation of a solid after around 5–6 hours and finally, pale white needles of **CC2** were observed to crystallize from solution after 3 days. The crystals were separated carefully from the sample using a spatula, washed with acetonitrile and air dried to give the acetonitrile solvate of **CC2.** To desolvate **CC2**, a sample was heated to 120 ºC under dynamic vacuum for 12 hours. The final isolated **CC2** yield was 37 %. Mass spectrometry showed $[M + H]^+$ and $[M+ Na]^+$ ions at m/z = 877 and 899, consistent with a [4+6] cage structure with formula $C_{54}H_{60}N_{12}$.

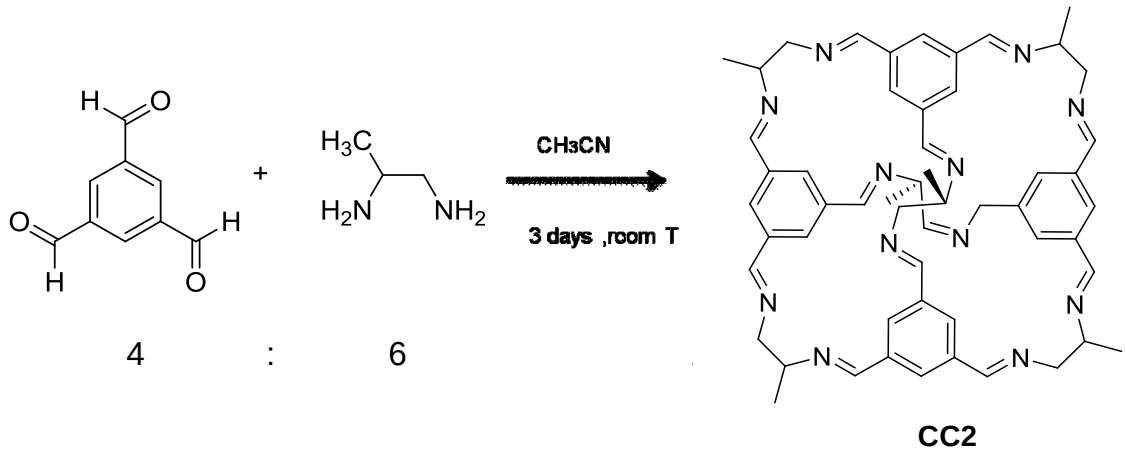

Scheme 2. Covalent synthesis of a [4+6] tetrahedral organic cage molecule, **CC2**.

CC2 exists as four isomers due to positional disorder of methyl groups on the vertices. The positional isomers were addressed by Dr Alexander Steiner and are shown in Figure 2. The four different isomers were named as 3111, 2220, 2211, and 3210, by noting the number of adjacent methyl groups to the phenyl rings within the cage. For example, '3' means three of the adjacent carbon atoms of $C_6H_3(CN)_3$ unit carry a methyl group. The **CC2** is chiral containing R or S enantimoers, even though a racemic mixture of the diamine was used. That is, each cage molecule is resolved into R or S configuration resulting from reaction of either 6 x S diamines or 6 x R diamines with 4 equivalents of triformylbenzene.

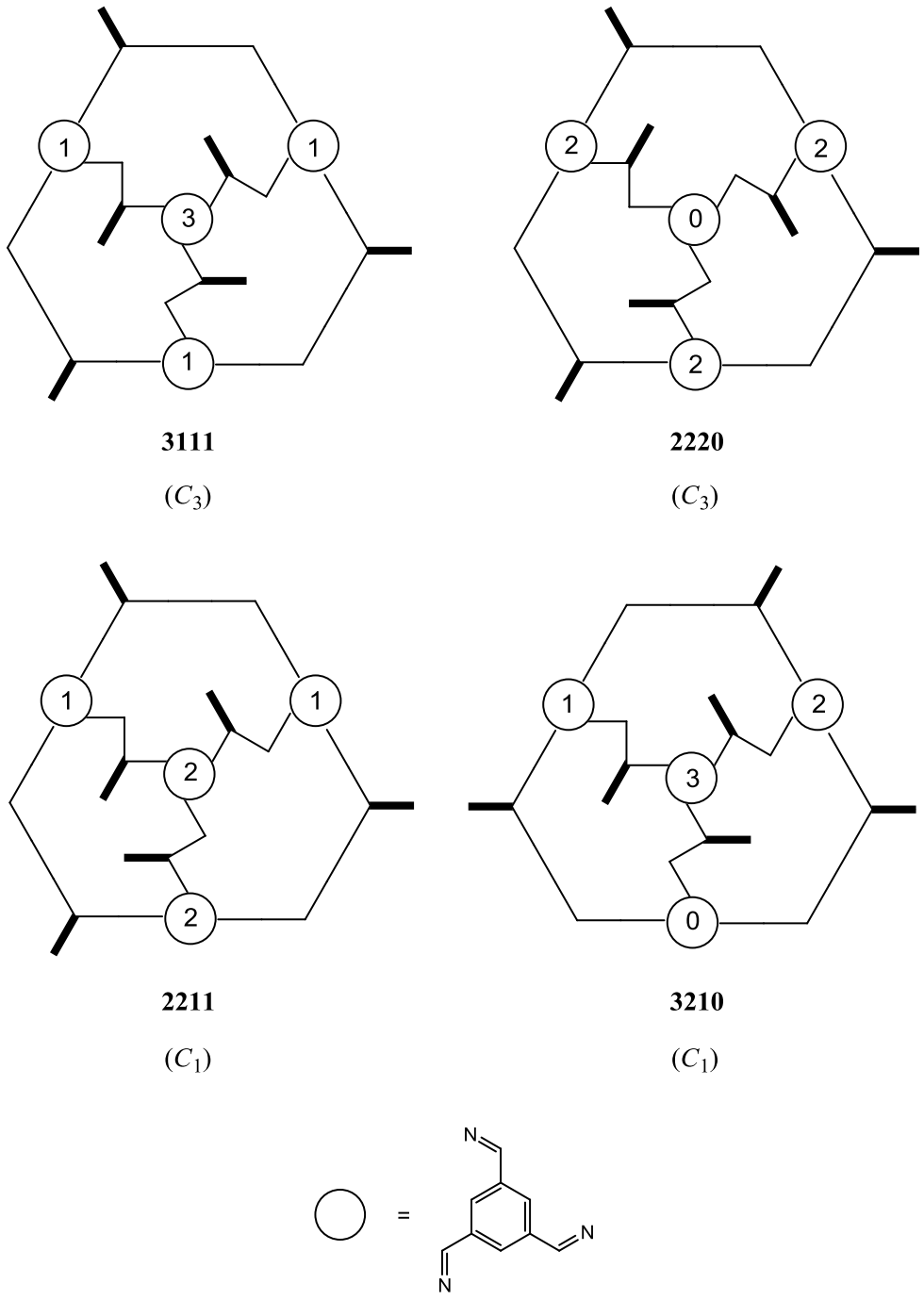

Figure 2. Positional isomers of CC2. (Figure taken from the Ref. [1])

3.4 Characterizations of CC2

3.4.1 NMR spectra of CC2

CC2 is fully soluble in chloroform and was characterized by ^{1}H and ^{13}C NMR spectroscopy. ^{1}H NMR chemical shifts of the imine protons were observed at 8.2 ppm where the integration of peaks is 12H (Figure 3). There are multiple peaks due to methyl groups on the cage vertices which give the different positional isomers of

CC2 shown in Figure 2. The multiple peaks at ~ 7.9 ppm are assigned to the protons on aromatic rings of **CC2** with 12H. The chemical shifts at 3.5, 3.9 and 4.1 ppm are consistent with protons on the cage bridges and they are multiple peaks with 6H for each one. The methyl groups exhibit a chemical shift of 1.3 ppm with 18H. The peaks with chemical shifts at 2.1 ppm and 1.56 ppm are the solvent acetonitrile and H_2O, respectively, in Figure 3 (red). In terms of ^{1}HNMR spectroscopy of desolvated **CC2** in Figure 3 (blue), the solvent acetonitrile peak at 2.1 ppm was not observed which shows solvents have been removed.

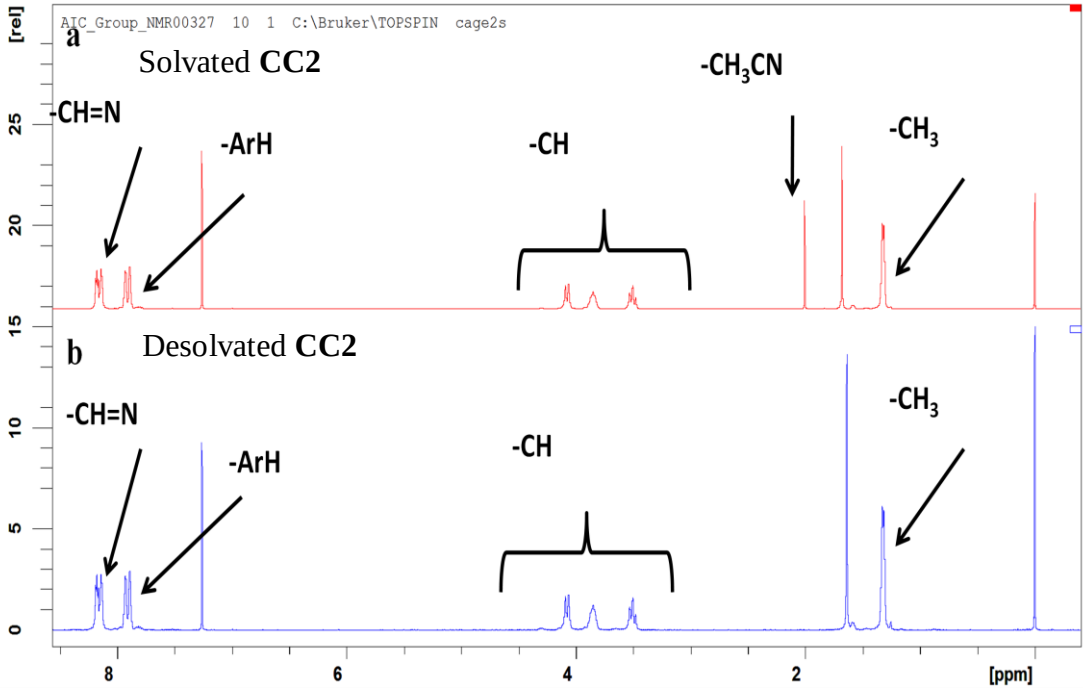

Figure 3. ^{1}H-NMR spectra of solvated (Red) and desolvated (Blue) **CC2**.

($CDCl_3$ at 7.27 ppm, H_2O at 1.56 ppm and TMS at 0 ppm)

A further analysis of the coupling between the methyl group CH_3 protons and the CH proton on the cage vertices was investigated using ^{1}H COSY NMR (Figure 4). The COSY analysis can assign the peaks at 3.5, 3.9 and 4.1 ppm, respectively, to the protons on the cage vertices. The protons on the cage vertices are labelled as **H1**, **H2** and **H3** as shown in the picture. A coupling between the methyl group CH_3 protons at 1.3 ppm and the CH proton at 3.9 ppm, was observed which is the proton **H2**. A coupling was also observed at 3.5 and 4.1 ppm which corresponded to the CH_2 group protons, **H1** and **H3**.

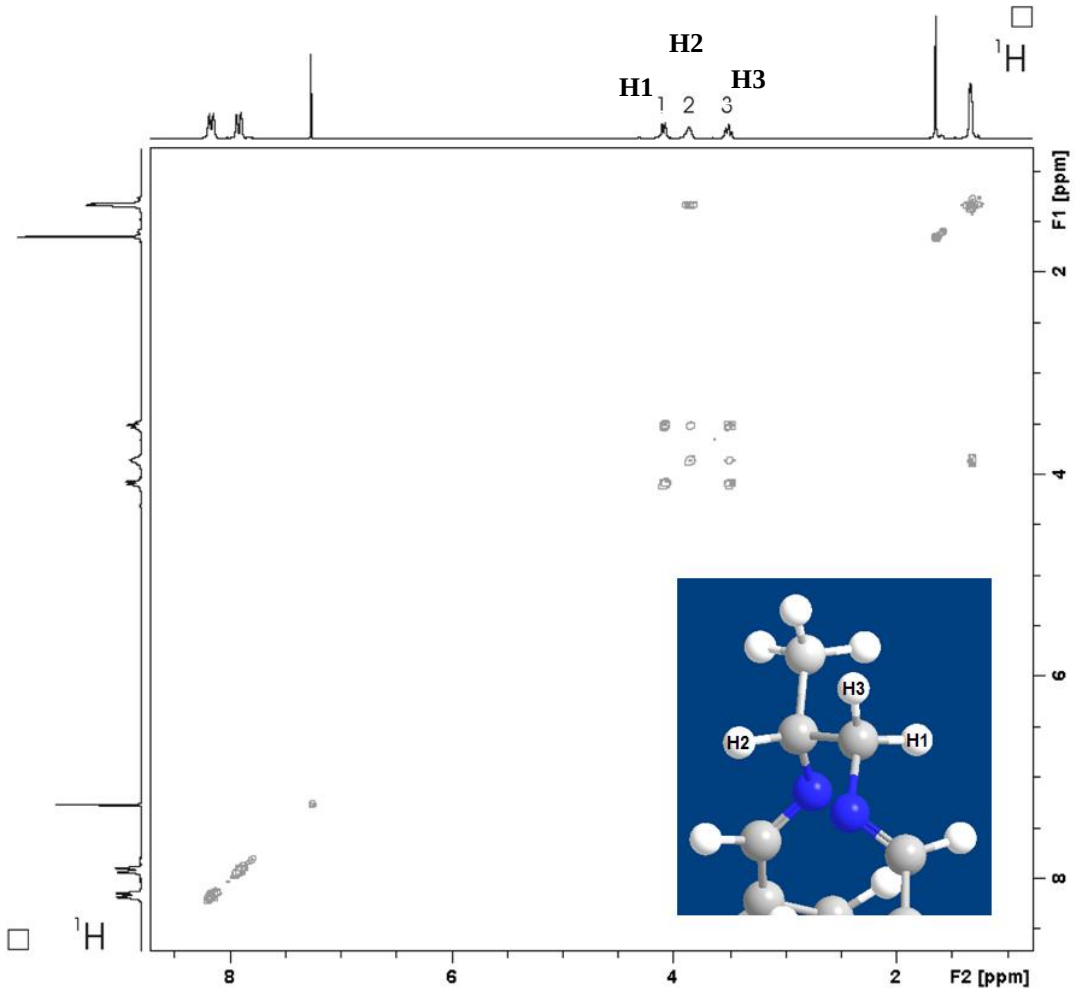

Figure 4. ^{1}H COSY NMR spectrum for **CC2**.

The ^{13}C NMR spectra of solvated and desolvated samples are shown in Figure 5. The ^{13}C chemical shifts of the imine bonds were observed at 161.0, 160.9, 159.3 and 159.1 ppm. The peaks at 136.5, 129.7, 129.6, 129.5 and 129.4 ppm were assigned to carbons on aromatic rings. The methyl groups on the cage vertices can result in different structural isomers for **CC2**, therefore, different carbon environments for imine bonds and aromatic rings were observed. The chemical shifts at 68.4 and 66.8 ppm are consistent with carbons on the cage bridges. The methyl groups have a chemical shift of 20.9 ppm. The peaks with chemical shifts at 116.4 ppm and 1.89 ppm are the solvent acetonitrile. No solvent peaks were observed in desolvated **CC2** ^{13}C NMR in Figure 5 (red).

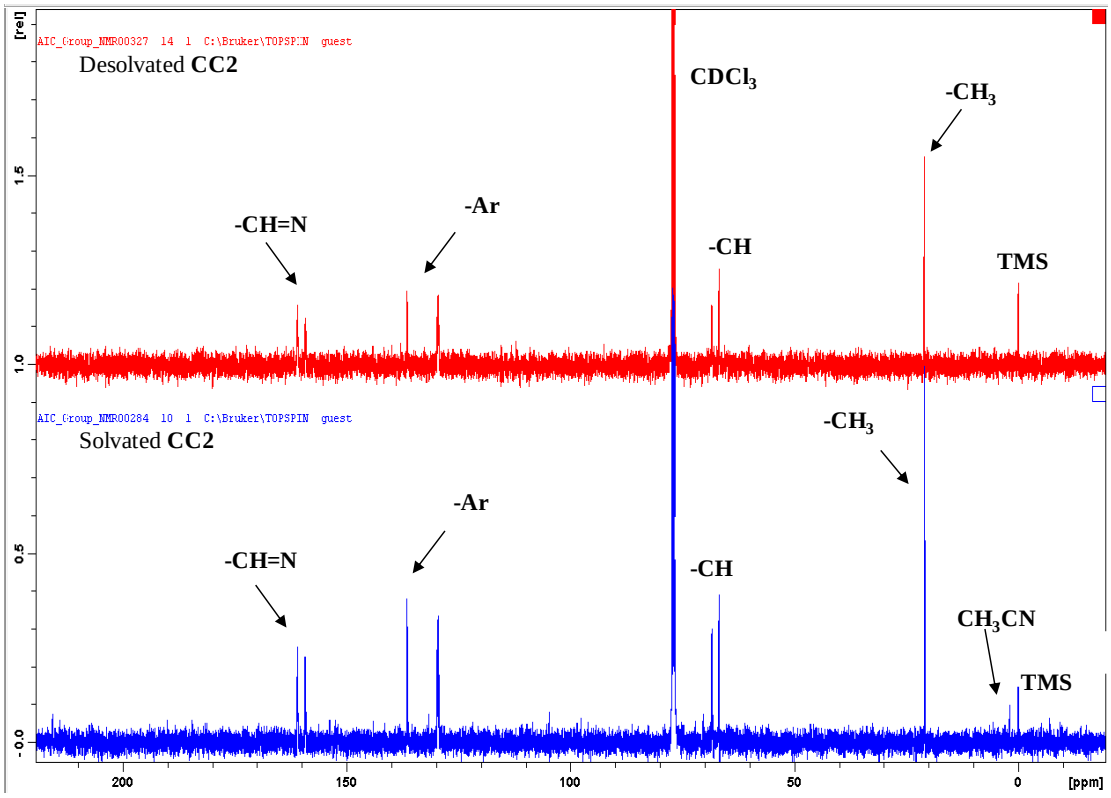

Figure 5. ^{13}C NMR spectra of solvated (Blue) and desolvated (Red) **CC2**.

($CDCl_3$ at 77 ppm)

3.4.2 Fourier Transform Infrared Spectroscopy (FTIR) for CC2

The solvated and desolvated samples were prepared as KBr disks for 16 scans with a resolution of 4 cm^{-1} FTIR analysis. Spectra were recorded in transmission mode (Figure 6). FTIR spectra for both solvated and desolvated samples show a strong imine stretch at 1640 cm^{-1}. Both materials have similar IR stretches and intensities. The C=O stretch at 1720 cm^{-1} was not observed, indicating no unreacted 1,3,5-triformylbenzene. In addition, the solvent CH_3CN absorption at 2240-2260 cm^{-1} was not found for either solvated and desolvated samples, whereas OH stretching occurred at ~ 3500 cm^{-1} indicating the presence of water molecules. There is no change of IR spectra after desolvation. This is because desolvation of **CC2** occurs spontaneously at ambient temperature. As such, some solvent is inevitably lost prior to FTIR analysis of the "solvated" sample.

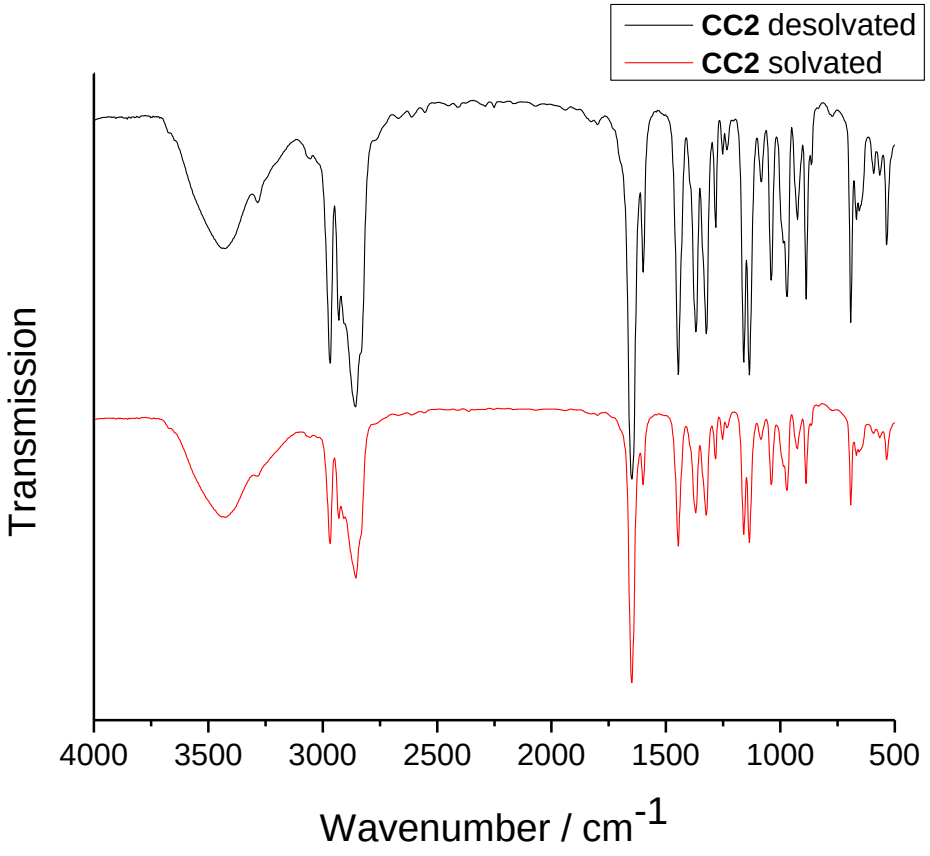

Figure 6. FTIR spectra for solvated and desolvated **CC2**.

3.4.3 Thermogravimetric analysis (TGA) for CC2

This rapid loss of solvent for as-synthesized **CC2** was further confirmed by TGA analysis under nitrogen flow. TGA was carried out using a nitrogen flow and heating rate of 5 ºC / min. **CC2** desolvates rapidly and spontaneously at ambient temperature to lose the solvent, CH_3CN. Therefore, the TGA analysis is similar for both solvated and desolvated samples in Figure 7. The small mass loss observed for the as-synthesized sample is most likely attributed to water molecules. The onset of decomposition for the desolvated sample occurs at 349 °C (622 K). The **CC2** material has a relative good thermal stability, comparable with many metal organic frameworks.

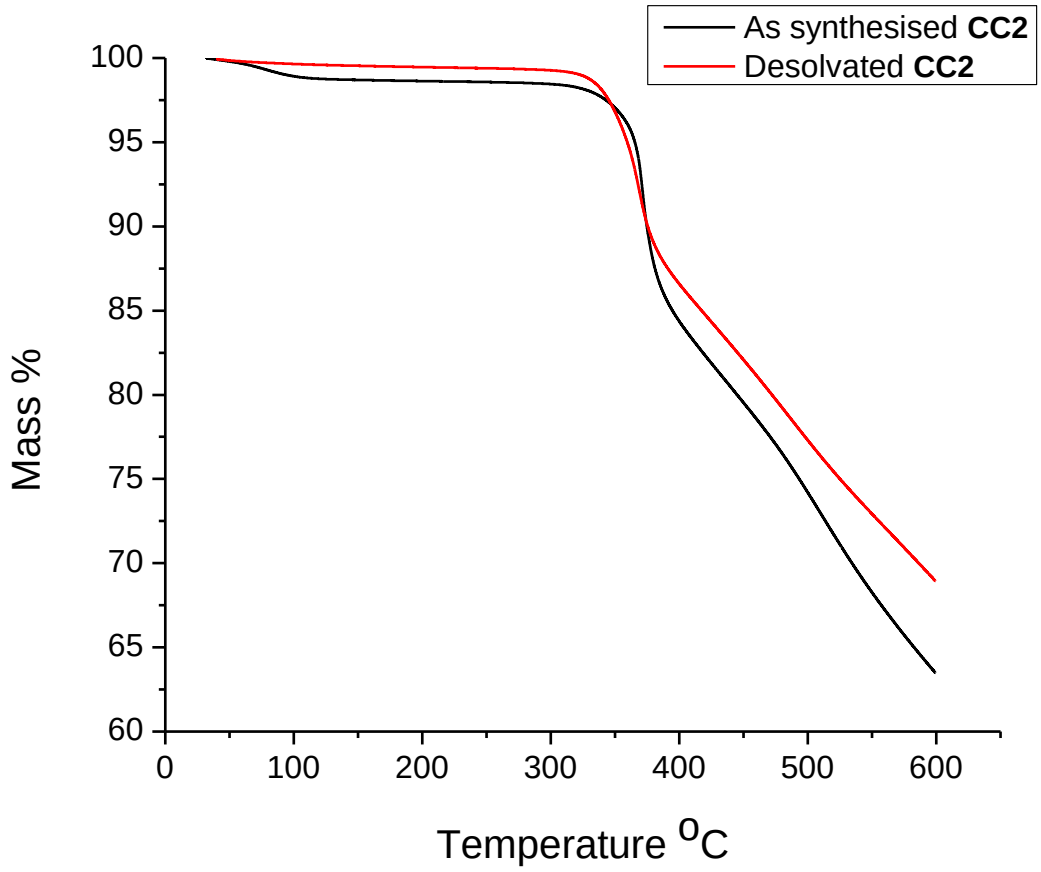

Figure 7. TGA analysis for solvated and desolvated **CC2**.

3.4.4 The single crystal X-Ray analysis for CC2

CC2 crystallized directly from acetonitrile and formed small, colourless needle crystals. The morphology of **CC2** crystals is shown by scanning electron microscope (SEM) and optical microscope images in Figure 8.

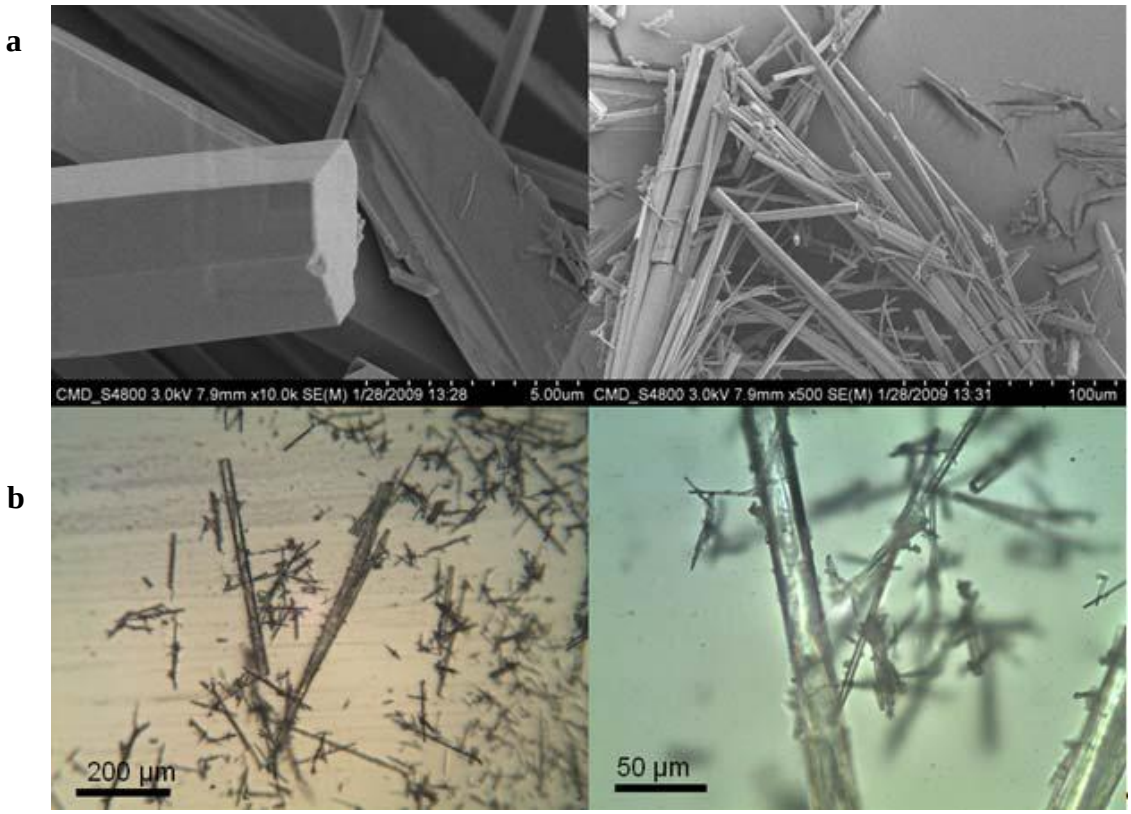

Figure 8. SEM images (a) and optical microscope images (b) for desolvated crystals of **CC2**. Scale bars for SEM images are 5 µm and 100 µm, respectively. Scale bars for optical microscope images are 200 µm and 50 µm, respectively. Images were collected by Dr Tom Hasell.

Single crystal X-ray data of **CC2** were collected and refined by Dr John Bacsa. The analysis shows that the molecules crystallize in the trigonal system with the space group, *P-3*. The unit cell is: $a = b = 18.770(3)$ Å, $c = 10.921(2)$ Å, and cell volume is 3332.1 Å^3. The unit cell contains three solvent accessible voids, two smaller ones with a volume 158 Å^3 inside the cage voids, and a larger void corresponding to the channel with a volume 568 Å^3 per unit cell. The electron density from X-ray diffraction suggested that guest molecules were accommodated in the solvent accessible voids, but the diffraction had a low resolution. No ordered guests could be located and refined. The SQUEEZE method in PLATON calculated a total of 100 electrons for guest molecules.[3] TGA and FTIR showed no CH_3CN solvents observed due to the solvent loss spontaneously at ambient temperature (Figures 6 and 7), but water molecules might adsorb in the material.[4] Approximately 6 H_2O molecules per unit cell were estimated.

The isolated **CC2** molecule exhibits [4+6] tetrahedral symmetry shown in Figure 9 (a) which is analogous to **CC1**.[1] Four $C_6H_3(CN)_3$ units of planar threefold symmetry are linked by six 1,2-propylenediamine vertices. The methyl groups on the propylene vertices are disordered. A vertex of **CC2** shows two possible locations for the methyl group, the *exo* and *endo* sites as shown in Figure 9 (b). The *exo* positions are pointing away from the cage and the *endo* positions are towards cage window. The positional disordered methyl group occupied at the *exo*-site per vertex observed in the crystal structure. The geometry optimization calculation for **CC2** molecule with one methyl group occupied at the endo site was performed by DMol3 in the Materials Studio Modelling 5.0 software package (Accelrys) with GGA, PBE functional and TNP basis set. Energy calculations show that that the *exo*-site is energetically favoured by 30 kJ/mol over the *endo*-site due to the steric interactions between the *endo*-methyl group and the hydrogen attached to the imine-carbon.

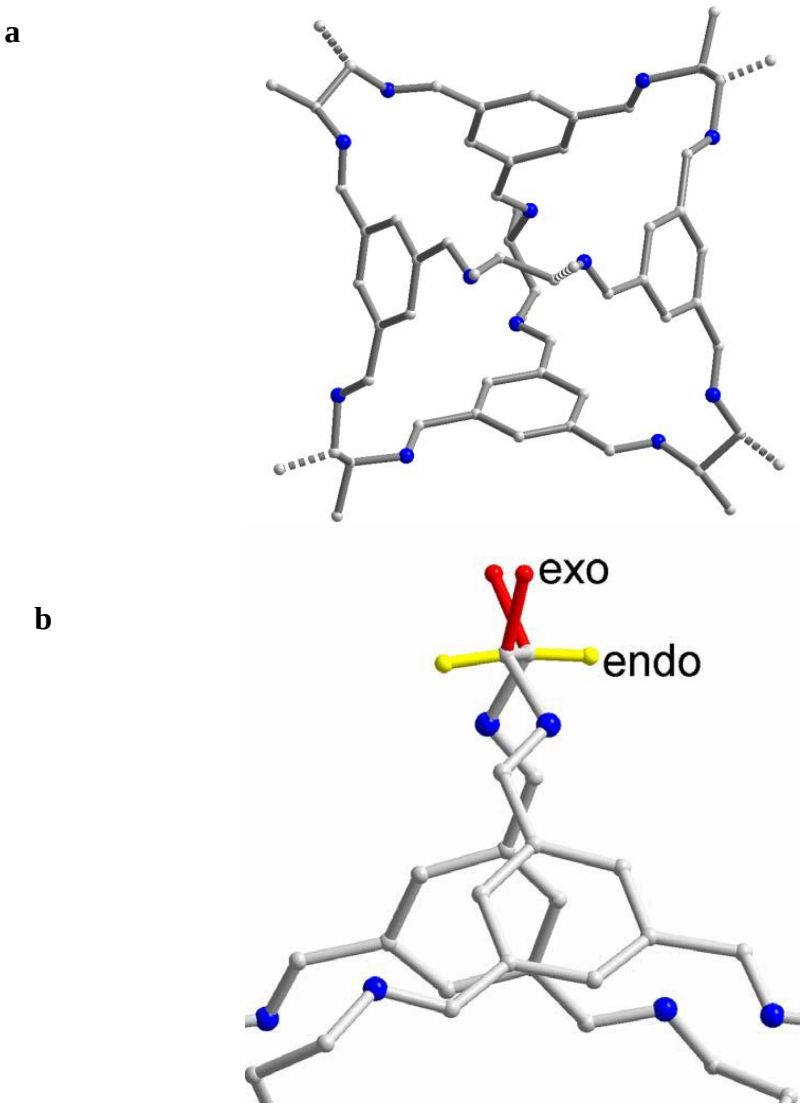

Figure 9. (a) Isolated **CC2** molecular structure obtained from single crystal XRD (b) a vertex of CC2 with *exo* (red) and *endo* (yellow) sites.

The **CC2** molecules assemble in the crystal via non-covalent interactions to form a hexahedral symmetry shown in Figure 10 (B). The cage voids are represented by Connolly surface area using a N_2 probe radius of 1.82 Å in Figure 10 (C-D). The molecular packing of **CC2** results in a 1D pore channel between the cages. The isolated cage voids are also generated due to the window to arene stacks of cage molecules. The channels and cage voids have a lack of formal connection because no cage windows facing towards the channels. The solvent accessible surface area for **CC2** calculated using N_2 probe radius is 660 m^2/g. The 1D channel has a diameter of

6.2 Å at the neck point which is defined by the methyl groups on neighbouring cages and a diameter of 14 Å at the widest point. Due to two potential sites on each vertex, partial occupancy for methyl groups existed in the crystal structure. There are two distinct environments for methyl groups, either facing to the channel or facing into another cage molecule.

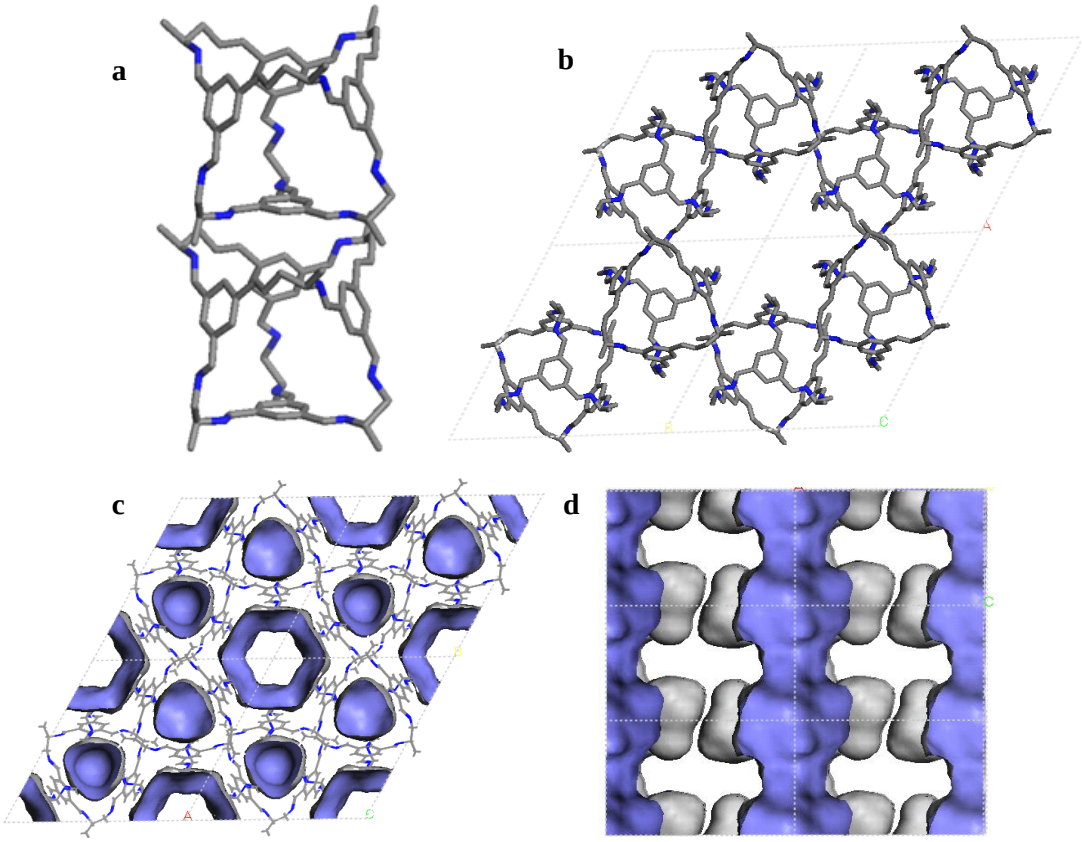

Figure 10. (A) The cage molecules show a window-to-arene stack. (B) The pseudohexagonal packing representation of **CC2** crystals. (C-D) The porosity illustrated by Connolly surfaces using a N_2 probe radius of 1.82 Å along c axis and b axis, respectively. The model is based on the desolvated crystal structure. The 1D pore channel is surrounded by six stacks of disconnected cage voids.

Energy calculations for 3111, 2220, 2211, and 3210 isomers were carried out to investigate the energy favourable isomer. The geometry optimization DFT calculations were performed using Gaussian code[5] with B3LYP functional group[6] and TZVP basis set [7]. The total energies for four **CC2** isomers are listed in **Table 1**. DFT calculations show that the 2220 isomer has the lowest energy, but there is only a small deviation between the four isomers. The energy difference between the highest energy isomer 2211 and the lowest energy isomer 2220 isomer is only 0.4 kJ

/mol, which is within the error of DFT calculations.[8] The calculations suggest that four positional isomers of **CC2** should co-exist in the solid state, unless the distribution is skewed, for example, by crystal packing forces in the solid state.

Table 1. DFT calculations for total energies of 3111, 2220, 2211, and 3210 isomers.

CC2 isomers	Total Energy (Hartree)	Relative Energy (kJ/mol)
2220	-2751.688327	0
3210	-2751.688301	0.068301999
3111	-2751.688232	0.24622
2211	-2751.688163	0.425827999

3.4.5. CC2 powder X-ray diffraction patterns

The phase purity of bulk **CC2** was confirmed from powder X-ray diffraction (PXRD). A comparison of the PXRD patterns recorded for the solvated and desolvated samples alongside the simulated pattern from the single-crystal structure is shown in Figure 11. The simulated PXRD was obtained using the Material Studio 5.0 powder pattern refinements. The as-synthesized sample was treated overnight at 120 °C under the vacuum before gas sorption. Therefore, the sample after gas sorption can be considered to be the desolvated sample. The X-ray patterns have no significant change between the as-synthesized and after gas sorption samples. This reveals that the **CC2** structure remains nearly intact after desolvation. Compared with the simulated PXRD pattern, the experimental PXRD patterns show the same peak positions. Therefore, the single crystal structure is representative of the bulk materials.

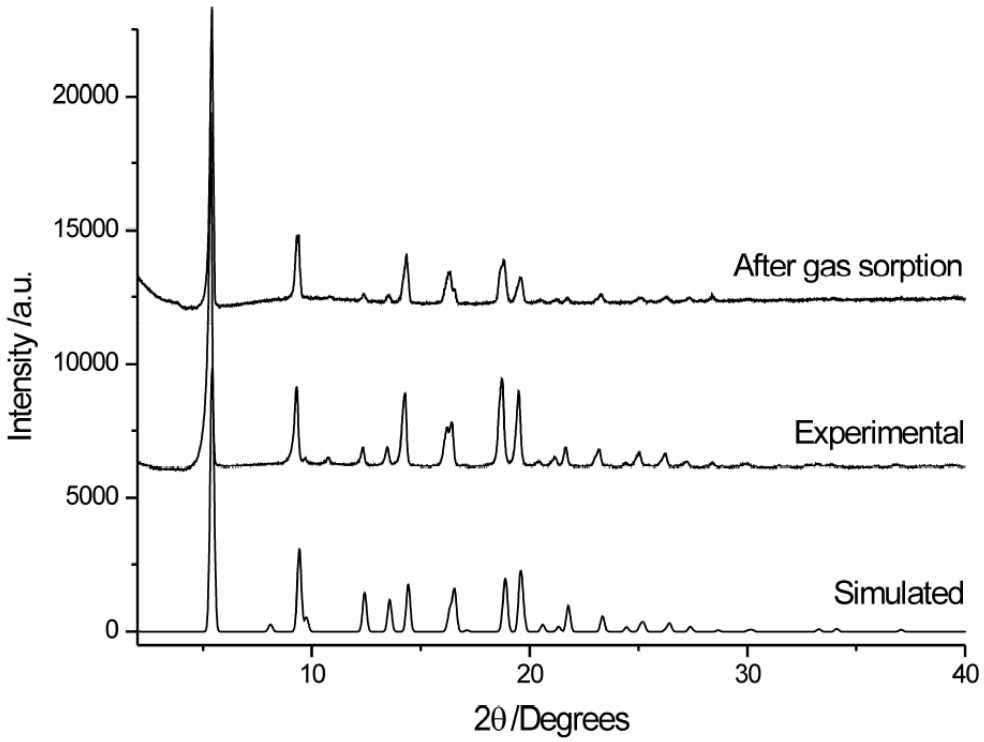

Figure 11. Powder X-ray diffraction patterns for as-synthesized (middle) and after gas sorption (top) samples. The simulated PXRD from single crystal X-ray diffraction data is shown in the bottom as a comparison.

3.4.6 CC2 gas sorption analysis

Gas sorption measurements for **CC2** were carried out. The sample was heated to 120 ºC under dynamic vacuum for 12 hours to fully desolvate and degas the sample before gas sorption analysis. The sample retains crystallinity and no phase changes occur upon desolvation according to the PXRD patterns. N_2 sorption measurement for **CC2** at 77.3 K showed a Type I isotherm indicating a permanent microporosity (Figure 12 A). The Brunauer-Emmett-Teller surface area of **CC2** is 533 $m^2 g^{-1}$ and the Langmuir surface area calculated is 600 $m^2 g^{-1}$, as calculated from the N_2 adsorption isotherm. The BET and Langmuir methods were applied in the relative pressure range of 0.01-0.10, $R^2 = 0.9999$ and C value = 2372.

The total N_2 uptake for **CC2** is 168.5 $cm^3 g^{-1}$ (corresponding to 7.5 mmol g^{-1}) at a relative pressure (P/P_0) of 0.998 and 77.3 K (Figure 12 (A)) in comparison with 3.8 mmol g^{-1} for cucurbit[6]uril,[9] 4.0 mmol g^{-1} for 1,2-dimethoxy-*p-tert*-butylcalix[4]dihydroquinone[10] and 4.4 mmol g^{-1} for 3,3′,4,4′-tetra(trimethylsilylethynyl)biphenyl [11] under comparable conditions. However the N_2

uptake of **CC2** is lower than other [4+6] imine cage molecules reported more recently in our group and the Mastalerz group. [12]

CC2 adsorbed 132.2 cm^3 g^{-1} (5.9 mmol g^{-1}) H_2 at 77.3K, 1 bar in Figure 12 (B) and further H_2 analysis for **CC2** showed 198.9 cm^3 g^{-1} (8.9 mmol g^{-1}) uptakes at 77.3 K and 7 bar. By comparison, a salicylbisimine cage compound synthesized by Mastalerz, *et al.* exhibited a BET surface area of 1375 m^2 g^{-1} and H_2 uptake of 5.6 mmol g^{-1} at 77 K and 1 bar.[12c] Although the BET surface area of **CC2** is low, the H_2 uptake of **CC2** exceeds reports for other porous organic molecules.[2, 9-11, 13]

CC2 also adsorbed substantial quantities of CO_2 and CH_4 at the ambient temperature. The CH_4 sorption capability was 21.3 cm^3 g^{-1} (0.9 mmol g^{-1}) at 287 K, 1 bar and 67.2 cm^3 g^{-1} (3.0 mmol g^{-1}) CO_2 uptake was observed at 275K, 1 bar (Figure 12 (C-D)). The **CC2** demonstrates a high CO_2 uptake of 3.0 mmol g^{-1} compared with other imine cages at 1 bar and 275 K such as 2.1 mmol g^{-1} for the salicylbisimine cage [12c] and 2.5 mmol g^{-1} for **CC3**.[1] All of the isotherms were repeated on different batches of samples.

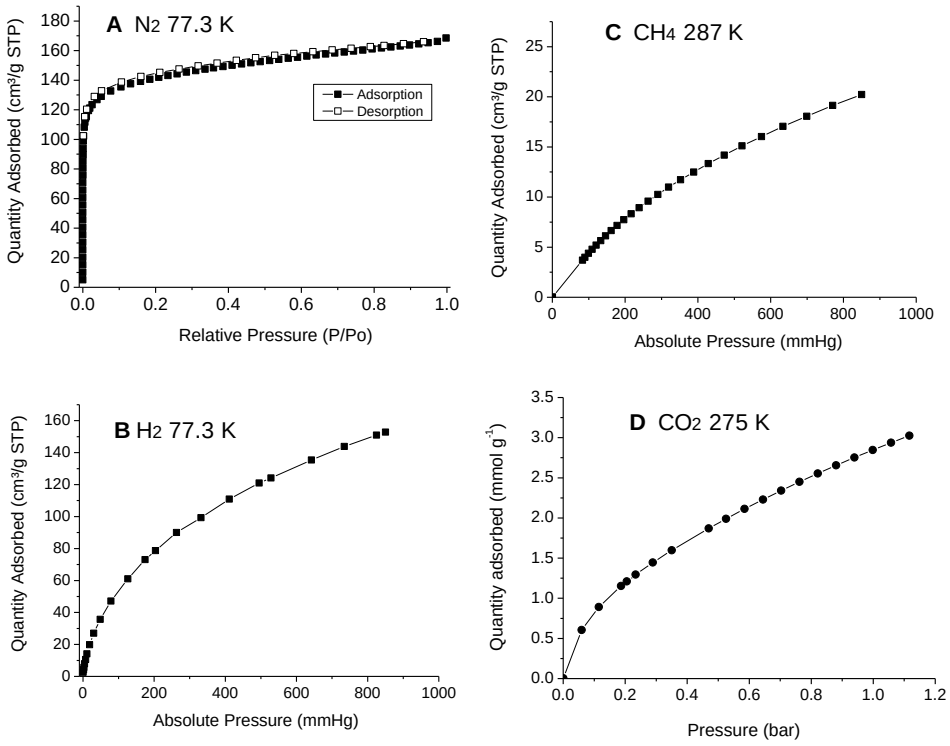

Figure 12. Gas sorption isotherms for **CC2**. (A) N_2 sorption and desorption isotherm at 77.3 K. Filled and open symbols represent adsorption and desorption, respectively. (B) H_2 isotherm at 77.3 K. (C) CH_4 isotherm at 287 K. (B) CO_2 isotherm at 275 K.

The pore size distribution of **CC2** was calculated by non-local density functional theory (NL-DFT) from the N_2 isotherm. **CC2** has pore widths of 9.9 Å and 15.6 Å, respectively (Figure 13). This is roughly consistent with the diameter of the channels in the X-ray crystal structure. The diameter of channels is 6.2 Å at the neck point and 14 Å at the widest point as shown in Figure 10 C.

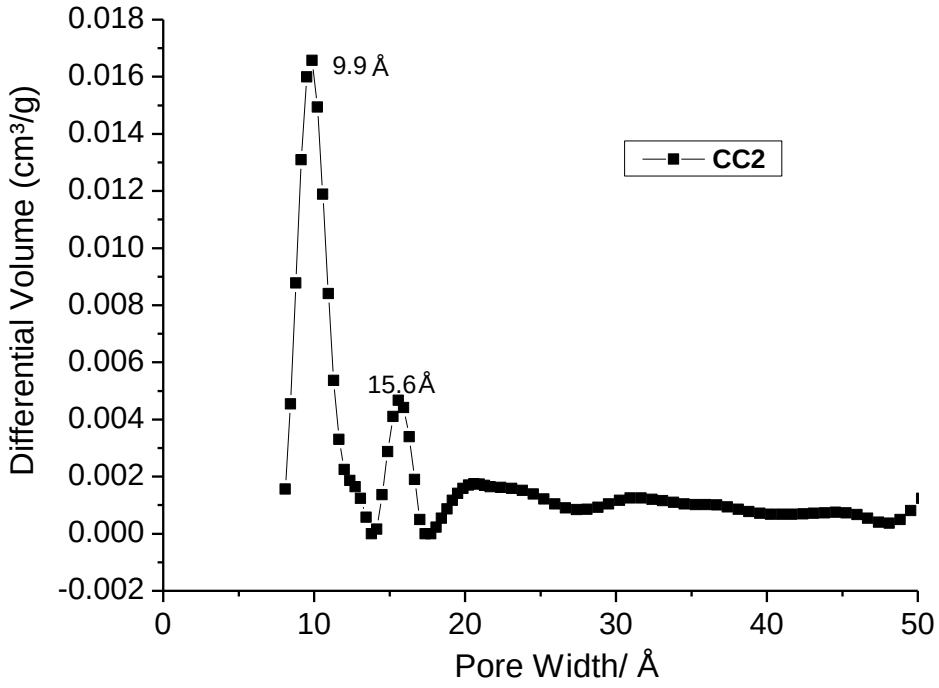

Figure 13. Pore size distribution curves obtained from the N_2 adsorption isotherm at 77.3 K for **CC2**.

3.5. Conclusions

Porous organic cage (**CC2**) was synthesized from 1,3,5-triformylbenzene and 1,2-propylenediamine. The synthesis is one step and the products, which directly crystallize from CH_3CN solvents, can be characterized by single X-ray diffraction. The shape-persistent cage molecule shows tetrahedral symmetry. Four positional isomers of **CC2** were observed due to disordered methyl groups on the cage vertices. Unlike **CC1**, the methyl groups direct the crystal packing to give a 1D channel running between the cages. The voids in the cages are isolated due to lack of interconnecting to the channel. As a result, the porosity in **CC2** results from the isolated voids in the cages (intrinsic porosity) and the inefficient packing of these molecules (extrinsic porosity). The **CC2** material demonstrates permanent porosity

upon desolvation with a BET surface area of 533 m^2/g and microporous volume of 0.26 cm^3/g. It can adsorb large amounts of gases. The H_2 and CO_2 uptakes of **CC2** exceed reports for other discrete organic molecules. Furthermore, a triply catenated **CC2** species was subsequently observed when the reactions were carried out in the presence of an acid catalyst.[14]

3.6 Chapter acknowledgements

In this chapter, I would like to thank Andy, Dave and Abbie for their supervision and suggestions on my work. Dr. John Bacsa solved the **CC2** crystal structure. Dr. Shashi Swamy helped me with cage synthesis in the lab. The gas sorption was done by Dr. James T.A. Jones.

3.7 Reference

1. Tozawa, T.; Jones, J. T. A.; Swamy, S. I.; Jiang, S.; Adams, D. J.; Shakespeare, S.; Clowes, R.; Bradshaw, D.; Hasell, T.; Chong, S. Y.; Tang, C.; Thompson, S.; Parker, J.; Trewin, A.; Bacsa, J.; Slawin, A. M. Z.; Steiner, A.; Cooper, A. I., Porous organic cages. *Nat. Mater.* **2009,** *8* (12), 973-978.
2. Atwood, J. L.; Barbour, L. J.; Jerga, A., Storage of Methane and Freon by Interstitial van der Waals Confinement. *Science* **2002,** *296* (5577), 2367-2369.
3. P. van der Sluis, A. L. S., BYPASS: an effective method for the refinement of crystal structures containing disordered solvent regions. *Acta Cryst. A* **1990,** *46*, 194-201.
4. Lockington, D. A.; Parlange, J. Y., Anomalous water absorption in porous materials. *J. Phys. D: Appl. Phys*. **2003,** *36* (6), 760.
5. M. J. Frisch, G. W. T., H. B. Schlegel, G. E. Scuseria, M. A. Robb, J. R. Cheeseman, G. Scalmani, V. Barone, B. Mennucci, G. A. Petersson, H. Nakatsuji, M. Caricato, X. Li, H. P. Hratchian, A. F. Izmaylov, J. Bloino, G. Zheng, J. L. Sonnenberg, M. Hada, M. Ehara, K. Toyota, R. Fukuda, J. Hasegawa, M. Ishida, T. Nakajima, Y. Honda, O. Kitao, H. Nakai, T. Vreven, J. A. Montgomery, Jr., J. E. Peralta, F. Ogliaro, M. Bearpark, J. J. Heyd, E. Brothers, K. N. Kudin, V. N. Staroverov, R. Kobayashi, J. Normand, K. Raghavachari, A. Rendell, J. C. Burant, S. S. Iyengar, J. Tomasi, M. Cossi, N. Rega, J. M. Millam, M. Klene, J. E. Knox, J. B. Cross, V. Bakken, C. Adamo, J. Jaramillo, R. Gomperts, R. E. Stratmann, O. Yazyev, A. J. Austin, R. Cammi, C. Pomelli, J. W. Ochterski, R. L. Martin, K. Morokuma, V. G. Zakrzewski, G. A. Voth, P. Salvador, J. J. Dannenberg, S. Dapprich, A. D. Daniels, Ö. Farkas, J. B. Foresman, J. V. Ortiz, J. Cioslowski, and D. J. Fox, Gaussian, Inc., Wallingford CT, 2009.
6. Becke, A. D., Density-functional exchange-energy approximation with correct asymptotic behavior. *Phys. Rev. A* **1988,** *38* (6), 3098-3100.

7. Atwood, J. W. S. a. J. L., *Supramolecular Chemistry*. Second Edition ed.; Wiley p990.
8. Li, H.; Shi, L.; Zhang, M.; Su, Z.; Wang, X.; Hu, L.; Chen, G., Improving the accuracy of density-functional theory calculation: The genetic algorithm and neural network approach. *J. Chem. Phys.* **2007,** *126* (14), 144101-8.
9. Lim, S.; Kim, H.; Selvapalam, N.; Kim, K.-J.; Cho, S. J.; Seo, G.; Kim, K., Cucurbit[6]uril: Organic Molecular Porous Material with Permanent Porosity, Exceptional Stability, and Acetylene Sorption Properties. *Angew. Chem. Int. Ed.* **2008,** *47* (18), 3352-3355.
10. Thallapally, P. K.; McGrail, B. P.; Atwood, J. L.; Gaeta, C.; Tedesco, C.; Neri, P., Carbon Dioxide Capture in a Self-Assembled Organic Nanochannels. *Chem. Mater.* **2007,** *19* (14), 3355-3357.
11. Msayib, K. J.; Book, D.; Budd, P. M.; Chaukura, N.; Harris, K. D. M.; Helliwell, M.; Tedds, S.; Walton, A.; Warren, J. E.; Xu, M.; McKeown, N. B., Nitrogen and Hydrogen Adsorption by an Organic Microporous Crystal. *Angew. Chem. Int. Ed.* **2009,** *48* (18), 3273-3277.
12. (a) Bojdys, M. J.; Briggs, M. E.; Jones, J. T. A.; Adams, D. J.; Chong, S. Y.; Schmidtmann, M.; Cooper, A. I., Supramolecular Engineering of Intrinsic and Extrinsic Porosity in Covalent Organic Cages. *J. Am. Chem. Soc.* **2011,** *133* (41), 16566-16571; (b) Jones, J. T. A.; Hasell, T.; Wu, X.; Bacsa, J.; Jelfs, K. E.; Schmidtmann, M.; Chong, S. Y.; Adams, D. J.; Trewin, A.; Schiffman, F.; Cora, F.; Slater, B.; Steiner, A.; Day, G. M.; Cooper, A. I., Modular and predictable assembly of porous organic molecular crystals. *Nature* **2011,** *474* (7351), 367-371; (c) Mastalerz, M.; Schneider, M. W.; Oppel, I. M.; Presly, O., A Salicylbisimine Cage Compound with High Surface Area and Selective CO_2/CH_4 Adsorption. *Angew. Chem. Int. Ed.* **2011,** *50* (5), 1046-1051; (d) Mitra, T.; Wu, X.; Clowes, R.; Jones, J. T. A.; Jelfs, K. E.; Adams, D. J.; Trewin, A.; Bacsa, J.; Steiner, A.; Cooper, A. I., A Soft Porous Organic Cage Crystal with Complex Gas Sorption Behavior. *Chem. Eur. J.* **2011,** *17* (37), 10235-10240.
13. Comotti, A.; Bracco, S.; Distefano, G.; Sozzani, P., Methane, carbon dioxide and hydrogen storage in nanoporous dipeptide-based materials. *Chem. Commun.* **2009,** (3), 284-286.
14. Hasell, T.; Wu, X.; JonesJames, T. A.; Bacsa, J.; Steiner, A.; Mitra, T.; Trewin, A.; Adams, D. J.; Cooper, A. I., Triply interlocked covalent organic cages. *Nat. Chem.* **2010,** *2* (9), 750-755.

Chapter 4

Selective Gas Sorption in a [2+3] ‘Propeller’ Cage Crystal

4.1 Introduction to gas selectivity in porous organic molecules

Some of the main conclusions of this Chapter were published in the following paper: S. Jiang, *et al.*, *Chemical Communications* **2011**, *47*, 8919-8921. Gas separation and molecular recognition are important in industry for energy and environmental applications, such as flue gas purification and carbon capture.[1] A variety of porous materials have been explored in this regard such as zeolites,[2] MOFs,[1b] and porous polymers.[3] The effect of gas selectivity in porous materials can be ascribed to several factors including the pore size or shape of materials, the interaction between the gas molecule and pore surfaces, gas diffusivities in porous systems, and kinetic effects.[4] One approach to gas separation is to design materials with well-defined pore structures, which allow the diffusion of the target adsorbate molecule but not other molecules. However, it is difficult to obtain selectivity between adsorbate molecules with similar sizes. Additionally, another method to achieve selective adsorption is to increase the affinity of porous materials for a particular target adsorbate molecule by functionalization of the absorbent surface.

As discussed in the Chapter One, porous organic molecules have gained a considerable attention in the last few years.[5] Furthermore, some studies have focused on porous organic molecules that are capable of selective guest binding in particular with respect to gas separations.[6] Here is a brief literature review on gas selectivity in porous organic molecules. *p-tert*-Butylcalix[4]arene is a well known molecular crystal which possesses large lattice voids. The material absorbed much more CO_2 than H_2 as reported by Atwood *et al.*[7] It was found that the CO_2 occupancy in the cavities of the crystal is 100 % at 3 atmospheres of CO_2. In contrast, the material showed only a small amount of H_2 adsorption at a pressure of up to 7 atm at the same temperature. Thus, *p-tert*-butylcalix[4]arene can be used to purify a H_2/CO_2 mixture.[7] Likewise, the molecular crystal tris(*o*-phenylenedioxy)cyclophosphazene (TPP) has a one-dimensional (1-D) pore channel which is generated by molecular hexagonal packing. It was found that TPP adsorbed large amounts of CO_2 and CH_4 compared to N_2 and H_2.[8] An uptake of 0.7 mol of CH_4 per mol of TPP at 1 atm and 195 K was observed. The CO_2 uptake is 1.24 mol CO_2 per mol of TPP at 1 atm and 195 K. However, the material exhibited a very low uptake of H_2, N_2, O_2 and Ar under comparable conditions. The NMR study indicated that CH_4 and CO_2 gas molecules resided in the 1D channel and had a close contact with the surrounding aromatic

rings of the TPP. Organic molecular cucurbit [6] uril (CB[6]) with 1D channels was studied by Kim *et al*.[9] The material showed a BET surface area of 210 m^2/g, as calculated from the N_2 isotherm, and adsorbed a large amount of acetylene.[9] Furthermore, cucurbit[6]uril was also shown to selectively adsorb CO_2 over CO where selectivity of CO_2 over CO was rationalised on the basis of the high enthalpy of CO_2 adsorption by Kim *et al*.[10] Atwood *et al*. reported amorphous cucurbit[7]uril (CB [7]) for highly selective CO_2 uptake over N_2 and CH_4.[11] The material showed a high CO_2 sorption capacity of 50 cm^3/g at 1 bar and 297 K which exceeded those of any known organic molecules. Mastalerz *et al.*[12] described a [4+6] salicylbisimine cage with a Brunauer-Emmett-Teller (BET) surface area of 1377 m^2/g. This salicylbisimine cage has an internal volume of approximately 678 $Å^3$ and crystal structure showed a 3D interconnected pore volume. This material showed a preference for CO_2 over CH_4. The CO_2/CH_4 selectivity was 10/1 at 1 bar, 273 K.[12] Our group recently demonstrated the gas selectivity by a [4+6] tetrahedral imine cage molecule, cage 1 (**CC1**). This cage can interconvert in the solid state between three polymorphs which are non-porous to both N_2 and H_2 (**CC1α**), selectively porous to H_2 only (**CC1β**), and non-selectively porous to both N_2 and H_2 (**CC1γ**), respectively.[13] The gas selectivity in **CC1β** can be attributed to the crystal packing. Recently, Mastalerz *et al.* has carried out a study to investigate the influence of the rigidity of the cage molecular structures on porosity.[14] The [2+3] cage compounds were synthesized by an imine condensation of triptycene triamine and bissalicylaldehyde.[14] One of [2+3] cage compounds consisting of rigid subunits adsorbs 286 cm^3g^{-1} of N_2 at 77 K and $P/P_o = 0.95$ and the calculated BET surface area is 744 $m^2\ g^{-1}$. By contrast, the other large and flexible [2+3] cage compound shows a low level of porosity with a BET surface area of 30 $m^2\ g^{-1}$. Interestingly, it exhibits a high uptake of CO_2 at 298 K and 1 bar and results in a high selectivity of 10 (mmol/mmol) or 29 (w t %/wt %) for CO_2 over CH_4.[14]

CO_2 capture and storage from flue gases is an important objective. To achieve the required adsorption capacity and separation, materials need a high selectivity for CO_2 over other fuel gas components and a high surface affinity for CO_2.[15] Zhang *et al.*[6a] synthesized a shape-persistent organic cage molecule in a [2+3] cycloimination reaction. The cage molecule has a very small internal void and the packing diagram shows that the molecules pack close to each other in a layered structure form. The

crystalline [2+3] cage material showed a low gas uptake of CO_2 and H_2 at 1 bar and 20 ºC. The uptake value of CO_2 was 4.46 cm^3/g, whereas the material hardly adsorbed N_2 (0.061 cm^3g^{-1}). However, the material displayed a high ideal CO_2/N_2 (CO_2/N_2 = 73/1) adsorption selectivity at 1 bar and 20 ºC. In addition, the imine reduction reaction for the cage molecule was carried out. The CO_2/N_2 adsorption selectivity for the amine cage material at 1 bar and 20 ºC decreased to 39/1. The authors suggested that the good gas selectivity was attributed to well-defined pore structure and the strong interaction of CO_2 with the imine groups of the cage molecules. The same research group also reported a series of related [2+3] cage compounds with different sizes of internal cavities which exhibited ideal CO_2/N_2 selectivity in the range from 36/1 to 138/1 at 20 ºC and 1 bar.[6b] Although the actual CO_2 adsorption capacity of these [2+3] cage molecules at 1 bar and 20 ºC is much lower than other organic molecules published,[12, 16] the selectivity is extraordinarily high. Moreover, a series of organic cage frameworks were reported by Zhang *et al.*[17] The ideal selectivity of CO_2/N_2 was up to 213/1 at 1 bar and 20 ºC.

In this Chapter, the synthesis and characterization of a new 'propeller' shaped porous organic cage molecule **CC6** will be introduced**.** The cage molecule has a [2+3] topology which is synthesized from the condensation reaction of 1,3,5-tri-(4-formylphenyl)benzene with 1,5-pentanediamine. The resulting molecular crystal is determined by NMR, PXRD, single crystal XRD and gas sorption isotherms. The cage molecule has a compact structure with a little void inside the cage. A narrow 1D channel is formed by molecular ineffective packing. The material demonstrates selective adsorption of hydrogen and carbon dioxide over nitrogen. The gas selectivity can be rationalized by pore connectivity on the basis of the crystal structure. A trade-off between sorption capacity and selectivity is observed for materials in this class.

4.2 Synthesis of the starting monomer (1,3,5-tri-(4-formylphenyl) benzene)

4.2.1 Synthetic procedure

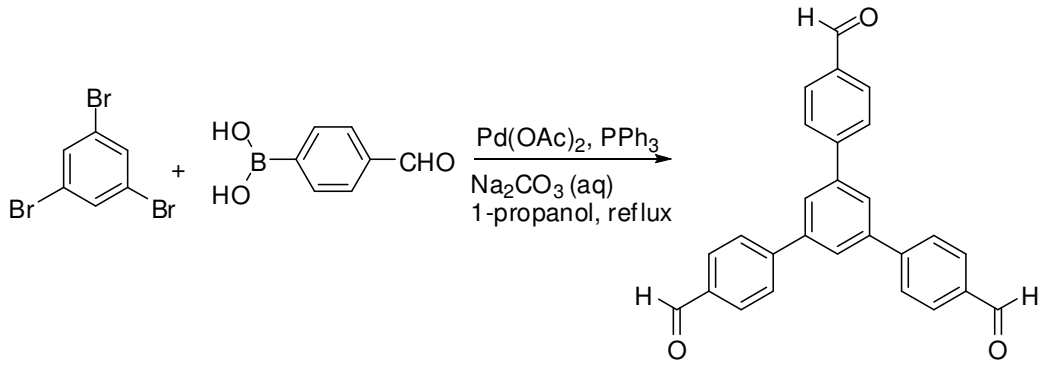

Scheme 1. 1,3,5-Tri-(4-formylphenyl) benzene as synthesized by Suzuki coupling.

As illustrated in the previous chapter, porous [4+6] imine cages were synthesized by the condensation reaction of 1,3,5-triformylbenzene and diamine. The motivation of this work was attempting to select commercial available or synthetic available monomers to discover more cage-like molecules and explore the gas sorption properties of the materials. 1, 3, 5-tri-(4-formylphenyl) benzene monomer and 1,5-pentanedaimine were chosen for the cage synthesis in this chapter. The synthesis of monomer, 1,3,5-tri-(4-formylphenyl) benzene was optimised at the bench experiments (Scheme 1) by Dr Xiaofeng Wu and it was then scaled up by using ChemSpeed SLT106 system to perform multiple parallel reactions and extraction steps.

Optimized procedure on bench scale:

An oven-dried 150 mL, two necked round bottom Radley flask equipped with a magnetic stir bar was flushed with N_2 gas and cooled to room temperature under a N_2 flow. Tribromobenzene (1.0 g, 3.18 mmol), 4-formylphenylboronic acid (1.7 g, 11.5 mmol), $Pd(OAc)_2$ (3 mg, 0.013 mmol), and PPh_3 (6 mg, 0.026 mmol) were added. After degassing this mixture three times, 1-propanol (20 mL) was added under N_2. The solution was left stirring at 60 °C until all of the solids dissolved. Once the clear solution turned to pale yellow (*ca.* 15 min), a solution of Na_2CO_3 (2M, 6 mL) and water (5 mL) were added under N_2. The resulting mixture was then heated to reflux for 2 h under N_2. The nitrogen sources were removed after reflux and another portion of water (20 mL) was added. The reaction mixture was left under stirring, open to the

air for 5 h at room temperature. The mixture was then extracted with chloroform (30 mL) and the organic layers were washed with a 2 wt% solution of $NaHCO_3$ (25 mL). A spoonful of activated charcoal was added into the organic solution and the mixture was stirred for 30 min at room temperature. The suspension was filtered through celite under reduced pressure. Evaporation of the solvent gave the crude product. The pure product was obtained after column chromatography with 70 % yield, or recrystallized from THF with 65 % yield. The calculated mass calculated for $C_{27}H_{18}O_3$: 390.13. Found: 391 $[M+H]^+$. Elemental analysis as $C_{27}H_{18}O_3$ (Calculated: C 83.06, H 4.65. Found: C 83.14, H 4.67). Melting point is 245-251°C (literature value 231-232 °C).[18]

Synthesis procedure using ChemSpeed synthesis robot for scale up:

Following the optimised procedure of bench scale synthesis, a Chemspeed workflow was developed by Dr Xiaofeng Wu and Dr Sean Higgins as follows. The reaction procedure is illustrated in Figure 1. This process was followed for the synthesis of the starting monomer, 1,3,5-tri-(4-formylphenyl) benzene.

1) Figure 1(a) shows a picture of the robot with a 2 x 4 reaction block. 100 mL reactors were used.

2) The four solid starting materials were added into each reactor shown in Figure 1(b-c).

3) The reactors were then purged with nitrogen which was kept on for the whole reaction time.

4) 1-Propanol was added to each reactor and the reactions were heated to 60 °C for 15 mins to form a homogeneous solution shown in Figure 1(d). The synthesizer was equipped with a vortex movement of the reactors in Figure 1(e).

5) Na_2CO_3 solution was added to start the reaction, followed by further aliquots of water. The reaction was heated to reflux at 100 °C for 2 hours with rapid vortexing

6) Once cooled down, chloroform solvent extraction was carried out and the crude product was placed to a collection bottle shown in Figure 1(f).

7) Automated cleaning and drying of the reaction flasks for repeat use.

Specific details and parameters for each of these steps are recorded within the software.

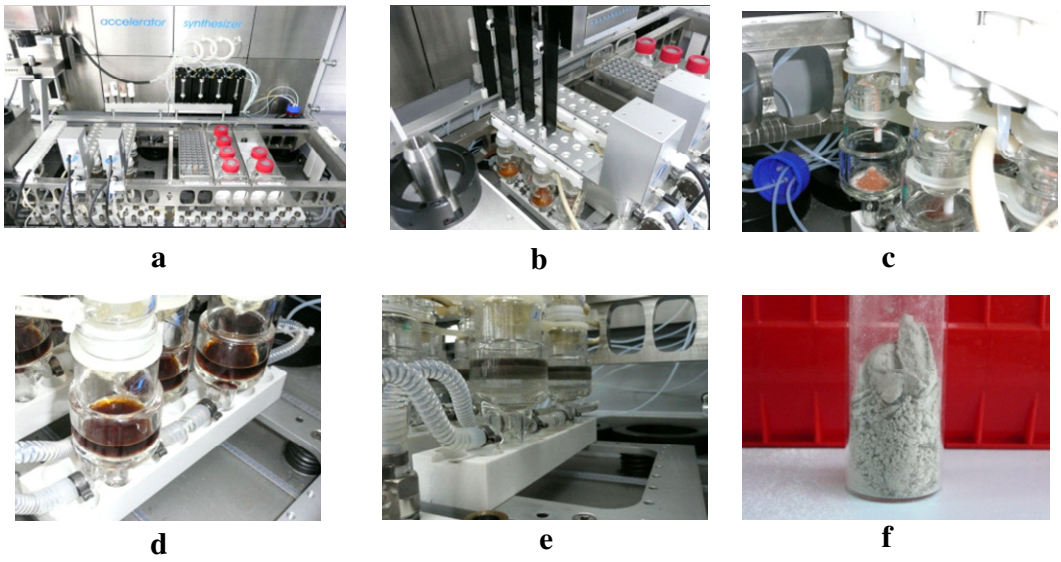

Figure 1. Synthesis procedure of 1,3,5-tri-(4-formylphenyl) benzene by ChemSpeed robot. (a) 6 X 100 mL reactors were used for six parallel reactions. (b-c) The starting materials were added into each reactor. (d) A homogeneous solution formed during the reaction. (e) A vortex movement was equipped for the reactors. (f) A crude product was obtained after the solvent extraction.

4.2.2 NMR spectra of the starting monomer (1,3,5-tri-(4-formylphenyl) benzene)

1,3,5-Tri-(4-formylphenyl) benzene is soluble in chloroform and was characterized by ^{1}H and ^{13}C NMR spectroscopy as shown in Figure 2 and Figure 3, respectively. The ^{1}H NMR chemical shift of the -CHO protons is observed at 10.11 ppm where the integration of peaks is 3 H. The multiple peaks at ~ 8.04-7.87 ppm are assigned to aromatic rings (-ArH) with 15 H. Chemical shifts at 4.12, 2.05 and 1.06 ppm are attributed to EtOAc solvent. δ 1.60 is H_2O solvent.

The ^{13}C NMR spectrum is shown in Figure 3. The ^{13}C chemical shift of the –CHO is observed at 191.76 ppm. The peaks 146.29, 141.60, 135.76, 130.44, 127.98, 126.48 ppm are assigned to carbons on aromatic rings. Chemical shift at 26.68 and 67.60 ppm is THF solvent.

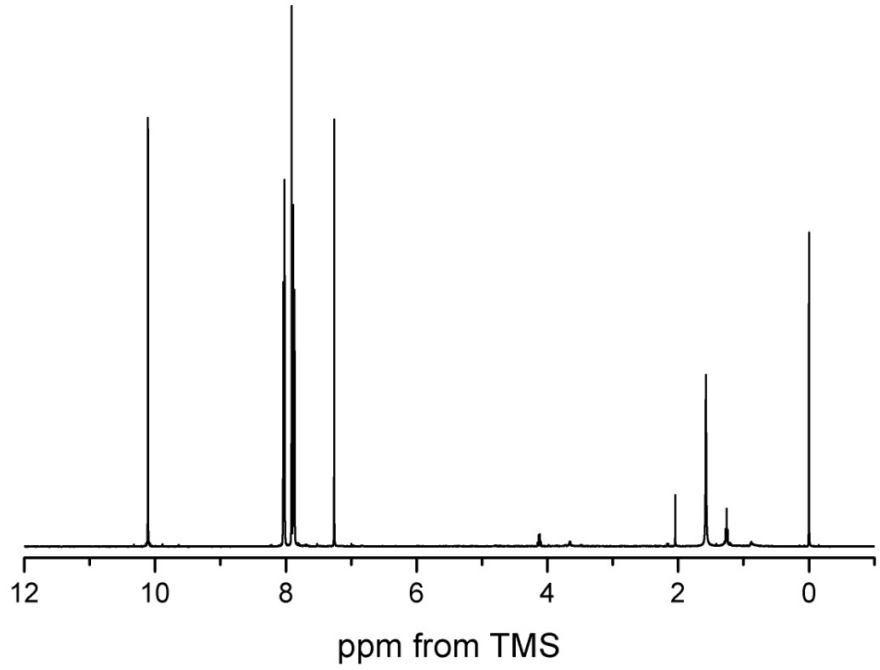

Figure 2.^{1}H NMR ($CDCl_3$) spectrum for 1,3,5-tri-(4-formylphenyl) benzene. (δ 4.12 , 2.05 , 1.06 is EtOAc solvent ; δ 1.60 is H_2O solvent)

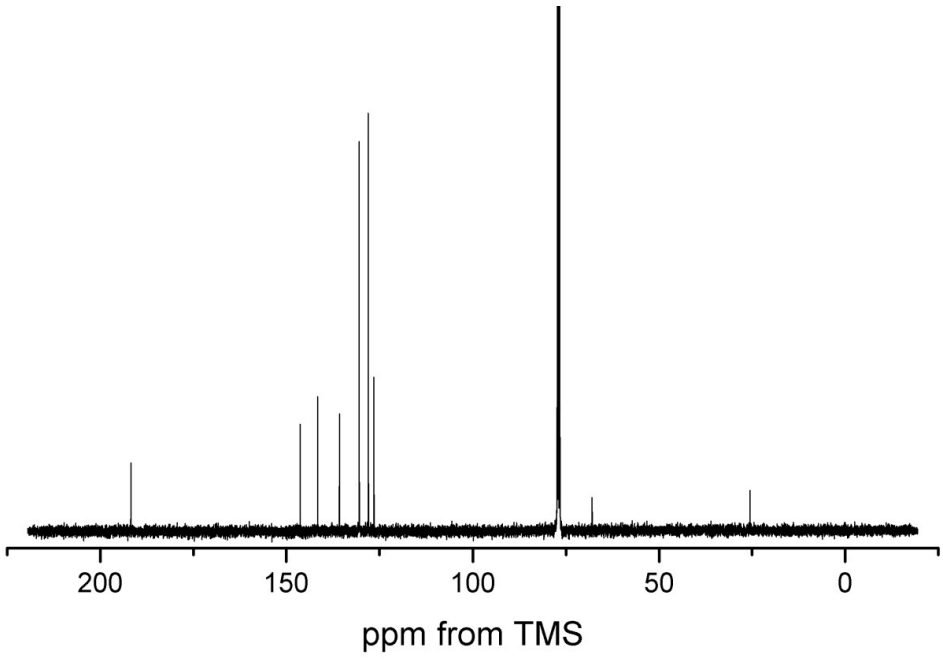

Figure 3. ^{13}C NMR ($CDCl_3$) spectrum for 1, 3, 5-tri-(4-formylphenyl) benzene. (δ 26. 68 and 67.60 are THF solvent)

4.3 Synthesis of [2+3] 'Propeller' Cage

4.3.1 [2+3] 'propeller' cage synthetic procedure

Optimization of cage reaction conditions:

The reaction conditions of the original cage (**CC1**-**CC3**) synthesis require that the ratio of trialdehyde and diamine monomers was at 2 : 3 in a diluted concentration. The reaction was kept for 5-7 days without stirring at room temperature. The cage products directly crystallized from the solution. It was found that the solvents had a significant effect on the cage formation. The test reactions were therefore carried out to examine the reactions of 1,3,5-tri-(4-formylphenyl) benzene with a series of diamines in various solvents. Chloroform ($CHCl_3$), dichloromethane (DCM), methanol (MeOH), ethyl acetate (EtOAc) and acetonitrile (CH_3CN) were chosen as solvents for this study. The parallel reactions were performed using 1,3,5-tri-(4-formylphenyl) benzene (20 mg, 0.051 mmol) with a series of diamines (0.076 mmol) in 30 mL solution. Table 1 summarises the products from these test reactions. It was observed that all the reactions in EtOAc or CH_3CN produced insoluble products which might be polymers. The reactions of 1,3,5-tri-(4-formylphenyl) benzene with 1,3-propanediamine or 1,4-butanediamine in $CHCl_3$, DCM and MeOH, respectively, formed partially soluble oligomers. The complicated NMR shows no CHO protons at chemical shift of 10.11 ppm for the starting monomer trialdehyde and multiple peaks at 8.16 ppm which are assigned to imine protons in Figure 4. The products could be in the intermediate state, and no evidence was found for forming cage molecules. Crystals were obtained by the reactions of 1,3,5-tri-(4-formylphenyl) benzene with 1,2-ethylenediamine in MeOH. However, single crystal XRD confirmed that the products were a 1,3,5-tri-(4-formylphenyl) benzene derivative as shown in Figure 5. The reaction by 1,3,5-tri-(4-formylphenyl) benzene and 1,5-pentanediamine, by contrast, gave a macrocyclic cage molecule.

In this Chapter, the cage material is synthesized by 1,3,5-tri-(4-formylphenyl) benzene and 1,5-pentanediamine in MeOH solvent due to crystal structure available. The solvent effect on the reaction will be discussed in the 4.4 section.

Table 1. The product description the parallel test reactions of 1,3,5-tri-(4-formylphenyl) benzene with 1,2-ethylenediamine, 1,3-propanediamine, 1,4-butanediamine, 1,5-pentanediamine in different solvents, respectively.

Monomers (1,3,5-tri-(4-formylphenyl)	Solvent ($CHCl_3$)	Solvent (DCM)	Solvent (MeOH)	Solvent (EtOAc)	Solvent (CH_3CN)
1,2-ethylenediamine	Not available	Not available	Single crystals	Insoluble products	Insoluble products
1,3-propanediamine	oligomer /polymer	oligomer /polymer	oligomer /polymer	Insoluble products	Insoluble products
1,4-butanediamine	oligomer /polymer	oligomer /polymer	oligomer /polymer	Insoluble products	Insoluble products
1,5-pentanediamine	Crystalline powders	Crystalline powders	Single crystals	Insoluble products	Insoluble products

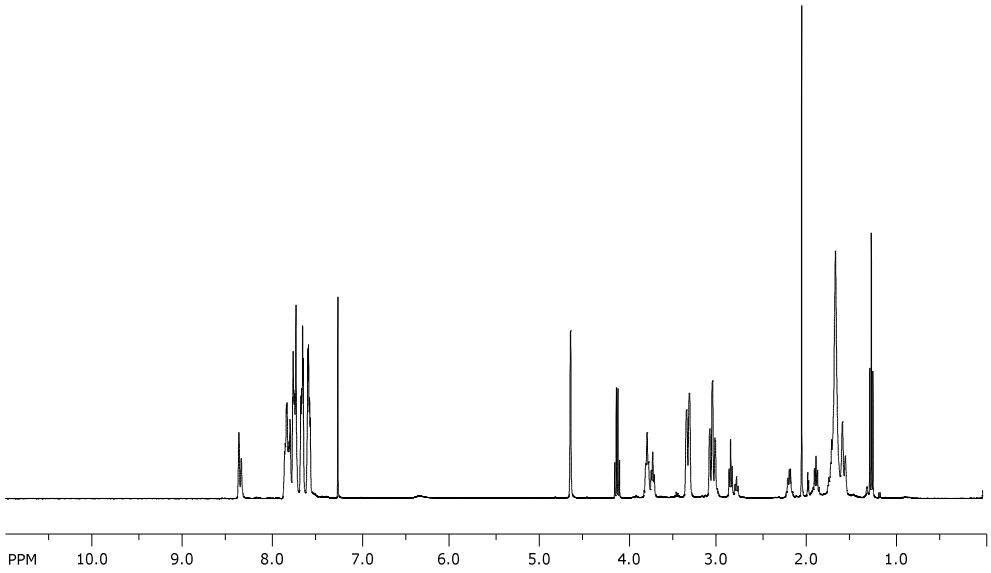

Figure 4. ^{1}H NMR spectrum for oligomers obtained from the reaction of 1,3,5-tri-(4-formylphenyl) benzene and 1,3-propanediamine in DCM solution.

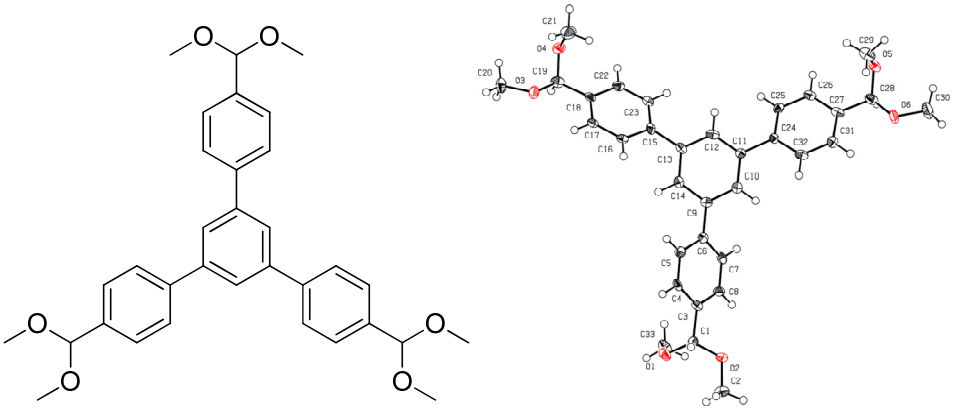

Figure 5. The product obtained from the reaction of 1, 3, 5-tri-(4-formylphenyl) benzene with 1, 2-ethylenediamine determined from single crystal XRD.

[2+3] 'Propeller' cage synthesis procedure:

Methanol (20 mL) was added to 1,3,5-tri-(4-formylphenyl) benzene (50 mg, 0.128mmol) in a sample vial at room temperature. A solution of 1,5-pentanediamine (20 mg, 0.192 mmol) in MeOH (20 mL) was added slowly. The reaction was left covered for 6-7 days without stirring. The products were observed to crystallize from solution. The crystals were separated carefully from the sample vial using a spatula

and washed with MeOH and air dried to give the solvated [2+3] cage. The synthesis of cage molecule is shown in Scheme 2. Crystals suitable for X-ray crystallography were removed directly from the sample vial. To desolvate [2+3] cage, a sample was heated to 100 ˚C under dynamic vacuum for 12 hours. The yield after desolvation was 45 %. Mass spectrometry showed [**CC6** + H]$^+$ and [**CC6** + Na]$^+$ ions at m/z = 979.49 and 1001.48, consistent with a [2+3] cage structure composed of two units of **1** and three units of **2** with formula $C_{69}H_{66}N_6$. In previous work, we showed the cycloimination reaction between 1,3,5-triformylbenzene and either ethylenediamine, 1,2-propylenediamine, or 1,2-cyclohexanediamine led to the formation of [4+6] cage structures. Here, a [2+3] cage structure was observed instead. This can be ascribed to both the greater flexibility of the 1,5-pentanediamine and also the larger size of the trialdehyde.

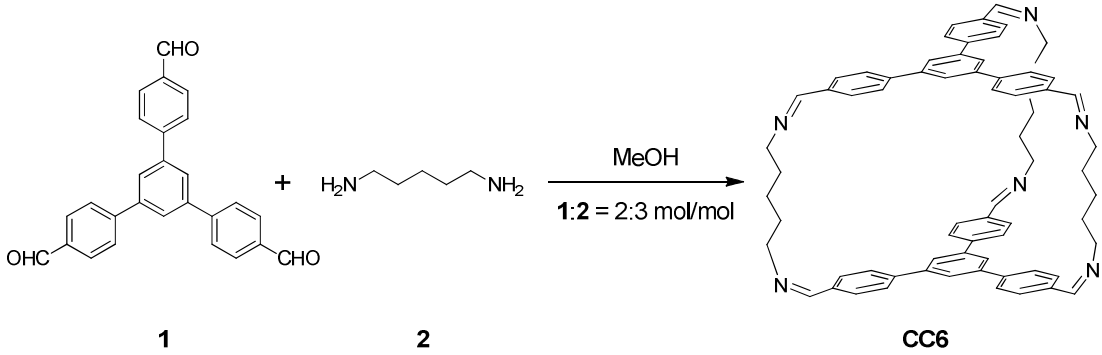

Scheme 2. Covalent synthesis of a [2+3] 'propeller'shaped organic cage molecule, **CC6**.

4.3.2 Characterizations of [2+3] 'Propeller' Cage

4.3.2.1 NMR spectra of [2+3] 'propeller' shaped organic cage molecule, CC6.

[2+3] 'Propeller' shaped organic cage molecule, **CC6**, is fully soluble in chloroform and was characterized by ^{1}H and ^{13}C NMR spectroscopy. The ^{1}H NMR chemical shift of the imine protons is observed as a singlet at 8.16 ppm where the integration of peak is 6 H (Figure 7). The multiple peaks at ~ 7.51-7.28 ppm are assigned to aromatic rings (-ArH) with 30 H calculated from the integration. The chemical shifts at 3.68, 1.77 and 1.32 ppm, respectively are consistent with protons on the cage bridges. Figure 6 illustrates a cage bridge fragment. The chemical shift at 3.68 ppm belongs to protons at the 'A' position labelled in Figure 6 which are next to imine bonds with an integration of 4H. The chemical shift at 1.77 ppm belongs to protons

at 'B' and the integration of the peak is 4H. Protons at the label of 'C' have a chemical shift of 1.32 ppm with an integration of 2H.

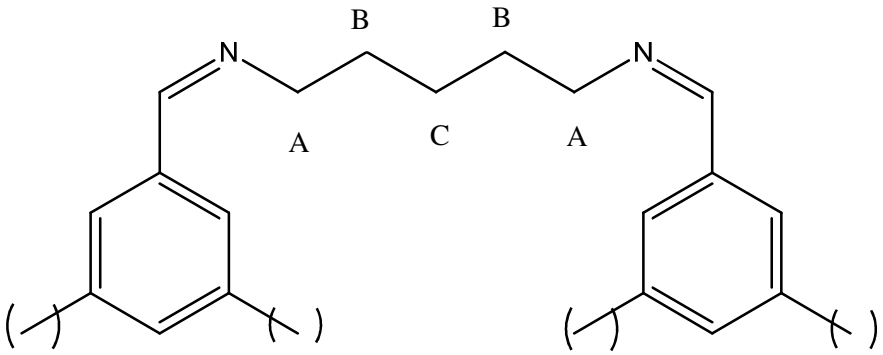

Figure 6. A fragment of [2+3] 'propeller' cage vertices

^{13}C NMR ($CDCl_3$) spectrum for [2+3] 'propeller' cage is shown in Figure 8. The ^{13}C chemical shift of the imine bond is observed at 160.95 ppm. The peaks 146.29, 141.60, 135.76, 130.44, 127.98, 126.48 ppm are assigned to carbons on aromatic rings. The chemical shift at 55.8 ppm belongs to the carbons on the cage vertices labelled as A in Figure 6. The chemical shifts at 31.3 and 24.8 ppm are the carbons B and C, respectively.

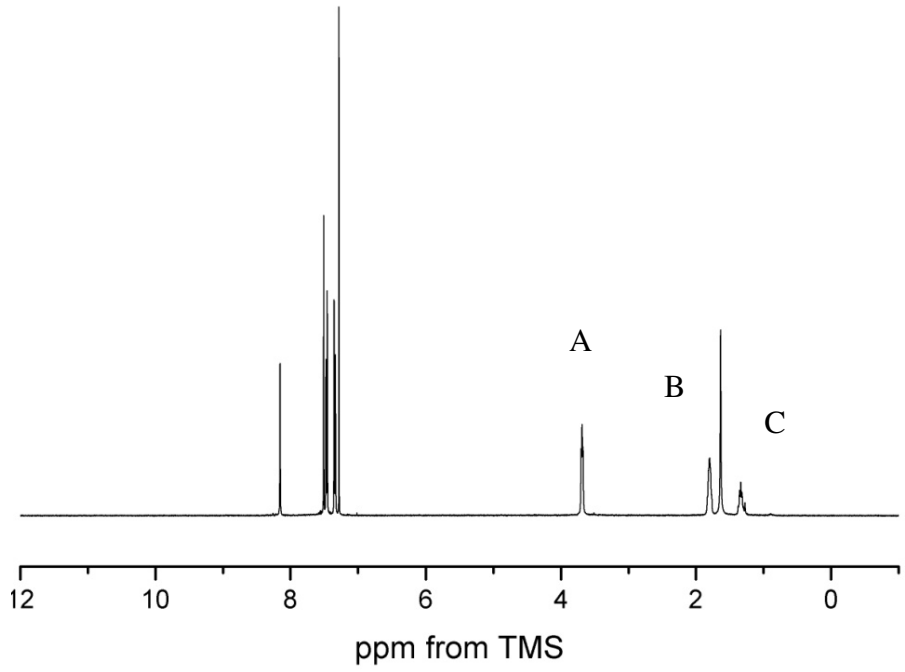

Figure 7. ^{1}H NMR ($CDCl_3$) spectrum for the [2+3] 'propeller' cage after gas sorption.

(δ 1.60 is H_2O solvent)

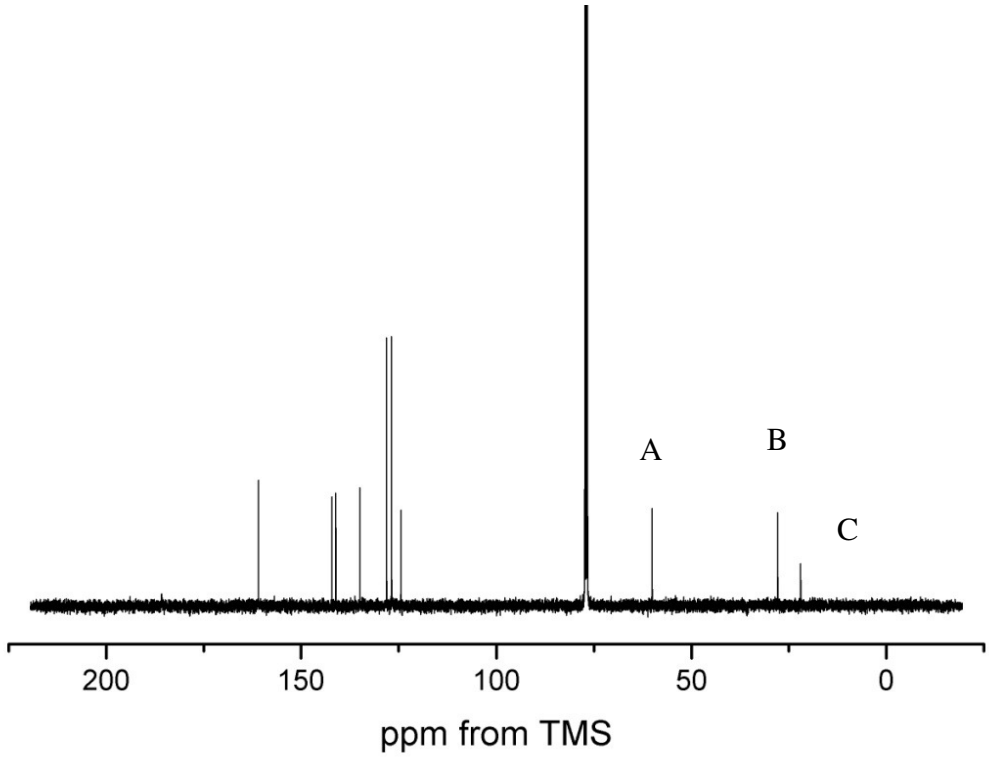

Figure 8. ^{13}C NMR ($CDCl_3$) spectrum for [2+3] 'propeller' cage after gas sorption.

4.3.2.2 X-Ray Crystallography details for [2+3] 'propeller' shaped organic cage molecule, CC6.

Single crystal X-ray data were collected and refined by Dr John Bacsa. Compound **CC6** crystallized directly from the reaction mixture as colorless, plate-like prisms. The crystal size was suitable for single crystal X-ray diffraction. The analysis showed that the molecules crystallized in the orthorhombic system with the chiral space group $Pca2_1$. The unit cell is: a = 26.055 Å, b = 15.571 Å, c = 14.686 Å and cell volume is 5958.3 $Å^3$. The solvated crytal structure was measured and refined at 100 K. Furthermore, the crystal was heated to 395 K in situ in the diffractometer for desovlation. After colling to 100 K to collect desolvated crystal data, the diffraction was too weak to refine the structure. Therefore, the desolvated structure is not available for **CC6**. All crystal and refinement details are listed in Table 2.

Table 2. Crystal and refinement data for **CC6**.

Crystal and Refinement Data	
$(C_{138}H_{132}N_{12})$, $6(CH_4O)$ $M = 2150.81$ colourless prism, $0.50 \times 0.20 \times 0.05$ mm^3 orthorhombic, space group $Pca2_1$ $a = 26.055(4)$ $b = 15.571(2)$ $c = 14.686(2)$ Å $V = 5958.3(14)$ Å^3, $Z = 2$, $D_c = 1.199$ g/cm^3 $T = 100(2)$K 19523 reflections collected, 10077 unique $R_{int} = 0.0423$ Final *GooF* = 0.949 *R1* = 0.0556 *wR2* = 0.1160 780 parameters, 439 restraints $\mu = 0.073$ mm^{-1}	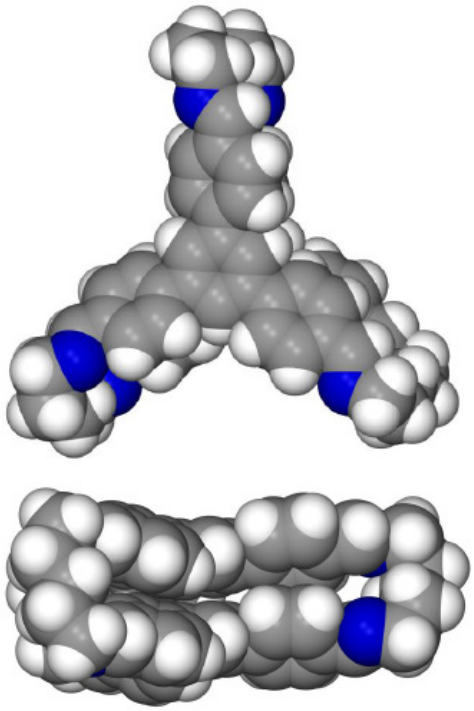

A [2+3] cage molecule (**CC6**) was observed and the cage molecule has pseudo 3-fold symmetry shown in Figure 9. **CC6** resembles a three-bladed propeller and is chiral due to a helical twist. Two of the three pentyl linkers are disordered, and this disorder could be modeled effectively by splitting each of these atoms into two distinct sites and restraining the equivalent 1, 2 and 1, 3 bond distances to be similar. Even though two 1,3,5-phenyl benzene groups are separated by pentyl linkers, **CC6** has a compact structure with little void space inside the cage. The distance between the two central phenyl rings is 3.7 Å, which is typical for π-π stacking.

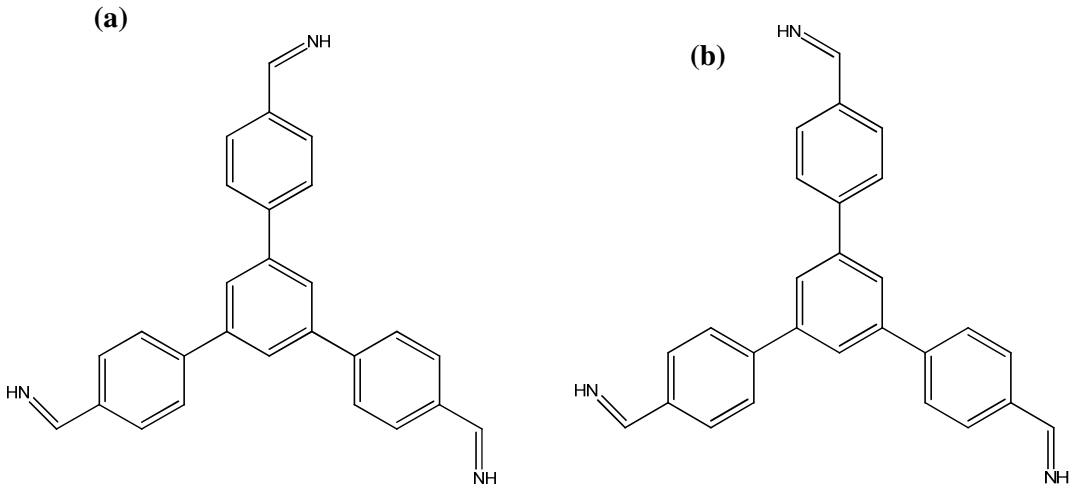

Figure 9. (a) Three-fold symmetry and (b) non-three fold symmetrical version where a C=N bond has been rotated by 180 degrees.

The solvated crystal structure viewed along the c-axis shows a layered, π-stacked system (Figure 10b). The distance between two layers in the crystal is approximately 5 Å. **CC6** assembles in the solid state to generate 1-D channels along the a-axis resulting from imperfect packing of the propeller-shaped molecules. The Connolly surface area of **CC6** generated using a N_2 radius of 1.82 Å is shown in Figure 10d-e. These channels are relatively narrow and constitute approximately 10 % of the volume of the structure. The MeOH solvent molecules can be identified as electron density within these voids, but these guests were only partially resolved and too disordered to be modeled effectively. The data was therefore treated by using PLATON/SQUEEZE [19] which calculates six MeOH molecules per cage molecule. The π -stacked layers run perpendicular to the 1-D MeOH-filled channels. There is no connectivity between the channels and the (negligible) void volume in the cage.

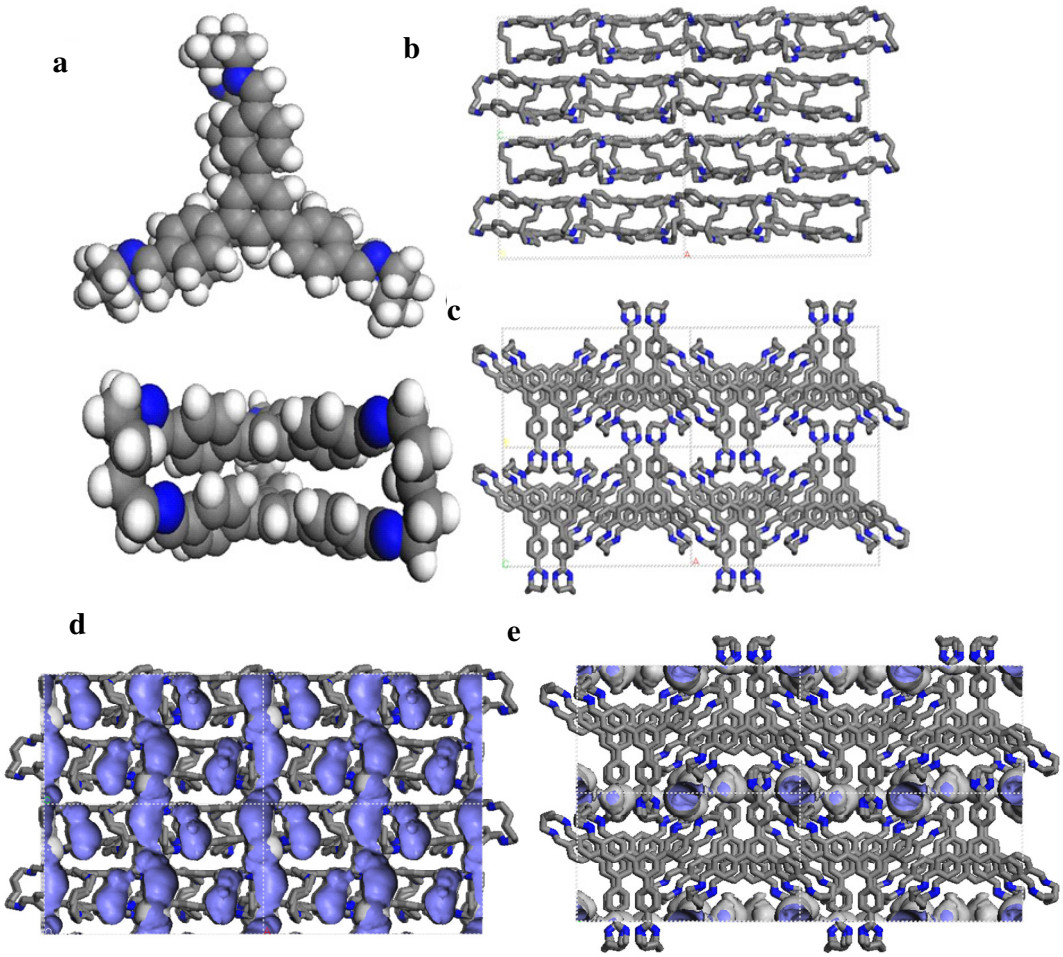

Figure 10. (a) Molecular structure of **CC6** viewed in different orientations (Grey: carbon; white: hydrogen; blue: nitrogen); (b) Molecular packing viewed along the c-axis (Hydrogen atoms are omitted for clarity); (c) Molecular packing viewed along the a-axis; (d-e) Connolly surface area generated using a probe radius of N_2 showing 1-D channel openings viewed along c-axis and a-axis, respectively.

4.3.2.3 Fourier Transform Infrared Spectroscopy (FTIR) for CC6

The FTIR spectroscopy of 1,3,5-tri-(4-formylphenyl) benzene shows a sharp absorption peak for aldehyde C=O stretch at 1689 cm^{-1} in Figure 11. Strong -C=C- aromatic stretch bands also appear at 1600-1580 cm^{-1}. The bands for C-H bends on aromatic rings appear at approximately 1000 cm^{-1} for the in-plane bends and at about 650 cm^{-1} for the out-of-plane bend. The normally weak aldehyde H-C stretch occurs at 2820-2710 cm^{-1}. FTIR spectroscopy for as-prepared **CC6** in Figure 12 demonstrates a strong imine C=N stretch at 1640 cm^{-1}. No starting material aldehyde C=O stretch at 1689cm^{-1} was observed. Broad adsorption bands at 3650-3450cm^{-1} are assigned to solvent MeOH which can be further confirmed by TGA (see Figure 15) and single crystal X-ray analysis.

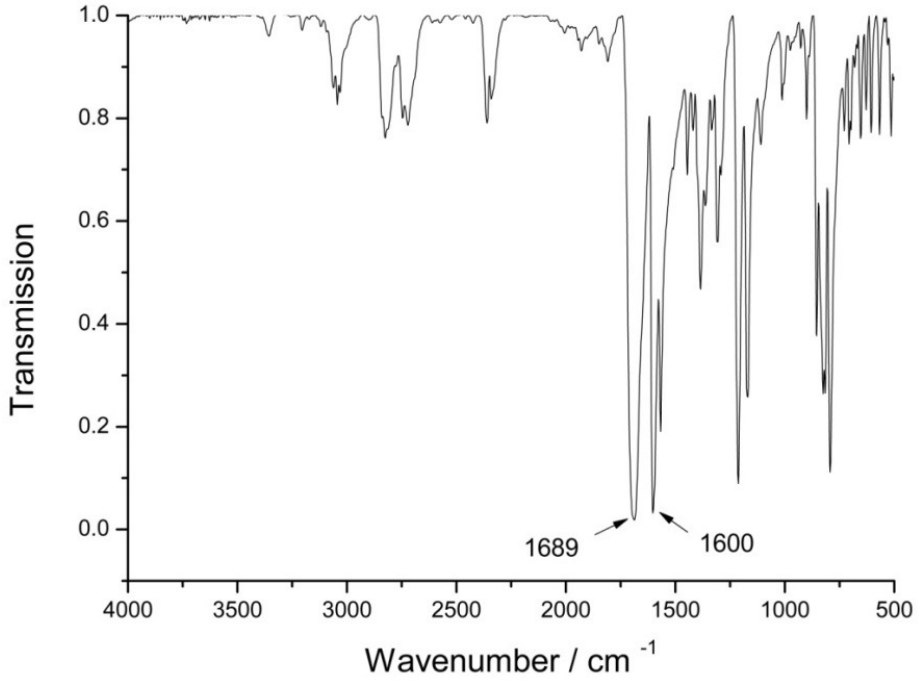

Figure 11. FTIR spectroscopy for starting monomer of 1,3,5-tri-(4-formylphenyl) benzene showing a strong C=O stretch at 1689 cm^{-1}.

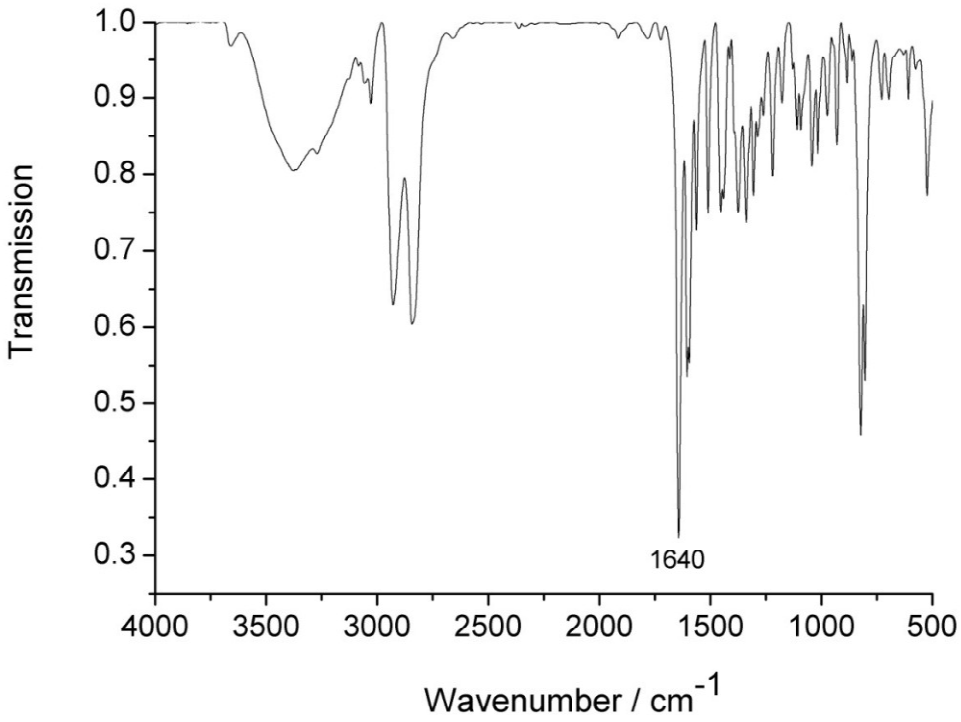

Figure 12. FTIR spectroscopy for **CC6** showing a strong imine stretch at 1640 cm^{-1}.

4.3.2.4 Powder X-ray diffraction patterns for [2+3] 'propeller' shaped organic cage molecule, CC6

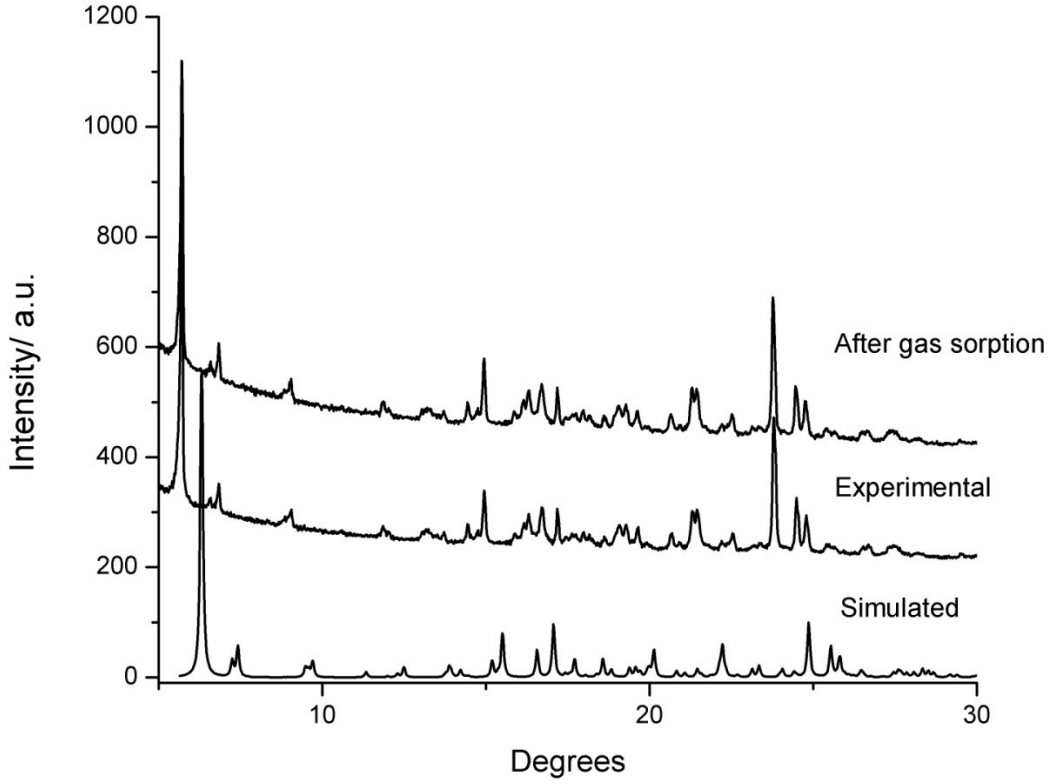

Figure 13. Powder X-ray diffraction patterns for **CC6** recorded for experimental data for the bulk sample as-synthesized before (middle) and after (top) gas sorption, compared with the simulated PXRD from single crystal structure (bottom).

A bulk sample of **CC6** was also analyzed by powder X-ray diffraction (PXRD), confirming it to be both phase pure and representative of the single crystal data in both solvated and desolvated forms. Figure 13 shows the PXRD patterns for as-synthesized sample, after gas sorption sample and simulated PXRD based on single crystal structure. The as-synthesized sample was prepared by heating at 100 ºC under dynamic vacuum for 12 hours before gas sorption analysis to fully desolvate. ^{1}H NMR has confirmed that the solvent molecules can be completely evacuated after gas sorption (see Figure 7). Therefore, the sample after gas sorption can be labeled as a desolvated sample. Figure 13 shows there are no significant differences between solvated and desolvated PXRD patterns. Consequently, the molecular structure remained nearly intact after desolvation. Compared with experimental diffraction

data, the simulated pattern of the single crystal structure produced by Mercury software showed systematic shifts in the peak positions due to thermal expansion, because the single crystal and PXRD data were collected at different temperatures. The single crystal X-ray data was determined at 100 K and PXRD data recorded at the room temperature.

In addition, the Le Bail fitting of PXRD was carried out by Dr James T. A. Jones in Figure 14. The analysis of the data using Le Bail fitting for **CC6** after gas sorption gives refined cell parameters : orthorhombic symmetry and $Pca2_1$ space group a = 26.00(1) Å, b = 15.545(1) Å, c = 15.0133(8) Å, V = 6068(7) Å^3 with good fit indicators (R_{wp}= 5.63 %). The data is consistent with the cell obtained from the single crystal XRD data measured at 100 K: a = 26.055 (4), b = 15.571(2), c = 14.686(2) Å, V = 5958.3(14) Å^3.

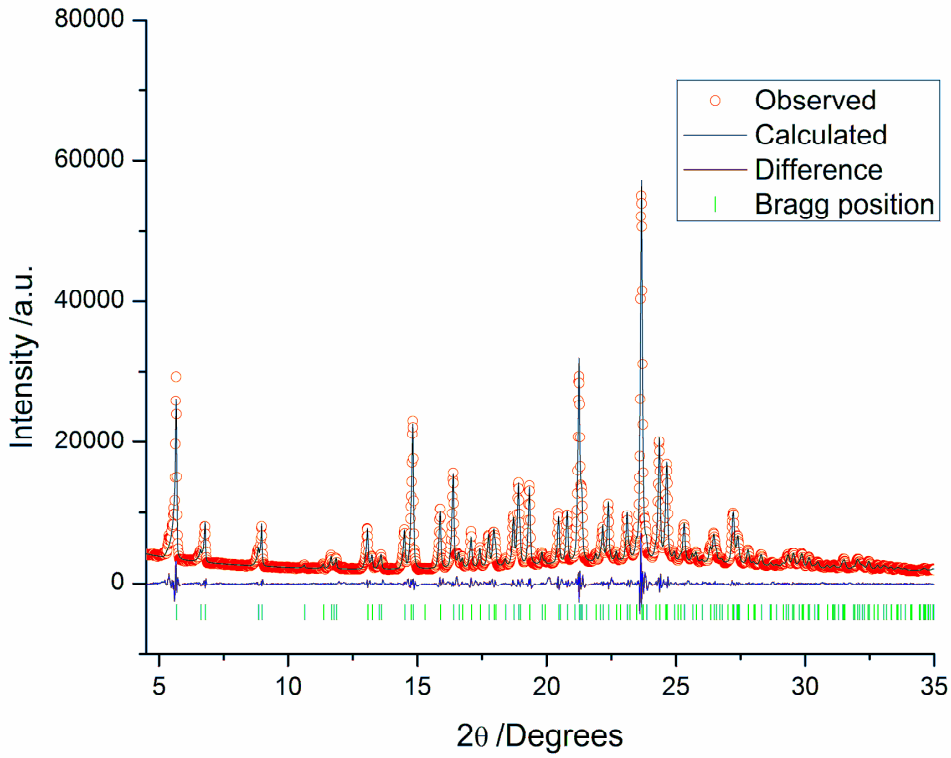

Figure 14. PXRD for the Le Bail refinements of **CC6**. Orthorhombic, Pca21 a = 26.00(1) Å, b = 15.545(1) Å, c = 15.0133(8) Å, V = 6068(7) Å^3. Lattice constants from single crystal data measured at 100 K: a = 26.055 (4), b = 15.571(2), c = 14.686(2) Å, V = 5958.3(14) Å^3. Agreement factors R_{wp}= 5.63 %, R_{exp} = 1.46 %, R_p = 4.02 %, GoF = 3.85. Final observed (circles), calculated (solid lines), difference

(blue line) and brag position (green). The cell parameters have a good agreement with the cell obtained from single crystal data.

4.3.2.5 Thermogravimetric (TGA) data for CC6

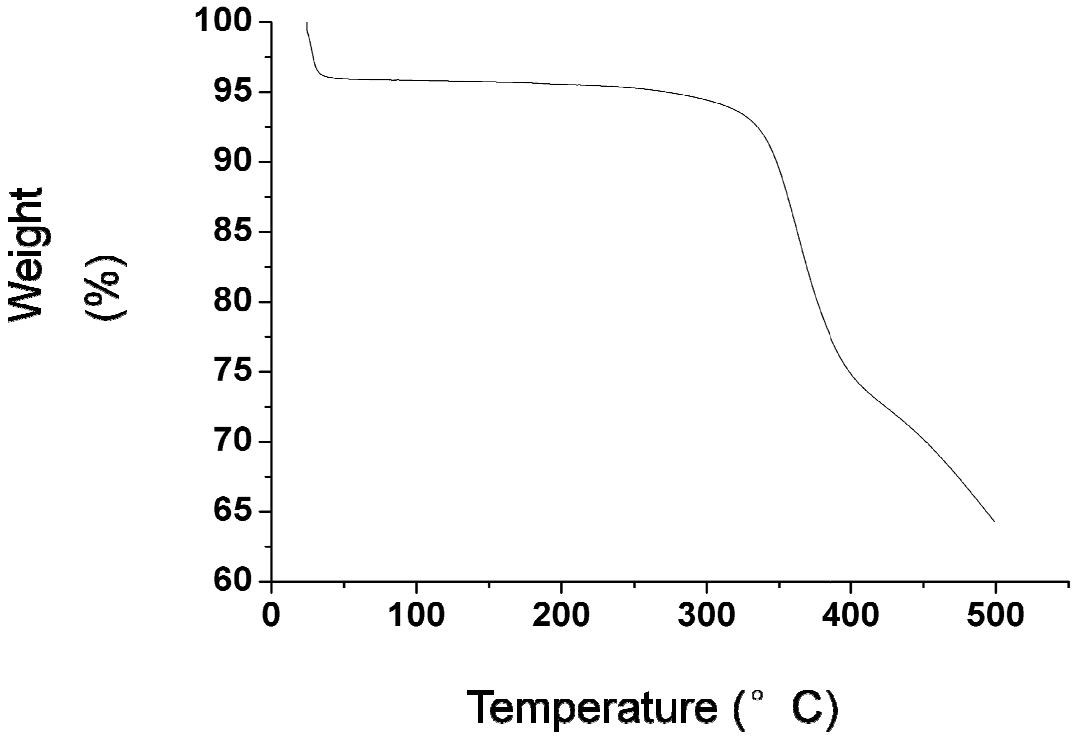

Figure 15. TGA data for [2+3] 'propeller' cage **CC6**.

In order to check the thermal stability of **CC6**, the as-synthesized sample of **CC6** was analysed by TGA in Figure 15. TGA was carried out under nitrogen flow and heating rate of 5 ºC / min to 500 ºC. The 5% mass loss observed for as-synthesized sample at ~ 40°C is attributable to the loss solvent MeOH. This is consistent with MeOH solvents observed in the single crystal structure. The onset of decomposition for the sample occurs at 350 °C (623 K). The decomposition temperature is very similar to our previously [4+6] porous organic cages.[16]

4.3.3 Gas sorption analysis for [2+3] 'propeller' shaped organic cage molecule, CC6.

Gas sorption analysis (N_2, H_2 and CO_2, respectively) was carried out for **CC6**. The gas sorption isotherms were measured by Dr James T. A. Jones and Dr Robert Dawson. The material was heated to 100 ˚C under dynamic vacuum for 12 hours to fully desolvate before gas sorption analysis. **CC6** is stable under these conditions, with no apparent loss of crystallinity. N_2 sorption measurements at 77 K showed a predominantly Type I isotherm (Figure 16a black squares) with a total uptake of 1.5 mmol g^{-1} at 1 bar. The BET model applied over a pressure range of P/P_0 =0.01-0.1 gives a surface area of 99 m^2g^{-1}. This is substantially lower than the [4+6] imine-based cages reported previously[16] because **CC6** exhibits only extrinsic porosity (between cages) and no intrinsic porosity (within the cages). **CC6** adsorbed 3.8 mmol g^{-1} of H_2 at 77 K and 1.2 bar (Figure 16a red circles) and saturation was not reached. Some hysteresis was observed in the H_2 isotherm upon desorption, which was attributed to the narrow pores which restrict H_2 diffusion.

Gas sorption measurements were also carried out closer to ambient temperature. The N_2 adsorption isotherm at 300 K and 1.2 bar revealed a low gas uptake (0.08 mmol g^{-1}) shown in Figure 16b black squares. By contrast, the CO_2 uptake for **CC6** was 0.9 mmol g^{-1} (Figure 16b red circles) under the same conditions, significantly greater than that reported for the [2+3] cage prepared by Zhang *et al.*[6] (0.1–0.25 mmol g^{-1}). This adsorption behaviour suggests that **CC6** or analogues might be candidates for gas separation applications. The ideal selectivity was calculated from these isotherms to be 11 for CO_2/N_2 at 300 K and 1 bar. In addition, the material had an ideal selectivity for H_2 over N_2 of 2.4 at 77 K.

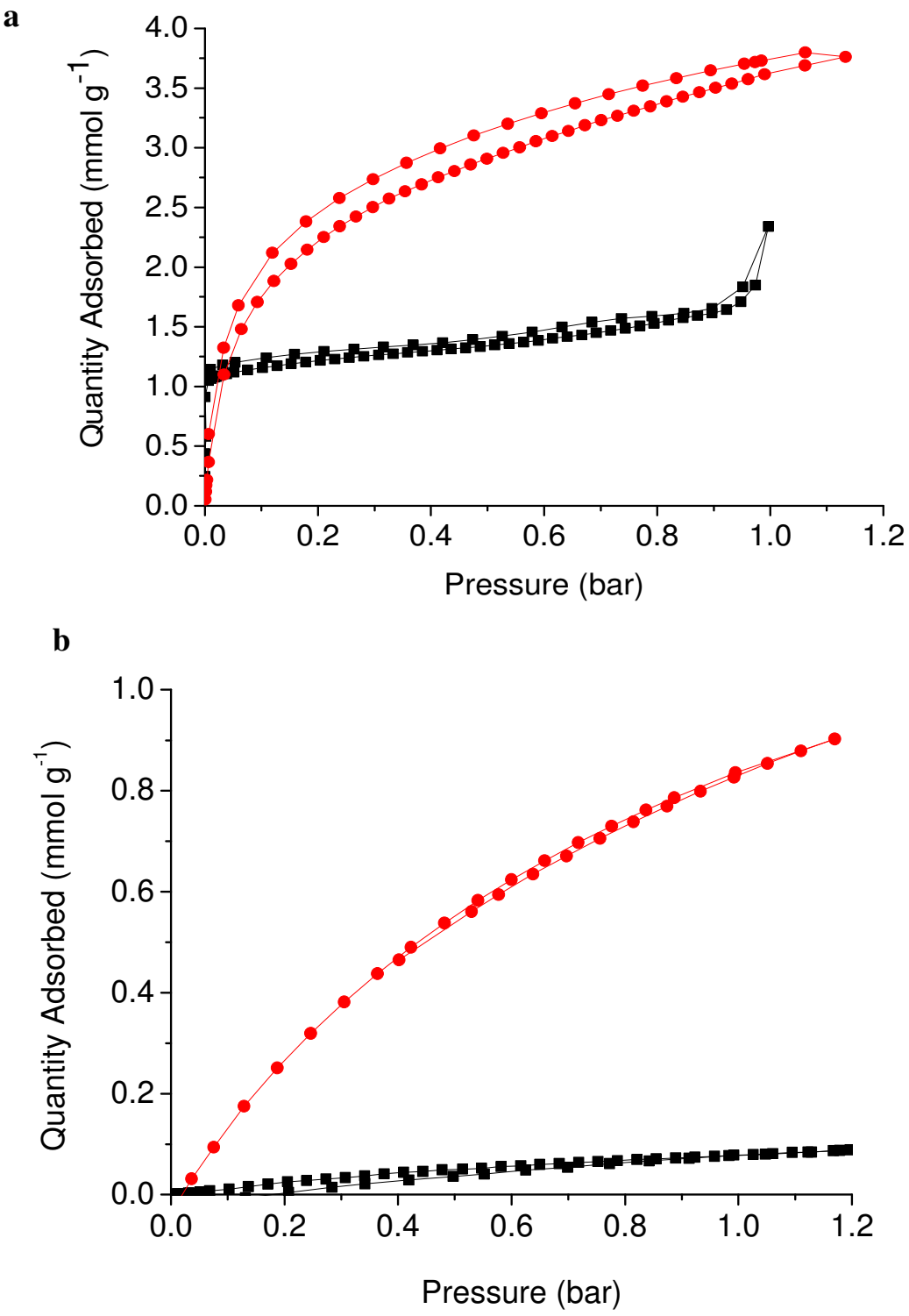

Figure 16. (a) Nitrogen (black squares) and hydrogen (red circles) sorption /desorption isotherms for **CC6** at 77 K. (b) Carbon dioxide (red circles) and nitrogen (black squares) sorption /desorption isotherms at 300 K, respectively.

The CO_2/N_2 selectivity for **CC6** is low compared with the [2+3] imine cages reported by Zhang *et al.* [6] where ideal selectivities in the range 36/1–138/1 were reported. However, in considering materials for applications, absolute gas uptakes must also be considered. The selectivity can be considered as a function of sorption capacity. Figure 17 shows a plot of ideal selectivity (CO_2/N_2) versus CO_2 uptakes for a series of porous materials. There is a clear trade-off between them. Increased CO_2 uptakes will lead to a decreased CO_2/N_2 selectivity. The selection of materials in this plot includes porous organic cages reported by our group (**CC**),[13, 16, 20] cage compounds synthesized by the Zhang group (**ZC**)[6b] and a selection of MOFs[21] which show CO_2/N_2 selectivity. Examples were chosen where the gas uptakes were measured under comparable conditions. Table 3 lists that the values of N_2, CO_2 uptakes and ideal selectivity (CO_2/N_2) for these materials. Although the CO_2 adsorption capacity of [2+3] cage molecules by Zhang *et al.* is much lower, the selectivity is extraordinarily high (red circles in Figure 17) which are top left side of the plot. For practical separation in industry, both uptake and selectivity need be considered. The plot shows a similar behaviour observed for gas permeable membranes, where there is a trade off between selectivity and permeability, as described in detail by Robeson.[22] To achieve the required adsorption capacity and separation, the future challenge is to discover materials with both high selectivity and gas uptake, which will be at the top right side of the plot in Figure 17.

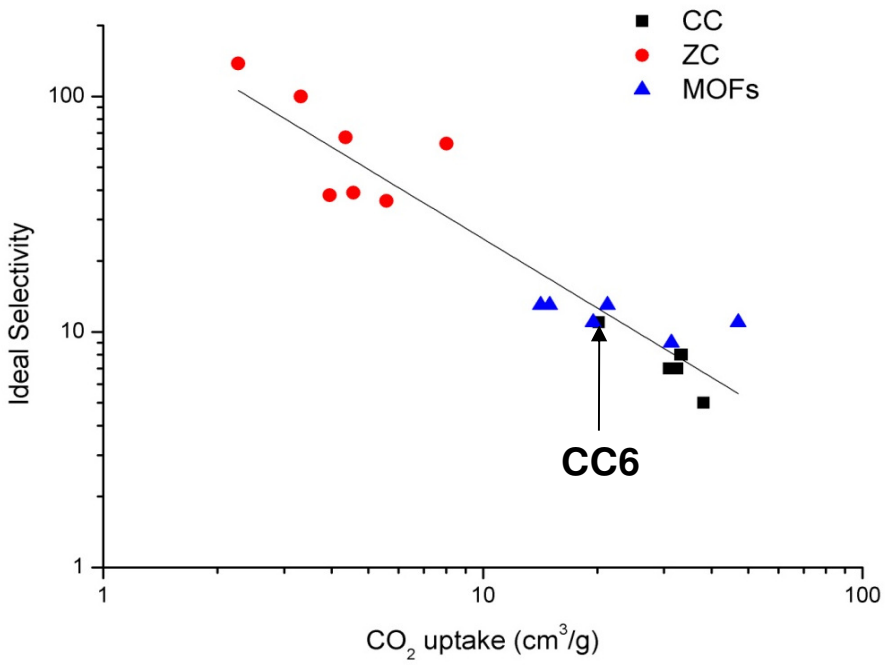

Figure 17. Logarithmic plot of ideal selectivity (CO_2/N_2) versus CO_2 uptakes with linear trend line showing cage compounds synthesized by Cooper group (square points), cage compounds synthesized by Zhang group (circles), and MOFs (triangles).

Table 3. Summary of CO_2 uptake, N_2 uptake and ideal selectivity (CO_2/N_2) in selected porous materials

Compound	N_2 uptake (cm^3/g)	CO_2 uptake (cm^3/g)	Ideal selectivity (CO_2/N_2)	Reference
CC1β[a]	4.26	33.15	8	13
CC2 [a]	7.17	38.08	5	16
CC3 [a]	4.26	30.91	7	16
CC4 [a]	4.03	33.38	8	20b
CC5 [a]	4.48	32.48	7	20a
CC6 [b]	1.79	20.16	11	

ZC1 [c]	0.033	3.32	100	6b
ZC2 [c]	0.065	4.35	67	6b
ZC3 [c]	0.157	5.58	36	6b
ZC4 [c]	0.016	2.27	138	6b
ZC2'[c]	0.117	4.56	39	6b
ZC13 [c]	0.104	3.95	38	6b
ZC14 [c]	0.127	8.01	63	6b
ZIF95 [d]	1.68	21.28	13	21c
ZIF100 [d]	1.79	19.5	11	21c
MIL102 [e]	4.48	47.04	11	21b
Post synthesized MOF 3 [f]	1.12	14.18	13	21a
Post synthesized MOF 4 [f]	3.584	31.36	9	21a
Post synthesized MOF 5 [f]	1.12	15	13	21a

[**a**] at 300 K, 1 bar [**b**] at 300 K, 1.2 bar [**c**] at 293 K, 1bar [**d**] at 298 K, 1.13bar [**e**] at 304 K, 1bar [**f**] at 298 K, 1bar

4.3.4 Pore structure of [2+3] 'propeller' shaped organic cage molecule, CC6.

The single crystal structure recorded at 100 K with solvent removed was used for structural analysis and rationalisation of the observed gas selectivity. PXRD has confirmed that the structure did not have a significant change after desolvation. Unlike cucurbit[6]uril,[10] where selectivity of CO_2 over CO was rationalised on the basis of the high enthalpy of CO_2 adsorption, we attribute the selectivity observed here to the crystal packing, because the 1-D channels of **CC6** have a diameter which

is just slightly larger than the kinetic diameter of many gases.[23] The Connolly surface constructed using a H_2 probe radius of 1.42 Å shows a 1-D channel with a fully connected 'side pore' (Figure 18 top). Using a probe radius of 1.72 Å for CO_2, a 1-D channel was observed but a narrow restricted neck to this side pore was observed (Figure 18 middle). The Connolly surface obtained using with a N_2 probe radius of 1.82 Å also demonstrated a narrow, restricted 1-D channel, but in this case the 'side pore' was not connected to the channel (Figure 18 below). This could rationalize the lower uptake for N_2 and also the relatively high H_2 uptake observed at 77 K.

Non local density functional theory (NL-DFT) pore size distribution curves is obtained from the N_2 adsorption isotherm at 77 K. The material has a 14 Å pore size shown in Figure 19a. The 1D pore channels are represented by Connolly surfaces generated using a N_2 probe of 1.82 Å in Figure 19b. The diameter of these channels based Connolly surfaces is about 3.9 Å. The diameter of side pores is ~ 3.6 Å. An approximate pore channel length of 14.5 Å can be defined as the distance between two necks in the continuous 1-D channels; this is consistent with the measured pore size distribution of 14 Å based on the N_2 isotherm. The pore size below 5 Å cannot be determined from experiments.

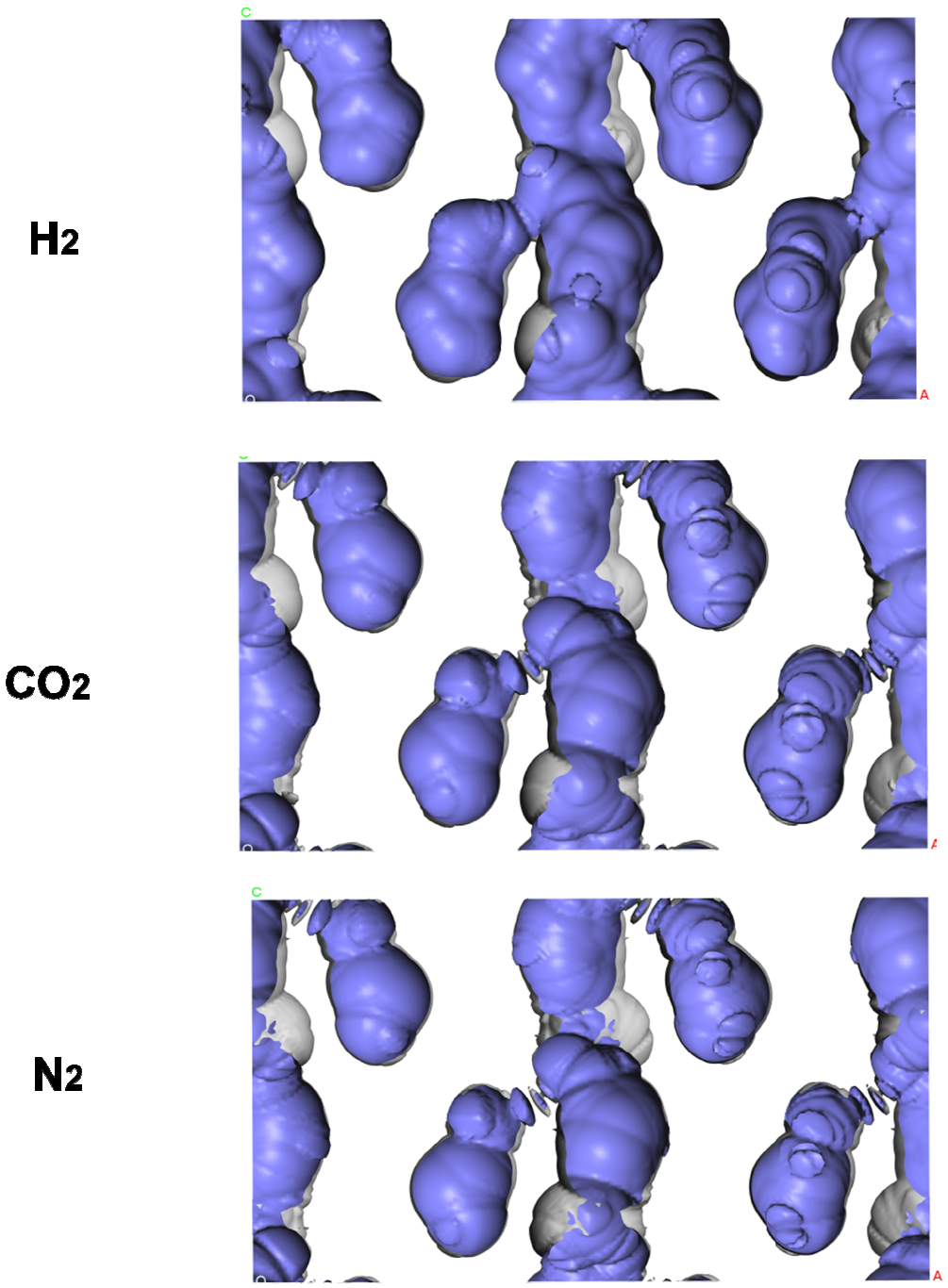

Figure 18. Connolly surfaces generated using probe radii of 1.42 Å, 1.72 Å, and 1.82 Å for H_2 (top), CO_2 (middle), and N_2 (bottom), respectively. The Connolly surface constructed using a H_2 probe radius of 1.42 Å shows a 1-D channel with a fully connected 'side pore' (top). Using a probe radius of 1.72 Å for CO_2, a 1-D channel was observed but a narrow restricted neck to this side pore was observed (middle). The Connolly surface obtained using with a N_2 probe radius of 1.82 Å also demonstrated a narrow, restricted 1-D channel, but in this case the 'side pore' was not connected to the channel (bottom).

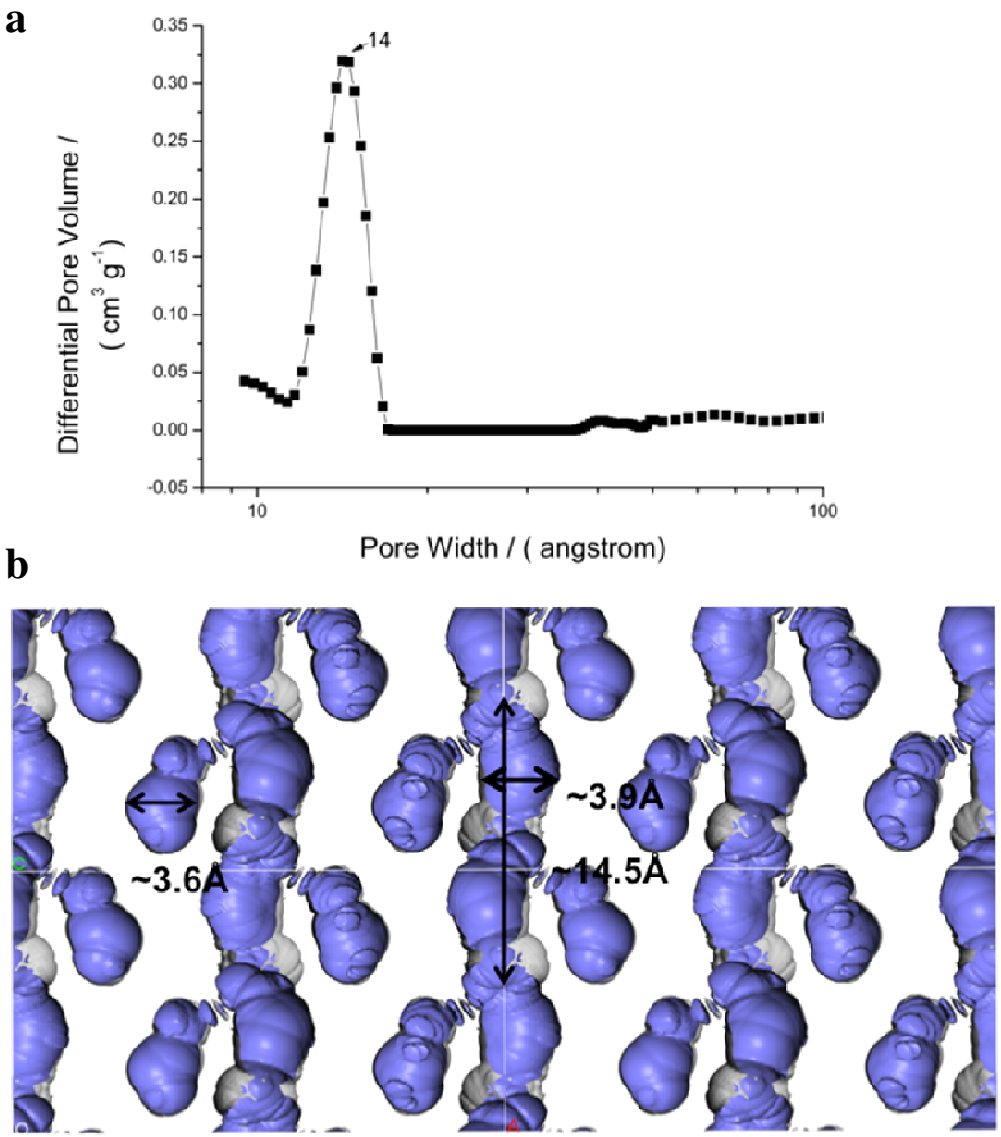

Figure 19. (a) Pore size distributions as calculated by application of non-local density functional theory (NL-DFT) analysis to N_2 adsorption isotherms obtained at 77 K. (b) The diameter of the 1-D pore channels based Connolly surfaces was calculated using a probe radius of 1.82 Å to be ~ 3.9 Å. The diameter of side pores is ~ 3.6 Å. An approximate pore channel length of 14.5 Å can be defined as the distance between two necks in the continuous 1-D channels; this is consistent with the measured pore size distribution of 14 Å based on the N_2 isotherm.

4.4 Topological building units design of molecular organic crystals

We described a [2+3] 'propeller' shape cage structure composed of two units of 1,3,5-tri-(4-formylphenyl) benzene and three units of 1, 5-pentanediamine which were synthesised in MeOH solution. Other topological structures for the cage

molecule by combining the triangle shape component (1, 3, 5-tri-(4-formylphenyl benzene) and linear component (1, 5-pentanediamine) might be tetrahedron ([4+6]) or cube ([8+12]), as shown in Figure 20. Initially, the reactions were tested in different solvents including $CHCl_3$, DCM and MeOH in order to check the effect of solvent on the cage formation. The experimental results showed that a cage stoichiometry change occurred by modifying the solvent and reaction conditions.

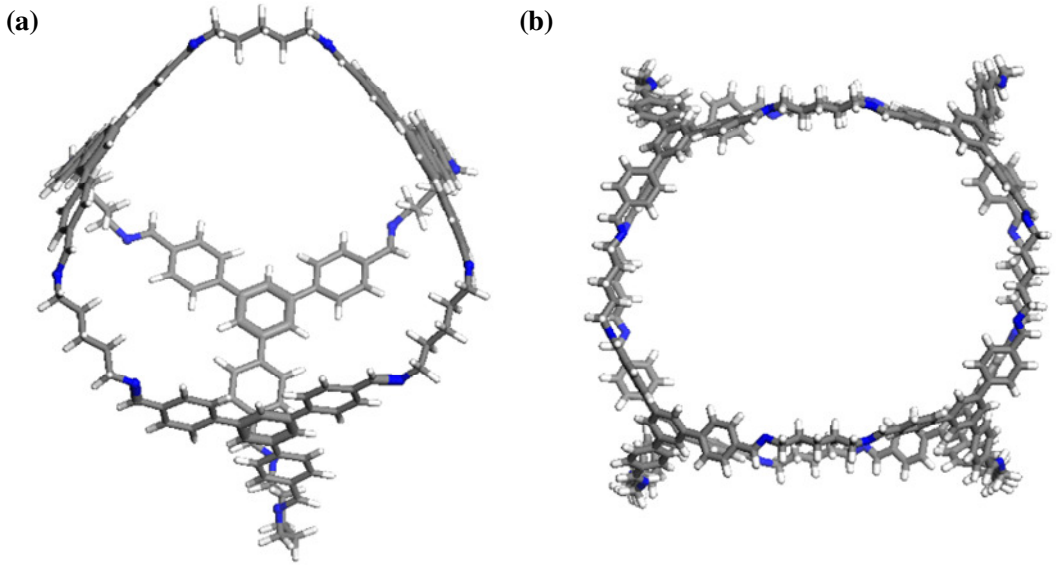

Figure 20. Two structural models of tetrahedral (a) and cube cages (b) by triangle and linear building blocks. (Grey: carbon; white: hydrogen; blue: nitrogen)

The new synthetic procedure was as follows: A solution of 1,3,5-tri-(4-formylphenyl) benzene (500 mg, 1.28 mmol) in DCM or $CHCl_3$ (300 mL) was added dropwise overnight to a solution of 1, 5-pentanediamine (200 mg, 1.92 mmol) in DCM or $CHCl_3$ (300 mL) in round-bottomed flask. The flask was cooled in an ice bath. After addition, the reaction was stirred for another 48 hours at room temperature. A slow addtion of reagents, low temperature and dilution solution were used for the synthesis to avoid imine polymer formation. The solution was then filtered through filter paper and the solvent was removed by the rotary evaporation. The products (**CC6'**) were white powders with 85% yield. The NMR spectra was the same as observed for [2+3] proppeller cage. ^{1}H NMR ($CDCl_3$, 400MHz) δ 8.16 ppm (s, 6H, CH=N), 7.51-7.28 ppm (m, 30H, -ArH), 3.68 ppm (m, 12H,-NCH), 1.77 ppm (m, 12H, $-CH_2$), 1.32 ppm (m, 6H, $-CH_2$) ppm.^{13}C NMR ($CDCl_3$) δ 160.95, 142.13, 141.12, 134.97, 128.10, 126.82, 124.40 ppm.

However, mass spectrometry showed [**CC6'** + Na] $^{+}$ ion at m/z = 1982.10, which is double the number of [2+3] cage molecular ion. It is consistent with a [4+6] cage structure composed of four units of 1, 3, 5-tri-(4-formylphenyl) benzene and six units of 1, 5-pentanediamine with formula $C_{138}H_{132}N_{12}$ or interlocked catenated **CC6**. A [2+3] cage molecule ion also was observed in the mass spectrometry shown in Figure 21.

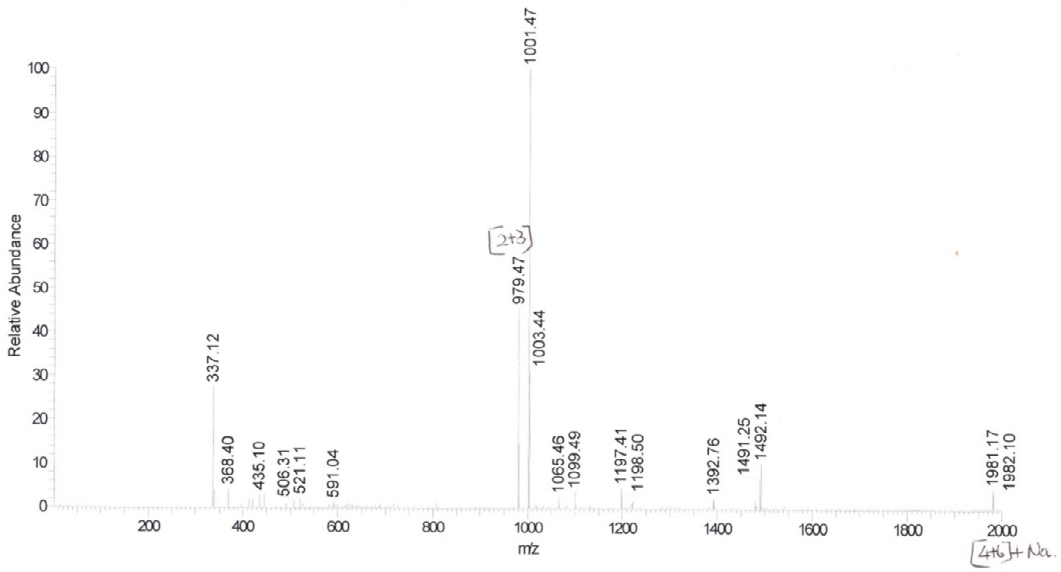

Figure 21. Mass spectrometry of the products obtained by the reaction in DCM ($CHCl_3$) solvent (**CC6'**).

Further analysis was carried on by PXRD and gas sorption. PXRD of bulk materials **CC6'** (the blue pattern) shows crystallinity in Figure 22. The simulated PXRD of single crystal structure for the [2+3] cage, **CC6**, produced by Mercury software is shown as a comparison (red pattern). The peaks of PXRD for **CC6'** have a good match with simulated PXRD for **CC6** below 2θ =15. New peaks were oberved for **CC6'** between 2θ = 15 and 2θ = 30 which might correspond to the new product.

The N_2 sorption measurements for **CC6'** at 77 K showed a Type I isotherm (Figure 23) with a total uptake of 2.5 mmol g^{-1} and a BET surface area of 200 m^2g^{-1} which is much higher than **CC6** (99 m^2g^{-1}).

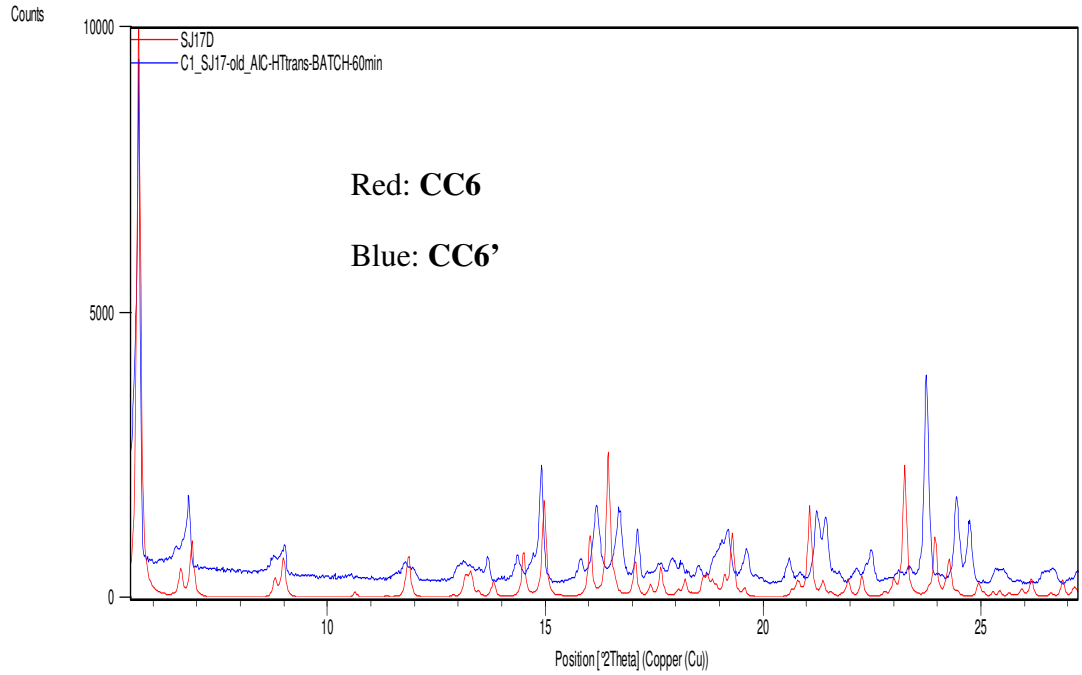

Figure 22. PXRD of **CC6'** (blue pattern) compared with simulated PXRD of **CC6**, produced by Mercury software (red pattern).

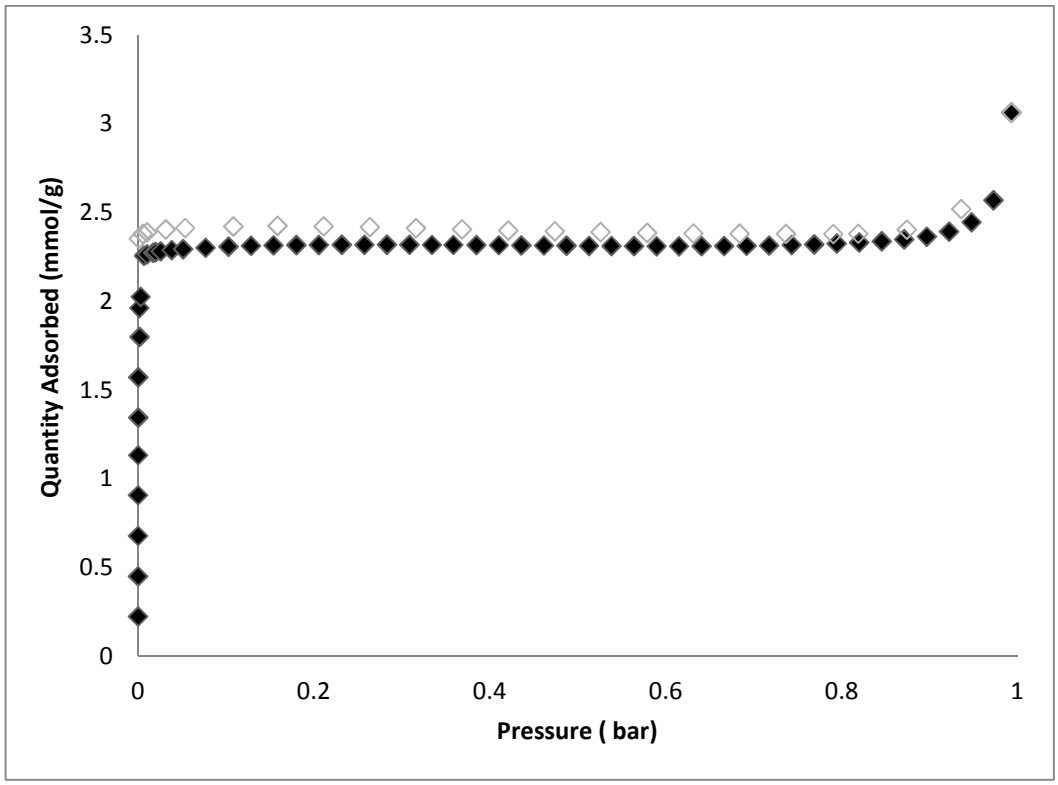

Figure 23. Nitrogen adsorption /desorption isotherm for **CC6'** at 77K. The full symbols are adsorption and open symbols are desorption.

These preliminary results suggest that cage topology can be controlled by modifying the reaction conditions. The reaction of 1,3,5-tri-(4-formylphenyl) benzene with 1,5-pentanediamine under a dilution solution, slow addition of reagents, a low temperature and DCM ($CHCl_3$) solvent gave different products, whether these are a [4+6] cage or a mixture of [2+3] and [4+6] cages or an interlocked catenane is currently uncertain. Recrystallization was not successful to get single crystals in this case.

It would be interesting to carry on more work to control cage topology by changing reaction conditions in the future. First, a HPLC methodology needs be designed to analyze and purify the cage molecules. The reaction conditions would be optimized to control the cage stoichiometry change. DFT calculations can be carried out to rationalize energy favourable cage topology. The correlation between gas porosity and cage topology could then be studied.

4.5 Conclusions

In summary, it have been shown the synthesis and characterization of a [2+3] imine-based cage molecule by the condensation reaction of 1,3,5-tri-(4-formylphenyl) benzene with 1, 5-pentanediamine in MeOH solvent. The cage molecule itself possesses a small cavity, but the crystal packing shows a 1D narrow channel. The material reveals selectivity for CO_2 over N_2 at modest pressures. It has an ideal selectivity of 11 for CO_2/N_2 at 300 K, 1 bar. Additionally, it exhibits a H_2/N_2 selectivity of 2.4 at 77 K, 1 bar. The observed gas selectivity can be rationalized by molecules packing and pore connectivity.

While the ideal selectivity of [2+3] 'propeller' cage is lower than other literature examples, the absolute uptakes are higher than other [2+3] imine cages. However, there is a trade-off between sorption capacity and selectivity for porous materials. The challenge will be to design materials with both high selectivity and high gas uptake.

When synthesising the cage in DCM ($CHCl_3$) it was found that solvent and reaction conditions had a significant effect on the cage topology. A [4+6] cage from 1,3,5-tri-(4-formylphenyl) benzene and 1,5-pentanediamine could be prepared in the future by optimizing the reaction conditions.

4.6 Chapter acknowledgements

In this chapter, I would like to thank Andy, Dave and Abbie for their supervision and suggestions on my work. Dr. John Bacsa solved the [2+3] cage crystal structure. Dr. Xiaofeng Wu helped me with synthesis of the starting monomer 1, 3, 5-tri-(4-formylphenyl) benzene. The gas sorption was done by Dr. James T.A. Jones and Dr. Robert Dawson. Le Bail refinement of PXRD was done by Dr. James T.A. Jones.

4.7 References

1. (a) Ferdi Schüth, K. S. W. S., Jens Weitkamp, *Handbook of Porous Solids*. Wiley: 2002; (b) Li, J.-R.; Kuppler, R. J.; Zhou, H.-C., Selective gas adsorption and separation in metal-organic frameworks. *Chem. Soc. Rev.* **2009,** *38* (5), 1477-1504.
2. Ackley, M. W.; Rege, S. U.; Saxena, H., Application of natural zeolites in the purification and separation of gases. *Microporous Mesoporous Mater.* **2003,** *61* (1–3), 25-42.
3. Jiang, J.-X., and Cooper, A.I., *Topics Curr. Chem.* **2010,** *293*, 1-33.
4. Yang, R. T., *Adsorbents: Fundamentals and Applications*. Wiley: 2003.
5. (a) Holst, J. R.; Trewin, A.; Cooper, A. I., Porous organic molecules. *Nat. Chem.* **2010,** *2* (11), 915-920; (b) McKeown, N. B., Nanoporous molecular crystals. *J. Mater. Chem.* **2010,** *20* (47), 10588-10597.
6. (a) Jin, Y.; Voss, B. A.; Noble, R. D.; Zhang, W., A Shape-Persistent Organic Molecular Cage with High Selectivity for the Adsorption of CO_2 over N_2. *Angew. Chem. Int. Ed.* **2010,** *49* (36), 6348-6351; (b) Jin, Y.; Voss, B. A.; Jin, A.; Long, H.; Noble, R. D.; Zhang, W., Highly CO_2-Selective Organic Molecular Cages: What Determines the CO2 Selectivity. *J. Am. Chem. Soc.* **2011**, *133* (17), 6650-6658.
7. Atwood, J. L.; Barbour, L. J.; Jerga, A., A New Type of Material for the Recovery of Hydrogen from Gas Mixtures. *Angew. Chem. Int. Ed.* **2004,** *43* (22), 2948-2950.
8. Sozzani, P.; Bracco, S.; Comotti, A.; Ferretti, L.; Simonutti, R., Methane and Carbon Dioxide Storage in a Porous van der Waals Crystal. *Angew. Chem. Int. Ed.* **2005,** *117* (12), 1850-1854.
9. Lim, S.; Kim, H.; Selvapalam, N.; Kim, K.-J.; Cho, S. J.; Seo, G.; Kim, K., Cucurbit[6]uril: Organic Molecular Porous Material with Permanent Porosity, Exceptional Stability, and Acetylene Sorption Properties. *Angew. Chem. Int. Ed.* **2008,** *47* (18), 3352-3355.
10. Kim, H.; Kim, Y.; Yoon, M.; Lim, S.; Park, S. M.; Seo, G.; Kim, K., Highly Selective Carbon Dioxide Sorption in an Organic Molecular Porous Material. *J. Am. Chem. Soc.* **2010,** *132* (35), 12200-12202.
11. Tian, J.; Ma, S.; Thallapally, P. K.; Fowler, D.; McGrail, B. P.; Atwood, J. L., Cucurbit[7]uril: an amorphous molecular material for highly selective carbon dioxide uptake. *Chem. Commun.* **2011,** *47* (27), 7626-7628.
12. Mastalerz, M.; Schneider, M. W.; Oppel, I. M.; Presly, O., A Salicylbisimine Cage Compound with High Surface Area and Selective CO_2/CH_4 Adsorption. *Angew. Chem. Int. Ed.* **2011,** *50* (5), 1046-1051.

13. Jones, J. T. A.; Holden, D.; Mitra, T.; Hasell, T.; Adams, D. J.; Jelfs, K. E.; Trewin, A.; Willock, D. J.; Day, G. M.; Bacsa, J.; Steiner, A.; Cooper, A. I., On–Off Porosity Switching in a Molecular Organic Solid. *Angew. Chem. Int. Ed.* **2011,** *50* (3), 749-753.
14. Schneider, M. W.; Oppel, I. M.; Mastalerz, M., Exo-Functionalized Shape-Persistent [2+3] Cage Compounds: Influence of Molecular Rigidity on Formation and Permanent Porosity. *Chem. Eur. J.* **2012,** *18* (14), 4156-4160.
15. Drage, T. C.; Snape, C. E.; Stevens, L. A.; Wood, J.; Wang, J.; Cooper, A. I.; Dawson, R.; Guo, X.; Satterley, C.; Irons, R., Materials challenges for the development of solid sorbents for post-combustion carbon capture. *J. Mater. Chem.* **2012,** *22* (7), 2815-2823.
16. Tozawa, T.; Jones, J. T. A.; Swamy, S. I.; Jiang, S.; Adams, D. J.; Shakespeare, S.; Clowes, R.; Bradshaw, D.; Hasell, T.; Chong, S. Y.; Tang, C.; Thompson, S.; Parker, J.; Trewin, A.; Bacsa, J.; Slawin, A. M. Z.; Steiner, A.; Cooper, A. I., Porous organic cages. *Nat. Mater.* **2009,** *8* (12), 973-978.
17. Jin, Y.; Voss, B. A.; McCaffrey, R.; Baggett, C. T.; Noble, R. D.; Zhang, W., Microwave-assisted syntheses of highly CO_2-selective organic cage frameworks (OCFs). *Chem. Sci.* **2012,** *3* (3), 874-877.
18. Weber, E.; Hecker, M.; Koepp, E.; Orlia, W.; Czugler, M.; Csoregh, I., New trigonal lattice hosts: stoicheiometric crystal inclusions of laterally trisubstituted benzenes-X-ray crystal structure of 1,3,5-tris-(4-carboxyphenyl)benzene[middle dot]dimethylformamide. *J. Chem. Soc., Perkin Trans. 2* **1988,**(7), 1251-1257.
19. P. van der Sluis, A. L. S., BYPASS: an effective method for the refinement of crystal structures containing disordered solvent regions. *Acta Cryst. A* **1990,** *46*, 194-201.
20. (a) Bojdys, M. J.; Briggs, M. E.; Jones, J. T. A.; Adams, D. J.; Chong, S. Y.; Schmidtmann, M.; Cooper, A. I., Supramolecular Engineering of Intrinsic and Extrinsic Porosity in Covalent Organic Cages. *J. Am. Chem. Soc.* **2011,** *133* (41), 16566-16571; (b) Mitra, T.; Wu, X.; Clowes, R.; Jones, J. T. A.; Jelfs, K. E.; Adams, D. J.; Trewin, A.; Bacsa, J.; Steiner, A.; Cooper, A. I., A Soft Porous Organic Cage Crystal with Complex Gas Sorption Behavior. *Chem. Eur. J.* **2011,** *17* (37), 10235-10240.
21. (a) Bae, Y.-S.; Farha, O. K.; Hupp, J. T.; Snurr, R. Q., Enhancement of CO_2/N_2 selectivity in a metal-organic framework by cavity modification. *J. Mater. Chem.* **2009,** *19* (15), 2131-2134; (b) Surblé, S.; Millange, F.; Serre, C.; Düren, T.; Latroche, M.; Bourrelly, S.; Llewellyn, P. L.; Férey, G., Synthesis of MIL-102, a Chromium Carboxylate Metal–Organic Framework, with Gas Sorption Analysis. *J. Am. Chem. Soc.* **2006,** *128* (46), 14889-14896; (c) Wang, B.; Cote, A. P.; Furukawa, H.; O/'Keeffe, M.; Yaghi, O. M., Colossal cages in zeolitic imidazolate frameworks as selective carbon dioxide reservoirs. *Nature* **2008,** *453* (7192), 207-211.
22. (a) Robeson, L. M., Correlation of separation factor versus permeability for polymeric membranes. *J. Membr. Sci.* **1991,** *62* (2), 165-185; (b) Robeson, L. M., The upper bound revisited. *J. Membr. Sci.* **2008,** *320* (1-2), 390-400.
23. Sircar, S., Basic Research Needs for Design of Adsorptive Gas Separation Processes. *Ind. Eng. Chem. Res.* **2006,** *45* (16), 5435-5448.

Chapter 5

Amorphous porous scrambled organic molecular solids

5.1 Introduction of amorphous porous molecular solids

The work in this Chapter has been (mostly) published in the following paper: S. Jiang, *et al.*, A. I. Cooper, *Nat. Commun.* **2011**, *2*, 207. An alternative synthetic strategy to crystalline porous cages[1] is to generate organic cages which are amorphous in the solid state. There has been less focus on the field of amorphous porous molecules compared with crystalline ones, because permanent porosity in amorphous molecular solids is extremely rare.[2] Amorphous molecular packing is not readily characterized due to lack of a periodic structure, therefore the understanding and design of such materials is more challenging. However, amorphous materials offer a number of potential advantages.[2-3] For example, desolvating molecular crystals often lead to a loss of porosity, which may not happen in a porous amorphous solid. The porosity of the materials might be further enhanced by encouraging 'bad' packing. Amorphous materials may form membranes or thin porous films due to good solubility and processability. Control and tuning of the properties of amorphous molecular solids might be achieved via functional group modification of the discrete molecules. The objective of this project was to synthesize organic cage molecules in an amorphous solid state, and to pack them inefficiently to create permanent porosity.

This is a brief overview of amorphous molecular solids in the literature. Polymers of intrinsic microporosity (PIMs) were prepared either as insoluble networks or soluble polymers.[4] The soluble linear PIMs with rigid and contorted molecular structures exhibit high surface areas (700 – 900 m^2/g) which can be considered as porous molecular materials with a range of molecular weights.[4] Their permanent porosity results from bad packing of macromolecular chain building blocks. It is noted that PIM-1 with small chains has a lower surface area and the porosity increases with increasing chain length.[5] A significant advantage of these materials is their solution processability. PIM-1 has been processed into porous thin films or membranes for gas separation. [5] On the other hand, there are a few examples of amorphous porous molecular solids comprised of small organic molecules. The Noria molecule shows a

'waterwheel' structure with a large hydrophobic cavity and exhibits gas adsorption properties in the amorphous state reported by Atwood *et al.*[6] It shows a low N_2 and H_2 uptake with BET surface area of 40 m^2/g calculated from the N_2 isotherm at 77 K. However, it displays a high absorption capacity for CO_2. The amorphous Noria material exhibits a type I CO_2 isotherm from which the surface area was calculated ranging from 280-350 m^2/g and a pore volume of 0.13 cm^3/g. Noria and its analogue are the first amorphous porous organic molecule to show selective uptake of CO_2 over H_2 and N_2. Furthermore, Atwood and coworkers reported amorphous cucurbit [7] uril material to show one of the highest CO_2 sorption capacities among known organic porous materials at 298 K.[7] Amorphous cucurbit[7]uril (CB[7]) exhibits high thermal stability and permanent porosity from intrinsic voids. The CO_2 sorption capacity is 50 $cm^3\ g^{-1}$ at 1 bar, 297 K. In contrast, the N_2 and CH_4 uptakes of amorphous CB[7] are very low with only 5.5 $cm^3\ g^{-1}$ and 6.0 $cm^3\ g^{-1}$ under the same conditions, respectively. The high selectivity of CO_2 over CH_4 and N_2 can be ascribed to the high affinity of CB[7] and CO_2. The paper suggested that the material is suitable application for recycling CO_2 or SO_2 from flue gas stream. Zhang *et al.* synthesized a series of amorphous [2+3] cage molecules by a one-pot reversible imine condensation reaction and the imine cages were further reduced to amine.[8] The materials showed a low CO_2 and N_2 uptake, but high ideal CO_2/N_2 selectivity in the range from 36 to 138 at 20 °C and 1 bar. The study indicated that the high selectivity of CO_2/N_2 is provided not only by the amino group of the cage molecules, also by size of intrinsic cavities. Mastalerz *et al.*[9] reported a procedure to control the morphology of periphery-substituted cage compounds during the synthesis. A BET surface areas comparison between bulk amorphous, nanospheric amorphous and bulk crystalline materials for these cages compounds were included. The amorphous cage materials exhibit BET surface areas of approximately 700 $m^2\ g^{-1}$. When these cage compounds are in the crystalline or nanospheric solid state, the surface areas are much lower. [9]

This Chapter will describe the synthesis and simulation of amorphous porous 'scrambled' cages. The dynamic nature of imine bonds provides us novel methods to synthesize them.[10] In general, the imine bond can participate in (a) Exchange –the imine bond may undergo dynamic exchange with a second amine. (b) Metathesis – two imine bonds can undergo interchange in the solution as Figure 1 illustrated. The synthesis approaches in this work are based on cage-diamine exchange, cage-cage interchange and co-reaction of 1, 3, 5-triformylbenzene (TFB) with a mixture of both 1, 2-ethylenediamine (EDA) and 1,2-cyclohexanediamine (CHDA), respectively.[11] **CC1** and **CC3** were used as templates for exchange reactions.

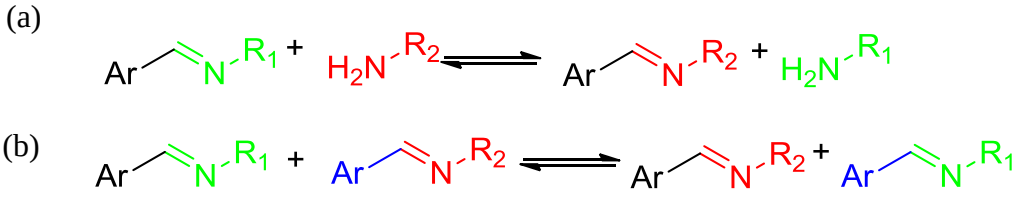

Figure 1. The dynamic nature of imine reactants imine condensation (a) exchange (b) metathesis (Figure is adapted from the Ref.[10]).

The materials are fully characterized by NMR, HPLC, PXRD and gas sorption analysis and gas selectivity will be addressed. A representative model is generated to rationalize the gas porosity in amorphous scrambled cages.

5.2 Cage-diamine dynamic exchange

Due to the dynamic nature of imine bonds, a tetrahedral imine cage was observed to participate in an exchange reaction with a second diamine in solution. Cage 1 (**CC1**) was synthesized from the condensation reaction of 1,3,5-triformylbenzene with 1,2-ethylenediamine and **CC1** has a tetrahedral symmetry with six unfunctionalized ethylene linkers on the vertices.[1] A solution of **CC1** was placed in solution of (1*R*, 2*R*)-cyclohexanediamine (CHDA). The vertices of **CC1** were replaced by CHDA one by one, and a series of asymmetrical organic cage molecules were produced. The dynamic process can be monitored by NMR and HPLC for characterizing the products.

5.2.1 Synthetic procedures

The dynamic interchange reaction of **CC1** with CHDA was performed as follows: **CC1** (50 mg, 0.063 mmol) was dissolved in chloroform (5 mL). CHDA (54 mg, 0.47 mmol) was dissolved in $CHCl_3$ (5 mL). The molar ratio of CHDA and **CC1** is 7.5 : 1. Therefore a slight excess CHDA was used in order to enable CHDA fully exchange with six vertices of **CC1**. The **CC1** solution was added directly to the CHDA solution at room temperature.

The kinetic NMR study of **CC1** and (1*R*, 2*R*)-cyclohexanediamine (CHDA) dynamic exchange was carried out as follows: **CC1** (5.0 mg, 0.0063 mmol) and CHDA (5.3 mg, 0.047 mmol) were dissolved in $CDCl_3$ (1 mL) in an NMR tube (molar ratio of CHDA: **CC1** = 7.5 : 1). The reaction was analyzed for up to 11 days.

The dynamic interchange reactions of **CC1** with CHDA at various reaction ratios were carried out as follows: **CC1** and CHDA were dissolved in $CHCl_3$ (10 mL).The amounts were listed in Table 1.

Table 1. Synthesis of dynamic exchange of **CC1** and CHDA at various reaction ratios.

CC1 : CHDA reaction ratio	**CC1**	CHDA
1: 6	50 mg, 0.0631 mmol	43.2 mg, 0.378 mmol
1: 5	50 mg, 0.0631 mmol	36.0 mg, 0.316 mmol
1: 4	50 mg, 0.0631 mmol	28.8 mg, 0.253 mmol
1: 3	50 mg, 0.0631 mmol	21.5 mg, 0.189 mmol
1: 2	50 mg, 0.0631 mmol	14.4 mg, 0.126 mmol
1: 1	50 mg, 0.0631 mmol	7.19 mg, 0.063 mmol

The kinetic NMR study of **CC3** and 1,2-ethylenediamine (EDA) dynamic exchange was carried out as follows: **CC3** (5.0 mg, 0.0045 mmol) and EDA (2.0 mg, 0.034 mmol) were dissolved in $CDCl_3$ (1 mL) in an NMR tube (molar ratio of EDA: **CC3** = 7.5 : 1). The reaction was analyzed for up to 11 days.

5.2.2 Characterizations of cage-diamine exchange

Initially, the exchange reaction was monitored by ^{1}H NMR. The kinetic NMR analysis of **CC1** and excess CHDA dynamic exchange in $CDCl_3$ (1 mL) solution (molar ratio of **CC1**: CHDA = 1 : 7.5) was carried out for 11 days. The NMR spectra were recorded every 3 hours for the first 2 days and subsequently every day up to 11 days. Figure 2(a) illustrates NMR spectra at t = 0, 1 day, 5 days and 11 days, respectively. The NMR spectrum at t = 0 shows that the chemical shift at 4.02 ppm (labeled by 'a' in the spectra) belongs to the protons of EDA- linkers (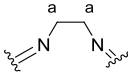) of the **CC1**. The peak for imine protons is observed at 8.18 ppm (labeled by 'b'). The chemical shift at 7.90 ppm (labeled by 'c') is assigned to the aromatic rings of cage molecules. The peaks in a range from 1.20 ppm to 2.80 ppm belong to protons of CHDA. The integration of EDA- linkers of **CC1** at 4.02 ppm decreases over time, whereas the integration of CHDA –linkers (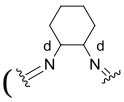) at 3.33 ppm (labeled by 'd') shows a proportional increase. The relative integration of **CC1** EDA- linkers and CHDA- linkers from products was plotted according to NMR data in Figure 2(b). It demonstrates that the exchange reaction occurs immediately after mixing two solutions of **CC1** and CHDA, and the reaction equilibration can be reached within 2-3 days at room temperature.

.

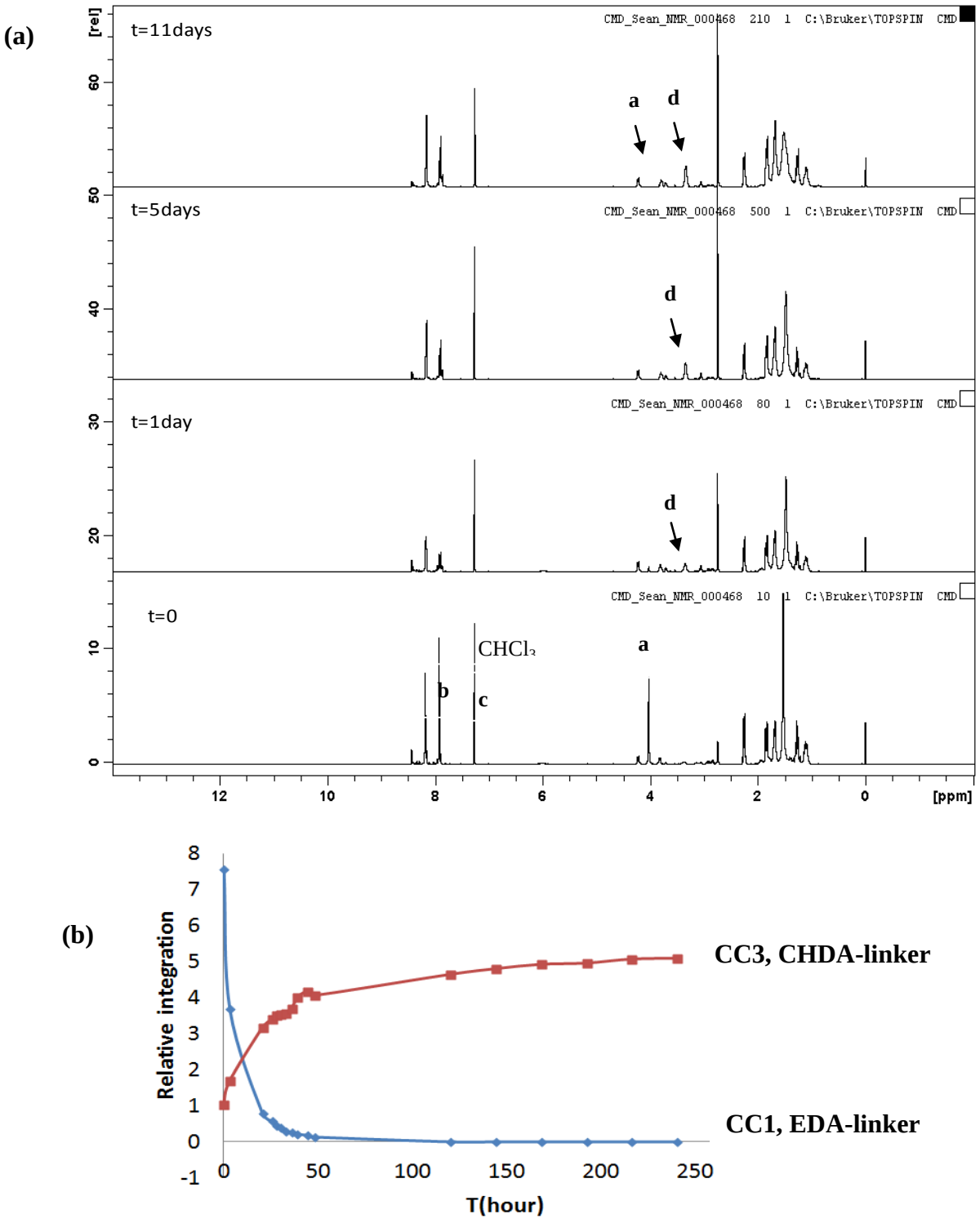

Figure 2. (a) Kinetic NMR study for **CC1** and CHDA dynamic exchange reaction. Showing NMR spectra at t = 0, 1 day, 5 days and 11 days, respectively. (b) The plot of integration of protons representing EDA- linkers and CHDA –linkers over time.

The cage-diamine exchange was observed from the NMR study, but the thermodynamically preferred products could not be identified. The products were therefore analyzed by high performance liquid chromatography (HPLC) combined with mass spectrometry (MS). HPLC-MS analysis showed that the products consist of a series of cage molecules incorporating both EDA- and CHDA- linked vertices in a single cage molecules as Figure 3 shown. The HPLC methodology for cage molecules was designed by Charlotte Blythe.

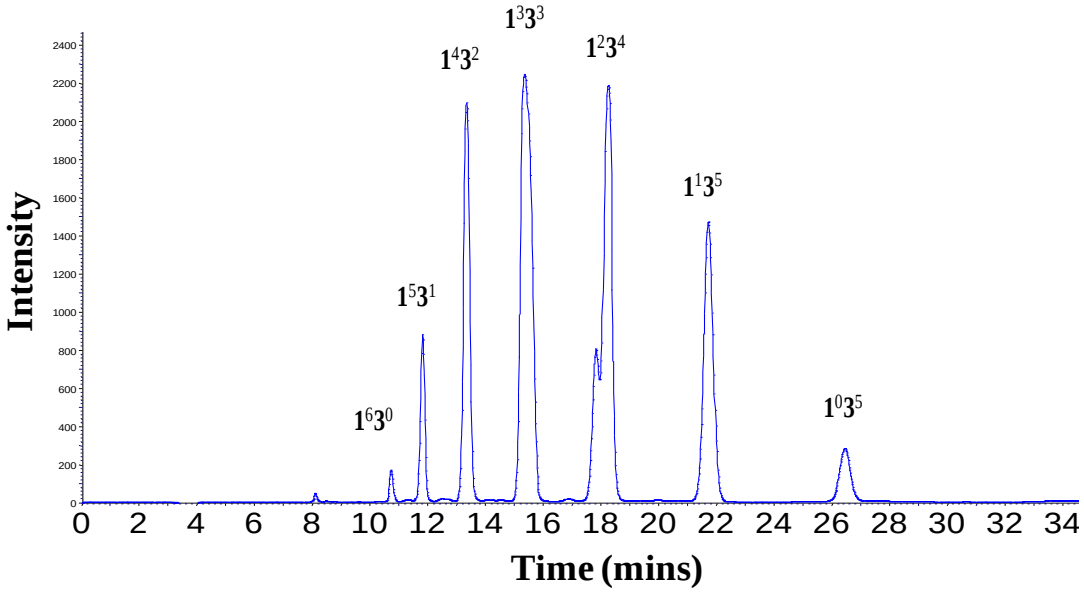

Figure 3. HPLC trace showing a distribution of produces by **CC1** and CHDA dynamic exchange reaction after 5 days.

The products are represented as $\mathbf{1}^n\mathbf{3}^m$ where **1** and **3** are EDA- and CHDA- linkers, respectively. n and m represent the number of EDA and CHDA linkers, respectively. Three of the products possess positional isomers. The $\mathbf{1}^2\mathbf{3}^4$ and $\mathbf{1}^4\mathbf{3}^2$ species exist as *cis* or *trans* isomers and $\mathbf{1}^3\mathbf{3}^3$ has meridional (*mer*) or facial (*fac*) forms. The high resolution chromatography shows two peaks for each the $\mathbf{1}^4\mathbf{3}^2$, $\mathbf{1}^3\mathbf{3}^3$ and $\mathbf{1}^2\mathbf{3}^4$ species, suggesting the possible isomeric forms are produced shown below in Figure 28. In summary, the cage-diamine dynamic exchange reaction is represented in Figure 4.

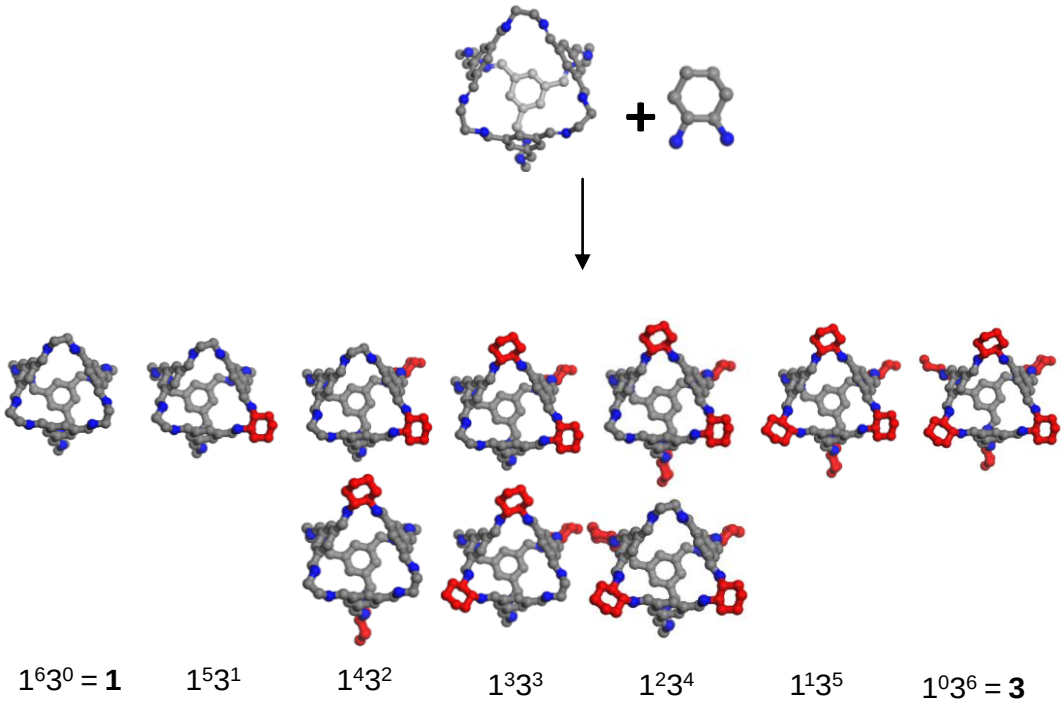

Figure 4. Dynamic exchange reaction of **CC1** and CHDA in the solution. The multifunctional and asymmetrical products could have been formed.

In order to control the distribution of products, the equilibration of the exchange reaction is affected by adjusting the reaction conditions such as reaction ratios and temperature. The effect of ratios of **CC1** and CHDA on the exchange reaction was investigated in detail by HPLC and MS. The reaction was maintained at a constant temperature of 30 °C. The product distribution of the reactions with various **CC1** and CHDA ratios is shown in Figure 5. Observed molecular weight in MS data can be assigned to accurate mass for $\mathbf{1}^n\mathbf{3}^m$ cage molecules. As we can see, the equilibrium $\mathbf{1}^n\mathbf{3}^m$ product distribution is controlled by the reaction ratio of **CC1** and CHDA. The HPLC retention times for **CC1** and **CC3** are 10 min and 26 min, respectively. Other species are observed between **CC1** and **CC3** in HPLC. The exchange reaction with a ratio of **CC1** and CHDA at 1:1 gives that a distribution of cage molecules with high values of n, such as **CC1** ($\mathbf{1}^6\mathbf{3}^0$), $\mathbf{1}^5\mathbf{3}^1$ and $\mathbf{1}^4\mathbf{3}^2$ species. However, high CHDA ratio (**CC1** : CHDA = 1 : 6) leads to a predominance of cage molecules with high values of m in the equilibrium $\mathbf{1}^n\mathbf{3}^m$ product distribution with more **CC3** ($\mathbf{1}^0\mathbf{3}^6$), $\mathbf{1}^1\mathbf{3}^5$ and $\mathbf{1}^3\mathbf{3}^3$ species formed.

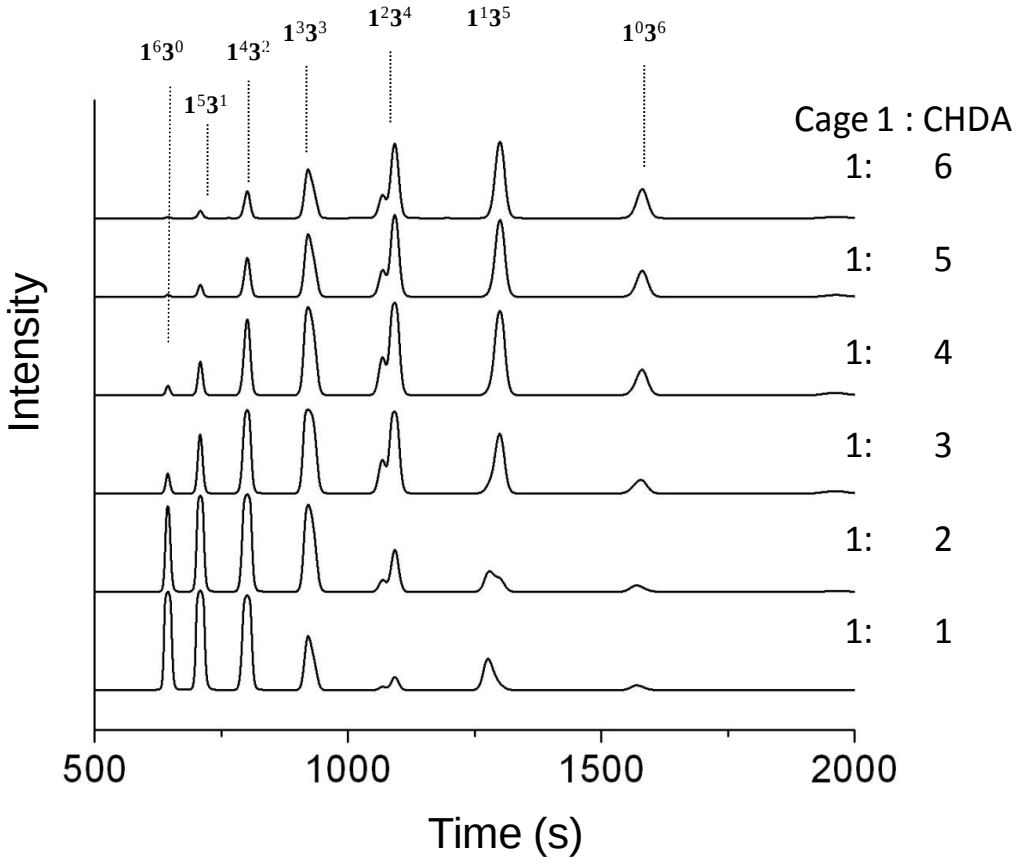

Figure 5. The product distribution of dynamic exchange reactions with various **CC1** and CHDA reaction ratios.

The exchange reaction also is affected by the reaction temperature to adjust the product distribution. The solutions of **CC1** and CHDA (molar ratio of **CC1**: CDHA = 1 : 7.5) were mixed in the chloroform solution at a 35 °C and 60 °C, respectively in the sealed HPLC vials. HPLC was used to follow the kinetic process of exchange reaction and determine the proportion of each cage molecule over the time. The peak areas from HPLC data for each cage molecule are plotted versus time in Figure 6. The reaction equilibration of the kinetic process occurs after 30 hours at 35 °C and the peak areas for each species keep constant. In contrast, the reaction is equilibrated after 8 hours at 60 °C. The peak area of **CC1** drops drastically at the beginning of the reaction at both 35°C and 60°C. The peak areas of $\mathbf{1}^5\mathbf{3}^1$, $\mathbf{1}^4\mathbf{3}^1$, $\mathbf{1}^3\mathbf{3}^3$ and **CC3** cage species were observed to increase at the beginning of the reaction and then decrease until they maintain a constant. The peak areas of $\mathbf{1}^2\mathbf{3}^4$ and $\mathbf{1}^1\mathbf{3}^5$ species continually

increase over time. The exchange reaction is driven forwards at a high temperature.

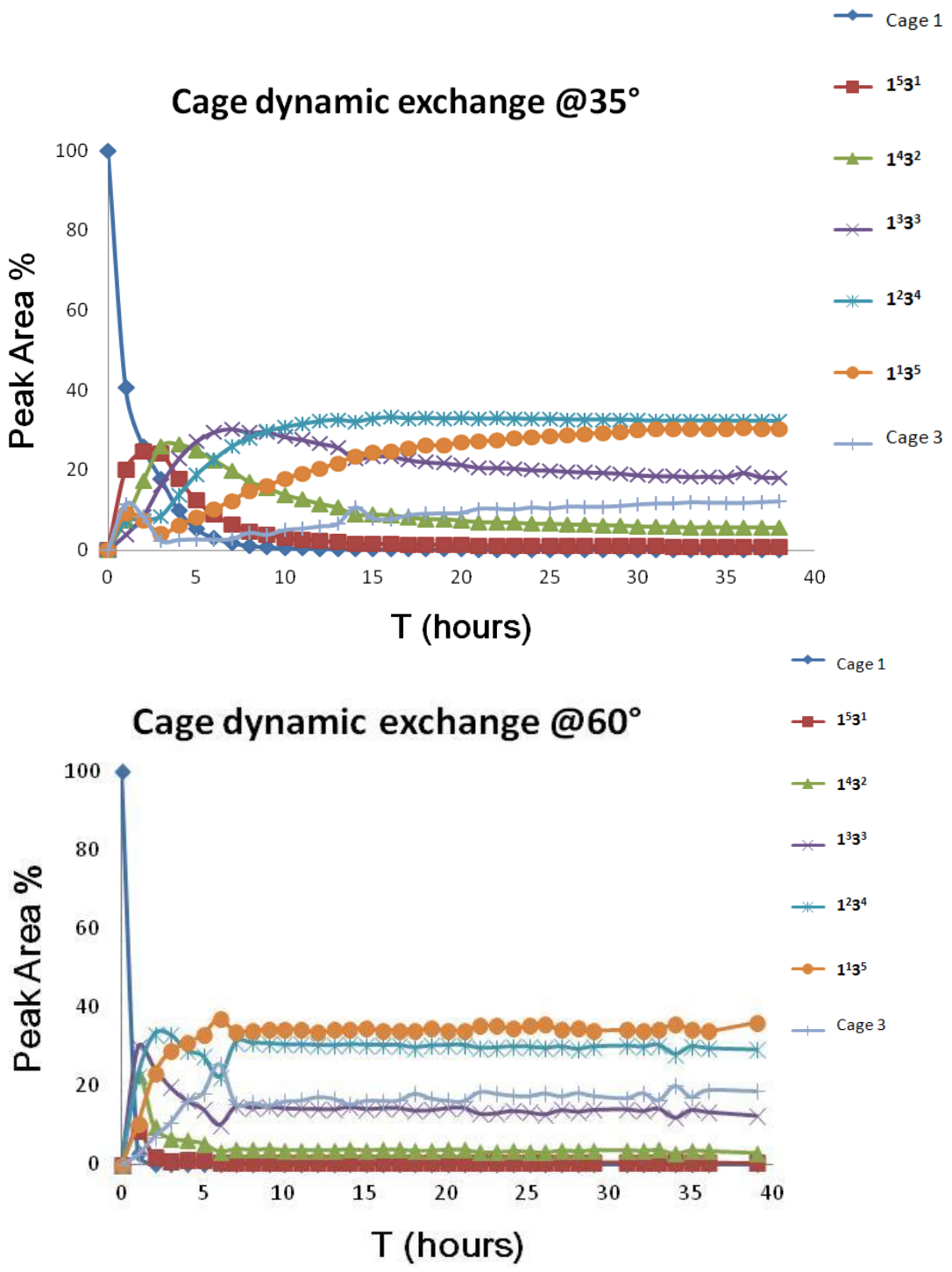

Figure 6. The distribution of molecular species analyzed by HPLC for the exchange reaction at different temperature.

We also investigated the dynamic exchange reaction of **CC3** with EDA to produce **CC1** and other cage molecule species. The reaction of **CC3** with excess 1,

2-ethylenediamine (EDA) in $CDCl_3$ solution (1 mL) was also followed by NMR for 11 days. The molar ratio of **CC3** and EDA is 1 : 7.5. The protons for CHDA- linkers on the **CC3** vertices were observed at 3.33 ppm (labeled by 'a' in the spectra) in Figure 7. There is no significant change of the integration of CHDA-linkers of **CC3** over the reaction time. The two peaks for the EDA- linkers of **CC1** were observed at 3.87 and 4.20 ppm after 5 days which ascribed to the scrambling of cages (labeled by 'b' in the spectra). The small amount of scrambled cages was formed after 11 days dynamic exchange reaction. The results indicate that the exchange process of **CC3** and EDA occurs slowly.

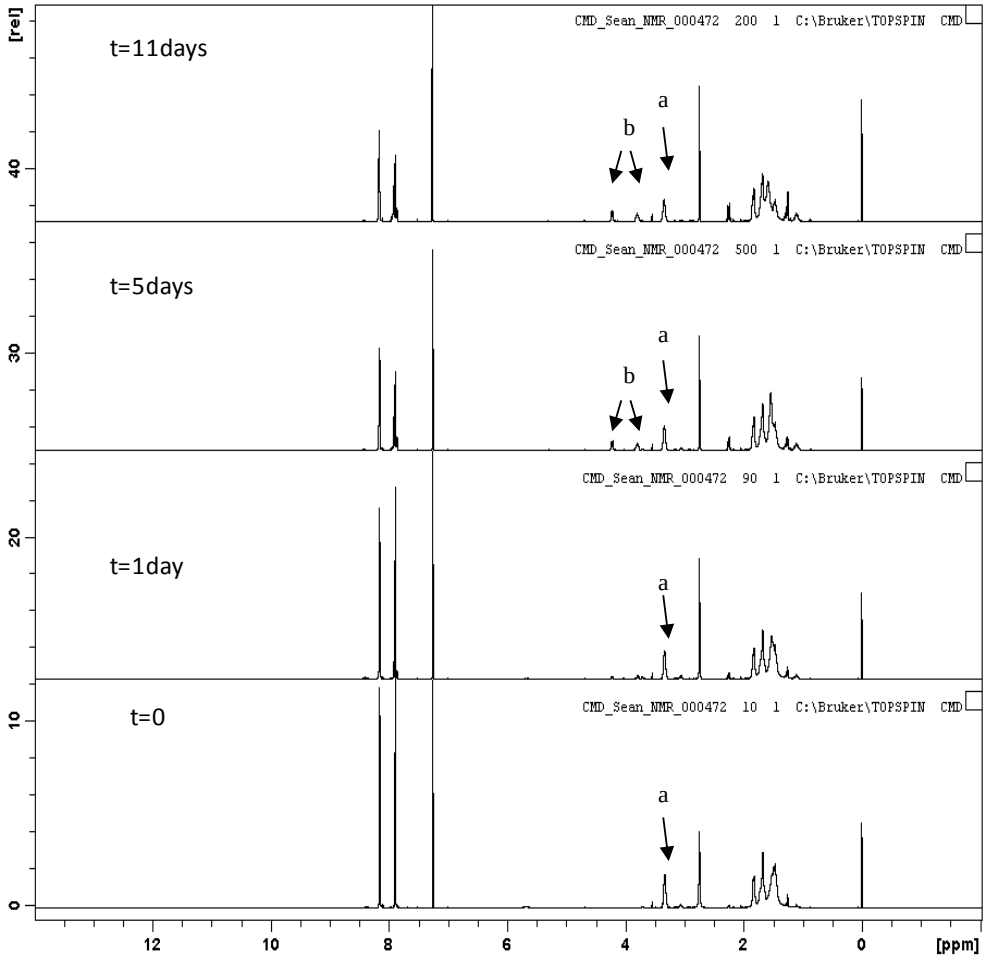

Figure 7. Kinetic NMR study for **CC3** and EDA dynamic exchange reaction. NMR spectra recorded at t = 0, 1 day, 5 days and 11 days, respectively.

In this study, density functional theory (DFT) with dispersion corrections

calculations was carried out for the formation energy of cage molecules, $\mathbf{1}^{n}\mathbf{3}^{m}$ which can be used to rationalize the exchange reaction. The formation energy can be calculated by the equation 5.1:

$$E_{formation\ energy} = E_{Cage\ molecule} + 12E_{H_20} - (4\,E_{TBA} + n\,E_{EDA} + mE_{CHDA}) \quad (5.1)$$

Figure 6 illustrates the density functional dispersion correction (DFT-D)[12] formation energies for single cage molecules calculated in a mixed Gaussian and plane-wave code CP2K [13] with the BLYP functional [14] and TZVP basis sets.[15] The positional isomers for $\mathbf{1}^{4}\mathbf{3}^{2}$, $\mathbf{1}^{3}\mathbf{3}^{3}$ and $\mathbf{1}^{2}\mathbf{3}^{4}$ species were included. The formation energy for **CC1** is -15.8 kcal/mol compared with -26.5 kcal/mol formation energy for **CC3**. The formation energies for scrambled cage molecules are much lower than **CC1**. The trend in Figure 6 rationalizes the dynamic exchange of **CC1** and CHDA to form a series of scrambled cage molecules. By constrast, **CC3** has a slow dynamic exchange with EDA due to unfavorable formation energies.

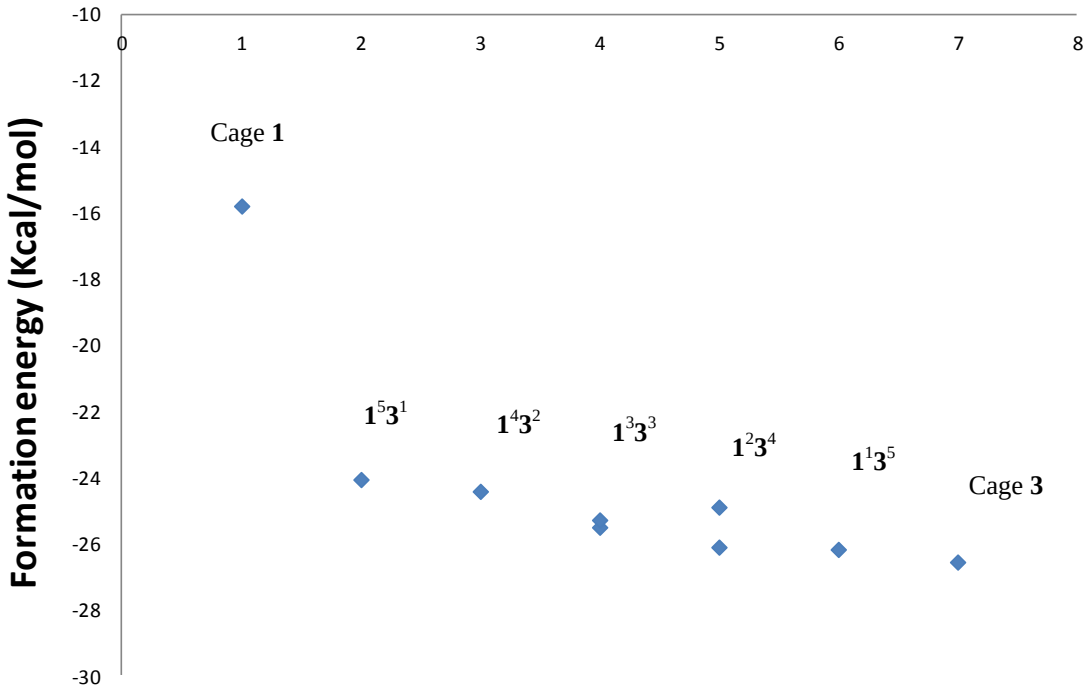

Figure 8. DFT-D3 calculating formation energies for scrambled cage molecules. The most favorable formation energy is $\mathbf{1}^{0}\mathbf{3}^{6}$ (**CC3**).

5.3 Cage –cage interchange

An alternative method to synthesize these scrambled cage molecules is using cage –cage dynamic interchange. The reaction of **CC1** with **CC3** was observed to be a slowly interchange in solution at 30 ˚C to form a comparable $\mathbf{1}^{n}\mathbf{3}^{m}$ product distribution. The study was carried out by Dr James T. A. Jones and Dr Tom Hasell. The cage mixed products were analyzed by the kinetic HPLC.

5.3.1 Synthetic procedure

100 mg **CC3** and 100 mg **CC1** were dissolved in 10 ml chloroform separately. The reaction was carried out in an HPLC autosampler for ease of sampling and the two solutions were kept separate until the start of the HPLC analysis. The solutions were mixed immediately before analysis in a proportion which achieved a 1:1 molar ratio of **CC1**: **CC3** (10 mL of **CC3** solution + 7.1 mL of **CC1** solution).

5.3.2 Characterizations of cage-cage interchange

HPLC chromatograms were then measured every hour for the first 48 hours and subsequently every 3 hours up to a total reaction time of 300 hours. The reaction was maintained at a constant temperature of 30 °C. The kinetic process of cage and cage interchange is shown in Figure 9. The peak areas of **CC1** and **CC3** from HPLC data drop dramatically when mixing two solutions. The proportions of $\mathbf{1}^{5}\mathbf{3}^{1}$ and $\mathbf{1}^{1}\mathbf{3}^{5}$ species vary as a function of time, first increasing and the decreasing. The populations of $\mathbf{1}^{4}\mathbf{3}^{2}$, $\mathbf{1}^{3}\mathbf{3}^{3}$and $\mathbf{1}^{1}\mathbf{3}^{5}$ species increase over time and keep constant when the reaction is equilibrated. The cage mixed products were obtained at the end of the reaction for NMR, PXRD, and gas sorption analysis.

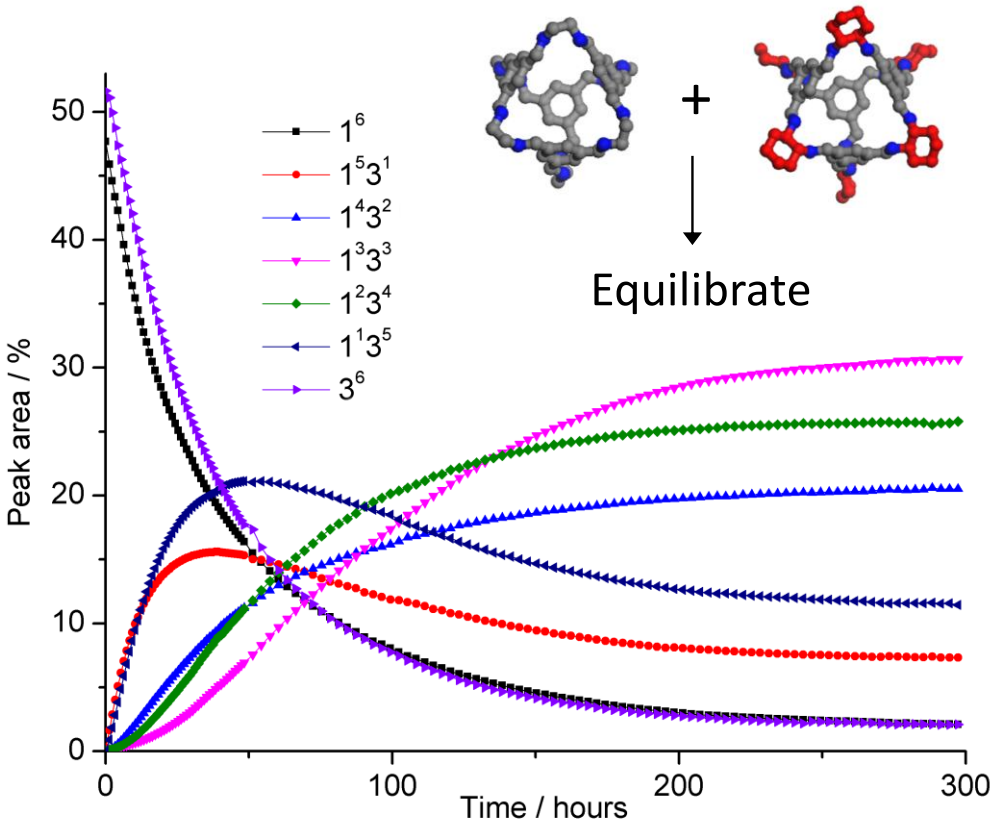

Figure 9. **CC1** and **CC3** interchange. Product distribution was analyzed by HPLC.

The scrambled cage molecules formed by cage-cage interchange are characterized by ^{1}H NMR. Figure 10 shows NMR spectra for **CC1**, **CC3** and scrambled cages, respectively. The imine protons of scrambled cages are at 8.18 ppm which is similar to **CC1** and **CC3**. The chemical shift at 7.90 ppm is assigned to aromatic rings of scrambled cages. These peaks are multiple and board compared with the ones for **CC1** and **CC3** due to asymmetrical symmetry of scrambled cages. The multiple peaks in a range from 1.20 ppm to 1.90 ppm are consistent with protons of cyclohexyl groups, ‘a’ and ‘b’ on the vertices (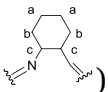). The peak at 3.33 ppm was assigned to the protons on the cage CHDA-linked vertices, ‘c’. The scrambling of the cages is confirmed by the splitting of the peak arising from **CC1** (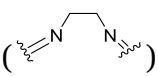) at 4.02 ppm into two peaks at 3.87 and 4.14 ppm.

The cage-cage interchange reaction has a practical advantage over the cage-diamine

method because there is no excess diamine to separate from the resulting product mixture at the end of the reaction. The product was obtained by rotary evaporating the solvents. The material showed no evidence for long range molecular order. It appeared to be close to amorphous phase on the basis of PXRD as shown in Figure 11. The gas sorption analysis will be discussed later.

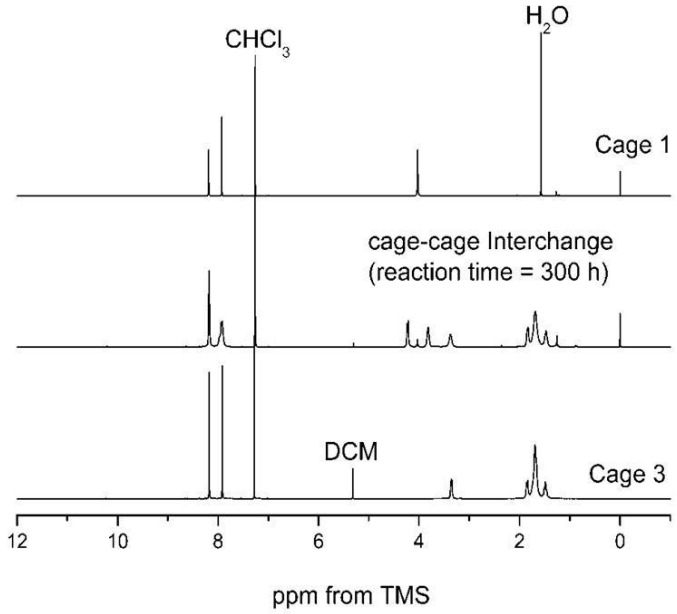

Figure 10. ^{1}H NMR ($CDCl_3$) spectra for scrambled cages produced by the cage-cage interchange reaction between **CC1** and **CC3** (reaction time = 300 h).

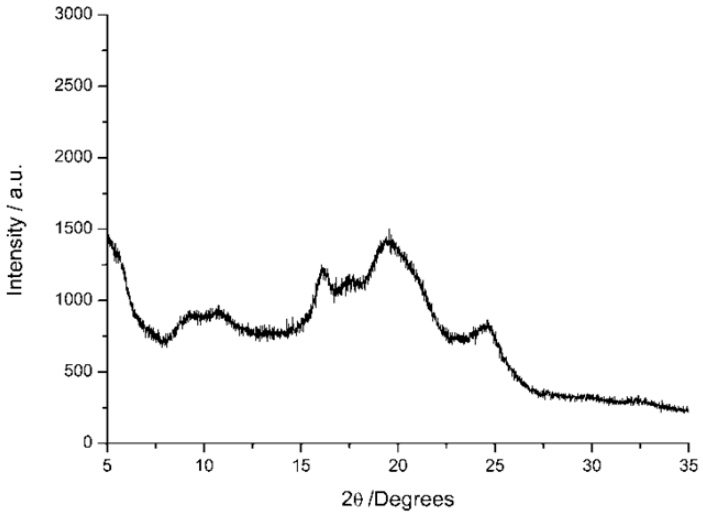

Figure 11. PXRD pattern for scrambled cages formed from the cage-cage interchange reaction between **CC1** and **CC3** (reaction time = 300 h).

5.4 Co-reactions

The co-reaction of 1,3,5-triformylbenzene (TFB) with a mixture of both 1,2-ethylenediamine (EDA) and (1*R*,2*R*)-1,2-cyclohexanediamine (CHDA) leads directly to an equilibrium distribution of $\mathbf{1}^{n}\mathbf{3}^{m}$ products. The co-reaction of TFB with EDA and CHDA was carried out with various EDA: CHDA ratios to produce the resulting product mixture. The products is shown in Figure 12 which is identical to the ones produced by cage-cage and cage-diamine dynamic exchange.

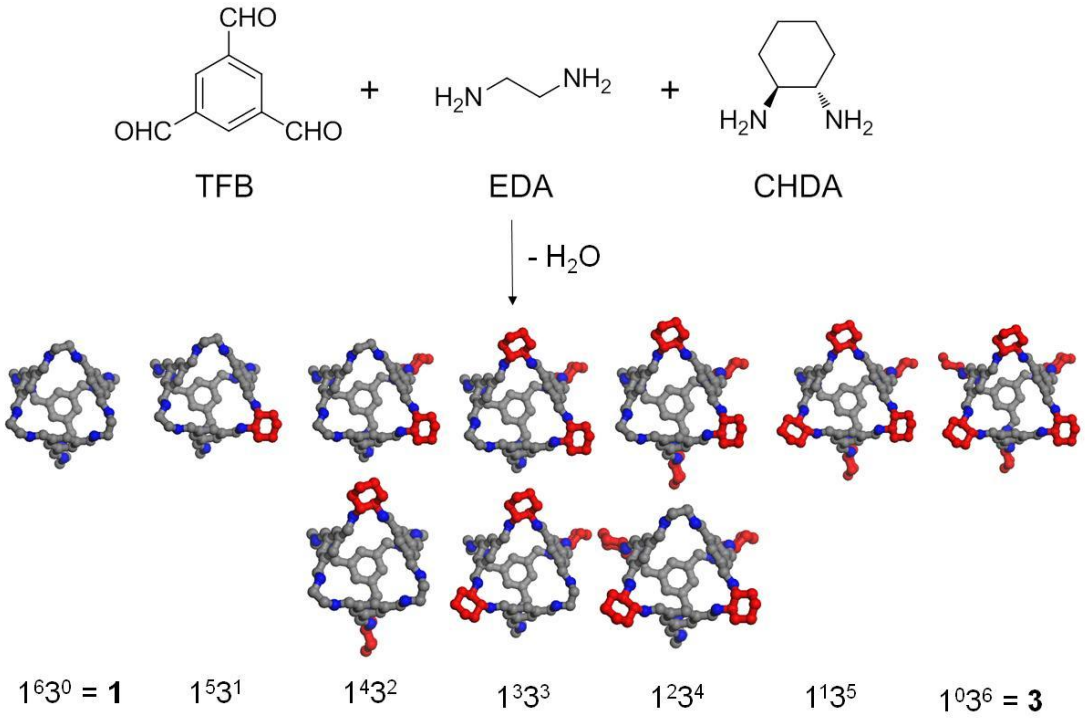

Figure 12. Direct co-reaction of two different diamines to form amorphous porous organic cages.

5.4.1 Synthetic procedure

General synthetic procedure is described as followed. Dichloromethane (25 mL) was slowly added to TFB (100 mg, 0.62 mmol) in a sample vial at room temperature. Under these conditions, the TFB did not dissolve immediately. A solution of EDA in DCM (5 mL) and a solution of CHDA in DCM (5 mL) were added respectively. Samples **A-E** were produced by the co-reaction of EDA and CHDA with TFB at

various molar ratios of EDA: CHDA. The amounts are listed in Table 2. After 5 days, a clear homogeneous solution was observed with no undissolved material being present. The products were obtained by solvent rotary evaporation and were white powders. The crude products were filtered, washed with ethyl acetate to remove any unreacted starting materials. The product was air dried overnight before analysis. Typical yield after washing = 55–60 %.

Table 2. Synthesis of mixed cages by direct co-reactions of two amines with TFB.

Sample ID	EDA:CHDA	EDA	CHDA
A	**5 : 1**	46.3 mg , 0.77 mmol	17.6 mg , 0.15 mmol
B	**4 : 2**	37.0 mg , 0.62 mmol	35.2 mg , 0.31 mmol
C	**3 : 3**	27.8 mg , 0.46 mmol	52.8 mg , 0.46 mmol
D	**2 : 4**	18.5 mg , 0.31 mmol	70.4 mg , 0.62 mmol
E	**1 : 5**	9.26 mg , 0.15 mmol	87.9 mg , 0.77 mmol

5.4.2 Characterizations of samples by co-reactions

The materials were characterized by HPLC-MS to assign individual molecular species (**CC1**, $\mathbf{1}^5\mathbf{3}^1$, $\mathbf{1}^4\mathbf{3}^2$, $\mathbf{1}^3\mathbf{3}^3$, $\mathbf{1}^2\mathbf{3}^4$, $\mathbf{1}^1\mathbf{3}^5$, and **CC3**). HPLC demonstrated that the equilibrium $\mathbf{1}^n\mathbf{3}^m$ product distribution was controlled by the diamine ratio shown in Figure 13. There is a direct correlation between the reaction ratio and the products distribution in this series of samples. High EDA ratios in the reagent mixture result in predominance of cage products with high value of n. For example, the products distribution of sample **A**-**B** was dominated by **CC1**, $\mathbf{1}^5\mathbf{3}^1$, and $\mathbf{1}^4\mathbf{3}^2$ species. High

CHDA ratios in the reagent mixture lead to cage molecules mixture incorporating more CHDA-linked vertices such as $\mathbf{1}^{2}\mathbf{3}^{4}$, and $\mathbf{1}^{1}\mathbf{3}^{5}$ and **CC3**. The HPLC patterns are similar to the ones produced by cage-cage and cage-diamine dynamic exchange.

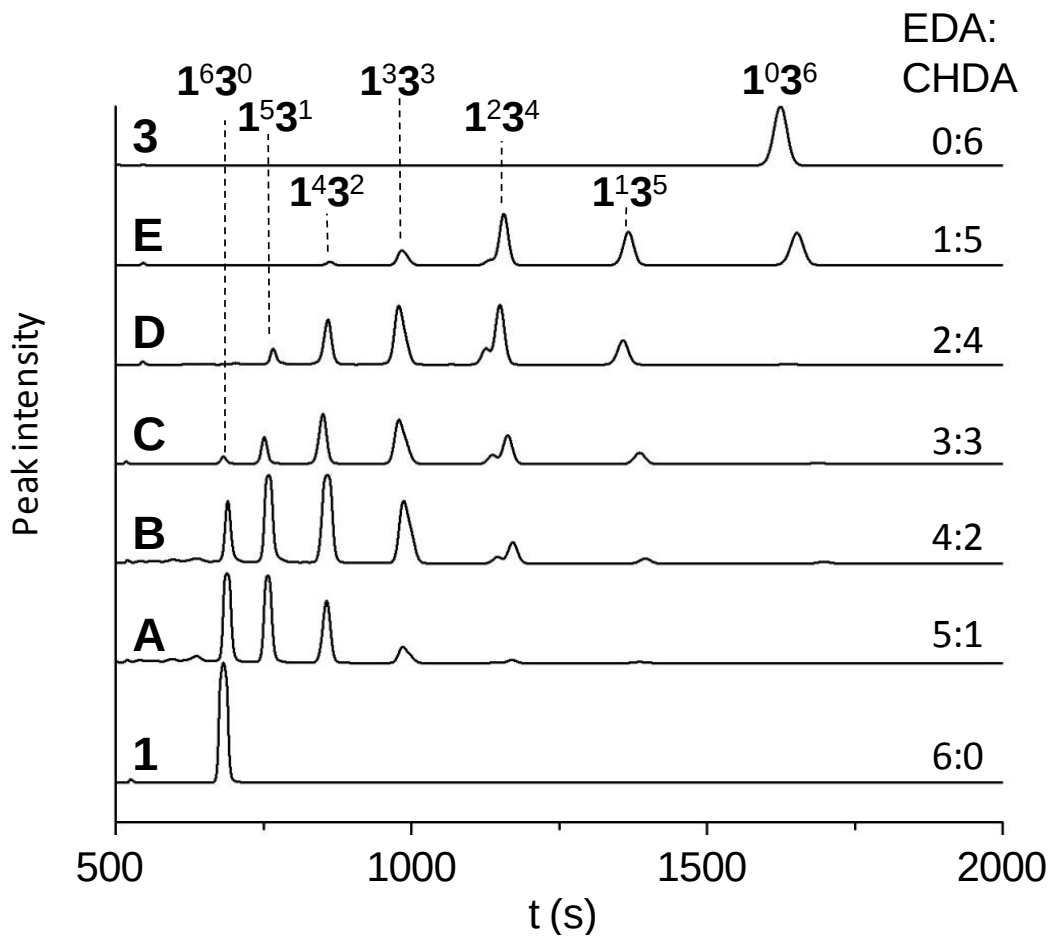

Figure 13. HPLC analysis for cage mixtures formed by co-reactions of TFB with various ratios of EDA and CHDA.

MALDI-TOF data for co-reaction samples **A** – **E** shown in the Figure 14. The calculated mass for cage **1** ($\mathbf{1}^{6}\mathbf{3}^{0}$), $\mathbf{1}^{5}\mathbf{3}^{1}$, $\mathbf{1}^{4}\mathbf{3}^{2}$, $\mathbf{1}^{3}\mathbf{3}^{3}$, $\mathbf{1}^{2}\mathbf{3}^{4}$, $\mathbf{1}^{1}\mathbf{3}^{5}$ and cage **3** ($\mathbf{1}^{0}\mathbf{3}^{6}$): 792, 846, 900, 954, 1008, 1062, and 1116, respectively. For sample **A**-**B**, we found 794, 848, 902, 956, 1010. The doubled masses (1588, 1642, 1696, 1750, and 1804) were assigned to interlocked catenated cages, as observed when the cage reactions are carried out under modified acidified conditions or for prolonged reaction times.[16] The HPLC methodology was not available to determine the interlocked cage molecules as shown in previous sections. For sample **C**-**E**, we found: 848 ($\mathbf{1}^{5}\mathbf{3}^{1}$), 902 ($\mathbf{1}^{4}\mathbf{3}^{2}$), 956

(**1**^{3}**3**^{3}), 1010 (**1**^{2}**3**^{4}), 1064 (**1**^{1}**3**^{5}) and 1119 (**CC3**), respectively. No catenation of cages was observed in these reactions. [16]

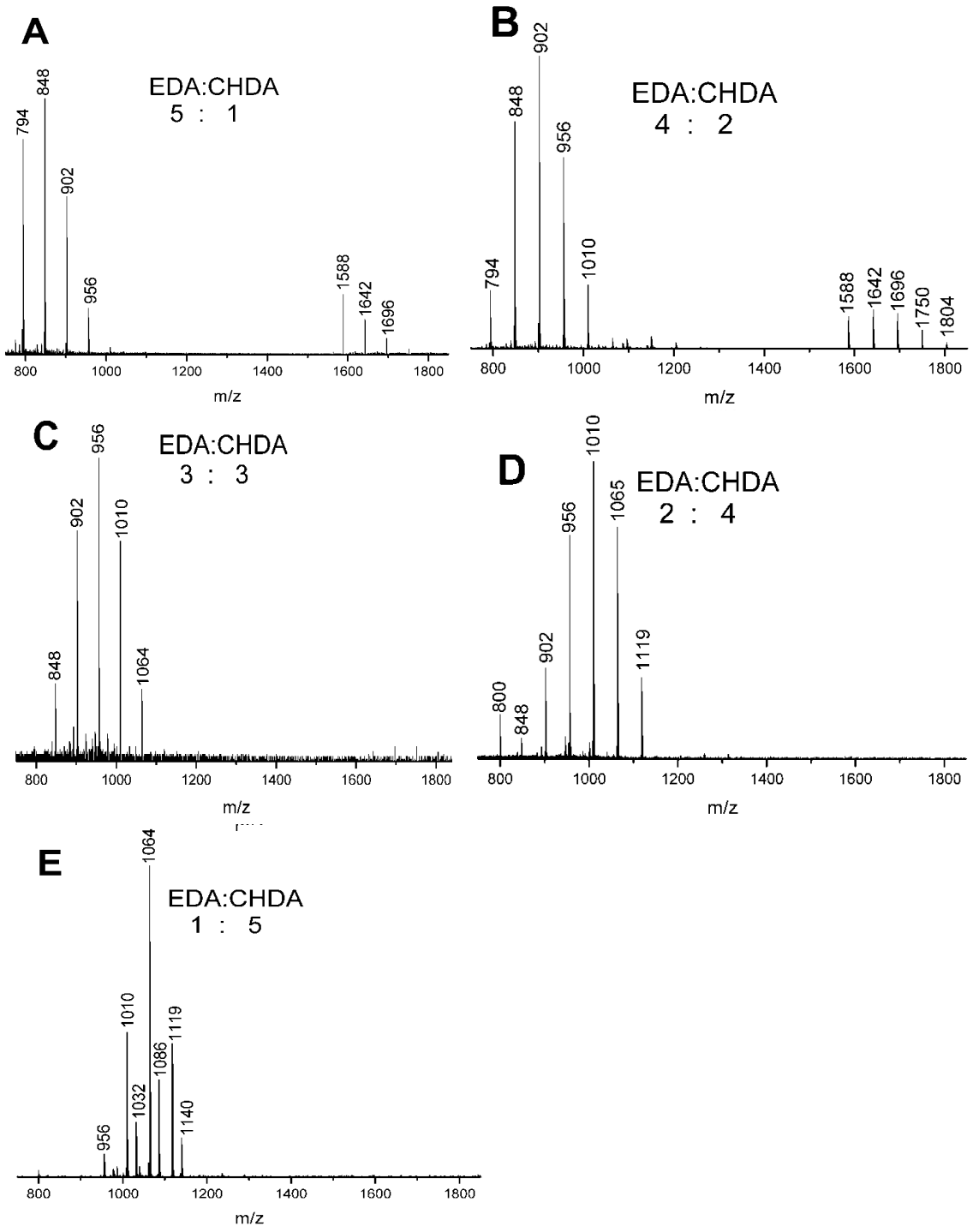

Figure 14. MALDI-TOF data for co-reaction samples **A – E**

The samples were analyzed by ^{1}H NMR. The NMR spectra for co-reaction samples shown in Figure 15 are similar to the sample from cage-cage interchange. The

multiple peaks at 8.18 ppm and 7.90 ppm are assigned to imine protons and protons on the aromatic rings of scrambled cage molecules. The multiple peaks in a range from 1.20 ppm to 1.90 ppm and 3.33 ppm are consistent with protons for CHDA-linked vertices. The peak arising from **CC1** (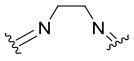) vertices at 4.02 ppm is split into two peaks at 3.87 and 4.14 ppm which indicates the scrambling of the cages. There is also the peak at 4.0 ppm in samples **A-B** due to **CC1** molecule ($\mathbf{1}^6\mathbf{3}^0$). Table 3 summarizes a comparison between the ratios of EDA and CHDA observed in the experimental and the theoretical ratios of EDA and CHDA. The ratios of EDA and CHDA vertices on the scrambled cage molecules by co-reactions are calculated from HPLC and NMR data which demonstrates a good agreement with theoretical reaction ratios of EDA and CHDA.

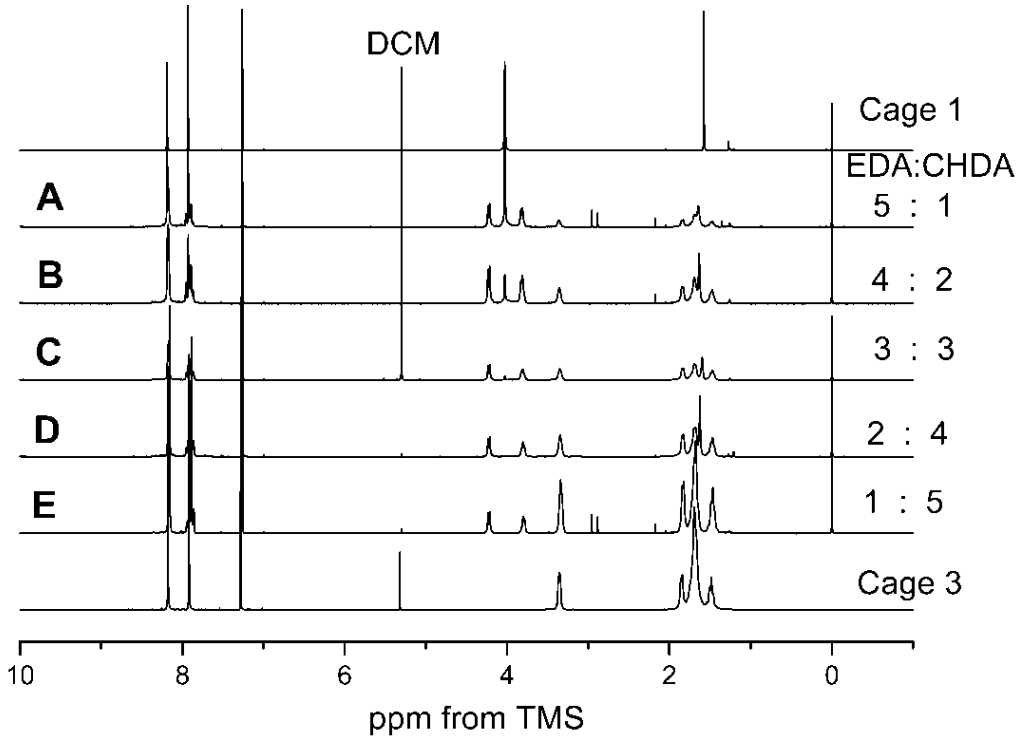

Figure 15. ^{1}H NMR ($CDCl_3$) spectra for cage mixtures produced by direct co-reactions using different ratios of the diamines, EDA: CHDA, sample **A-E**.

Table 3. The ratios of EDA and CHDA-linked vertices from co-reactions with various diamine ratios calculated from HPLC and NRM data.

Reaction ratios EDA:CHDA	HPLC EDA vertices :CHDA vertices	NMR EDA vertices :CHDA vertices
5:1	3.9 : 1	4.4 : 1
4:2	1.8 : 1	2.0 : 1
3:3	1 : 1.1	1 : 1.1
2:4	1 : 1.4	1 : 1.7
1:5	1 : 3.6	1 : 3.4

Analysis of the samples **A**-**E** by powder X-ray diffraction (PXRD) shows no evidence of long-range molecular order with the exception of sample **E** where some phase separation of crystalline phases is evident shown in Figure 16. Therefore, samples **A**-**D** demonstrate amorphous phase in PXRD. In the case of sample **E**, weak diffraction peaks were observed which could be ascribed to phase separation of crystalline **CC3**.

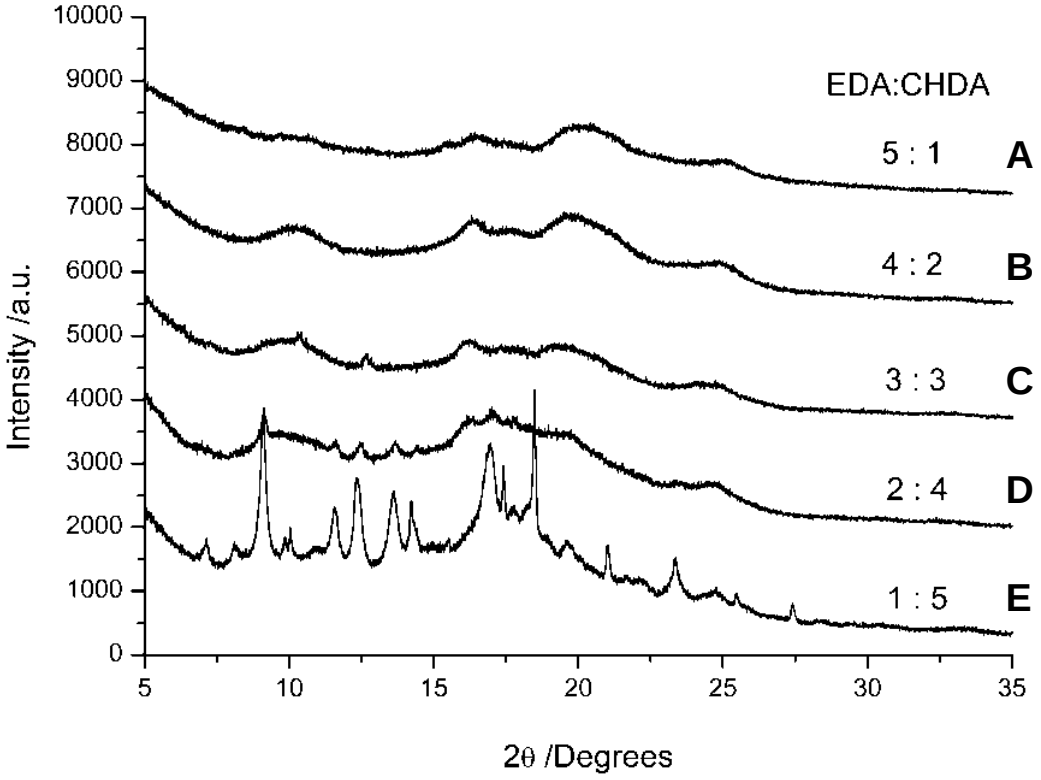

Figure 16. Powder XRD patterns for products obtained from the co-reactions of EDA and CHDA at various EDA: CHDA ratios. The materials show amorphous phases, apart for **E**.

The morphology of materials was determined by scanning electron microscopy (SEM). SEM data were collected by Dr Tom Hasell. SEM analysis confirmed the amorphous products from sample **A**-**D** as the observations by PXRD. SEM images of the products obtained from the co-reaction of EDA and CHDA at a ratio of 1:5 (sample **E**) show that the bulk of the material appeared amorphous, as for samples **A**-**D**. However, localized areas containing regular crystals can also be found in sample **E** as shown in Figure 17(E). A mixture of amorphous and needle-like crystals morphology was observed in SEM which confirmed the phase separation of sample **E**.

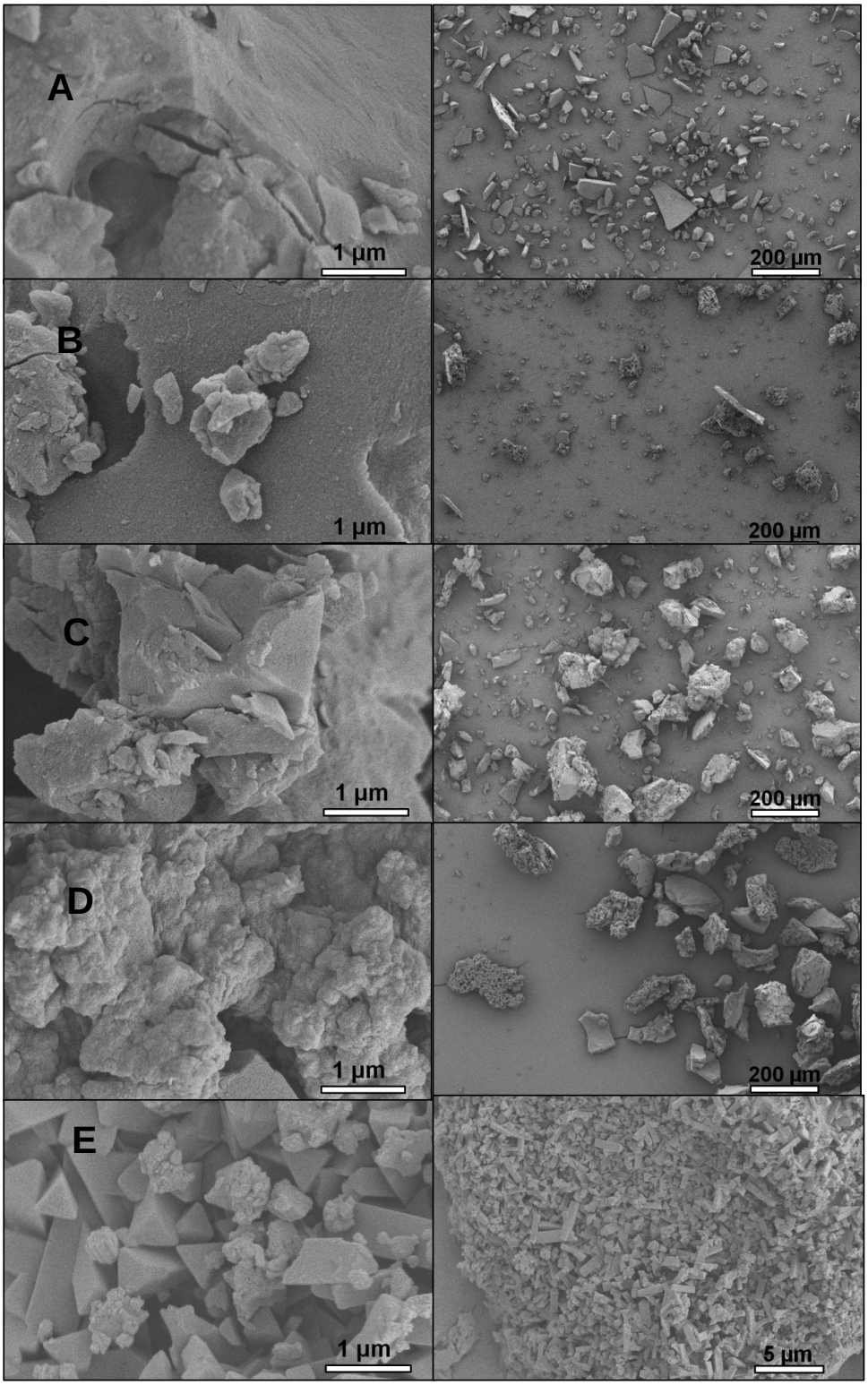

Figure 17. SEM images of the amorphous products obtained from the co-reactions with various reaction ratios of EDA and CHDA. Scale bars for sample **A-D** show 1 µm (left) and 200 µm (right). Scale bars for sample **E** show 1 µm (left) and 5 µm (right).

The co-reaction samples (**C**-**E**) were used for TGA analysis. Thermogravimetric analysis (TGA) was carried out under a nitrogen flow and a heating rate of 5 ºC / min to 500 ºC. All the samples produced by co-reactions were desolvated by heating to 120 °C for 15 hours prior to TGA analysis. The onset of decomposition for the desolvated sample occurs at 350 °C (623 K). The decomposition temperature is very similar to our previously [4+6] porous organic cages.[1] This suggests that amorphization does not significantly reduce the thermal stability of these cage materials.

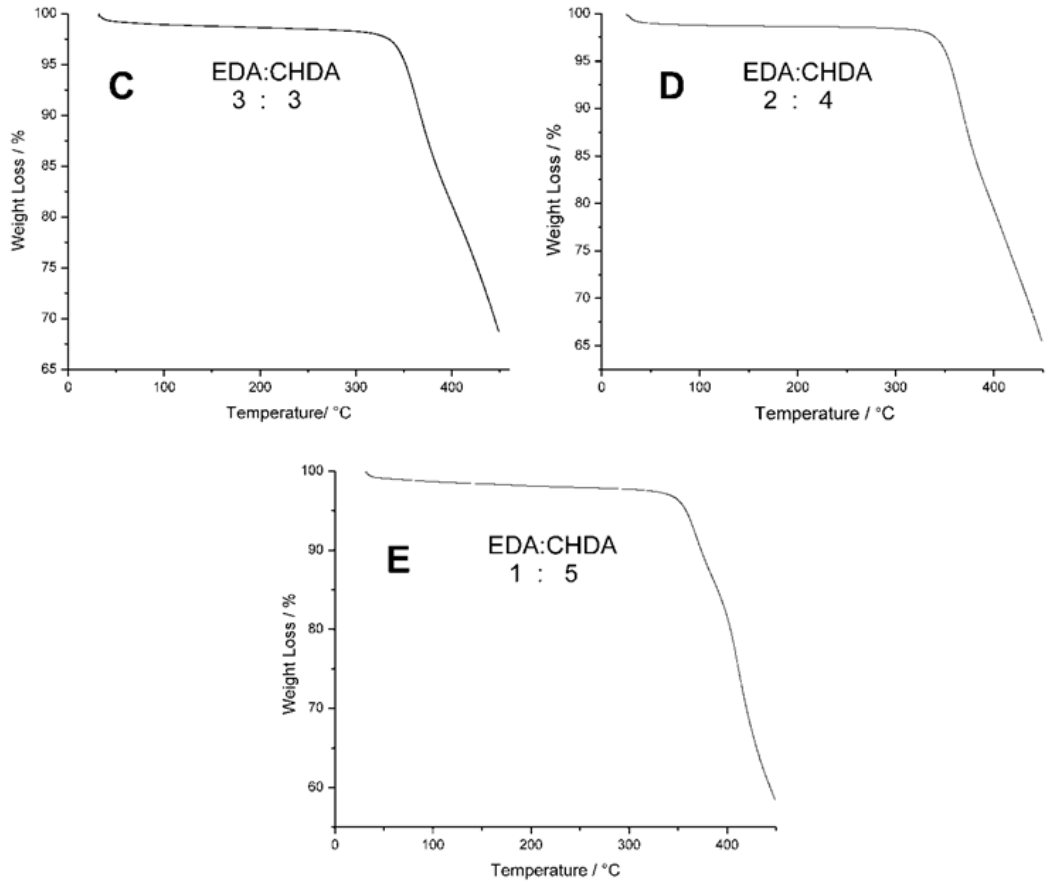

Figure 18. Thermogravimetric (TGA) data for the products obtained from the coreaction of EDA and CHDA with TFB at three different molar ratios (samples **C**, **D** and **E**, respectively).

5.5 Gas sorption analysis for the samples produced by co-reactions and cage-cage interchange

Gas sorption analysis was carried out for all the samples by co-reactions (**A**-**E**) and the sample by cage-cage interchange (**F**). All gas sorption isotherms were measured by Dr James T. A. Jones and Dr Tom Hasell. The materials were heated to 100 ˚C under dynamic vacuum for 12 hours to fully desolvate and degas the samples before gas sorption analysis. N_2 sorption measurements at 77 K show Type I isotherms for all samples (**A**-**F**). The Brunauer-Emmett-Teller (BET) surface areas are obtained from N_2 sorption isotherms at 77 K. The surface areas for samples **C**-**E** are 522, 623 and 704 $m^2\ g^{-1}$, respectively. The BET method is applied in the relative pressure range of 0.01-0.10 to calculate surface areas. Samples **A**-**B** do not demonstrate permanent porosity to N_2. Likewise, the sample **F** by cage-cage interchange shows a surface area of 818 m^2g^{-1} which has exceeded comparable amorphous molecular solids.[6-8, 17] Total N_2 uptakes for sample **C**-**F** are 7.52, 9.21, 10.7 and 11.0 mmol g^{-1} at 1 bar and 77.3 K, respectively.

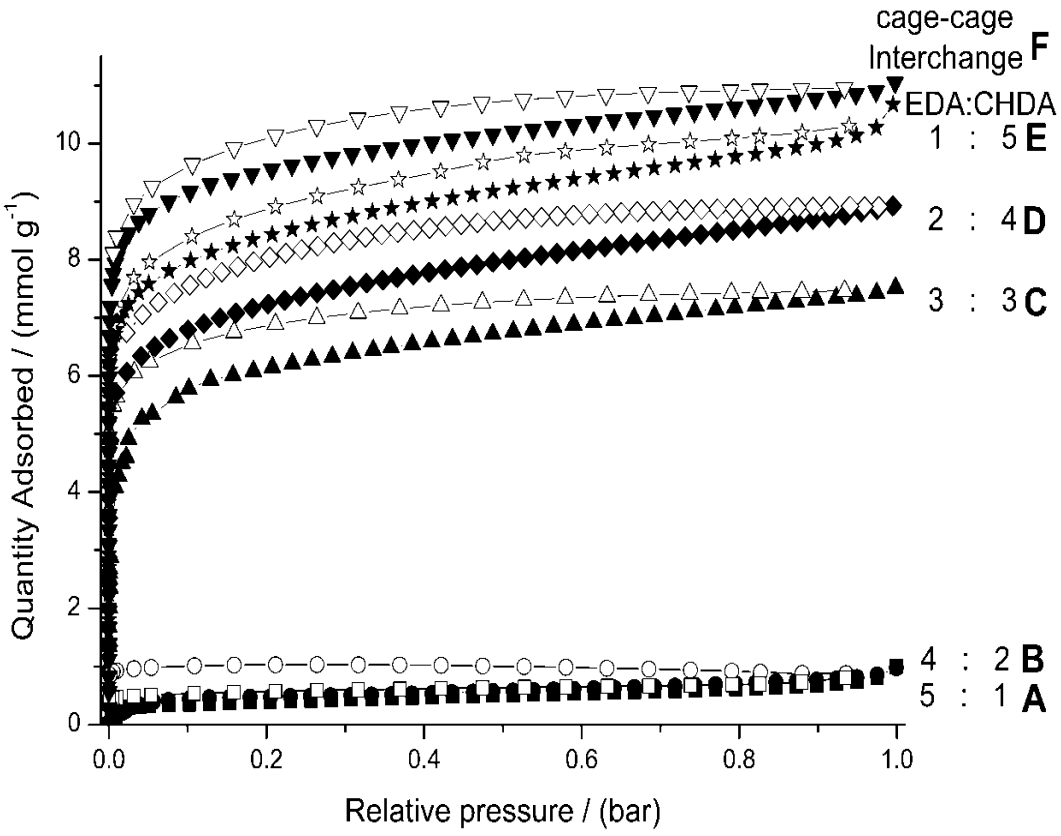

Figure 19. Nitrogen adsorption / desorption isotherms at 77 K for the products obtained from the co-reaction of EDA and CHDA in various ratios (**A**-**E**) and the cage-cage interchange product, **F**. The filled and open symbols represent adsorption and desorption, respectively.

These amorphous materials are not only porous to N_2, but also adsorb H_2 (Figure 20a) and CO_2 (Figure 20b). They adsorb amounts of CO_2 in the range 1.60 -1.93 mmol g^{-1} (7.0-8.7 wt. %) at 293 K ant 1.2 bar. The CO_2 uptake for sample **F** at 273 K and 1.2 bar is 2.84 mmol g^{-1}. The materials are able to adsorb a large amount of H_2, 3.70 – 6.07 mmol g^{-1} for sample **A**-**F** at 77 K and 1.2 bar. The H_2 uptakes for sample **A** and **B** was 4.81 and 3.71 mmol g^{-1}, respectively, although they had a very low N_2 uptake. Therefore, H_2/N_2 gas selectivity was observed for sample **A**-**B**. Table 4 summarizes gas sorption data for all the samples **A**-**F** which include N_2, H_2, CO_2 uptakes, BET , Langmuir surface areas, total and micoporous volumes.

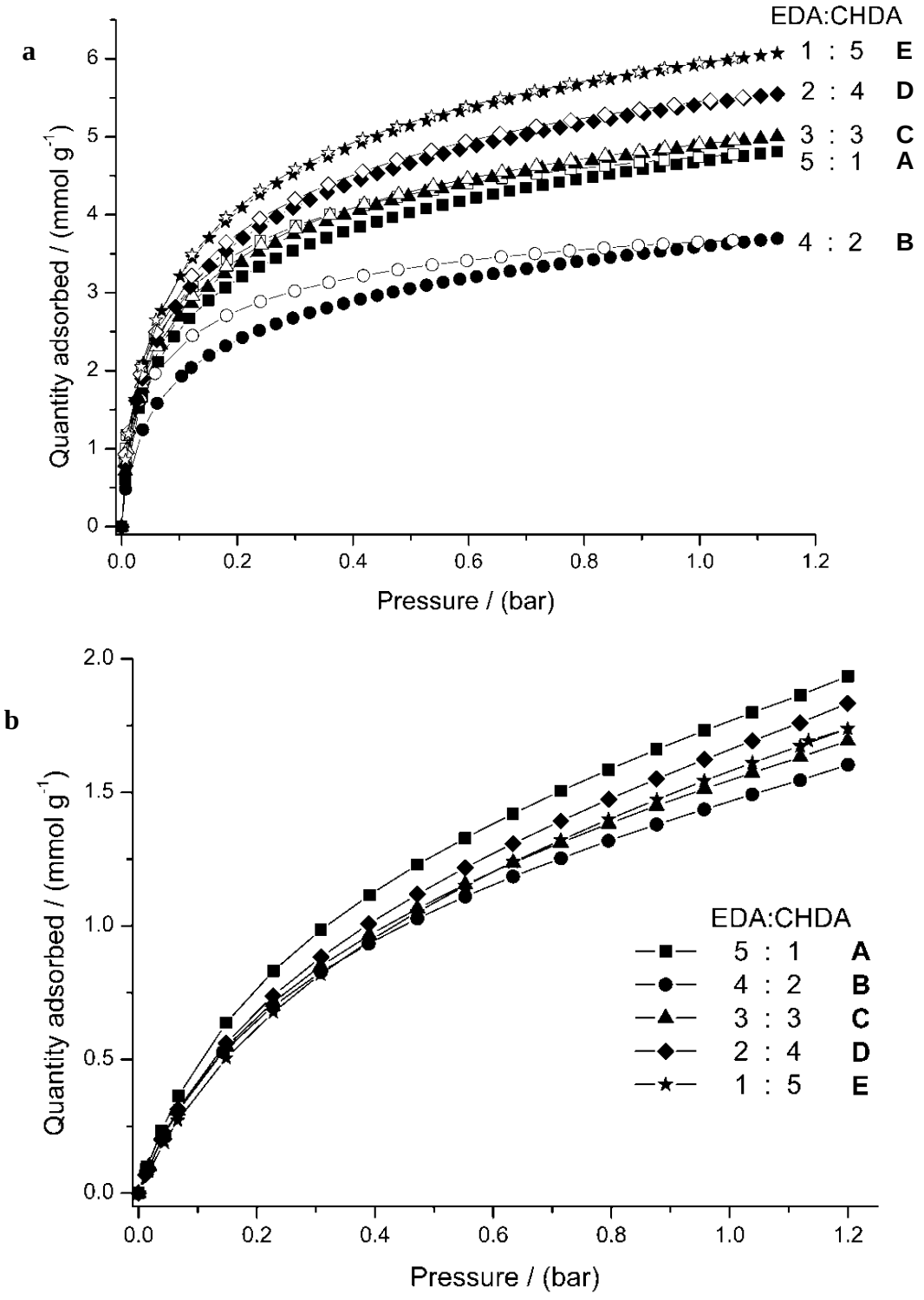

Figure 20. (a) H_2 sorption isotherms at 77 K of the products obtained from the co-reaction of EDA with CHDA in various ratios. Filled and open symbols represent adsorption and desorption, respectively. (b) CO_2 sorption isotherms measured at 293 K for products obtained from the co-reactions at various EDA: CHDA ratios.

Table 4. Gas sorption data for amorphous cage materials.

	EDA:CHD	N_2 (mmol g^{-1}) P/P_0 = 0.998, 77.3 K	CO_2 (mmol g^{-1}) 1 bar, 293 K	H_2 (mmol g^{-1}) 1.2 bar 77.3 K	SA_{LANG} (m^2 g^{-1}) (N_2)	SA_{BET} (m^2 g^{-1}) (N_2)	V_{micro} (cm^3 g^{-1}) N_2, ≤ 20 Å	V_{total} (cm^3 g^{-1}) N_2, P/P_0 = 0.998
A	**5 : 1**	1.00	1.93	4.81	36	32	0.003	0.03
B	**4 : 2**	0.98	1.60	3.70	54	46	0.012	0.03
C	**3 : 3**	7.52	1.69	5.00	592	522	0.185	0.26
D	**2 : 4**	9.21	1.83	5.55	702	623	0.220	0.32
E	**1 : 5**	10.7	1.74	6.07	798	704	0.252	0.37
F	**CC1/CC3** exchange	11.0	2.84*	6.00	896	818	0.299	0.38

* Uptake at 273 K, not 293 K

These amorphous materials consist of a distribution of molecular species which can be controlled by the diamine ratio. The gas sorption properties can be tuned by varying this molecular distribution. The products distribution of sample **A-B** was dominated by **CC1**, $\mathbf{1}^5\mathbf{3}^1$ and $\mathbf{1}^4\mathbf{3}^2$ species with more unfunctional EDA-vertices, resulting in lower porosity materials. In contrast, the samples **C-E** have shown a higher level of porosity because the products comprise of more $\mathbf{1}^2\mathbf{3}^4$, $\mathbf{1}^1\mathbf{3}^5$ and **CC3** species with more bulky CHDA-vertices. It was observed that the gas selectivity (H_2/N_2) is a strong function of the CHDA: EDA ratio for co-reaction samples. As shown in Figure 21(a), materials with low CHDA ratios (**A** and **B**) adsorb much more H_2 than N_2 at a comparable condition. Sample **A** (a ratio of EDA and CHDA at 5 : 1)

in particular adsorbs around five times as much H_2 as N_2. However, materials with high CHDA rations do not display H_2/N_2 gas selectivity. Sample **E** (a ratio of EDA and CHDA at 1 : 5) is porous to both H_2 and N_2.

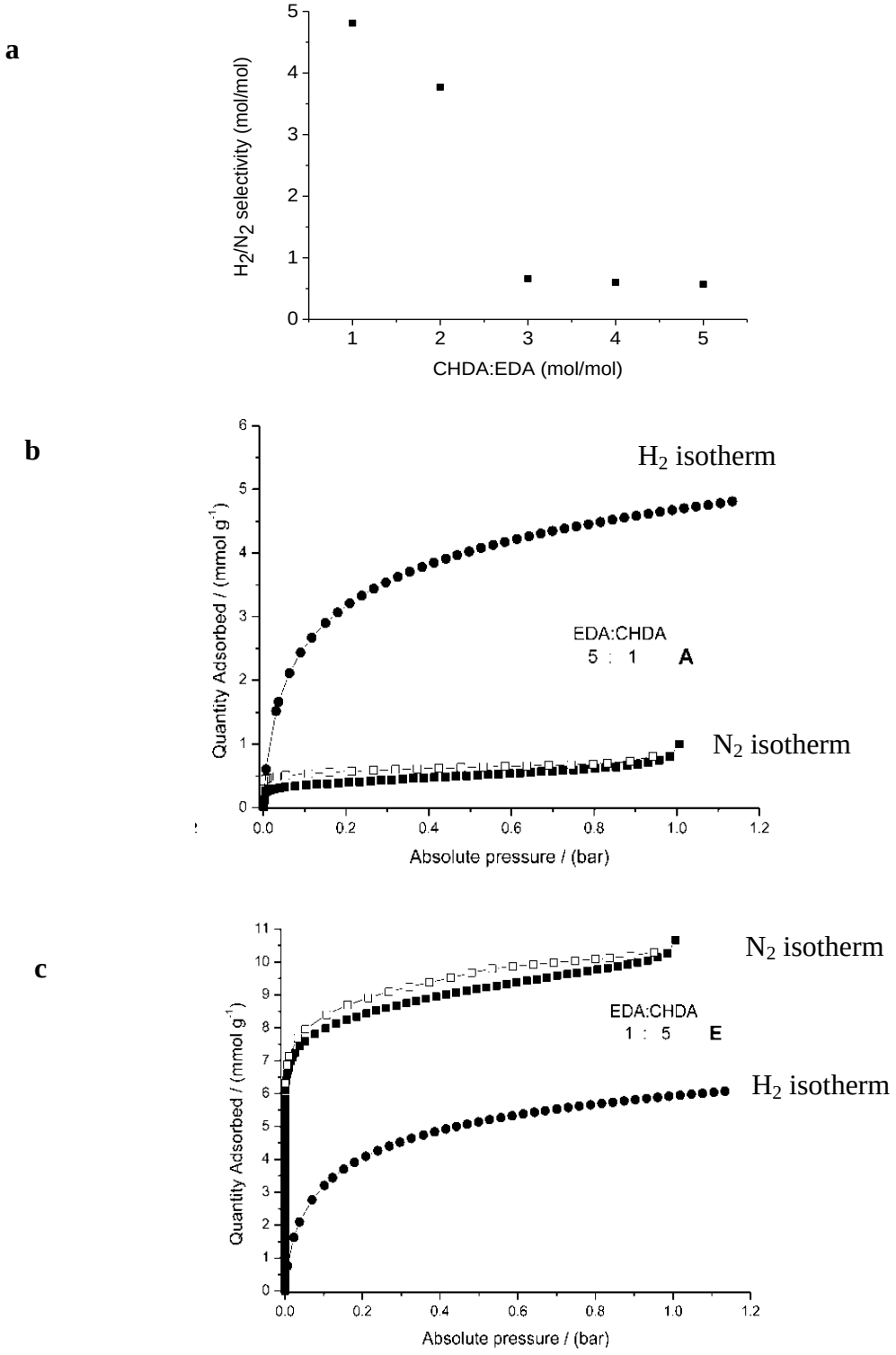

Figure 21. (a) Gas selectivity data for amorphous cage mixtures prepared by

co-reactions, sample **A-E**. (b) H_2 (black circles) and N_2 (black squares) gas sorption isotherms for sample **A**. Sample **A** (CHDA: EDA=1:5) exhibits the highest H_2 selectivity over N_2. (c) H_2 (black circles) and N_2 (black squares) gas sorption isotherms for sample **E**. Sample **E** (CHDA: EDA=5:1) are porous to both H_2 and N_2

Non local density functional theory (NL-DFT) pore size distribution curves for sample **A-E**, crystalline **CC1** and **CC3** are obtained from the N_2 adsorption isotherm at 77 K in Figure 22. For crystalline **CC3**, micropores are shown at 7 Å and 12 Å, respectively. These amorphous materials (samples **C-E**) exhibit a larger pore size than crystalline **CC3**. They display pore sizes of 10 Å and 20 Å. The absence of significant peaks for samples **A-B** and crystalline **CC1** is consistent with their low N_2 uptakes.

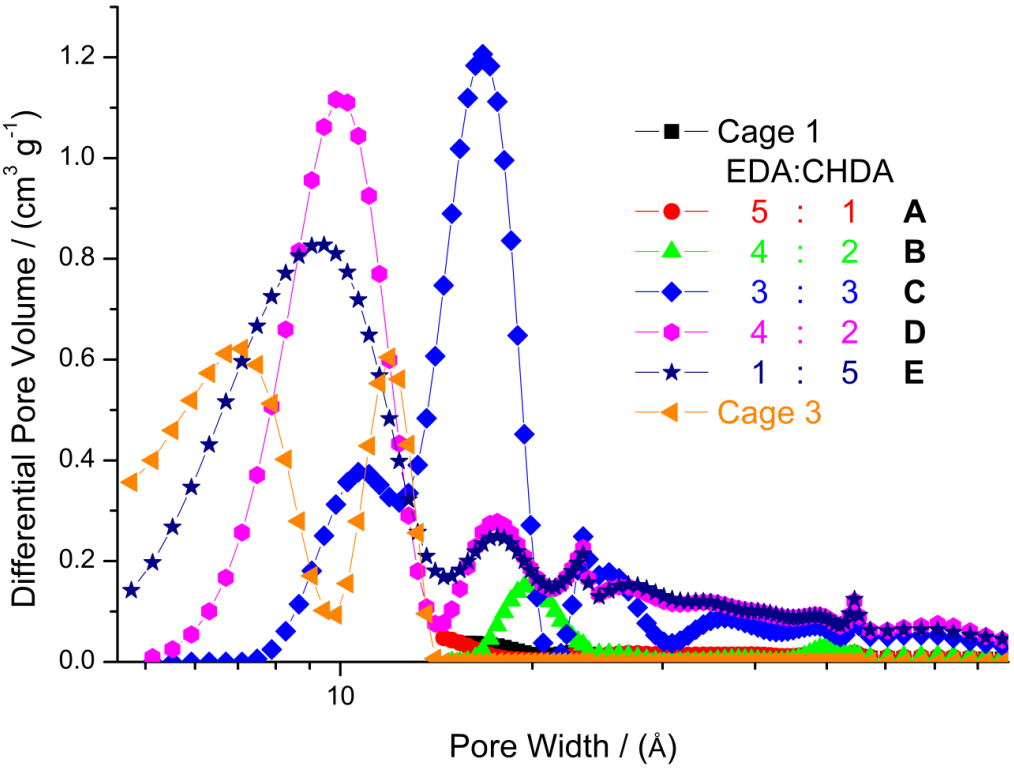

Figure 22. Pore size distributions as calculated by application of non-local density functional theory (NL-DFT) analysis to N_2 adsorption isotherms obtained at 77 K.

5.6 The effect of solvent on co-reaction

A series of reactions were carried out to investigate the effect of solvent on porosity.

Sample **D** (EDA : CHDA=2:4) was synthesized in a range of solvents. Dichloromethane (DCM), methanol (MeOH), a mixture of DCM and MeOH and chloroform ($CHCl_3$) were chosen. The product distribution of the reactions in various solvents is shown in Figure 23. The solvents do not have significant effect on the product distribution.

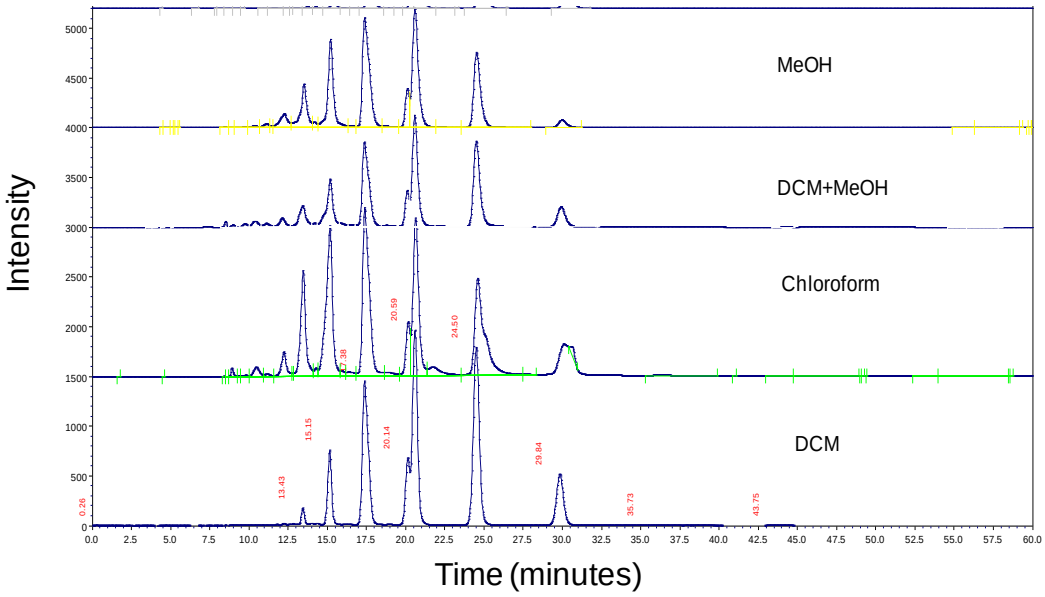

Figure 23. The product distribution obtained by co-reaction (sample **D**) with various solvents.

The N_2 sorption measurements were carried out for these samples. As shown in Figure 24, the porosity is not strongly sensitive to the solvent used in the synthesis. The solvent effect is relatively modest. The porosity is slightly enhanced by the addition of methanol to dichloromethane.

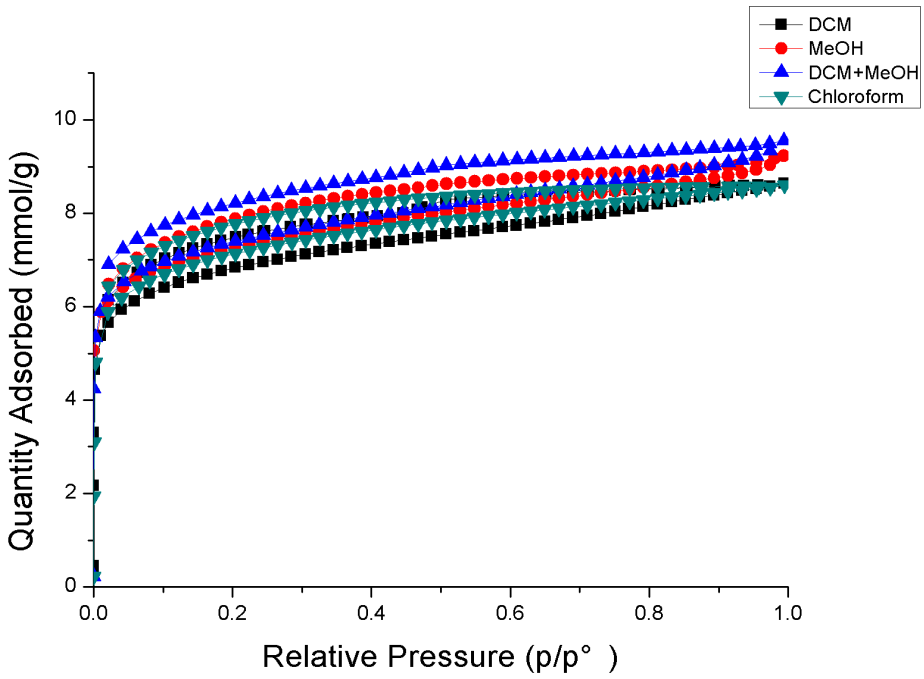

Figure 24. N_2 sorption /desorption isotherms for samples produced with EDA : CHDA=2:4 in various solvents.

Furthermore, gas sorption analysis was performed for two samples where sample **D** was redissolved in either 1:1 DCM/MeOH or DCM/EtOH. The products were isolated by evaporating solvents. The N_2 isotherms are shown in Figure 25. Enhanced porosity was observed from isotherms for these two samples, which is consistent with the observation for the sample synthesized directly from a DCM/MeOH (see Figure 24). This indicates that the solvent used to process these molecules can influence the resultant molecular porosity to some degree.

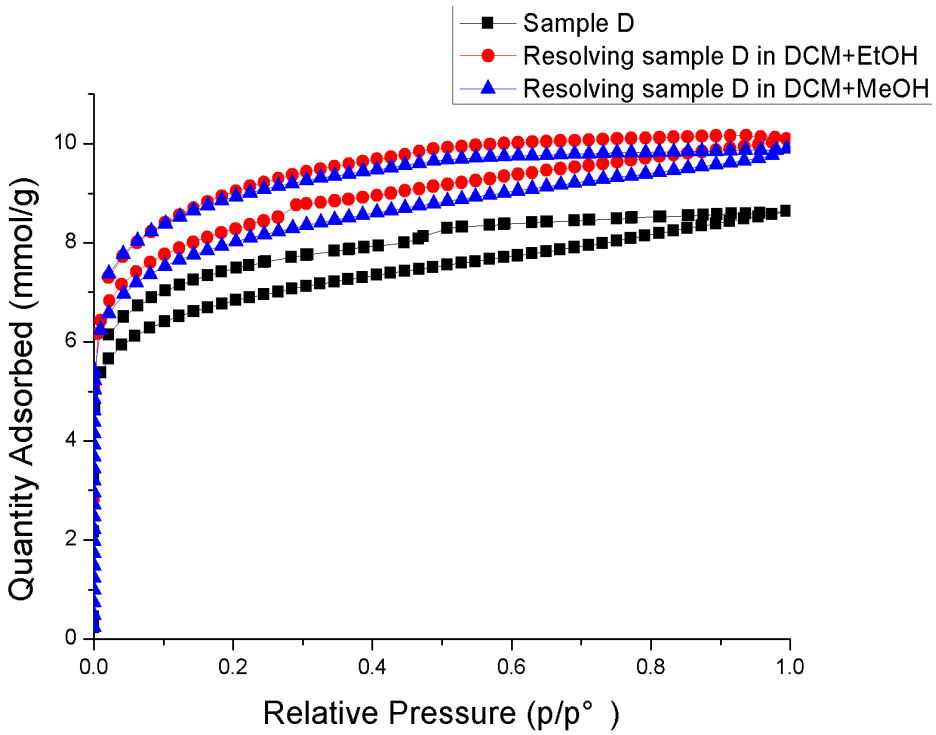

Figure 25. N_2 sorption /desorption isotherms for sample **D** as synthesized in dichloromethane (DCM) as well as two samples of **D** which were redissolved in 1:1 DCM/alcohol mixtures and then isolated by solvent evaporation.

5.7 Doping amorphous scrambled cages into filter paper

The objective of this section was to introduce microporosity into macroporous filter paper and enhance its surface area. The potential application is to separate small molecules. The experimental procedure was as follows: Sample **D** produced by the co-reaction was used for the filter paper doping. Sample **D** showed type I gas sorption isotherm and SA_{BET} = 623 m^2 g^{-1} (see Figure 19 above). Sample **D** (80 mg) was dissolved in chloroform (5 mL). The filter paper (93.2 mg) was immersed in sample **D** solution. The filter paper was obtained from the Fisher Scientific with particle retention > 20 μm. After 3 days, the filter paper was vacuumed dried overnight before analysis. The weight of filter paper after doping with amorphous scrambled cage solids was 103.8 mg. The weight increased by 11.4 %. Before doping, SA_{BET} of pure filter paper was 3 m^2 g^{-1}. After doping with amorphous scrambling cage solids, filter paper showed type I gas sorption isotherm and SA_{BET} of filter paper is 161 m^2 g^{-1} compared to 623 m^2 g^{-1} for sample **D** on its own. The gas sorption isotherms for filter paper before and after doping were shown in Figure 26. The filter paper becomes porous after doping with amorphous cages.

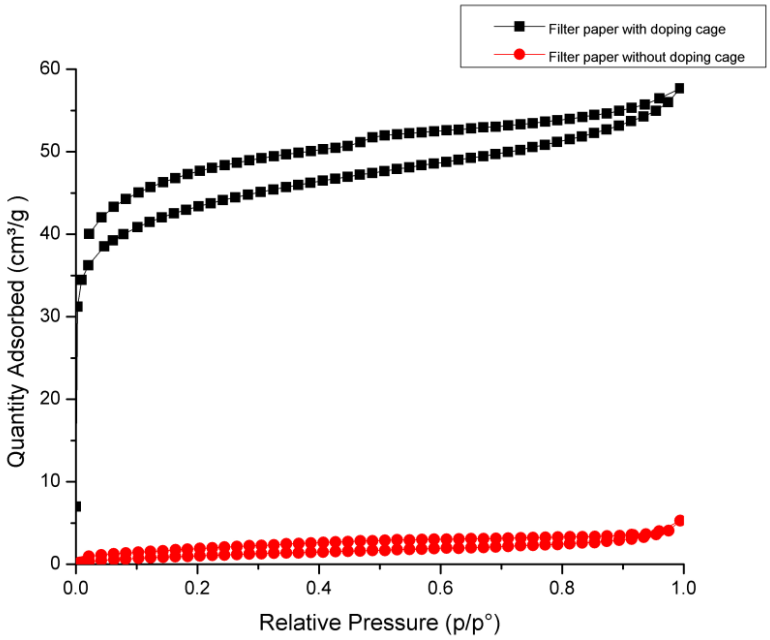

Figure 26. N_2 sorption isotherms for filter paper without doping amorphous cages

(red) and filter paper with doping amorphous cages (black).

SEM images showed a significant change in fiber morphology after doping with amorphous cages in Figure 27. As observed by SEM, amorphous cage materials were localized between fibers. The preliminary results show that the molecular pores can be imbibed into the filter paper, in order to introduce a degree of microporosity.

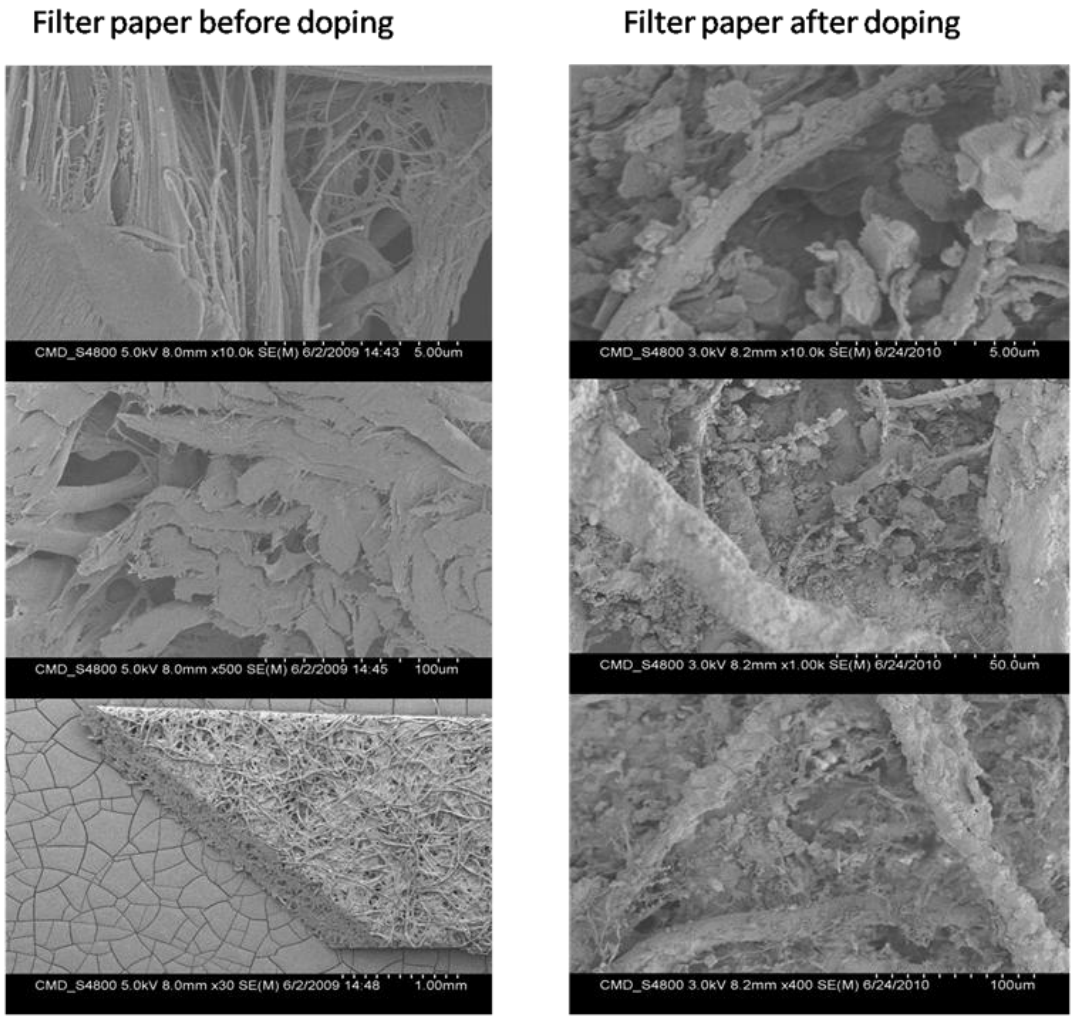

Figure 27. SEM images for filter paper before and after doping with amorphous cages. Scale bars for the sample before doping are 5μm, 100 μm and 1 mm, respectively. Scale bars for the sample after doping are 5μm, 50 μm and 100 μm, respectively. SEM images were determined by Dr Tom Hasell.

5.8 Isolating asymmetrical cage molecules

Figure 28 shows a HPLC products distribution with a high resolution. Two separated peaks for each of $\mathbf{1}^2\mathbf{3}^4$, $\mathbf{1}^3\mathbf{3}^3$ and $\mathbf{1}^4\mathbf{3}^2$ species were observed which suggested that the possible isomeric forms exist for each species. The HPLC trace shows splitting of peaks for the species $\mathbf{1}^4\mathbf{3}^2$, $\mathbf{1}^3\mathbf{3}^3$ and $\mathbf{1}^2\mathbf{3}^4$ which can be ascribed to *cis*/*trans* ($\mathbf{1}^4\mathbf{3}^2$ and $\mathbf{1}^2\mathbf{3}^4$) and *mer*/*fac* ($\mathbf{1}^3\mathbf{3}^3$) isomers. HPLC-MS and MALDI-TOF experiments confirm the molecular mass of these species but it was not possible to assign peaks to specific isomers.

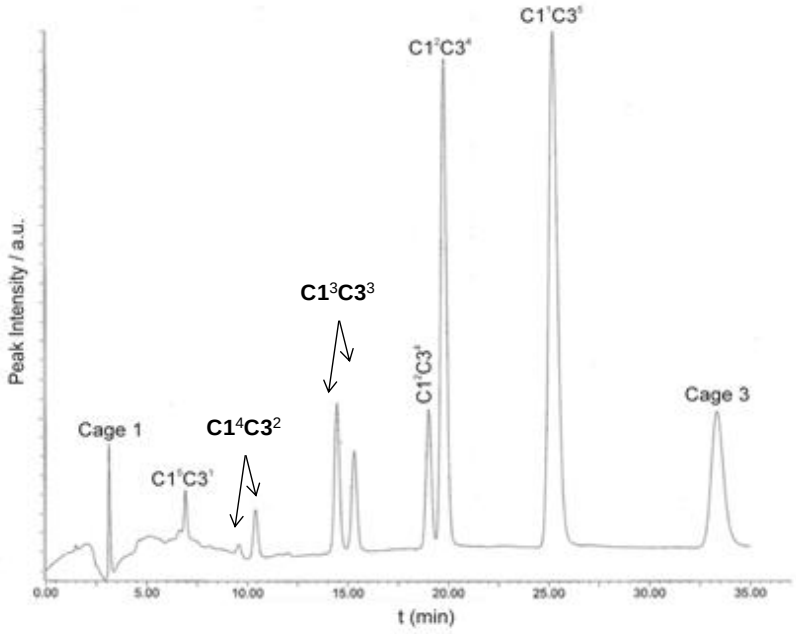

Figure 28. HPLC distribution of cage products produced by dynamic exchange reaction between **CC1** and CHDA.

These asymmetrical cage molecules could be isolated by preparative HPLC scale as shown in Figure 29 for each cage molecule. The isolation of the asymmetrical cages was done by a company, Peakdale Molecular. These cage molecules were purified by HPLC using Hypersil GOLD phenyl, 150 x 4.6 mm, 5 µm linked to Hypersil GOLD 150 x 4.6 mm, 5 µm columns. The mobile phase used for molecular separation was ethanediol /MeOH, 5/95 (pre-mixed) at a flow rate of 0.5 mL/min. The materials

were obtained by rapidly precipitating cage molecules from solution. The purpose of quickly evaporating solvents was to avoid dynamic exchange occurred for these asymmetrical cage molecules. PXRD confirmed that these asymmetrical cage materials exhibited amorphous phase in the solid state in Figure 30.

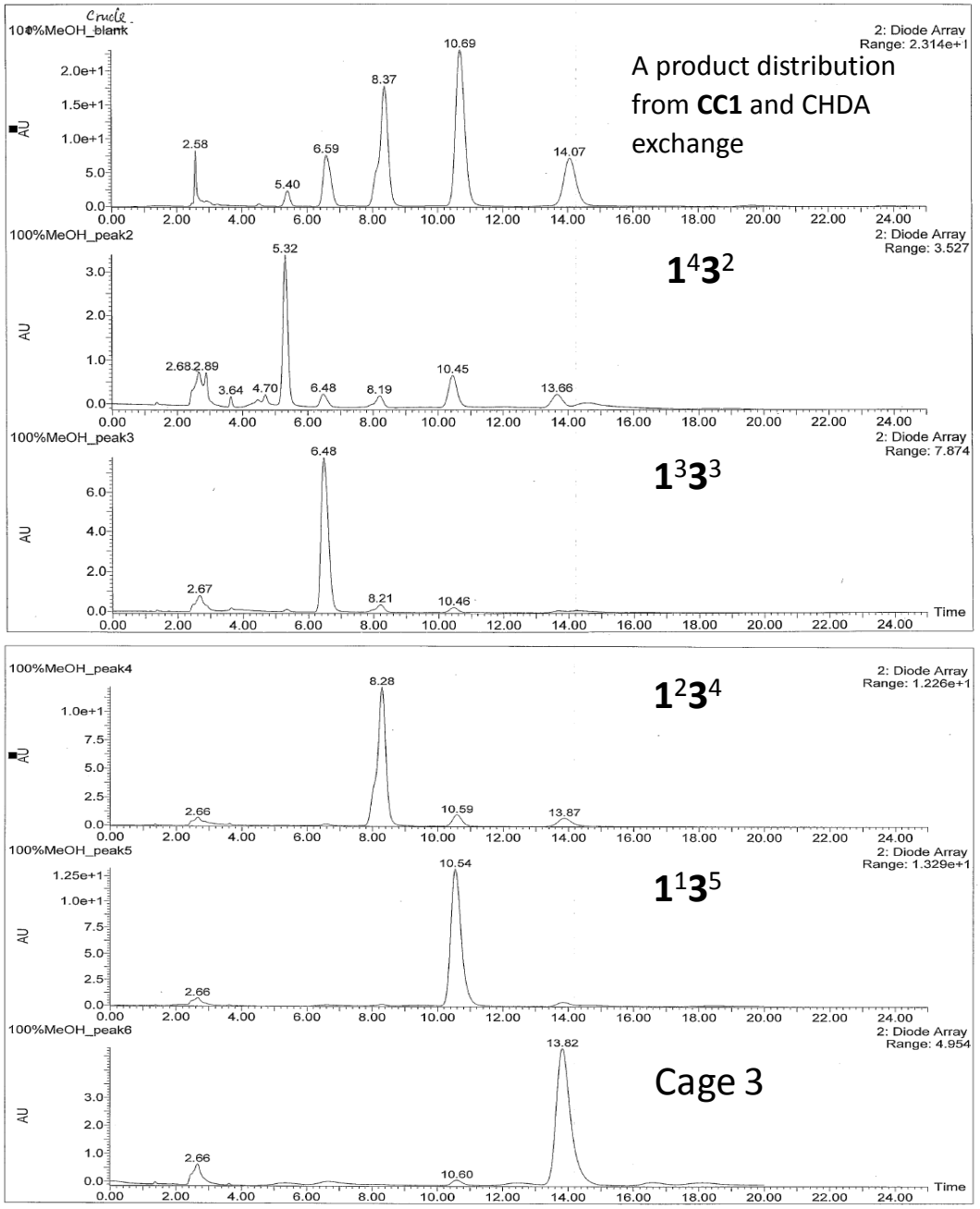

Figure 29. HPLC analysis for each cage molecule.

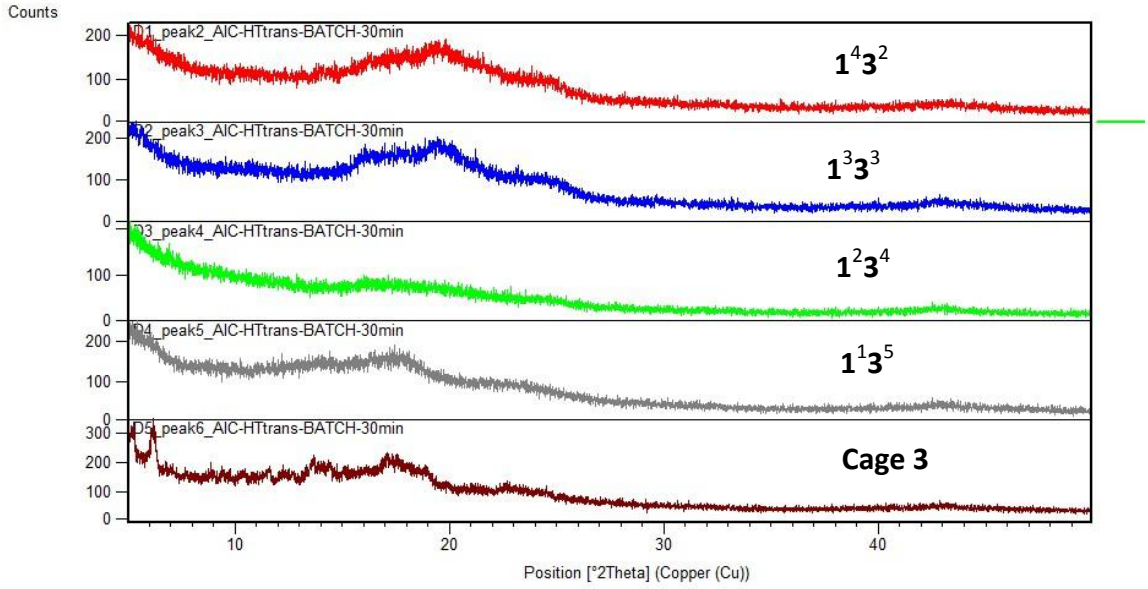

Figure 30. PXRD patterns for each cage molecule.

Gas sorption measurements were carried out for amorphous **CC3**, $\mathbf{1}^1\mathbf{3}^5$, $\mathbf{1}^2\mathbf{3}^4$ and amorphous **CC1** materials. The amorphous $\mathbf{1}^1\mathbf{3}^5$ and $\mathbf{1}^2\mathbf{3}^4$ cages were obtained by the method above. The amorphous **CC1** and amorphous **CC3** were performed by the freeze-drying method reported in our group.[18] The N_2 adsorption/desorption isotherms were shown in Figure 31 and were type I. The BET surface areas calculated for amorphous **CC3**, $\mathbf{1}^1\mathbf{3}^5$, $\mathbf{1}^2\mathbf{3}^4$ and amorphous **CC1** were 860, 677, 616 and 5 $m^2 g^{-1}$, respectively. The porosity in these amorphous materials was tuned by the functional groups on the vertices of cage molecules. Gas uptake for amorphous **CC3** exceeded crystalline **CC3**.[18]

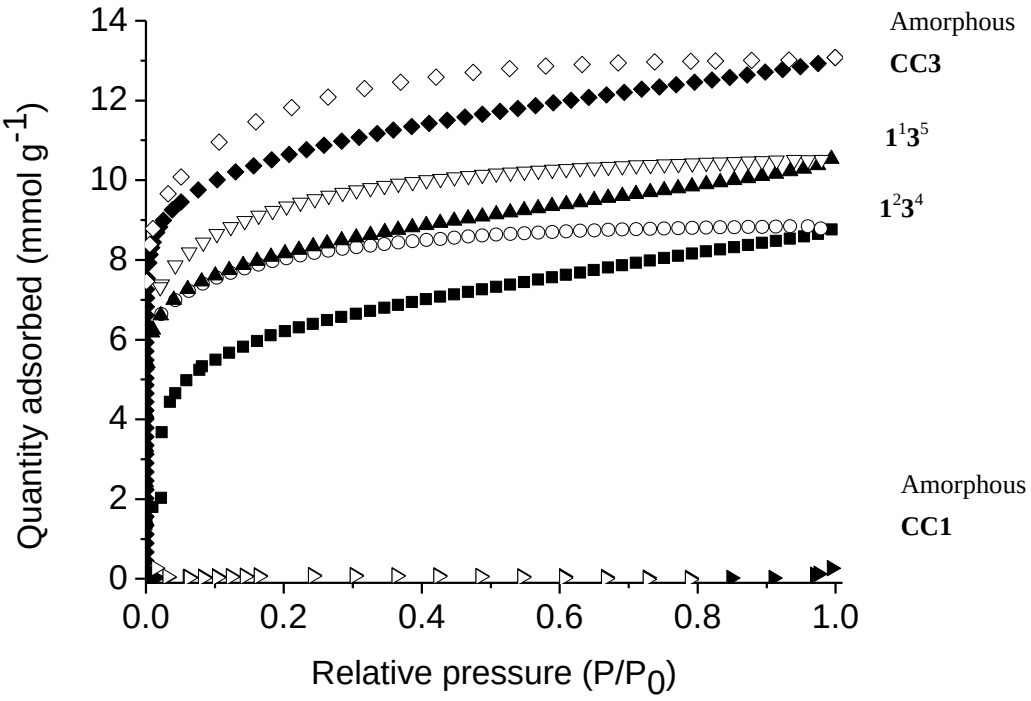

Figure 31. The N_2 adsorption/desorption isotherms for amorphous **CC3**, **1**[1]**3**[5], **1**[2]**3**[4] and amorphous **CC1** materials.

5.9 Simulation for amorphous scrambled cages

Molecular simulation was used to study the enhanced gas sorption properties of these amorphous scrambled cages materials. A model for the co-reaction of EDA and CHDA at a reaction ratio of 2: 4 (sample **D**) was constructed using Accelrys Materials Studio 5.0. The model was built in two steps. Firstly, a periodic simulation cell was constructed containing 33 cage molecules chosen to represent the numerical distribution of species observed by HPLC for sample **D**. The 33 cage molecules ($1 \times \mathbf{1}^5\mathbf{3}^1$, $5 \times \mathbf{1}^4\mathbf{3}^2$, $9 \times \mathbf{1}^3\mathbf{3}^3$, $12 \times \mathbf{1}^2\mathbf{3}^4$, $5 \times \mathbf{1}^1\mathbf{3}^5$ and $1 \times \mathbf{1}^0\mathbf{3}^6$) were treated as rigid bodies and loaded into an amorphous cell at a low density of 0.3 g cm^{-3} using the Universal Forcefield (UFF).[19] The initial model was then geometry optimized under external pressure using the Forcite module and the COMPASS force field [20]. The external pressure was continually ramped up until the simulation density matched the 'target' density. Finally the model was then totally relaxed using the geometry optimization and the simulation density remained close to the experimental 'target' density. The target bulk density for the model is 0.716 g cm^{-3} which can be gained from the equation $W_o = 1/\rho_{app}\text{-}1/\rho_{tr}$.[21] W_o is the micropore volume (0.212 $cm^3\,g^{-1}$ for sample **D**), the absolute density, ρ_{tr}, was measured by helium pycnometry, 0.844 g cm^{-3}. Therefore, the bulk density was calculated to be 0.716 g cm^{-3}. The simulated bulk density for the model was 0.766 g cm^{-3}, which is close to the measured experimental 'target' density. A solvent accessible surface area of 577 $m^2\,g^{-1}$ was calculated using a probe radius of N_2, 1.82 Å, compared with experimental surface area, SA_{BET}, for sample **D** of 623 m^2g^{-1}. Interconnected pore channels were identified in the model in terms of the inherent pores in the cage molecules, and the ineffective packing that results from the distribution of molecular shapes. The Connolly solvent volume is fully connected and shown in Figure 32(b). In addition, the contribution of extrinsic pore volume was estimated from this atomistic model, although it is difficult to probe it experimentally. In the model of sample **D**, 80 % of the total free volume in the simulation cells arises from the voids of inefficient packing, compared with 20 % calculated for the internal cage volume. However, in the crystalline **CC3**,

37.6 % of the pore volume can be attributed to voids between cages and 63.4 % to the internal cage voids. As a result, the porosity in amorphous scrambled cages (sample **D**) results predominantly from the large increase inefficient packing. We suggest that the molecular packing in the amorphous scramble cage has analogies with computer game 'Tetris' showed in Figure 32(c).

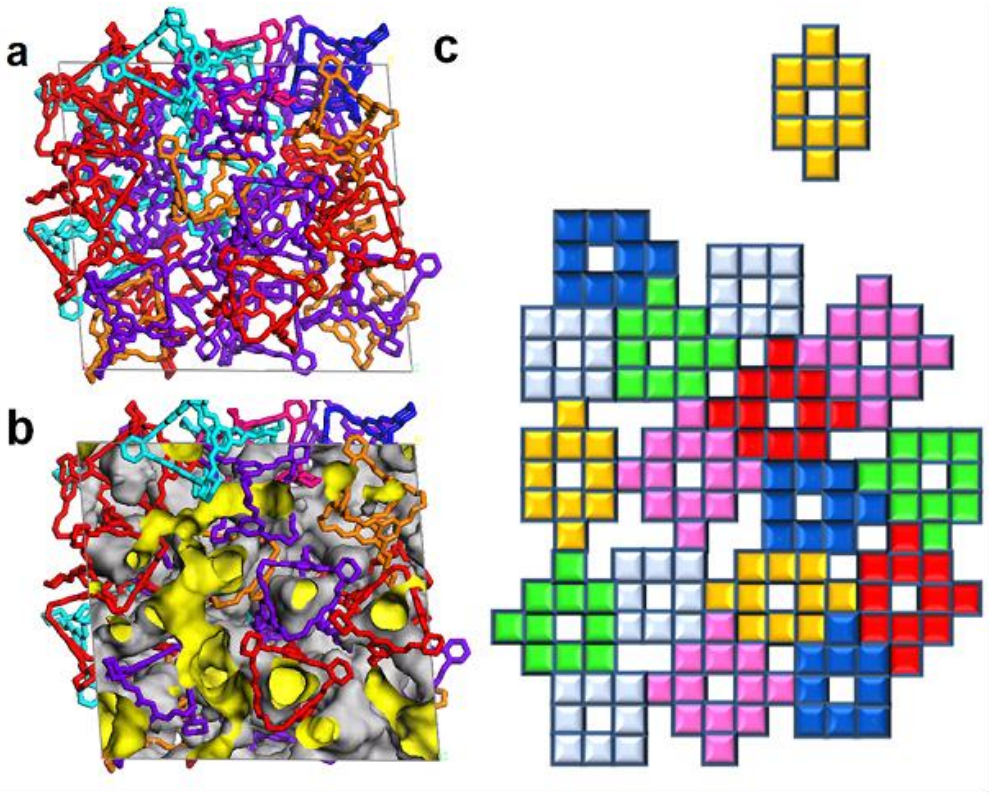

Figure 32. (a) Atomistic simulation for amorphous sample **D** (EDA:CHDA = 2:4). An amorphous cell was constructed containing 33 cage molecules ($1 \times 1^5 3^1$, $5 \times 1^4 3^2$, $9 \times 1^3 3^3$, $12 \times 1^2 3^4$, $5 \times 1^1 3^5$, $1 \times 1^0 3^6$) chosen to represent the molecular distribution as calculated from HPLC peak areas. The Connolly surface (b) is also shown using a probe radius of 1.82 Å. (c) The molecular packing in this system has analogies with computer games such as 'Tetris'.

Simulation of N_2 sorption in amorphous sample **D** was carried out using Materials Studio 5.0 Sorption locator module in order to identify N_2 sorption location. N_2

molecules locations were described as follows shown in Figure 33: (1) green – within the solvent accessible surface or 'accessible zone'. A solvent accessible surface was calculated using a kinetic radius of N_2, 1.82 Å, shown in yellow in Figure 33, (2) orange- voids immediately adjacent to the accessible zone, (3) red-isolated void volume which is 'inaccessible zone'. The simulation showed the uptake for the accessible zone is 193 N_2 molecules per simulation cell which is close to the experimental uptake at P/P_0 = 0.1(202 N_2 molecules) from the isotherm (see Figure 19 above). 321 N_2 molecules per simulation cell were observed as total gas uptake which slightly overestimated the experimental gas sorption, even at P/P_0 = 0.1(288 N_2 molecules) in Figure 19. This might attribute to inaccessible volume included in the simulation. Consequently, this model is consistent with the material and is representative of it.

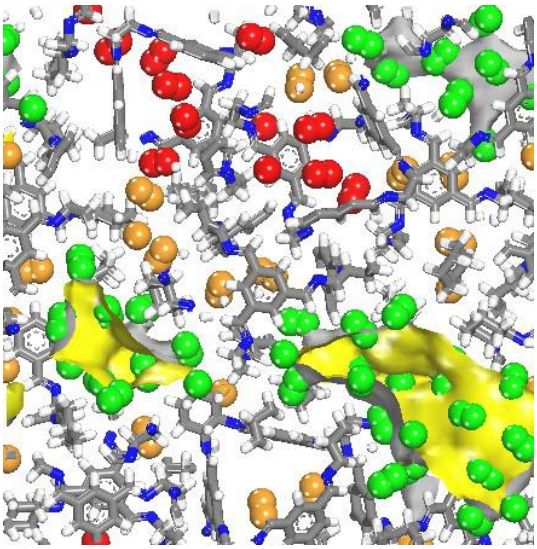

Total N_2 uptake per unit cell	No. of N_2 molecules in accessible zone (green atoms)	No. of N_2 molecules in partially accessible zone(orange atoms)	No. of N_2 molecules excluding formally inaccessible zone (green + orange atoms)	No. of N_2 molecules in formally inaccessible zone (red atoms)	Experimental N_2 uptake , expressed in units of molecules per simulation cell (P/P_0 = 0.1-0.99)
321	193	80	273	48	202--288

Figure 33. Simulated physisorbed N_2 molecules location for amorphous sample **D**.

5.10 Conclusions

We have demonstrated asymmetrical and multifunctional cage molecules which are synthesized by three novel methods. They are based on cage-diamine exchange, cage-cage interchange, and direct co-reaction of TFB with a mixture of both EDA and CHDA, respectively. The cage molecules were observed to incorporate both EDA- and CHDA- linked vertices in a single cage molecule. A distribution of molecule species packs together ineffectively, and creates permanent porosity in the amorphous solid. The gas sorption properties in samples **A**-**E** can be controlled as a function of EDA : CHDA reaction ratio, and H_2/N_2 gas selectivity behavior can be tuned. The amorphous cage materials with a high EDA ratio can adsorb much more H_2 than N_2. However, the materials with a low EDA ratio are highly porous to both H_2 and N_2. The BET surface area of one of these amorphous scrambled cage materials is up to 818 $m^2 g^{-1}$ which has exceeded crystalline porous cage molecules and other porous amorphous molecules. A simulation model is built to rationalize the porosity of amorphous cage molecules. Molecular simulations suggest that the enhanced porosity in these amorphous scrambled solids result predominantly from extrinsic porosity inter cage voids. The asymmetrical cage molecules have been isolated and performed for gas sorption analysis. N_2 uptakes for these materials are as a function of cage vertex functionality. Amorphous **CC3** with six bulky and cyclohexyl vertices exhibits a high N_2 uptake. However, the porosity of asymmetrical cage molecules decreases with less cyclohexyl groups. Amorphous **CC1** without cyclohexyl vertices is non-porous to N_2. The preliminary results show that the amorphous cage molecules can be doped into the filter paper to introduce a degree of microporosity.

The future work could focus on enhancing porosity by introducing more bulky functionality of cage vertices, such biphenyl or naphthyl groups. It would also be interesting to combine different molecule topologies ([2+3], [4+6] or [8+12] cage) in a single amorphous solid. Molecular simulations could be used to rationalize gas selectivity in these amorphous scrambled systems.

5.11 Chapter acknowledgements

In this chapter, I would like to thank Andy, Dave and Abbie for their supervision and suggestions on my work. Charlotte Blythe designed the HPLC methodology to determine the scrambled cage molecules. James Jones and Tom Hasell carried out the cage-cage interchange method. The gas sorption measurements were done by James Jones. SEM images were measured by Tom Hasell.

5.12 References

1. Tozawa, T.; Jones, J. T. A.; Swamy, S. I.; Jiang, S.; Adams, D. J.; Shakespeare, S.; Clowes, R.; Bradshaw, D.; Hasell, T.; Chong, S. Y.; Tang, C.; Thompson, S.; Parker, J.; Trewin, A.; Bacsa, J.; Slawin, A. M. Z.; Steiner, A.; Cooper, A. I., Porous organic cages. *Nat. Mater.* **2009,** *8* (12), 973-978.
2. Tian, J.; Thallapally, P. K.; McGrail, B. P., Porous organic molecular materials. *Cryst.Eng.Comm.* **2012,** *14* (6), 1909-1919.
3. Holst, J. R.; Trewin, A.; Cooper, A. I., Porous organic molecules. *Nat. Chem.* **2010,** *2* (11), 915-920.
4. Budd, P. M.; Ghanem, B. S.; Makhseed, S.; McKeown, N. B.; Msayib, K. J.; Tattershall, C. E., Polymers of intrinsic microporosity (PIMs): robust, solution-processable, organic nanoporous materials. *Chem. Commun.* **2004,** (2), 230-231.
5. McKeown, N. B.; Budd, P. M., Polymers of intrinsic microporosity (PIMs): organic materials for membrane separations, heterogeneous catalysis and hydrogen storage. *Chem. Soc. Rev.* **2006,** *35* (8), 675-683.
6. Tian, J.; Thallapally, P. K.; Dalgarno, S. J.; McGrail, P. B.; Atwood, J. L., Amorphous Molecular Organic Solids for Gas Adsorption. *Angew. Chem. Int. Ed.* **2009,** *48* (30), 5492-5495.
7. Tian, J.; Ma, S.; Thallapally, P. K.; Fowler, D.; McGrail, B. P.; Atwood, J. L., Cucurbit[7]uril: an amorphous molecular material for highly selective carbon dioxide uptake. *Chem. Commun.* **2011,** *47* (27), 7626-7628.
8. Jin, Y.; Voss, B. A.; Jin, A.; Long, H.; Noble, R. D.; Zhang, W., Highly CO_2-Selective Organic Molecular Cages: What Determines the CO_2 Selectivity. *J. Am. Chem. Soc.* **2011**, *133* (17), 6650-6658.
9. Schneider, M. W.; Lechner, L. G.; Mastalerz, M., Uniform porous nanospheres of discrete shape-persistent organic cage compounds. *J. Mater. Chem* .**2012,** *22* (15), 7113-7116.
10. Belowich, M. E.; Stoddart, J. F., Dynamic imine chemistry. *Chem. Soc. Rev.* **2012,** *41* (6), 2003-2024.
11. Jiang, S.; Jones, J. T. A.; Hasell, T.; Blythe, C. E.; Adams, D. J.; Trewin, A.; Cooper, A. I., Porous organic molecular solids by dynamic covalent scrambling. *Nat. Commun.* **2011,** *2*, 207.
12. Grimme, S.; Antony, J.; Ehrlich, S.; Krieg, H., A consistent and accurate ab initio parametrization of density functional dispersion correction (DFT-D) for the 94 elements H-Pu. *J. Chem. Phys.* **2010,** *132* (15), 154104-19.
13. VandeVondele, J.; Krack, M.; Mohamed, F.; Parrinello, M.; Chassaing, T.; Hutter, J., Quickstep: Fast and accurate density functional calculations using a mixed Gaussian and plane waves approach. *Comput. Phys. Commun.* **2005,** *167* (2), 103-128.
14. Becke, A. D., Density-functional exchange-energy approximation with correct asymptotic behavior. *Physical Review A* **1988,** *38* (6), 3098-3100.
15. VandeVondele, J.; Hutter, J., Gaussian basis sets for accurate calculations on

molecular systems in gas and condensed phases. *J. Chem. Phys.* **2007,** *127* (11), 114105-9.
16. Hasell, T.; Wu, X.; JonesJames, T. A.; Bacsa, J.; Steiner, A.; Mitra, T.; Trewin, A.; Adams, D. J.; Cooper, A. I., Triply interlocked covalent organic cages. *Nat. Chem.* **2010,** *2* (9), 750-755.
17. Jin, Y.; Voss, B. A.; Noble, R. D.; Zhang, W., A Shape-Persistent Organic Molecular Cage with High Selectivity for the Adsorption of CO_2 over N_2. *Angew. Chem. Int. Ed.* **2010,** *49* (36), 6348-6351.
18. Hasell, T.; Chong, S. Y.; Jelfs, K. E.; Adams, D. J.; Cooper, A. I., Porous Organic Cage Nanocrystals by Solution Mixing. *J. Am. Chem. Soc.* **2011,** *134* (1), 588-598.
19. Rappe, A. K.; Casewit, C. J.; Colwell, K. S.; Goddard, W. A.; Skiff, W. M., UFF, a full periodic table force field for molecular mechanics and molecular dynamics simulations. *J. Am. Chem. Soc.* **1992,** *114* (25), 10024-10035.
20. Sun, H., COMPASS: An ab Initio Force-Field Optimized for Condensed-Phase ApplicationsOverview with Details on Alkane and Benzene Compounds. *J. Phys. Chem. B* **1998,** *102* (38), 7338-7364.
21. Trewin, A.; Willock, D. J.; Cooper, A. I., Atomistic Simulation of Micropore Structure, Surface Area, and Gas Sorption Properties for Amorphous Microporous Polymer Networks. *J. Phys. Chem. C* **2008,** *112* (51), 20549-20559.

Chapter 6

Simulation of gas diffusion in amorphous porous organic cages

6.1 Introduction

We have recently demonstrated that cage organic molecules can sometimes pack poorly and create permanent porosity in the amorphous solid state.[1] The amorphous cage materials were synthesized via co-reactions of a mixture of different diamines or dynamic exchange reactions, as discussed in Chapter 5 and they comprise a distribution of multifunctional and asymmetrical molecular species.[1a] We also synthesized amorphous cage **1** (**CC1)** and amorphous cage **3** (**CC3)** by a freeze-drying method.[1b] These amorphous cage materials showed a high level of porosity and tunable gas selectivity. BET surface areas up to 898 m^2 g^{-1} exceed comparable amorphous molecular solids. The gas sorption properties were tuned by varying the cage vertex functionality. H_2/N_2 gas selectivity was observed as a function of the 1, 2-diaminoethylene (EDA): 1,2-diaminocyclohexane (CHDA) ratio on cage vertex in these amorphous cage materials. Amorphous **CC1**, with fully EDA vertices, displayed a selectively porous to H_2 and gives a H_2/N_2 selectivity of 12 at 77 K, 1 bar. Amorphous cage materials with high EDA ratios can adsorb much more H_2 than N_2. For example, materials from scrambling reactions with a ratio of EDA and CHDA to be 5: 1 exhibited a H_2/N_2 selectivity of 5. However, amorphous materials with low EDA ratios showed non-selectively porous to both N_2 and H_2, such as amorphous **CC3** with fully CHDA vertices. We suggested that the enhanced porosity in these amorphous scrambled solids results predominantly from the extrinsic inter-cage void volume according to molecular simulations.[1a] Although experimental approaches such as measuring the adsorption isotherms can be used to characterize the properties of porous materials in the macroscopic scope, there is also a need for a more fundamental molecular-level understanding of materials. An alternative approach for characterizing these amorphous molecular systems is based on molecular simulations.[2] The pore structure and connectivity of crystalline micoporous materials are well understood, and pore size and shape are therefore more designable for applications because the crystal structures are available from single crystal XRD data.[3] However, amorphous materials have no long-range order,

meaning that the experimental characterization of amorphous porous materials is mainly achieved from surface areas, pore volumes and pore size distributions.

In order to simulate the properties and performance of amorphous porous materials, a representative structural model must be generated. However, the generation of a realistic model for amorphous materials is a challenging task. There are two common approaches to produce representative polymer structures.[4] One is packing polymer chains at the experimental density, either by using geometry energy minimisation or by using Monte Carlo chain growth techniques. Another method is to generate polymer structures at low densities and then follow several steps of compression and relaxation with MD simulations until a target experimental density is achieved.[4] However, some drawbacks exist for both methods. First, the simulations rely on an experimental target density. The schemes make the density of the model as close to the experiment density, in some cases, which can lead to poor estimations of the physical properties.[4c, 5] Also, some procedures cannot build a realistic structure due to atomic overlaps of large, rigid repeat units.[6] Several computational studies have generated amorphous porous organic polymers structures, such as polymers of intrinsic microporosity (PIMs)[7], hyper-cross-linked polymers (HCPs)[8] and conjugated microporous polymers (CMPs).[9] We have presented a method for the construction of HCPs via clusters that are grown using an in-house code with a Monte Carlo approach.[10] A range of different cluster sizes is generated during the growth of monomers and then packed into amorphous cells. Recently, Colina and co-workers reported a simulation scheme for generating HCPs models that followed the synthesis route of simultaneous growth of chains and cross-linkers.[11] The cross-linking and polymerization were performed by linking closer repeat units together. The final step of structure generation was followed by a 21-step compression and slow decompression protocol which results in experimental-like densities. The same approach has been applied to generate PIM models by Colina and co-workers.[12]

In this Chapter, the methodology for generating organic cage molecules packed into the amorphous solid state is described. Following on from the structure generation,

we will simulate gas diffusion in these amorphous porous materials to rationalize gas selectivity. Typically, the diffusion in porous materials is affected by a variety of factors, such as the shape and size of the pores and the guest molecules, as well as the interaction between the guest molecules and pore surfaces.[3a, 13] The interconnectivity of the pore structure contributes to the overall diffusion and transport properties. A better understanding of this phenomenon will aid the optimization and development of industrial applications of these materials in separation and catalytic processes.

The reliable computational prediction of diffusion properties of guest molecules in amorphous organic cages will be a valuable tool in designing appropriate materials in future. There are only a few reports simulating gas diffusion in porous organic molecules using MD simulations. All of them are based on crystalline porous organic molecules. Alavi *et al.* [14] has studied *p-tert*-butylcalix[4]arene inclusion small guest molecules using molecular simulations. The generic AMBER force field was used for MD simulations and the calixarene molecules were kept rigid. The unit cell volume, density and inclusion energy were determined. Ripmeester and co-workers [15] reported an experimental and molecular simulation study on hydrogen adsorption and diffusion in *p-tert*-butylcalix[4]arene. Rawashdeh and co-workers [16] indicated the inclusion complexation of methyl viologen with cucurbit[*n*]uril using MD simulation. The energy barriers for the host and guest inclusion process were obtained from the potential of mean force (PMF). A number of studies have determined the diffusivities of gases in amorphous polymers.[17] In some cases, there is a discrepancy between theoretical and experimental results.[18] A hopping mechanism has been suggested for gas diffusion in amorphous polymers.[19] The gas molecule resides in the pore cavity, and from time to time, jumps to the adjacent cavity because of interconnection of pore cavities. We have observed that H_2 molecules can hop from one cavity to another cavity from MD simulation in crystalline **CC1β**, a polymorph of crystalline **CC1**.[20]

In this Chapter, the structures and gas diffusion properties of amorphous **CC1** and **CC3** materials are analysed with use of MD simulations. Experimental observations show that amorphous **CC1** is selectively porous to H_2 than N_2 and amorphous **CC3** is porous to both H_2 and N_2. Amorphous **CC3** also demonstrates a higher porosity. This Chapter describes the design of a methodology for packing porous organic cages in the amorphous solid state and study a dynamic diffusion of guest molecules (mainly H_2, N_2) through cavities or pores of amorphous organic cages. A special emphasis is placed on the calculation of hopping and diffusion coefficients to understand the behaviour of guest molecules in amorphous porous organic molecules.

6.2 Experimental results for amorphous cage 1 (CC1) and amorphous cage 3 (CC3)

To synthesize amorphous **CC1** and **CC3**, as-synthesized racemic **CC1** and homochiral **CC3**-R were dissolved in dichloromethane, and frozen rapidly in the liquid nitrogen.[1b] We used the freeze drying approach to evaporate solvents, in order to rapidly precipitate cage molecules from solution and render the **CC1** or **CC3** in an amorphous state. The freeze-drying experiments were carried out by Dr Tom Hasell. Six samples of amorphous **CC3** were generated to establish the reproducibility of the method. All samples lack crystallinity on the basis of PXRD.[1b] SEM images showed irregular amorphous morphologies which confirmed PXRD observation.[1b]

N_2 and H_2 adsorption and desorption were carried out for amorphous **CC1** and **CC3** at 77 K and 1 bar. The samples were degassed offline at 100 °C for 15 h under dynamic vacuum before analysis. The amorphous **CC1** demonstrated a low N_2 uptake at 77 K, 1 bar. Therefore, amorphous **CC1** was considered to be non-porous to N_2. In contrast, H_2 sorption of amorphous **CC1** showed an uptake of 3.1 mmol g^{-1} shown in Figure 1. This adsorption behaviour suggested that amorphous **CC1** might be a good candidate for gas separation. The ideal selectivity was calculated from these isotherms to be 12 for H_2/N_2 at 77 K, 1 bar.

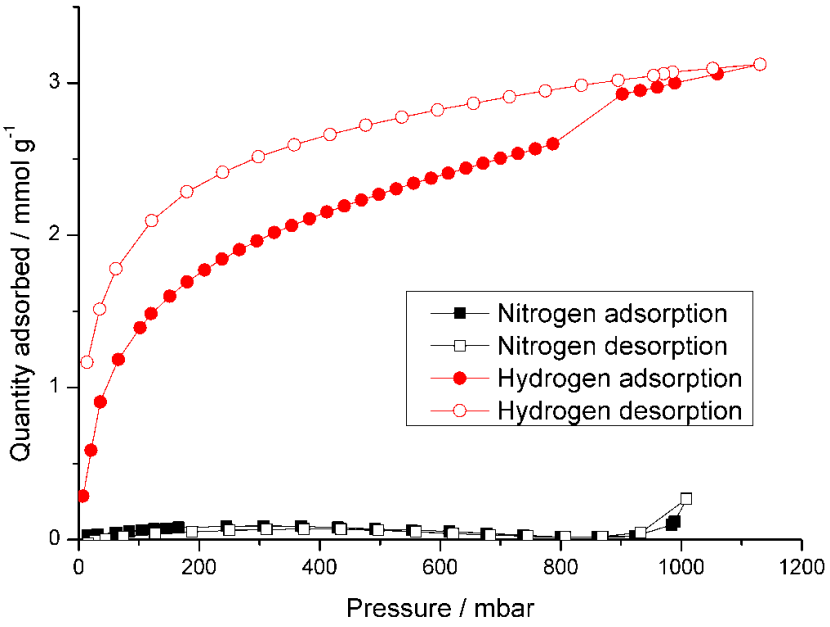

Figure 1. Hydrogen (red circles) and nitrogen (black squares) adsorption/desorption isotherms for amorphous **CC1** sample.

The N_2 isotherm for amorphous **CC3** was type I in character with a total uptake of 12.85 mmol g^{-1} at 77 K, 1 bar (Figure 2). Amorphous **CC3** adsorbed a large amount of H_2, 5.88 mmol g^{-1} under the same conditions. Pore size distributions of amorphous **CC3** and crystalline **CC3** were calculated by application of non-local density functional theory (NL-DFT) analysis to N_2 adsorption isotherms at 77 K shown in Figure 3. Crystalline **CC3** displayed a uniform pore size of 10 Å. However, amorphous **CC3** showed a broad range of pore sizes including larger micropores and mesopores. Amorphous **CC3** showed a significantly higher porosity than crystalline **CC3**. The enhanced porosity and a broadening pore size distribution were observed as the degree of disorder was increased.[1b] Some hysteresis was shown in N_2 isotherms of amorphous **CC3** upon desorption, which was attributed to a broader range of pore sizes. Unlike amorphous **CC1**, amorphous **CC3** was porous to both H_2 and N_2.

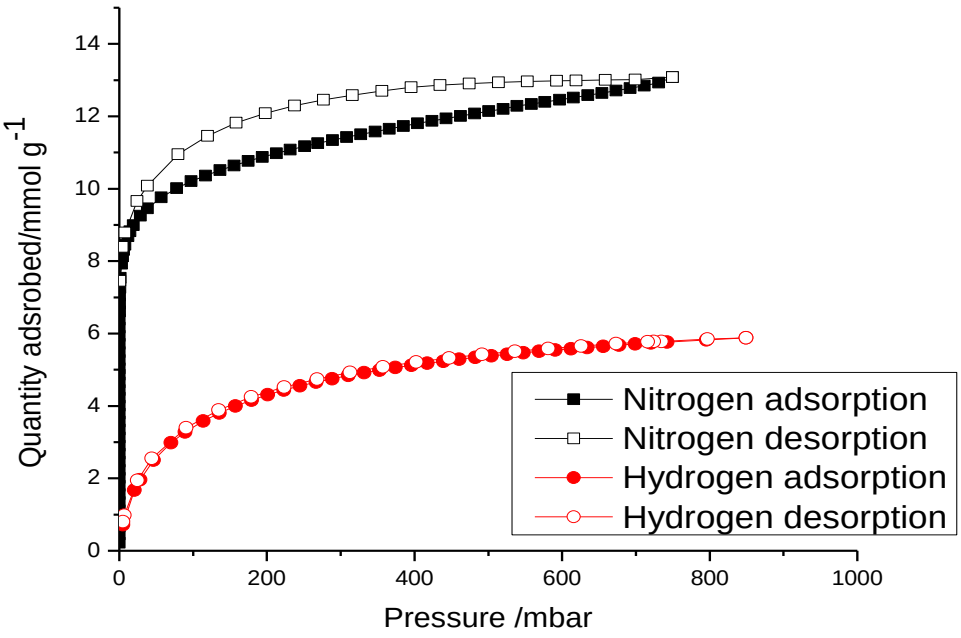

Figure 2. Hydrogen (red circles) and nitrogen (black squares) adsorption/desorption isotherms for amorphous **CC3** sample.

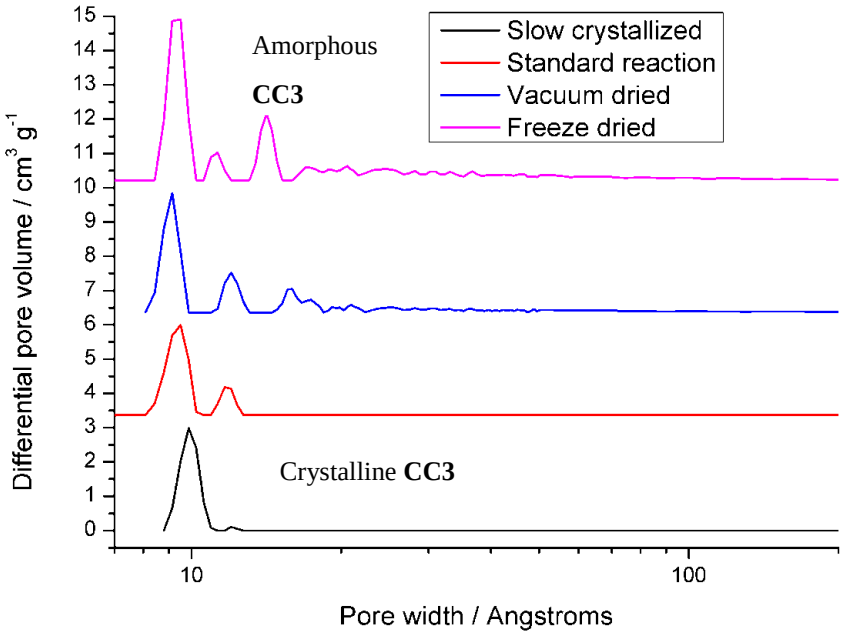

Figure 3. Differential pore size distributions for **CC3** samples produced by a variety of synthesis methods. The top one represents amorphous **CC3** and the bottom one represents crystalline **CC3**. (Figure from reference [1b])

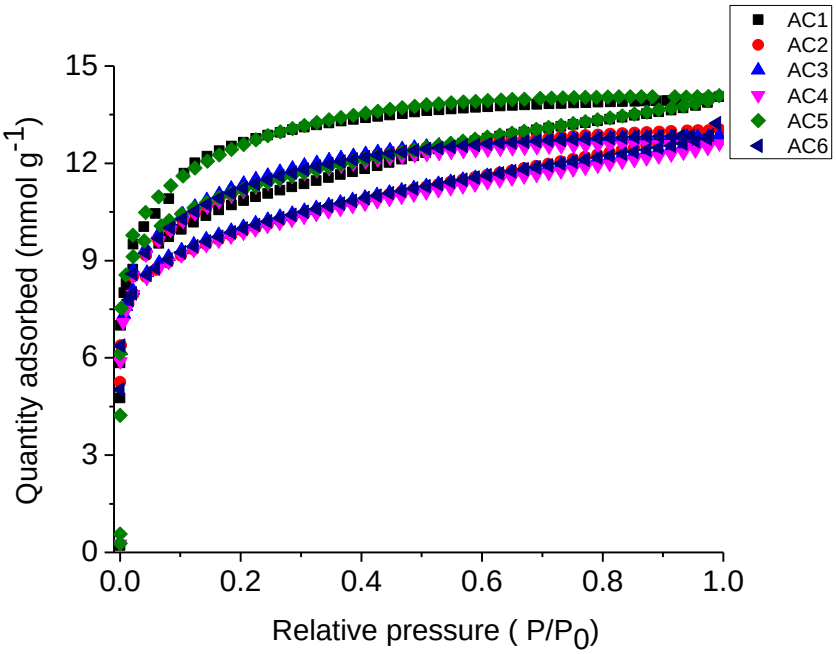

Figure 4. The nitrogen adsorption/desorption isotherms for all six repeated amorphous **CC3** samples.

Six samples of amorphous **CC3** were generated to establish the reproducibility of the method which is labelled AC1-AC6. Figure 4 showed the nitrogen adsorption/desorption isotherms for all six amorphous **CC3** samples (AC1-AC6). The average BET surface area of amorphous **CC3** was 860 m^2/g with a standard deviation of 47 m^2/g, compared with crystalline **CC3** BET surface area of 409 m^2/g with a standard deviation of 8 m^2/g. The variation in amorphous **CC3** isotherms was observed due to the nature of amorphous materials and freeze drying process.

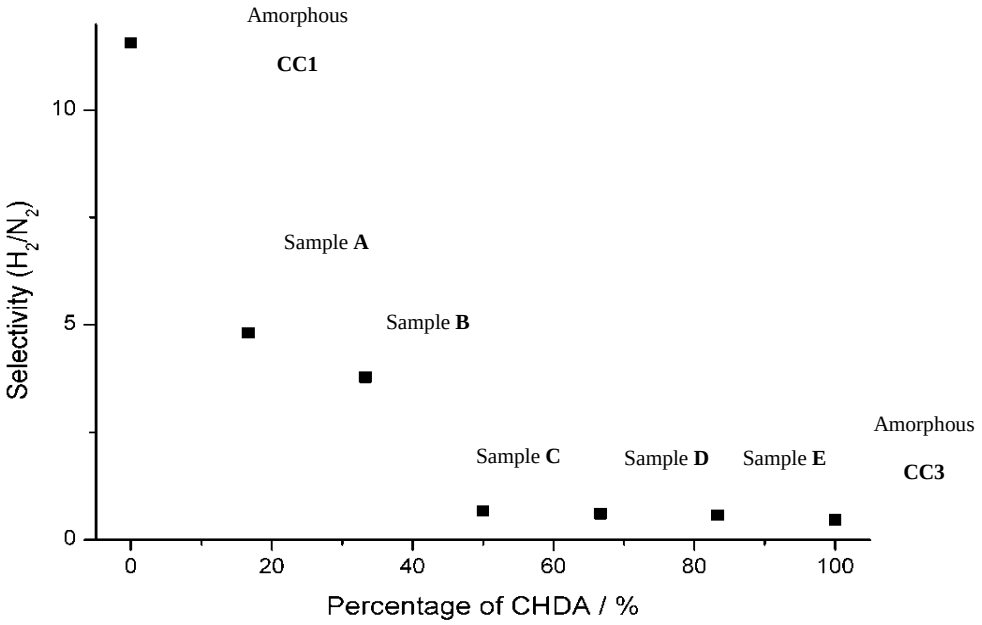

Figure 5. H_2/N_2 Gas selectivity is function of the EDA: CHDA ratio for amorphous cage materials.

Figure 5 showed H_2/N_2 selectivity as a function of the EDA: CHDA ratio on cage vertices in these amorphous materials. The graph includes amorphous **CC1**, amorphous **CC3** and amorphous scrambled cages formed by co-reaction of 1,3,5-triformylbenzene with various ratios of EDA and CHDA as described in Chapter 5. Samples **A**-**E** are from the co-reactions in Figure 5. Materials with low CHDA ratios (amorphous **CC1**, sample **A** from a co-reaction) adsorbed much more H_2 than N_2 at 77 K, 1 bar. Amorphous **CC1** demonstrated selective adsorption of H_2 over N_2 with the selectivity of 12. Although amorphous **CC3** did not have a good selectivity of H_2/N_2, amorphous **CC3** had a high porosity for both H_2 and N_2.

6.3 Simulation of structures for amorphous organic cages

In this section, we describe the simulation methodology for packing amorphous organic cages. A Cage Specific Force Field (CSFF) was used in this work which was developed by Daniel Holden.[21] CSFF was parameterized based on PCFF [22] and fitted for cage molecules. The force field (FF) parameters for the intra-molecular bonds, angles and dihedral potentials for the cage fragment were fitted using Density Functional Theory (DFT) with a B3LYP functional and 6-31G (b,p) basis set.[23] The energy curves from DFT have a good agreement with FF optimized energy plots. Lennard-Jones (LJ) 9-6 potentials were used to describe the non-bonding interactions between cages. The atomic charges were obtained from force field parameters. It has been shown that the CSFF minimized structures for crystalline cage **1**, cage **2** and cage **3** compare well to the structures obtained from single crystal XRD. All MD simulations in this work are undertaken using the DL_POLY2.20 [24] with Verlet leapfrog algorithm [25] for integrating the equations of motion of interaction and trajectories.

In order to obtain reliable physical properties of amorphous materials, an important consideration is to generate realistic structural models for molecular simulations. The approach described here for generating models of amorphous porous cages is implemented in the following steps: (1) Generate an initial configuration which is composed of 40 cages placed randomly in the cubic simulation cell at a low density; (2) An MD simulation of 500 ps using a NVE ensemble to stabilize the initial configuration; (3) An MD simulation of 8 ns using a NPT ensemble to fully equilibrate and compress the system; (4) Force field geometry optimization for the final configuration. The simulation procedure is shown in Scheme 1 and explained in the following:

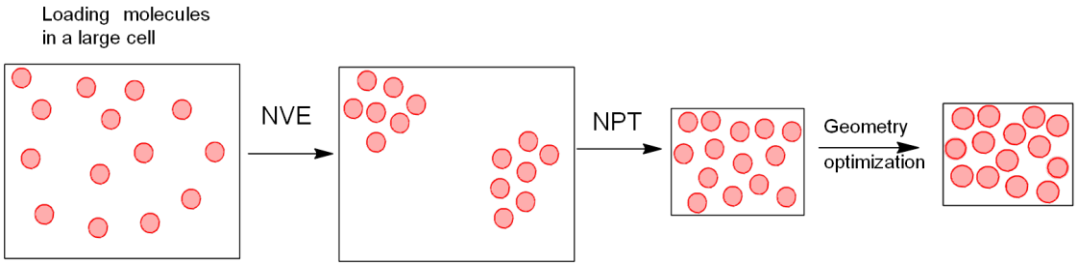

Scheme 1. Simulation procedure for generation of amorphous cage structures

(1) The single cage molecules (cage **1** and cage **3**, respectively) as repeated units in the cell are taken from the single crystal X-ray structures (obtained from the Cambridge crystallographic database with reference number CCDC 720848 for cage **1** and CCDC 720850 for cage **3**). Cage **1** (**CC1**) has unhindered ethylene vertices and Cage **3** (**CC3**) has bulky cyclohexane vertices. Both of molecules exhibit structural chirality. The homochiral (*R*,*R*)-1,2-diaminoethylene cage **1**, **CC1**-R and (*R*,*R*)-1,2-diaminocyclohexane cage **3**, **CC3**-R were used for the simulations. The models for amorphous cages were built using the Amorphous Cell module in the Materials Studio Modelling 5.0 software package (Accelrys). All cage molecules were treated as rigid bodies and the amorphous cell was loaded with cage molecules at a low density of 0.1-0.25 g cm^{-3} using the Universal Forcefield (UFF).[26] Six different initial configurations were generated for each amorphous system for a sampling purpose. Each model consists of 40 cage molecules. The simulation cell contains either 4320 atoms for amorphous **CC1** or 6720 atoms for amorphous **CC3**.

(2) An MD run using a NVE ensemble for 500 ps was used to stabilize the low density structure obtained in step 1. The simulation was performed with the Nose-Hoover thermostat and barostat [27] at 300 K, a pressure of 1 atm and the thermostat and barostat relaxation times of 0.5 ps. The total production time was 500 ps with a 50 ps equilibration time and a time step of 0.5 fs.

A short NVE ensemble simulation stabilizes the initial configuration, whereas a direct NPT ensemble MD simulation for an unstable configuration might lead to a failure of the program due to violating basic assumptions in the code. As shown in

the Figure 6, the configuration energy drops rapidly and maintains a constant average for the 500 ps NVE simulation. The temperature /pressure fluctuations can be used to improve the energy conservation. The last configuration from the simulation was observed that cage molecule clusters were formed as illustrated in scheme 1.

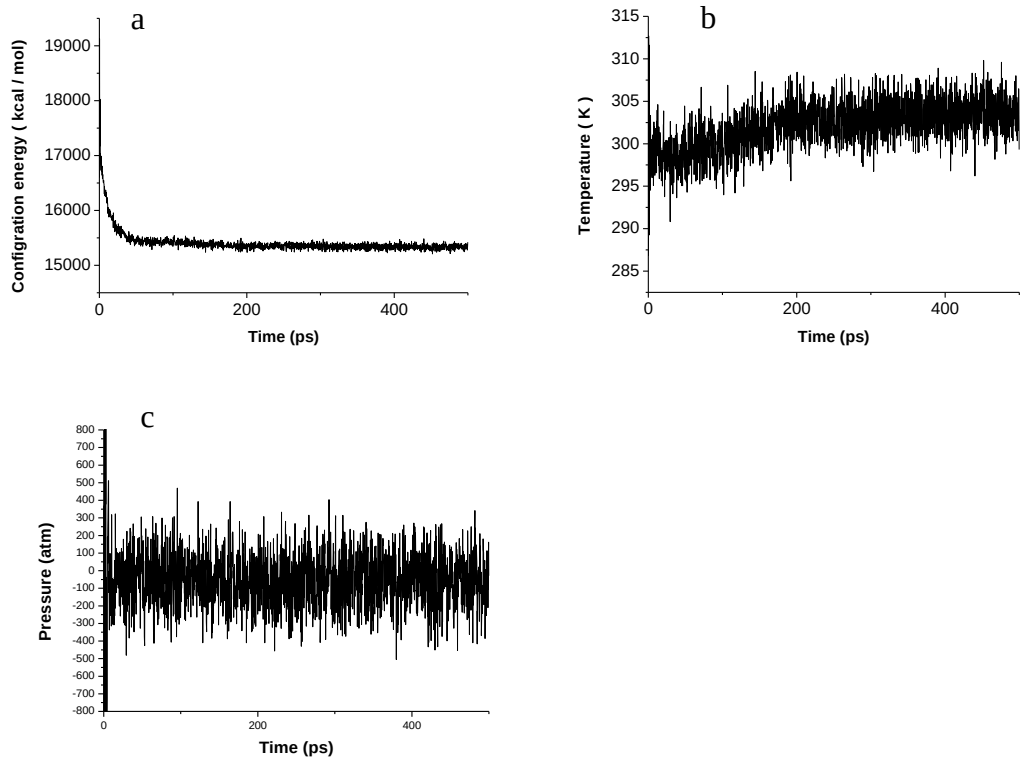

Figure 6. (a) Configuration energy plot for NVE MD simulation. (b,c) temperature and pressure fluctuation during NVE dynamics.

(3) Following directly from the NVE MD simulation, an NPT ensemble MD simulation was run. The starting configuration was taken from the last configuration of NVE MD simulation. The simulation was performed with the Berendsen thermostat and barostat [27] at 300 K and a pressure of 1 atm. The total production time was 8 ns with an equilibration time of 400 ps and a time step of 0.5 fs. Six different initial configurations were generated for each amorphous system. The volume and energy vs time plots for different initial configurations of amorphous **CC3** are shown in Figure 7. The volume and configuration energy drop at the

beginning of NPT and then they maintain a constant average. Typical fluctuations of volume and energy were observed after full equilibration of systems. Simulations with equilibration times of 50 ps, 100 ps and 400 ps respectively were ran to check the effect of equilibrium time on the final packing of cages. The cell volume and configuration energy were not found to differ significantly.

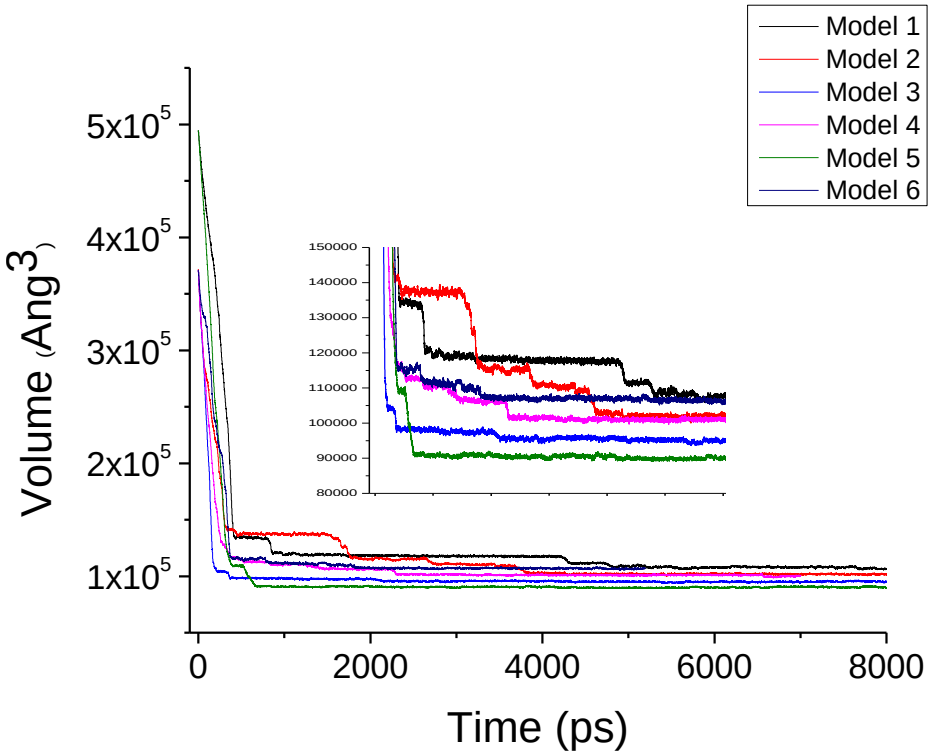

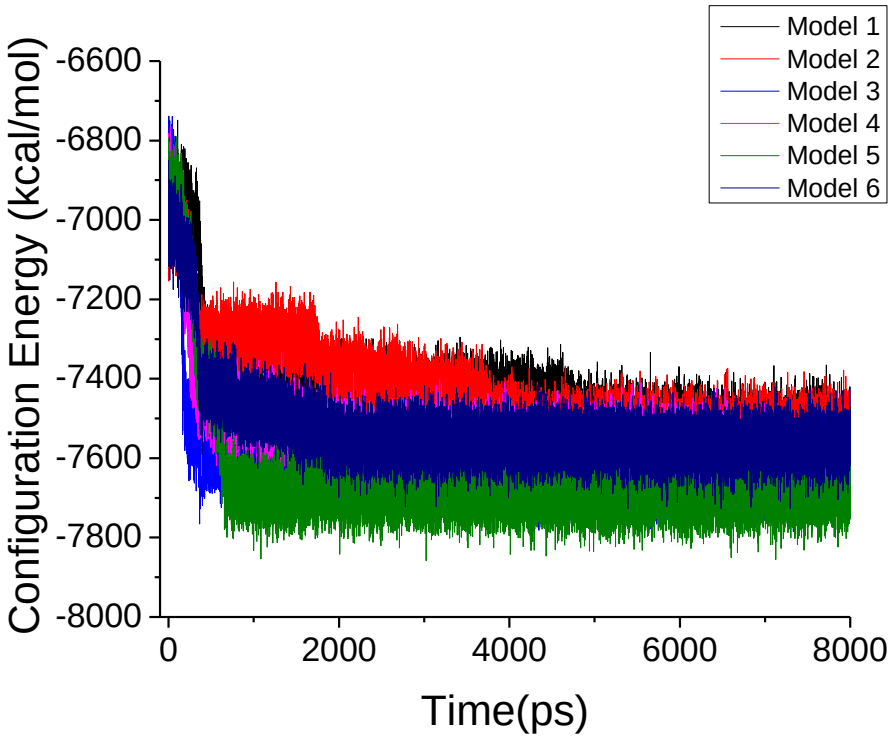

Figure 7. The volume and configuration energy plots of amorphous **CC3** models (Model 1- Model 6) during 8 ns NPT with different intial configurations.

(4) In the last step, a geometry optimization calculation is carried out for the last configuration from NPT simulaiton using the Discover in Materials Studio with CSFF. The conjugate gradient method was used and the cell volume was fully relaxed during the energy minimization. The calculation energy was considered converged when the energy change between optimization steps was less than 0.1 kcal /mol/Å.

In order to ensure no furthur volume compression would occur after the 8 ns NPT simulation, a further 7 ns NPT simulation in step 3 was carried out for one of the amorphous **CC1** and **CC3** models giving a total simulation time of 15 ns. As shown in Figure 8, both amorphous **CC3** and **CC1** systems have been fully equilibrated after 4-5 ns NPT simulation. A volume fuctuation is observed after the system equilibration during the NPT MD run. As a result, we conclude that 8 ns NPT dynamics is long enough to equilibrate these amorphous cage systems.

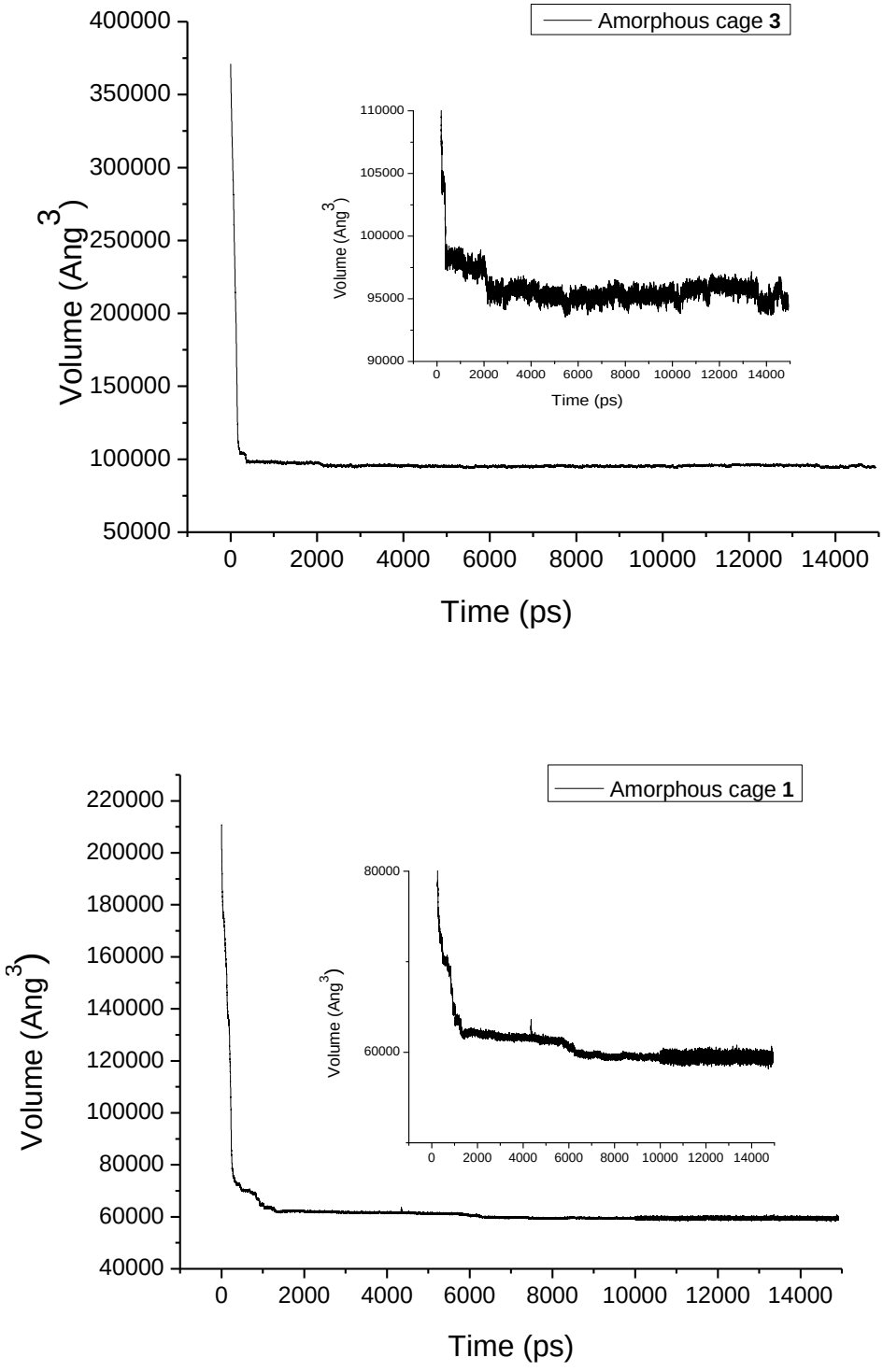

Figure 8. The volume plots for 15 ns NPT dyanmics for amorphous **CC3** and **CC1**. A zoom of Y axis set of plots is included.

6.4 Characterization of structural models of amorphous CC1 and CC3.

The structure generation scheme described above presents a methodolgy for packing cages into the amorphous solid state. In general, for the simulation of amorphous materials, a large simulation cell is required and different models should be constructed and their properties are averaged in order to better represent bulk materials. However, there is a trade-off between simulation time and statistical numbers of models. In this work, for each of amorphous **CC1** and amorphous **CC3**, six different independent samples were constructed following the procedure outlined previously (labelled as Model 1-Model 6). In order to ensure that the simulation models are representative of experimental bulk materials, the structual models (Model 1-Model 6) were then characterizated in terms of surface areas and pore volumes which can then be compared to experimental data (AC1 – AC6).

In the case of amorphous **CC3,** the surface area and pore volume of the six independent simulation models generated using the procedure outlined previously are given in Table 1 and are compared with the experimental BET surface area, Langmuir surface area and t-plot microporous volume in Table 2. In Table 1, the range of density for the final configurations is from 0.76 to 0.89 g/cm^3. The average density over six simulation samples is 0.82 g/cm^3 with a standard deviation of 0.05 g/cm^3. The solvent accessible surface areas (SASA) were generated using a N_2 probe radius of 1.82 Å for all of the final configurations. The average SASA is 744 m^2/g compared with average BET surface areas of 860 m^2/g over six experimental samples. The simulated pore volumes are determined from an average of Connolly pore volume and solvent accessible pore volume.[28] The average simulated pore volume is 0.25 cm^3/g compared with the experimental micropore volume of 0.29 cm^3/g. As can be seen, the standard deviation of simulated SASA or pore volume over six models is relatively high. This might be due to the feature of inherently nonequilibrium structures of amorphous materials. In other words, each individual sample for amorphous materials produced either in the experiment or simulation has a different equilibrium state which can lead to a different physical properties. To

conclude, simulated data presented above have a reasonable agreement with experimental data.

Table 1. Structural properties of simulation models for amorphous **CC3** generated using the procedure outlined above.

Sample ID	Initial density (g/cm^3)	Average density during MD (g/cm^3)	Average configuration energy per cage during MD (kcal/mol)	Last configuration from MD			Final configuration after Geometry optimization		
				Density (g/cm^3)	SASA [1] (m^2/g)	Pore volume[2] (cm^3/g)	Density (g/cm^3)	SASA [1] (m^2/g)	Pore volume[2] (cm^3/g)
Model 1	0.2	0.71	-187.91	0.71	1086	0.44	0.78	966	0.28
Model 2	0.2	0.73	-188.23	0.73	1058	0.40	0.80	882	0.27
Model 3	0.15	0.78	-190.78	0.78	737	0.30	0.85	630	0.21
Model 4	0.15	0.74	-189.36	0.74	862	0.38	0.79	838	0.27
Model 5	0.2	0.82	-192.31	0.81	560	0.23	0.89	444	0.16
Model 6	0.15	0.70	-188.92	0.70	1024	0.50	0.76	951	0.33
						Average	0.82	744	0.25
						Standard deviation	0.05	206	0.06

[1] Solvent accessible surface areas generated using a probe radius of 1.82 Å for N_2.[29]

[2] Pore volumes determined from a average of Connolly pore volume and solvent accessible pore volume.

Table 2. Experimental data for amorphous **CC3** from adsorption isotherms.

Sample ID	BET surface area (m^2/g)	Langmuir surface area (m^2/g)	t-plot microporous volume (cm^3/g)
AC1	893	1073	0.32
AC2	882	1133	0.28
AC3	815	1025	0.27
AC4	927	1156	0.32
AC5	829	1040	0.28
AC6	814	1020	0.28
Average	860	1074	0.29
Standard deviation	47	58	0.02

The surface areas and pore volumes of six independent simulation models for amorphous **CC1** are listed in the Table 3. Due to amorphous **CC1** being non-porous to N_2, surface areas and micropore volumes are not available from the isotherms. The average density over six simulation samples for amorphous **CC1** is 0.92 g/cm^3 and the average SASA is 236 m^2/g. It should be noted that one of the structural models (Model 2) demonstrates a relatively high SASA of 462 m^2/g and pore volume of 0.2 cm^3/g. This model is probably a bad representation for amorphous **CC1**. The configuration energy is comparatively high compared to the other structural models because a high energy configuration was trapped during the MD simulation. This model was therefore not included for the further analysis of structural properties.

Table 3. Structural properties of simulation models for amorphous **CC1** generated using the procedure outlined above.

Sample ID	Initial density (g/cm^3)	Average density during MD (g/cm^3)	Average configuration energy per cage during MD (Kcal/mol)	Last configuration from MD			Final configuration after Geometry optimization		
				Density (g/cm^3)	SASA (m^2/g)	Pore volume (cm^3/g)	Density (g/cm^3)	SASA (m^2/g)	Pore volume (cm^3/g)
Model 1	0.15	0.88	-140.47	0.88	240	0.17	0.94	214	0.13
Model 2	0.2	0.81	-137.76	0.80	500	0.27	0.87	462	0.20
Model 3	0.2	0.85	-140.34	0.85	300	0.21	0.91	193	0.15
Model 4	0.15	0.86	-139.93	0.86	260	0.17	0.92	184	0.14
Model 5	0.2	0.88	-140.13	0.89	225	0.15	0.94	187	0.14
Model 6	0.15	0.86	-140.51	0.87	218	0.17	0.93	177	0.14
						Average	0.92	236	0.15
						Standard deviation	0.03	111	0.25

6.5 Porosity analysis of crystalline cage structures and amorphous cage structures

The structures of crystalline **CC1** and **CC3** are shown in Figure 9. **CC1** was synthesized from the condensation reaction of 1, 3, 5-triformylbenzene with 1,2-ethylenediamine and **CC3** from 1, 2- diaminocyclohexane. **CC1** has six unhindered ethylene linkers on the vertices resulting in the cages being able to pack much closer. Disconnected Connolly volumes were observed using a probe radius of 1.82 Å. **CC3** has more bulky and rigid cyclohexyl groups which direct the cages to window to window packing in the crystal structure. Consequently, crystalline **CC3** has an interconnected 3- dimensional diamondoid pore channels.

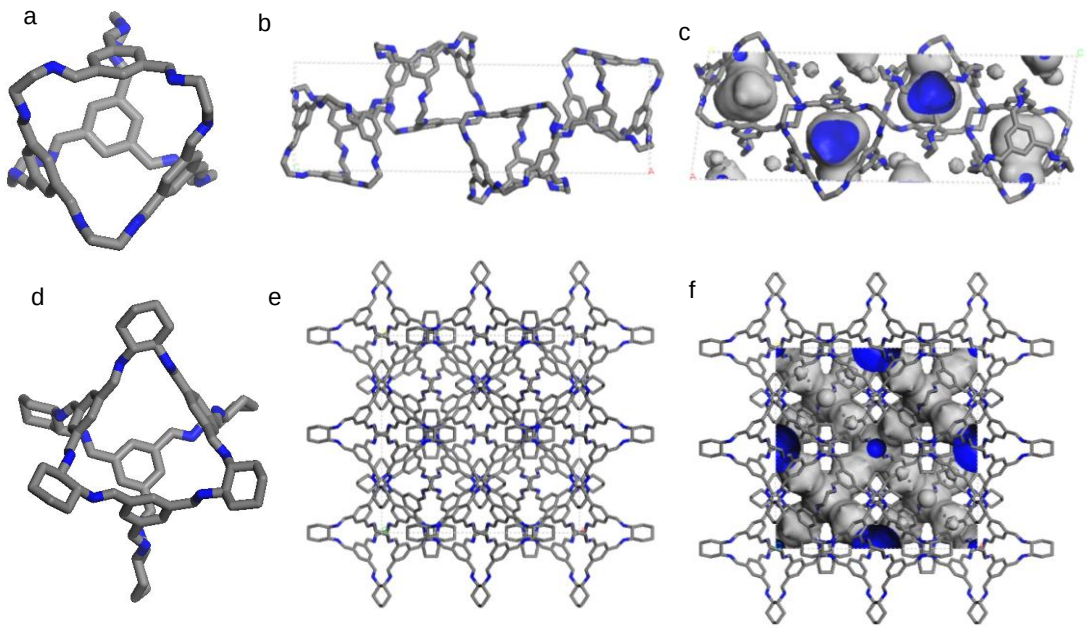

Figure 9. a ,d) Isolated **CC1** and **CC3** molecule (hydrogen atoms are omitted for clarity. Carbon and nitrogen atoms are coloured by grey and blue). b, e) crystal structures of **CC1** and **CC3**. c,f) Connolly surface areas of crystalline **CC1** and **CC3** generated using N_2 radius of 1.82 Å.

The structural models of amorphous **CC3** (Figure 10) and **CC1** (Figure 11) are shown below. Amorphous cage models have a larger unit cell than crystalline cage structures. The average unit cell over six models of amorphous **CC1** is 39.0 Å x 39.0

Å x 39.0 Å containing 4320 atoms compared with the unit cell of crystalline **CC1**: a = 12.8 Å, b = 10.9 Å c = 36.8 Å. The average unit cell over six models of amorphous **CC3** is 45.6 Å x 45.6 Å x 45.6 Å with 6720 atoms in a comparison to 24.8 Å x 24.8 Å x 24.8 Å for the crystalline **CC3** unit cell. In Figure 10 (a) and 11 (a), solvent accessible surface areas of six models of amorphous **CC3** and **CC1** respectively, are shown using a probe radius of N_2 (1.82 Å). The void structure available to N_2 in amorphous **CC3** is fully connected leading to a porous network. The porosity of amorphous **CC3** arises from both intrinsic intra cage voids and extrinsic inter cage voids. By contrast, amorphous **CC1** has isolated voids which are lack of connectivity as illustrated by the solvent accessible surface area. Therefore, amorphous **CC1** is non-porous to N_2 based on the static structure.

The solvent accessible surfaces calculated using a H_2 radius of 1.42 Å for amorphous **CC3** and **CC1** are displayed in Figure 10 (b) and Figure 11 (b). The H_2 accessible volume is partially interconnected in amorphous **CC1** and fully connected in amorphous **CC3**. As shown in Figure 10 (b), a large extrinsic pore cavity in amorphous **CC3** is observed which is also connected with adjacent cages. The analysis of the static structure indicates that the gas molecule of H_2 is capable of diffusing through the amorphous **CC1** and **CC3**. In principle, the analysis of pore connectivity based on the static structure suggests that amorphous **CC1** will be porous to H_2 but not to N_2 and amorphous **CC3** is porous to both H_2 and N_2. These observations are consistent with experimental results. However, analysing the surface of static structures only does not give reliable information on the connectivity of pores or the diffusion mechanism. In order to gain these understandings, we use molecular dynamic simulations to investigate gas diffusion in amorphous cage systems.

(a)

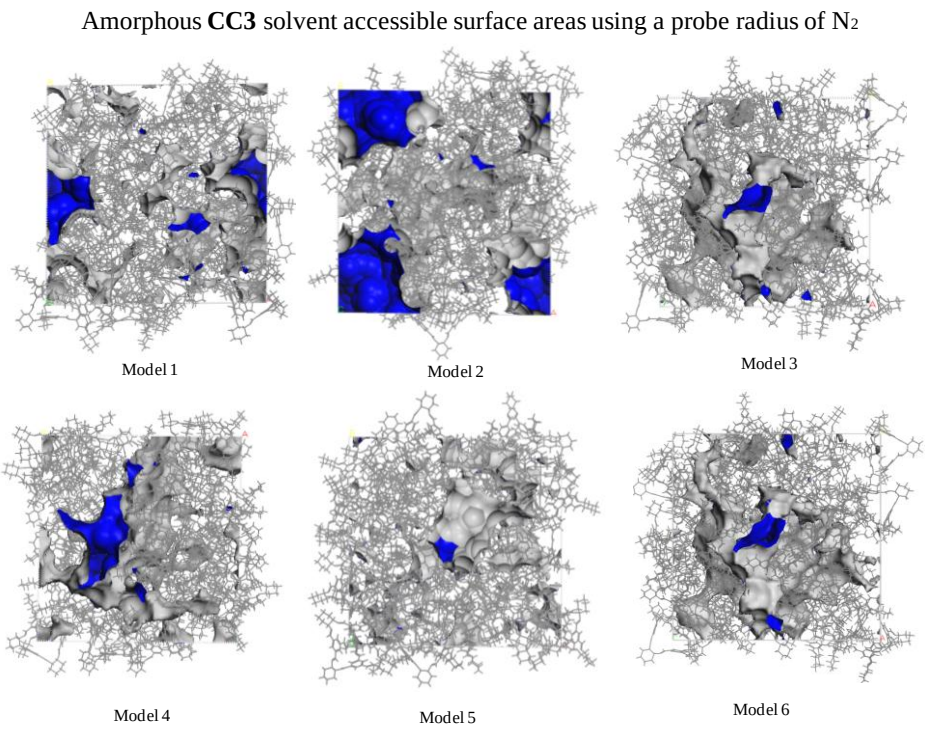

(b)

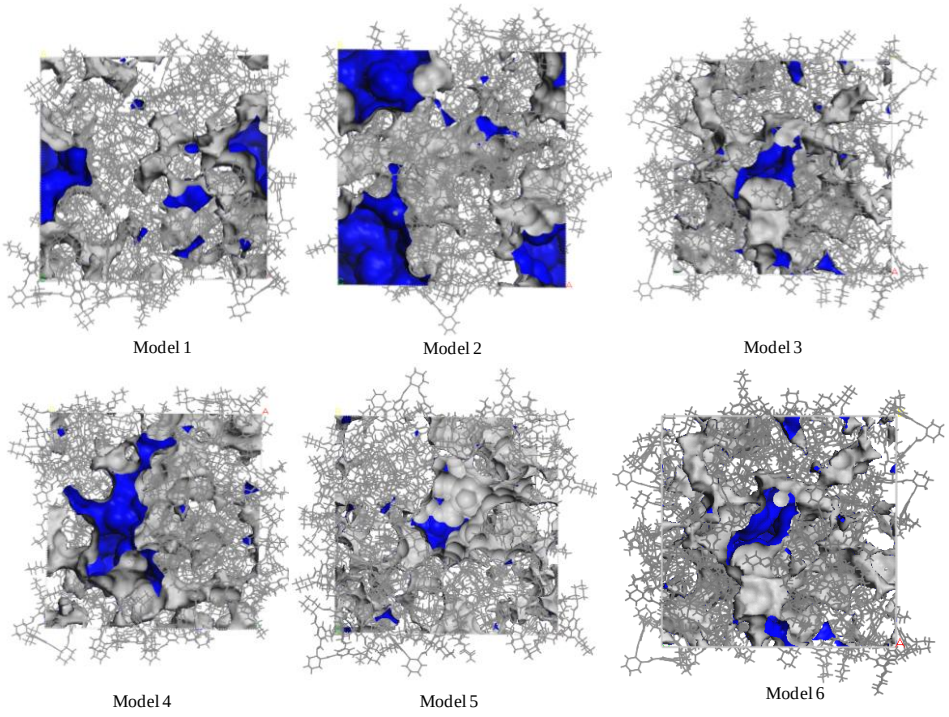

Figure 10. Solvent accessible surface areas generated using a N_2 probe radius of 1.82 Å. (a) and a H_2 probe radius of 1.42 Å (b) for six models of amorphous **CC3**.

(a)

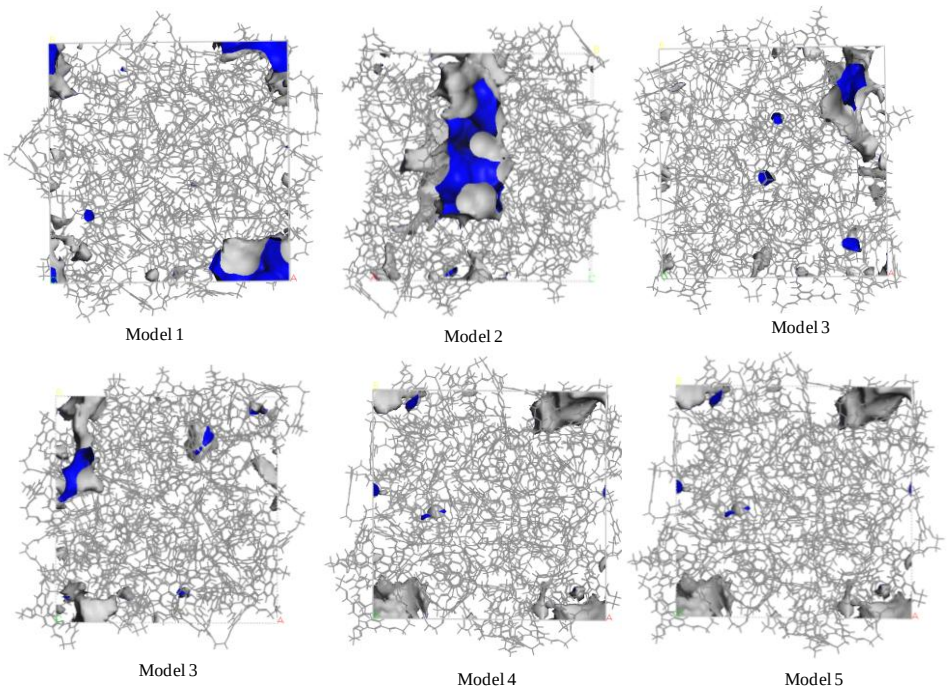

(b)

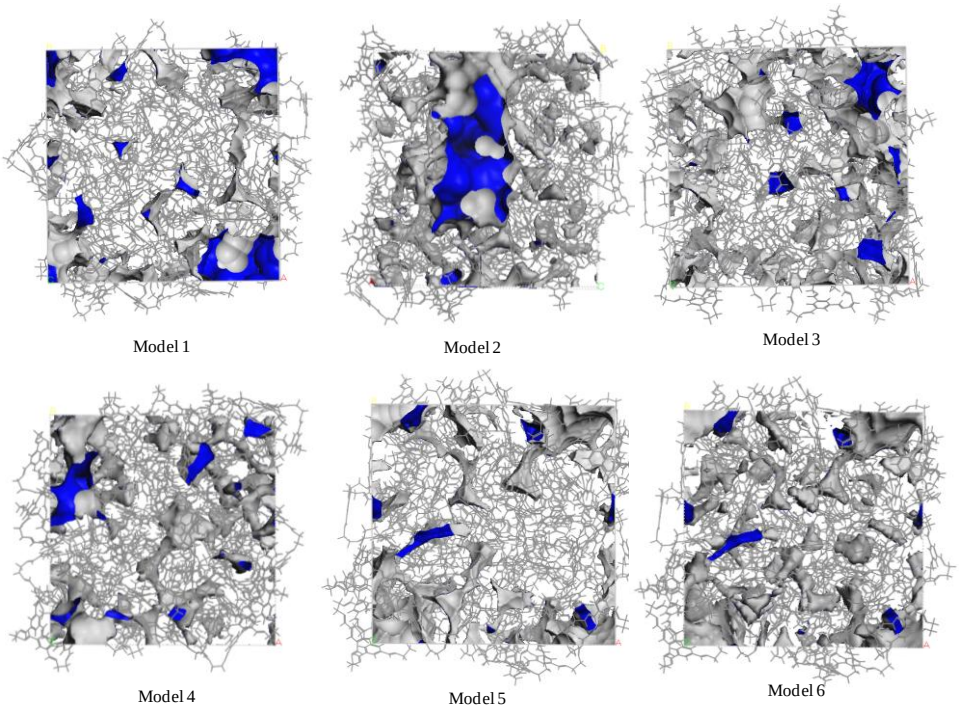

Figure 11. Solvent accessible surface areas generated using a N_2 probe radius of 1.82 Å. (a) and a H_2 probe radius of 1.42 Å (b) for six models of amorphous **CC1**.

6.6 Gas diffusion in amorphous CC1 and CC3

In this section, we describe gas diffusion and hopping in amorphous cage systems. The simulations using DLPOLY 2.20 were ran with an NPT ensemble and the Nose-Hoover thermostat and barostat. The Verlet leapfrog algorithm was used to integrate Newton equations. All the Lennard-Jones interactions were calculated with a cut off of 10 Å and the long range coulomb interactions were calculated by the Ewald summation method. The time step used in this work was 0.5 fs and periodic boundary conditions were used. The simulations were carried out at 300 K, and a pressure of 1 atm. A total production time of 10 ns (4 $x10^7$ steps) was used with an equilibration time of 50 ps (1 x 10^5 steps). The trajectory was generated at every 200 steps which is equal to every 0.1 ps sampling for subsequent analysis of the diffusion mechanism. The time interval for sampling the trajectory is small enough to track of the H_2 and N_2 diffusion. A smaller sampling time would lead to extremely large output files.

We are studying H_2 and N_2 gas molecules which are both described as linear rigid molecules. The potential parameters of H_2 molecule are obtained from CSFF force field without charge consideration. The N_2 molecule is treated as the 'Bean' model which has been suggested by Potoff and Siepmann.[30] In this model, the nitrogen atoms of the N_2 molecule have their own repulsion /dispersion interactions (Lennard-Jones) and their own distinct partial charge with q= -0.482. To compensate for these partial negative charges, the centre of mass of nitrogen molecule is given a charge with q=+0.964. The N-N bond distance is set as 1.1 Å according to the experimental data.

The amorphous cage models are obtained from the structure generation procedure outlined above. Initially, some simulations were carried out to check the effect of different amorphous models on gas diffusion, as the porous physical properties were observed to vary in different amorphous models as shown in Table 1 and Table 3. Three amorphous **CC3** models were chosen. The simulation density was 0.78

(**CC3**-1), 0.77 (**CC3**-2) and 0.73 g/cm^3 (**CC3**-3) and the solvent accessible surface areas were 737, 751 and 1058 m^2/g respectively. N_2 diffusion in these three models was simulated during a 3 ns NPT simulation at 300 K. Three different amorphous **CC3** models showed that N_2 molecule diffusion through a broad area, as illustrated in Figure 12 (a). The simulation density of the three amorphous **CC1** models chosen was 0.88 (**CC1**-1), 0.86 (**CC1**-2) and 0.87 (**CC1**-3) g/cm^3 respectively. N_2 diffusion was restricted to a limited zone for the three different models as shown in Figure 12 (b). In term of the diffusion trajectories, gas diffusion behaviour did not have a significant difference in different amorphous models.

Therefore, one of the amorphous **CC1** and **CC3** models is chosen for a further analysis. The simulated density of amorphous **CC1** model is 0.88 g/cm^3 with solvent accessible surface area of 240 m^2/g (Model 1 in Table 3) and the simulated density of amorphous **CC3** model is 0.78 g/cm^3 with solvent accessible surface area of 737 m^2/g (Model 3 in Table 1). The structural properties of these models have a reasonable agreement with experimental data of amorphous **CC1** and **CC3**. The cage molecules are treated as flexible during MD simulations. All the corresponding atomic partial charges and interatomic potential parameters are obtained from CSFF force field.

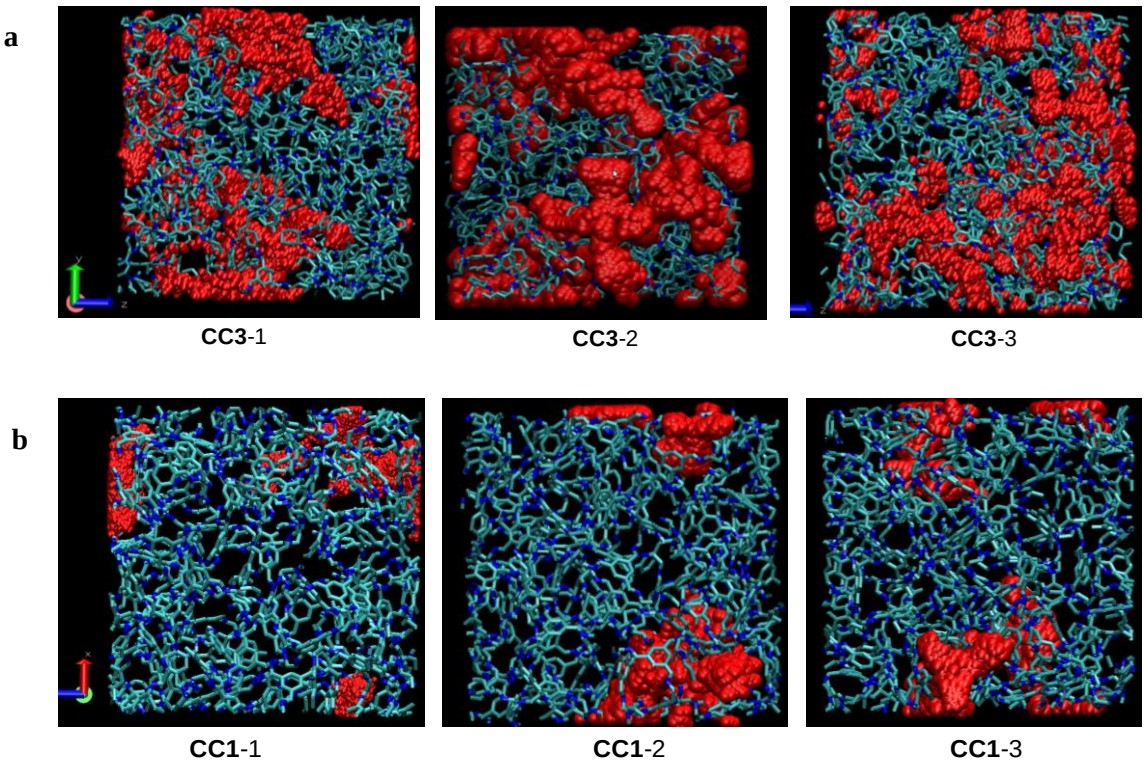

Figure 12. (a) The trajectories of N_2 diffusion in different amorphous **CC3** models. (b) The trajectories of N_2 diffusion in different amorphous **CC1** models.

6.6.1 Gas location analysis

To rationalize the gas selectivity and understand gas diffusion in these amorphous systems, it is important to understand the mechanism of N_2 and H_2 diffusion through cages. To do this, we analysed the position of the N_2 and H_2 during the MD simulations.

The MD output data was analysed with an in-house script written in PERL. All of the PERL scripts used in this work were written by Dr Kim Jelfs. The script takes the HISOTRY file from MD and calculates position of the cage centre of mass for each of the forty cages; thereby it is able to identify the positions of gas molecule relative to the cage centre. The following information was provided:

1. The location of the gas molecule at each sampled step and describing it as inside cage, outside all cages or a cage window. Everything less than 3.5 Å from the cage centre of mass is defined as inside cage. Between 3.5 and 4.5 from the centre of mass is in cage window. The rest is outside of the cage which can be thought of as in the extrinsic pore volume.

   Molecular simulations of a H_2 or N_2 placed randomly in amorphous **CC1** and **CC3** were run for 10 ns using the NPT ensemble for gas location analysis. Figure 13 shows the analysis of the gas molecule location for a 3 ns time period of the full MD simulation. Frequent hopping is observed for both H_2 and N_2 for amorphous **CC1**. However, this can be attributed to the movement of a gas molecule from the cage window and then back to its original cage cavity. This might be due to limited accessible volume in amorphous **CC1**. The location analysis in amorphous **CC3** shows that a larger portion of the simulation is spent outside cage voids in amorphous **CC3** than **CC1**. This may be due to the greater amount of extrinsic pore volume and connectivity of amorphous **CC3**.

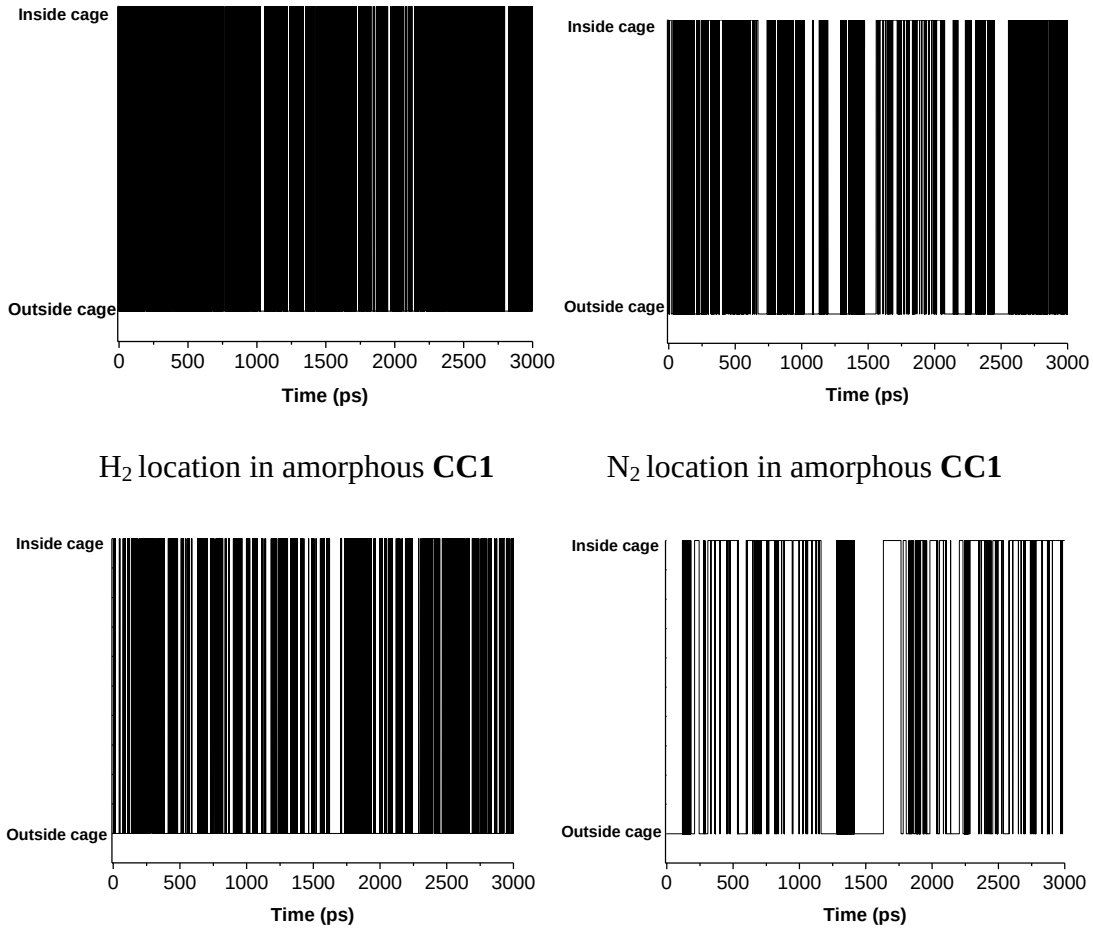

H_2 location in amorphous **CC1** N_2 location in amorphous **CC1**

H_2 location in amorphous **CC3** N_2 location in amorphous **CC3**

Figure 13. H_2 and N_2 location anlaysis in amorphous **CC1** and **CC3** respectively.

2. The cage number from 1 to 40 is printed out if a gas molecule is inside the cage at every sampled step. The total residence time of a gas molecule in a cage can be calculated. Figure 14 shows the total residence time of gas molecules in each cage over 10 ns MD simulations. For H_2 diffusion in amorphous **CC1**, H_2 molecule occupied all of the cages and in one cage, the 38^{th}, a particularly long residence time is observed, possibly due to H_2 trapped in a less accessible zone. In contrast, the total residence time distribution of H_2 in amorphous **CC3**, H_2 molecule accommodated each cage between 20 to 120 ps. The N_2 molecule was observed to occupy 19 cage molecules out of 40 in amorphous **CC1** and 22 cage molecules out of 40 for amorphous **CC3**.

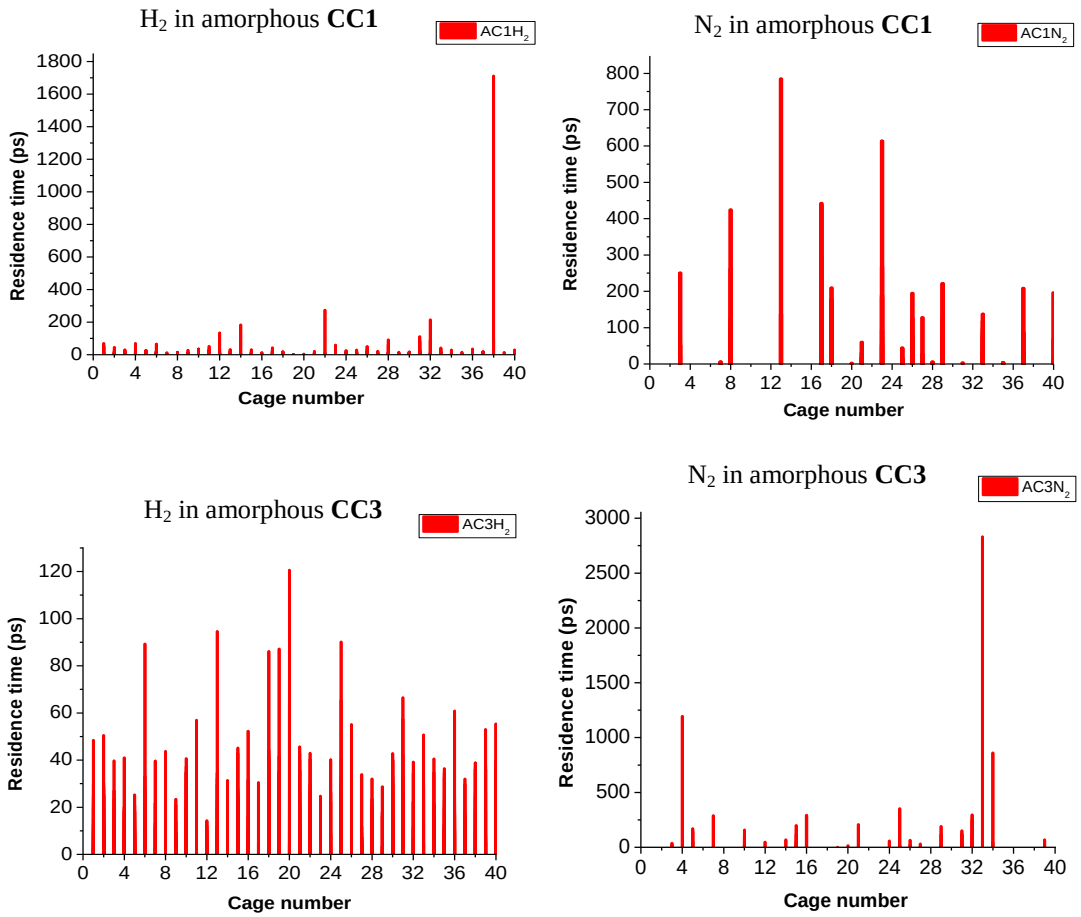

Figure 14. The total residence time for H_2 or N_2 in each occupied cage for amorphous **CC1** and **CC3** respectively.

3. Figure 15 demonstrates which cage molecules are occupied by gas molecules over the period of the MD simulation. Also the cumulative cage occupancy is calculated, which is the percentage of cages occupied by gas molecule overall. 100 % cage occupancy was observed for H_2 in amorphous **CC1**. 19 cage molecules were occupied by N_2 during the MD simulation in amorphous **CC1** which corresponds to 47.5 % of cages occupied. 100 % cage occupancy for H_2 and 55 % cage occupancy for N_2 in amorphous **CC3** were observed respectively.

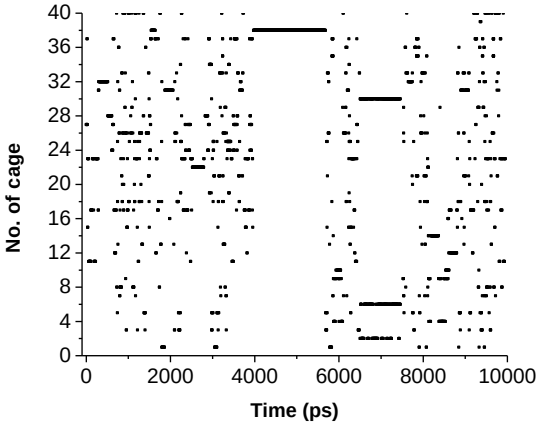

The cage molecule occupied by H_2 in amorphous **CC1** over a 10 ns MD simulation

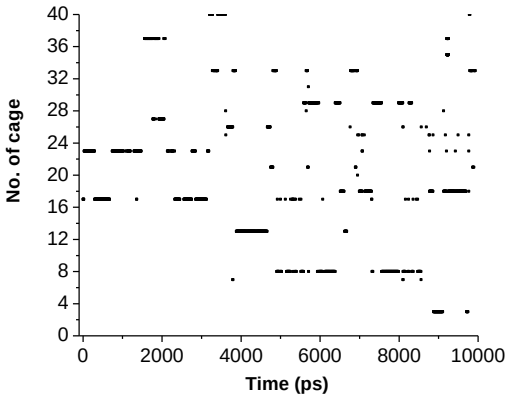

The cage molecule occupied by N_2 in amorphous **CC1** over a 10 ns MD simulation

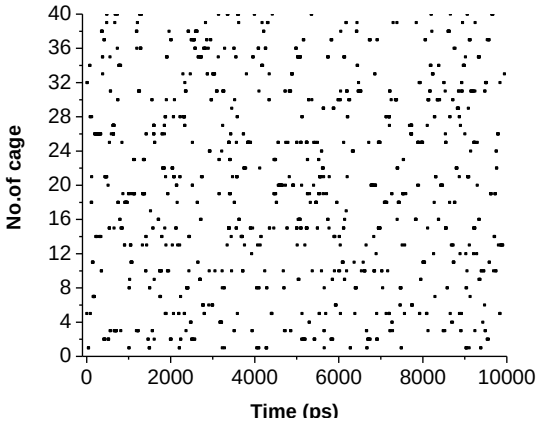

The cage molecule occupied by H_2 in amorphous **CC3** over a 10 ns MD simulation

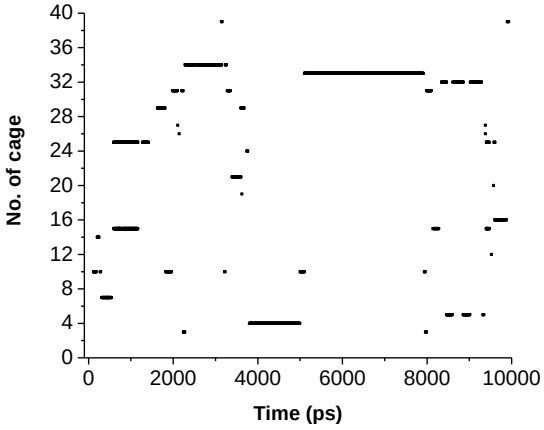

The cage molecule occupied by N_2 in amorphous **CC3** over a 10 ns MD simulation

Figure 15. The cage molecules occupied by H_2 and N_2 in amorphous **CC1** and **CC3** during the 10 ns MD simulation

To check the effect that the starting position had on the occupancy of the cages, the simulations were repeated for gas molecules randomly placed at different starting positions. These included both inside cages and at interstitial sites between cages. Summarising the results in Table 4 shows that different starting positions of H_2 molecule in amorphous **CC1** and **CC3** does not have a significant influence on H_2 diffusion. More than 80 % of the cages are occupied over a 3 ns simulation of H_2 diffusion in both amorphous **CC1** and **CC3**. When different starting positions are analysed for N_2, it is clear that different starting positions affects the cage occupancy for N_2 diffusion in amorphous **CC1** and **CC3**. For example, 40 % cage occupancy is

observed for N_2 diffusion in amorphous **CC3** when the N_2 starting position is inside the cage, whereas 17.5 % cages are occupied when the N_2 starting position is between cages.

Table 4. Comparison of cumulative cage occupancy for H_2 and N_2 in amorphous **CC1** and **CC3** with different starting positions.

Gas molecule	Host	Gas position	Production time of simulation	Print steps	Percentage of cages occupied
H2	Amorphous **CC1**	Inside cages	3 ns	500	82.5 **%**
H2	Amorphous **CC1**	Interstitial site between cages	3 ns	500	85 **%**
N2	Amorphous **CC1**	Inside cages	3 ns	500	10 **%**
N2	Amorphous **CC1**	Interstitial site between cages	3 ns	500	22.5 **%**
H2	Amorphous **CC3**	Inside cages	3 ns	500	95 **%**
H2	Amorphous **CC3**	Interstitial site between cages	3 ns	500	85 **%**
N2	Amorphous **CC3**	Inside cages	3 ns	500	40 **%**
N2	Amorphous **CC3**	Interstitial site between cages	3 ns	500	17.5 **%**

To confirm the inaccessibility of the non-occupied cages, a N_2 molecule was placed in a cage which had not been occupied in the previous MD simulation in both amorphous **CC1** and **CC3**. The models were subjected to 8 ns NPT MD simulations. Analysis of the cage occupancy for these models showed that the percentage of cages occupied by N_2 in amorphous **CC1** is 7.5 % (only 3 cage molecules occupied) compared with 42. % cage occupancy in the previous simulation (N_2 was randomly placed as the starting position) in Table 5. This indicates that the pore volume in amorphous **CC1** is not well connected for N_2 leading to isolated voids and hence N_2 diffusion is restricted. It also shows that N_2 diffusion in amorphous **CC1** is

significantly dependent on the starting position of the gas molecule. To some extent, it suggests that amorphous **CC1** is not porous to N_2. The cage occupancy for N_2 in amorphous **CC3** is 45 % when the starting position of N_2 molecule is placed randomly. Furthermore, the 50 % cage occupancy is observed when the N_2 is placed in the non-occupied cage in the previous simulation. Although the cage occupancy is different for different N_2 starting positions in amorphous **CC3**, N_2 diffusion in restricted areas is not observed and the majority of cages are accessible for N_2 diffusion.

Table 5. Comparison of cumulative cage occupancy for H_2 and N_2 placed in the non-occupied cage in amorphous **CC1** and **CC3** to check inaccessibility.

Gas molecule	Host	Gas starting position	Production time of simulation (ns)	Print steps	Percentage of cages occupied
N_2	Amorphous **CC1**	Randomly	8	500	42.5 %
N_2	Amorphous **CC1**	The non-occupied cage in the previous simulation	8	500	7.5 %
N_2	Amorphous **CC3**	Randomly	8	500	45 %
N_2	Amorphous **CC3**	The non-occupied cage in the previous simulation	8	500	50 %

4. Cumulative occupied cages by a H_2 or N_2 in amorphous **CC1** and **CC3**.

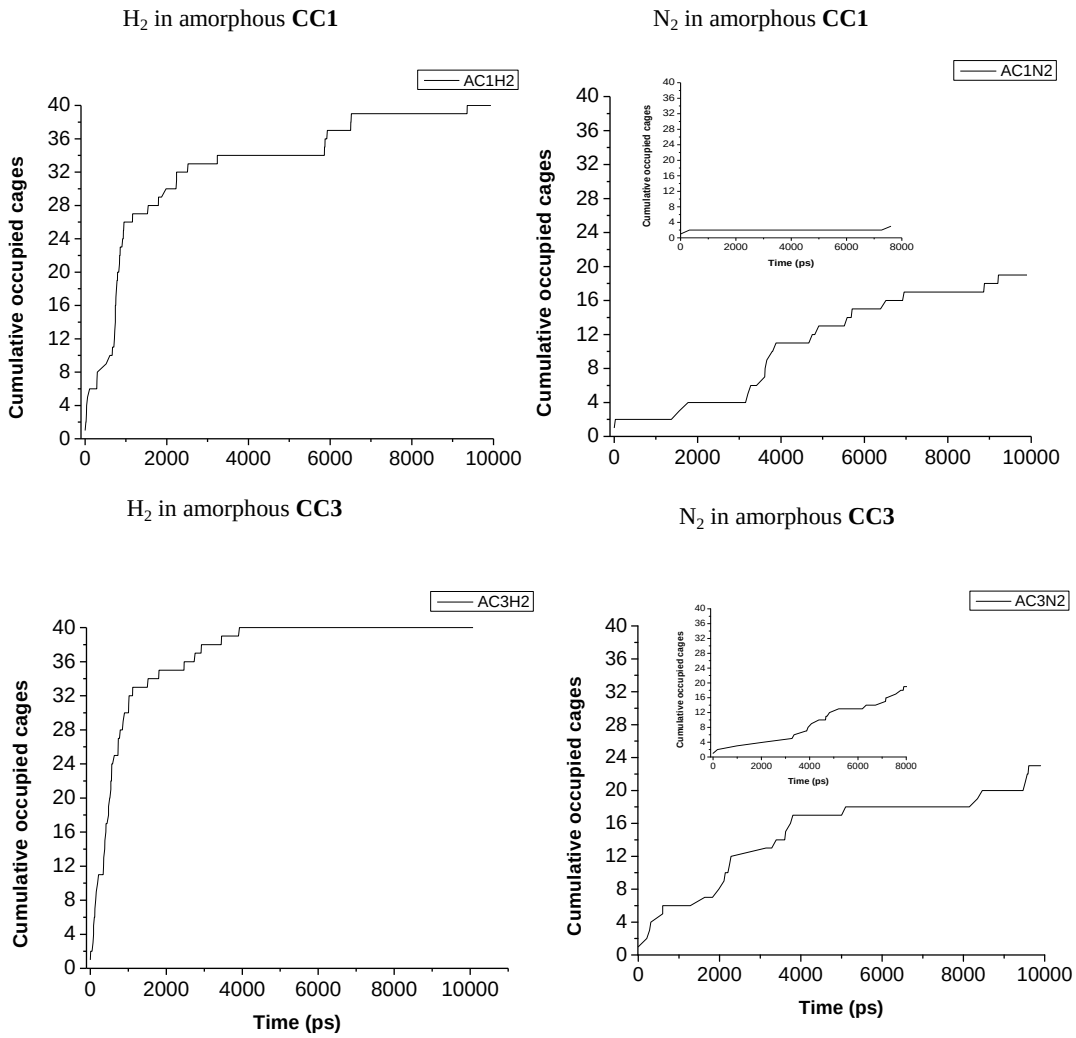

Figure 16. Cumulative occupied cages during the MD simulation for H_2 and N_2 diffusion in amorphous **CC1** and **CC3** respectively. Two different starting positions included for N_2 diffusion in amorphous **CC1** and **CC3**.

Figure 16 demonstrates the cumulative number of cages occupied by a H_2 or N_2 gas molecule over a 10 ns simulation time in the amorphous **CC1** and **CC3** systems. As shown, the time taken for H_2 molecules to diffuse into all 40 cages in amorphous **CC1** was approximately 10 ns, whereas, in amorphous **CC3**, the time was 5 ns. This indicates that H_2 in amorphous **CC3** can diffuse faster than H_2 in amorphous **CC1**. The cumulative cage occupancy for N_2 in amorphous **CC1** and **CC3** is shown in Figure 16 and Table 6.

Table 6. A comparison of the time of 10 % cage occupancy for N_2 diffusion in amorphous **CC1** and **CC3** with N_2 starting in different positions.

N_2 starting position	The time of 10 % cage occupancy for N_2 in amorphous **CC1**	The time of 10 % cage occupancy for N_2 in amorphous **CC3**
N_2 starting position 1	~ 3800 ps	~ 2000 ps
N_2 starting position 2	$>$ 8000 ps	~ 4000 ps

As noted previously, N_2 diffusion in amorphous **CC1** and **CC3** is dependent on the starting positions. All 40 cages are not occupied by N_2 during a 10 ns simulation for both amorphous **CC1** and **CC3** systems shown in Figure 16. Table 6 shows a comparison of the time of 10 % cage occupancy for N_2 diffusion in amorphous **CC1** and **CC3** with different N_2 starting positions. The time at which 10 % cage occupancy observed for N_2 diffusion in amorphous **CC1** is ~ 3800 ps and $>$ 8000 ps, respectively with different N_2 starting positions. One of the starting positions in amorphous **CC1** results in restricted N_2 diffusion and only 3 cage molecules are visited by N_2 during an 8 ns NPT MD simulation. In amorphous **CC3**, the time for 10 % cage occupancy for N_2 diffusion is ~ 2000 ps and ~ 4000 ps, respectively. The results indicate a faster diffusion in amorphous **CC3** than **CC1**.

6.6.2 Gas hopping analysis

Molecular simulations of a H_2 or N_2 in amorphous **CC1** and **CC3** were run for 10 ns using an NPT ensemble for gas hopping analysis. The total number of window hop and true hop are calculated in this work. A window hop is where a gas molecule moves from the cage window and then back to its original cavity. A true hop is defined as the movement of a gas molecule through the cage window to a different cage.

In order to check the effect of the time interval for sampling the trajectory on the gas hopping analysis, a 500 ps MD simulation of N_2 diffusion in amorphous **CC3** was carried out with a various steps of printing trajectory. Table 7 shows that the number of window hops is significantly dependent on how frequently the trajectory is printed. For example, the number of window hops is 4531 when the trajectory is printed every 100 steps, however, the number of window hop becomes 481 when printing the trajectory every 1000 steps. Unlike the window hops, the number of true hops is kept constant with different time interval for printing the trajectory as it is a less frequent event. It is noted that a large number of window hops occurred for N_2 diffusion in amorphous **CC3**. If the trajectory is printed every 100 steps, the window hop is roughly 1000 times more frequent than the true hop.

Table 7. Calculating the number of window hops and true hops with various trajectory printing frequencies.

Simulation ID	Production time of the simulation	Print trajectory	The number of 'Window hops'	The number of 'True hops'
1	500 ps	Every 1000 steps	481	3
2	500 ps	Every 500 steps	946	3
3	500 ps	Every 200 steps	2306	3
4	500 ps	Every 100 steps	4531	3

Table 8. Calculated time for one true hops for H_2 and N_2 in amorphous **CC1** and **CC3** respectively.

Gas molecule	Host	Production time of simulation	Print trajectory	The number of True hops	Percentage of cages occupied	Calculated time for 1 true hop
H_2	Amorphous **CC1**	10 ns	Every 200 steps	818	40/40 = 100 %	12.2 ps
N_2	Amorphous **CC1**	10 ns	Every 200 steps	164	19/40 = 47.5 %	61.0 ps
H_2	Amorphous **CC3**	10 ns	Every 200 steps	739	40/40 = 100 %	13.5 ps
N_2	Amorphous **CC3**	10 ns	Every 200 steps	521	22/40 = 55 %	19.2 ps

Table 8 reports the number of true hops for the H_2 or N_2 in the amorphous cage systems during the 10 ns MD simulations. The number of true hops for H_2 in amorphous **CC1** and **CC3** is 818 and 739 respectively. The time of one true hop for H_2 is similar in both amorphous cage systems. However the number of true hopping

for N_2 in amorphous **CC1** is 164 compared with 521 for amorphous **CC3**. The time of one true hop in amorphous **CC1** is 61 ps, three times longer than one true hop time of 19 ps for N_2 in amorphous **CC3**.

The hopping analysis indicates that N_2 diffusion is hindered in amorphous **CC1** in comparison to H_2 diffusion in amorphous **CC1**, presumably due to the smaller size of the H_2 gas molecule. Amorphous **CC3** has a larger amount of accessible pore volume and greater connectivity, therefore allowing the N_2 or H_2 molecule diffuse faster. The results are consistent with the observations from cage occupancy analysis.

6.6.3 The trajectories of gas molecules in amorphous CC1 and CC3

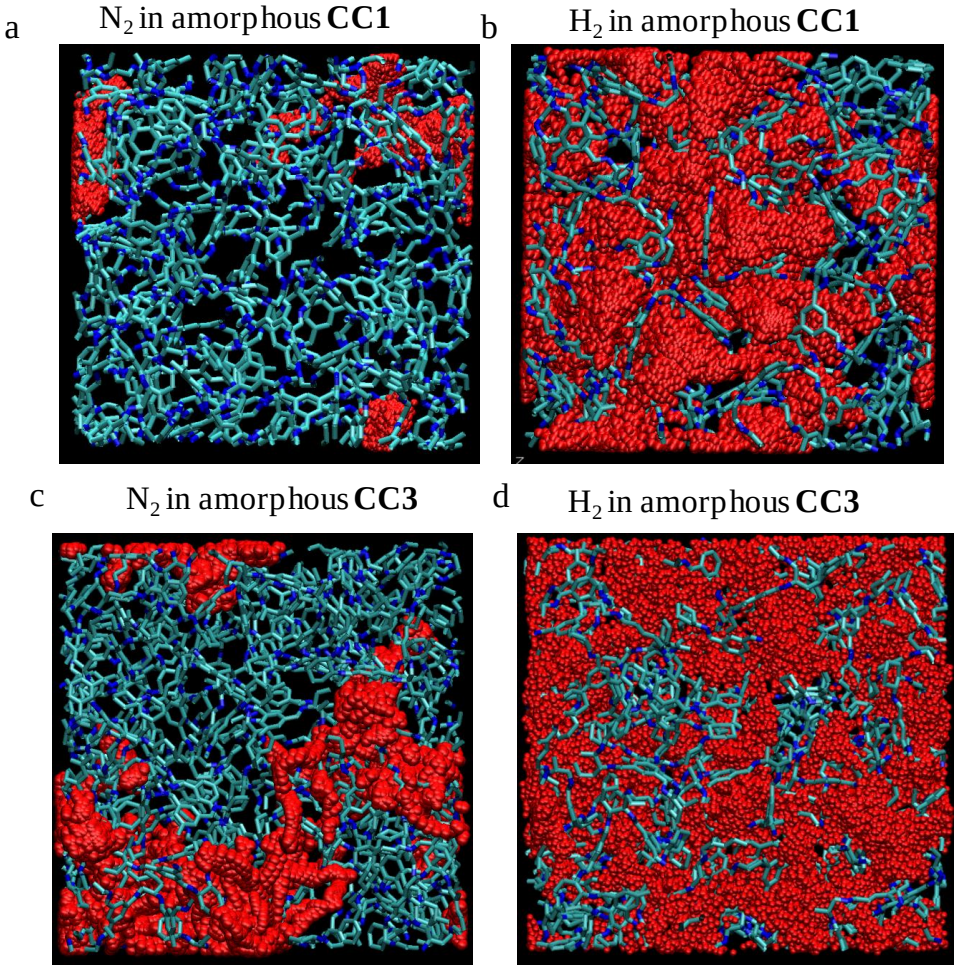

Figure 17. The trajectories of H_2 or N_2 in amorphous cage systems. (a) N_2 trajectory in amorphous **CC1**. (b) H_2 trajectory in amorphous **CC1**. (c) N_2 trajectory in amorphous **CC3**. (d) H_2 trajectory in amorphous **CC3**.

Figure 17 shows the H_2 or N_2 trajectory in amorphous **CC1** and **CC3** during a 3 ns NPT simulation with every 0.1 ps step sampling. The simulation temperature is 300 K. The results show that the H_2 molecule has a broader range of displacement compared with N_2 in both amorphous **CC1** and **CC3**. N_2 diffusion is in a limited region in amorphous **CC1** as shown in Figure 17 (a). The N_2 in amorphous **CC3** is able to access a greater range of cages than N_2 in amorphous **CC1**. The difference in the range of trajectory between H_2 and N_2 in amorphous **CC1** indicates the gas selectivity of amorphous **CC1** which is porous to H_2, but not to N_2. Amorphous **CC3** is porous to both H_2 and N_2.

6.7 Self-diffusivities of H_2/N_2 in amorphous cage systems to correlate the observation

MD simulations were performed to study the self-diffusivities of N_2 and H_2 in amorphous **CC1** and amorphous **CC3**. The simulations were run using NVT ensemble for one gas molecule loaded in each model. The total production run is 4 x10^7 MD steps (20 ns) and with each MD system was equilibrated with 1 x 10^5 MD steps. The trajectory was generated every 2000 steps.

The self-diffusivity describes a movement of a molecule diffusing through a system. It can be determined by the mean square displacement of molecular trajectories after t time. It is defined using the Einstein expression:

$$D_s(c) = \lim_{t\to\infty} \frac{1}{6t} \langle \left| \underset{r}{\rightarrow}(t) - \underset{r}{\rightarrow}(0) \right|^2 \rangle \quad (6.1)$$

$\underset{r}{\rightarrow}(t)$ is the position vector of a diffusing molecule at time t. $\underset{r}{\rightarrow}(t) - \underset{r}{\rightarrow}(0)$ is the vector distance travelled by a diffusing molecule over time interval of the length t. The angular brackets indicate an ensemble average.

Theoretically, self diffusion coefficients D_s can only be accurately calculated when t is close to ∞. Therefore, in MD simulations, a longer simulation time is required to give a reliable value. Here, a simulation time of 20 ns was used to improve the

statistics in this work. Figure 18 shows the simulated mean square displacements (MSD) plots for H_2 and N_2 in amorphous **CC1** and **CC3**. At extremely short times, the motion of the gas molecule is ballistic and the equation can be written as $\langle \left| \underset{r}{\rightarrow}(t) - \underset{r}{\rightarrow}(0) \right|^2 \rangle \sim t^2$, therefore the slope of logarithmic plot of MSD is 2.[31] There is an intermediate region after the ballistic motion on the MSD plot and the slope of logarithmic plot is 0.5.[31] The motion of gas molecule in this region is single file diffusion. Normal diffusion occurs when the slope of logarithmic plot is 1.[31] The self-diffusivities for H_2 and N_2 in amorphous cage systems were determined from the data of normal diffusion region. For the normal diffusion, the MSDs should increase linearly with the time which was observed in Figure 18. The self-diffusivities were calculated in a linear range, 2000 ps $<$ t $<$ 3000 for H_2 in amorphous **CC1**, 8000 ps $<$ t $<$ 10000 ps for N_2 in amorphous **CC1**, 2000 ps $<$ t $<$ 3000 ps and 11000 ps $<$ t $<$ 12000 ps for H_2 in amorphous **CC3**, and 12000 ps $<$ t $<$ 14000 ps for N_2 in amorphous **CC3**. Two different linear ranges are observed for H_2 in amorphous **CC3** in Figure 18 (a).

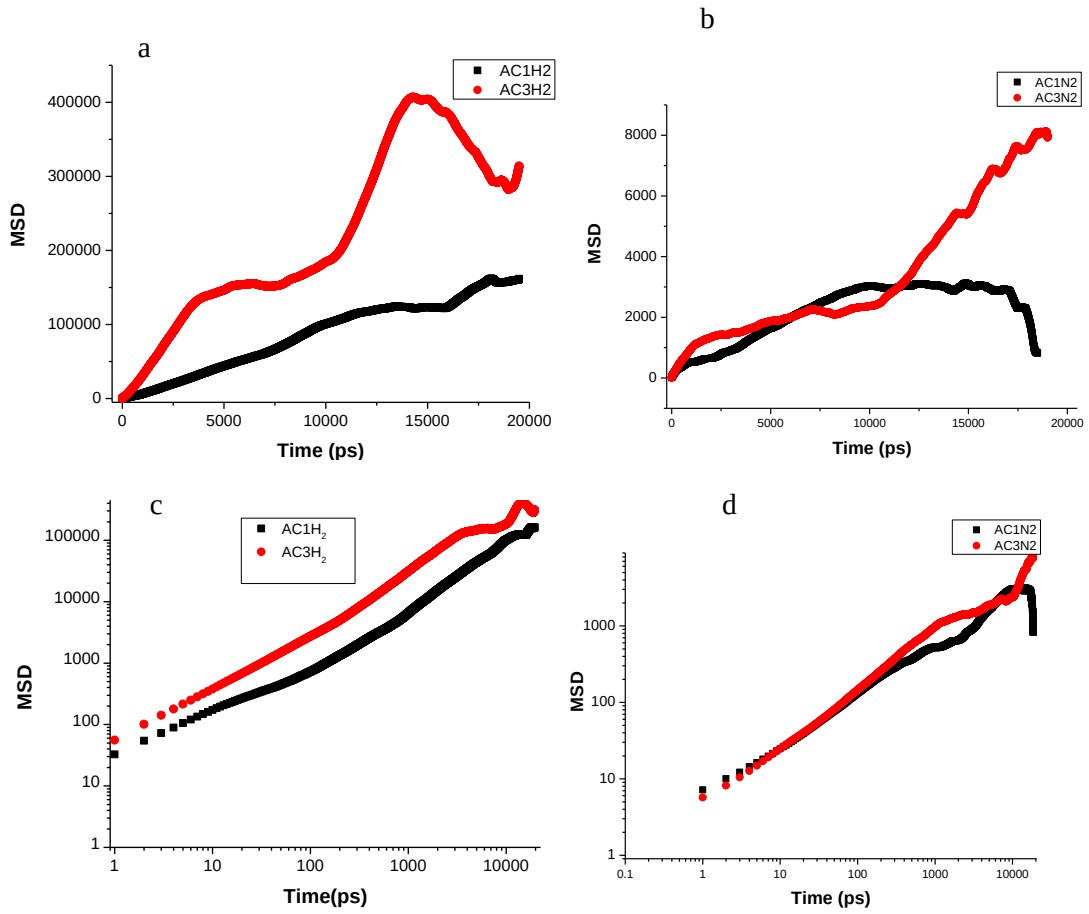

Figure 18. Mean square displacements (MSD) of H_2 and N_2 in amorphous **CC1** (black) and amorphous **CC3** (red). (a) The raw data plots of simulated MSD versus time for H_2 in amorphous **CC1** and amorphous **CC3**. (b) N_2 in amorphous **CC1** and amorphous **CC3**. (c, d) logarithmic plots of simulated MSD versus time.

The calculated self-diffusivities at 300 K are 1.1 x 10^{-7} m^2/s or 2.2 x 10^{-8} m^2/s for H_2 in amorphous **CC3**. The solvent accessible surface area calculated using a H_2 radius of 1.42 Å for the amorphous **CC3** model shows different diffusion areas in Figure 19. The large cavities allow H_2 diffusing faster and narrow channels or small cavities which can slow H_2 diffusion which results in different H_2 self-diffusivities.

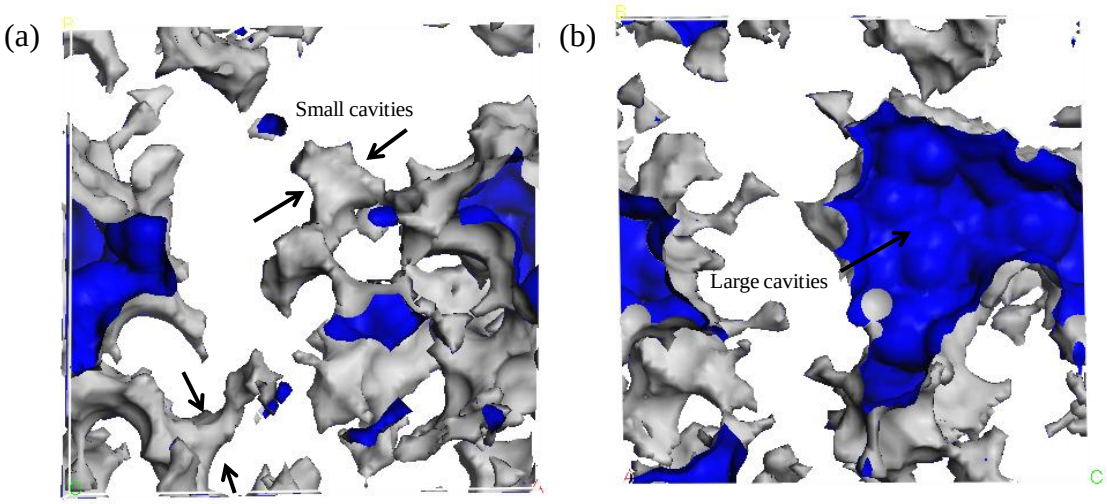

Figure 19. The solvent accessible surface area generated using a H_2 radius in amorphous **CC3** to show different diffusion areas, large accessible pore cavities and small and narrow pore cavities.

The self-diffusivities are 1.6 x 10^{-9} m^2/s for N_2 in amorphous **CC3**, 1.2 x 10^{-8} m^2/s for H_2 in amorphous **CC1**, and 3.0 x 10^{-10} m^2/s for N_2 in amorphous **CC3**, respectively. A smaller number of self-diffusivities indicate a slower diffusion. The gas diffusion in amorphous **CC1** is much slower than amorphous **CC3**. A comparison of self-diffusion coefficients was shown in the Table 9 between different types of porous materials. The H_2 and N_2 diffusion in amorphous **CC1** and **CC3** are much slower than MOF-5 due to a larger pore volume of MOF-5, but comparable to ZIF-68 and ZIF-70. [32]

Table 9. Summary of self-diffusion coefficients in selected porous materials.

Materials	BET Surface area (m^2/g)	Pore volume (cm^3/g)	T (K)	*Ds* (m^2/s)	Data type	Reference
ZIF-68	1090	0.552 (calculated with N_2 kinetic diameter)	300	$Ds(CO_2)$ = (1.5-8.0) x 10^{-10}	Simulation	[32a]
ZIF-70	1730	0.691 (calculated with N_2 kinetic diameter)	300	$Ds(CO_2)$ = (1.8-5.5) x 10^{-9}	Simulation	[32a]
MOF5	2250--3000	1.04	RT	$Ds(H_2)$ = (1.0 – 2.0) x 10^{-7}	Simulation	[32b]
MOF5	2250--3000	1.04	RT	$Ds(N_2)$ = 3.0 x 10^{-8}	Simulation	[32b]
ZIF-68	1090	0.552 (calculated with N_2 kinetic diameter)	298	$Ds(H_2)$ = 3.0 x 10^{-8}	Simulation	[32a]
ZIF-70	1730	0.691 (calculated with N_2 kinetic diameter)	298	$Ds(H_2)$ = 2.0 x 10^{-7}	Simulation	[32a]
Amorphous CC3	**854**	**0.29 (t-plot)**	**300**	***Ds*(H_2) =1.1 x 10^{-7} Or 2.2 x 10^{-8}**	**Simulation**	
Amorphous CC3	**854**	**0.29 (t-plot)**	**300**	***Ds*(N_2) = 1.6 x 10^{-9}**	**Simulation**	
Amorphous CC1	**N/A**	**N/A**	**300**	***Ds*(H_2) = 1.2 x 10^{-8}**	**Simulation**	
Amorphous CC1	**N/A**	**N/A**	**300**	***Ds*(N_2) = 3.0 x 10^{-10}**	**Simulation**	

6.8 A slab simulation to demonstrate the gas selectivity of amorphous CC1.

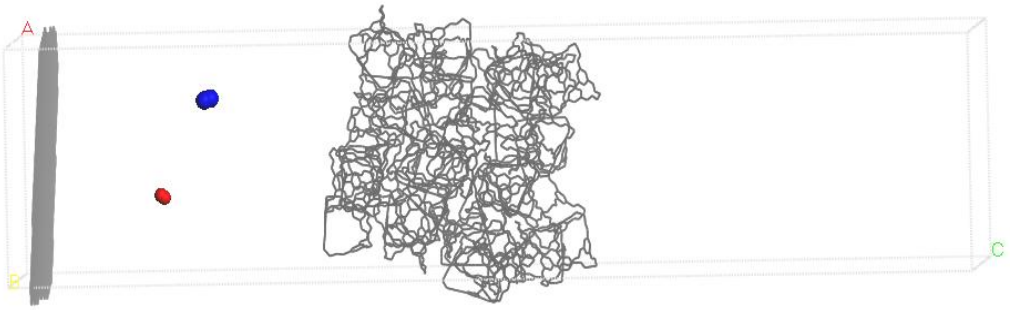

Figure 20. The starting configuration for multiple gas diffusion in amorphous **CC1**.

The objective of this simulation is to demonstrate gas diffusion and selectivity in amorphous **CC1**. A model was built as shown in Figure 20. The unit cell was 40 x 40 x 170 Å. A slab of amorphous **CC1** was placed in the middle of the cell consisting of 40 cages and 39 Å x 39 Å x 39 Å dimensions. A slab of graphite was used as a boundary which prevented gas molecules flowing in one direction. One N_2 (blue colour) and one H_2 (red colour) molecules were placed in the empty space between the graphite and the amorphous **CC1** slab. A simulation was performed using a NVE ensemble with a total production time of 8 ns and an equilibration time of 50 ps. The Verlet leapfrog algorithm was used to integrate the Newton equations. All the Lennard-Jones interactions were calculated with a cut off of 10 Å. The time step was 0.5 fs and periodic boundary conditions were applied. The simulation was performed at 100 K, a pressure of 1 atm. In addition, the atoms of graphite slab were fixed during MD simulation. Two cage molecules were fixed in order to prevent movement of the slab. The remaining cage molecules were allowed to be fully flexible during the simulation.

Figure 21 visualises the trajectories of the respective gas molecules through the amorphous **CC1**. The results are as follows: the H_2 molecule penetrates into the amorphous **CC1** slab. Occasionally it is observed that it diffuses back to the starting

position and travels back into the amorphous **CC1** slab. The trajectory shows that the H_2 molecule is able to diffuse through amorphous **CC1** slab and reach the other side of the slab. In contrast, N_2 is able to diffuse into the slab, but it is then trapped inside the cages, remaining in a limited area of the cage slab for the 8 ns simulation.

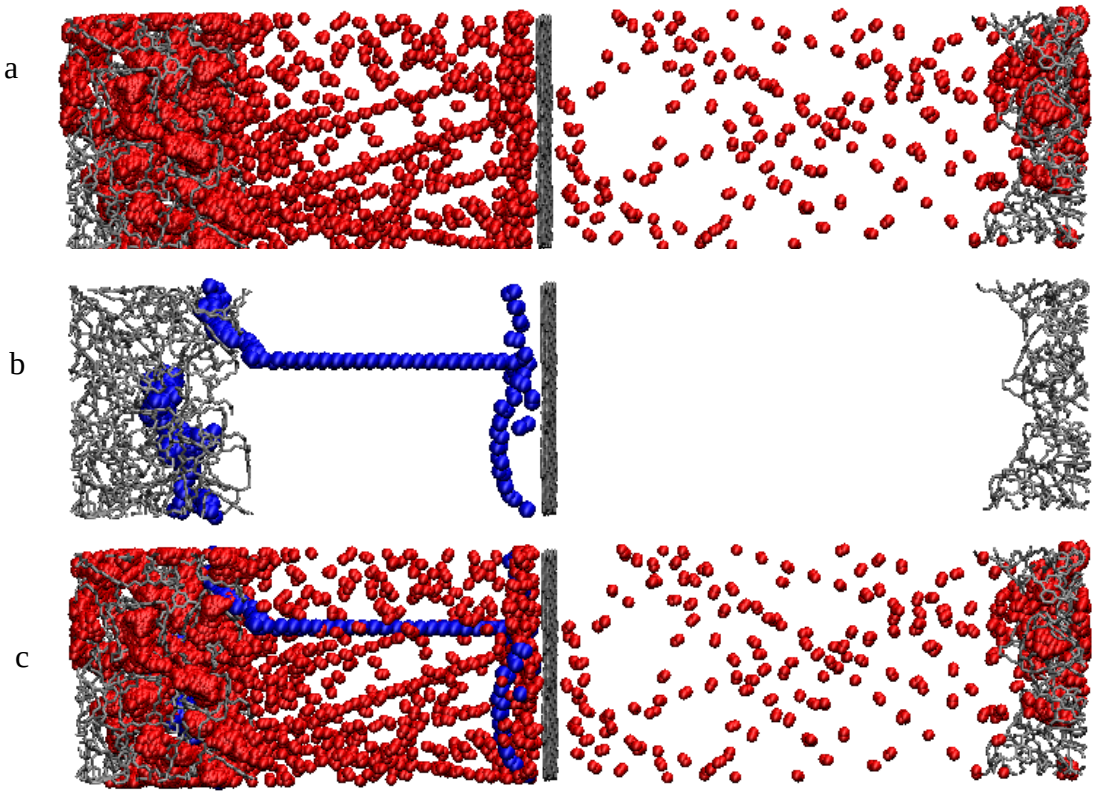

Figure 21. (a) H_2 diffusion trajectory of slab simulation (b) N_2 diffusion trajectory of slab simulation (c) Overlap H_2 and N_2 trajectories. The N_2 molecule is coloured blue and H_2 molecule is coloured red. The graphite and cages are coloured as grey.

6.9 Multiple gas molecules diffusion in the supercell of amorphous CC1 and amorphous CC3

Simulations were performed to investigate multiple gas molecules diffusion in amorphous cage systems. A 2 x 1 x 1 supercell was used for amorphous **CC1** and **CC3**. The supercell was loaded with 20 N_2 molecules or 20 H_2 molecules in amorphous **CC1** and **CC3** respectively. The initial configuration was shown in Figure 22. The gas molecules were placed at one side of the cell and form a thin layer. The simulation was performed in the NVT ensemble at 300 K and 1 atm pressure. The Verlet leapfrog algorithm was used and all the Lennard-Jones interactions were calculated with a cut off of 10 Å. The time step was 0.5 fs. A total simulation time was 3 ns with an equilibration time of 50 ps.

Figure 23 shows that H_2 molecules are able to diffuse through the whole cells in amorphous **CC1** and **CC3**. The pores are fully connected for H_2 in both amorphous **CC1** and **CC3**. The trajectory of N_2 molecules in amorphous **CC1** (Figure 23 b) shows a limited area due to a disconnecting pore volume. In contrast, N_2 molecules in amorphous **CC3** are able to access a broader range (Figure 23 d). The results from multiple gas molecules in the supercell of amorphous cage systems are consistent with the observations from the single gas molecule diffusion previously. The results clearly demonstrate a H_2/N_2 selectivity in amorphous **CC1** and amorphous **CC3** is non-selectively porous to H_2 and N_2.

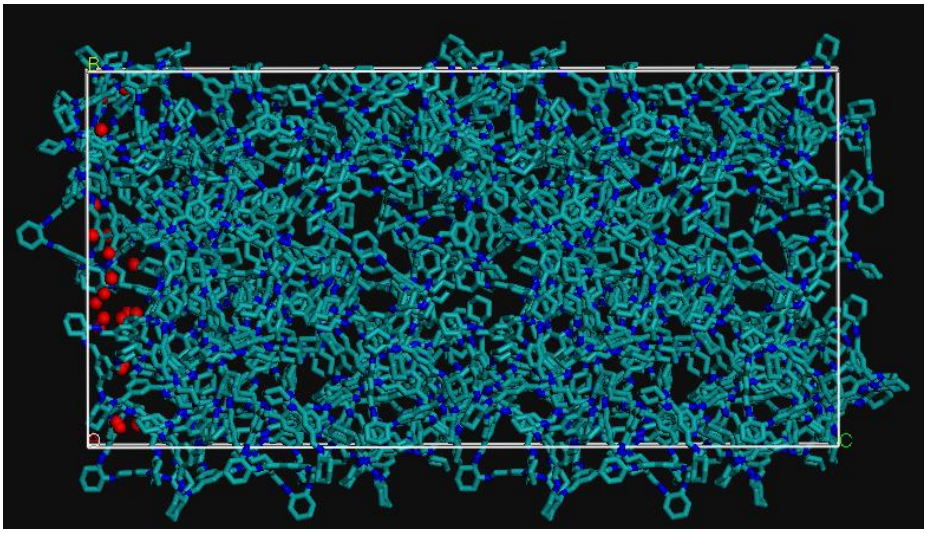

Figure 22. An example of the initial configuration of multiple gas molecules in amorphous cage systems. There are 20 H_2 molecules (red colour) in amorphous **CC3**.

a) H_2 in amorphous **CC1**

b) N_2 in amorphous **CC1**

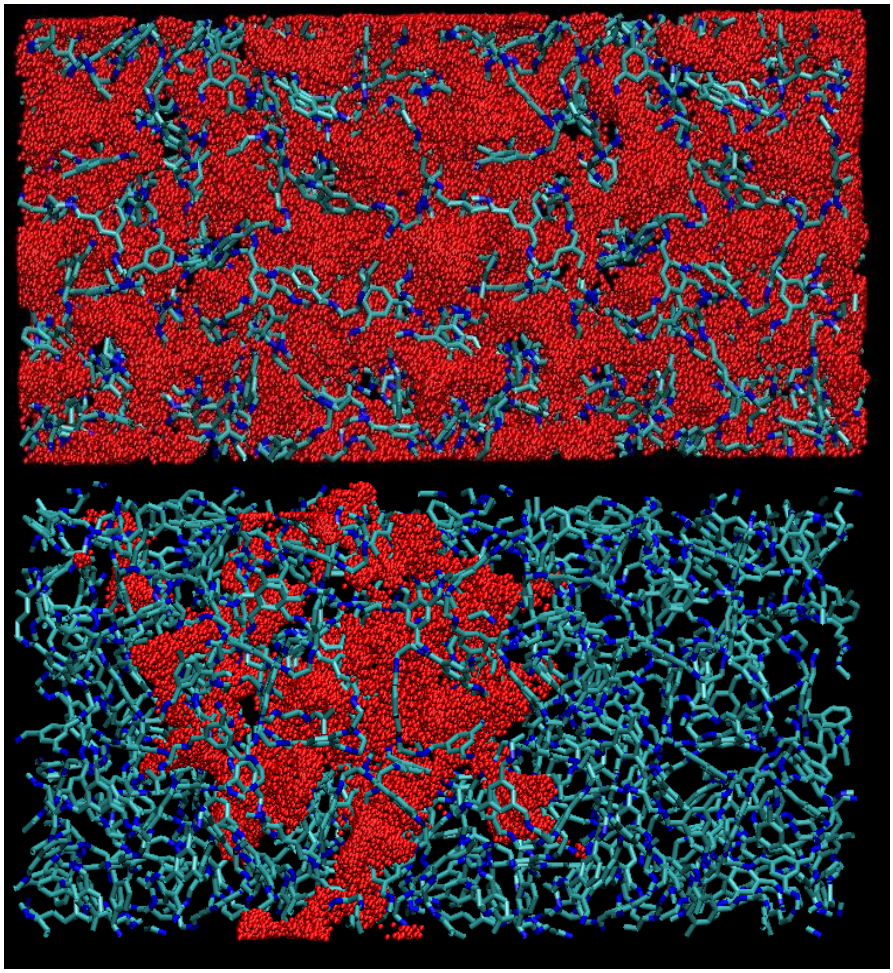

c) H_2 in amorphous **CC3**

d) N_2 in amorphous **CC3**

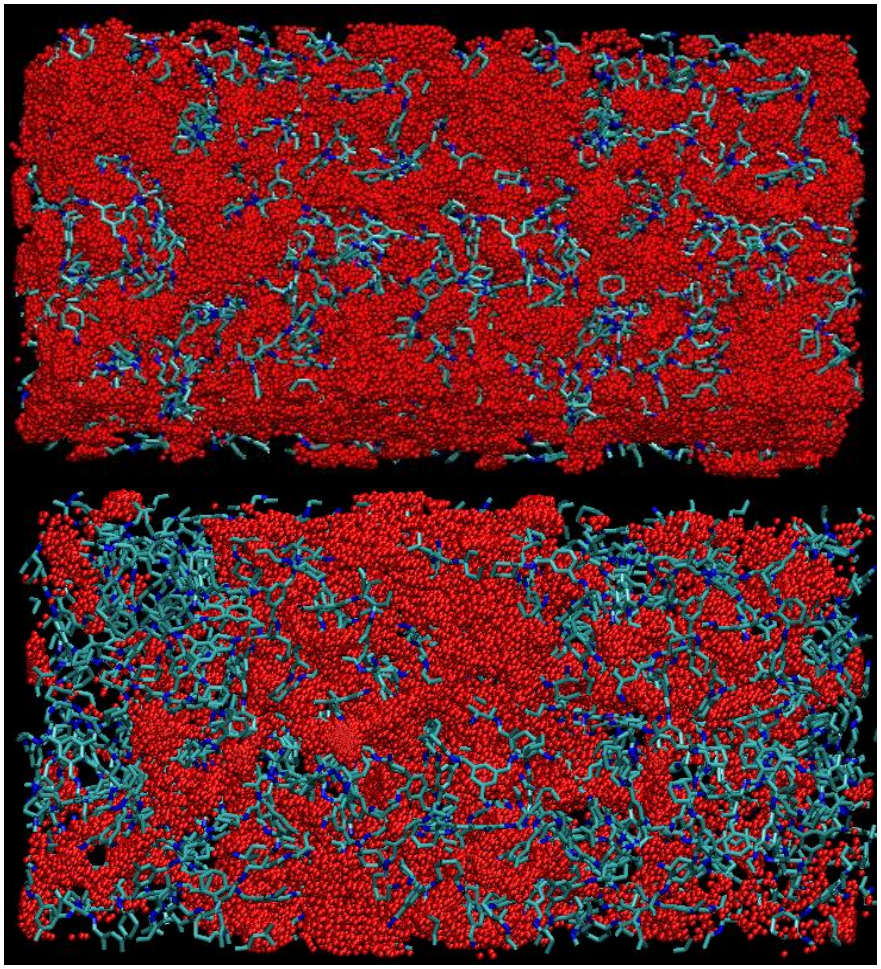

Figure 23. (a) 20 H_2 molecules diffusion trajectories in amorphous **CC1**. (b) 20 N_2 molecules diffusion trajectories in amorphous **CC1**. (c) 20 H_2 molecules diffusion trajectories in amorphous **CC3**. (d) 20 N_2 molecules diffusion trajectories in amorphous **CC3**.

The 20 N_2 molecules diffusion trajectories in amorphous **CC1** and **CC3** are generated during 0.25 ns, 1 ns, 2 ns and 3 ns simulation time respectively in Figure 24. The longest distance of N_2 molecules diffusion is plotted at each simulation time. The N_2 molecules in amorphous **CC1** diffuse in a limited area, and the diffusion area does not expand after 1 ns. The longest distance of N_2 molecules diffused in amorphous **CC1** is 69 Å at the simulation time of 3 ns. By contrast, N_2 molecules in amorphous **CC3** diffuse a broader area and the diffusion area is expanding over the simulation time. The longest distance of N_2 molecules diffused in amorphous **CC3** is

106 Å at 3 ns simulation time and N_2 molecules have diffused through the whole simulation cell.

(a)

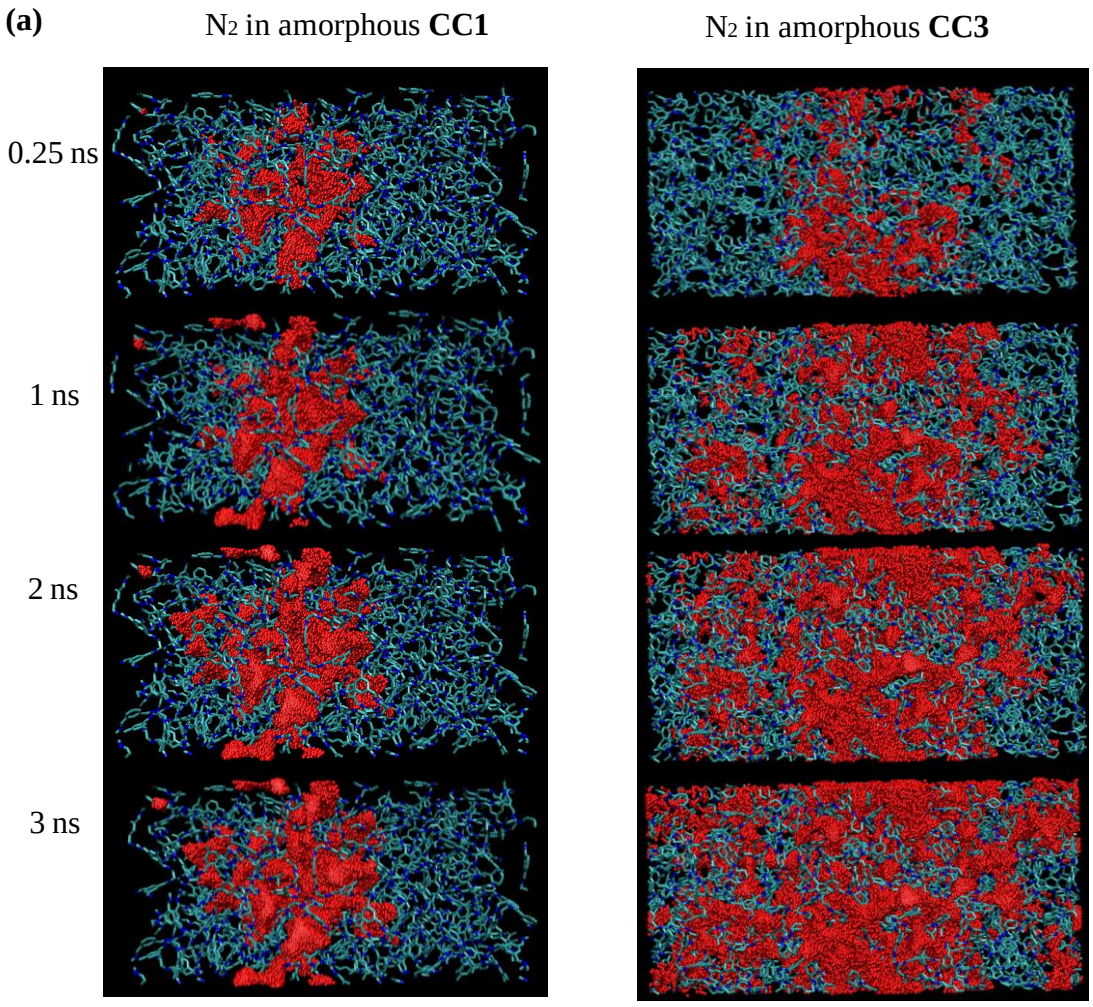

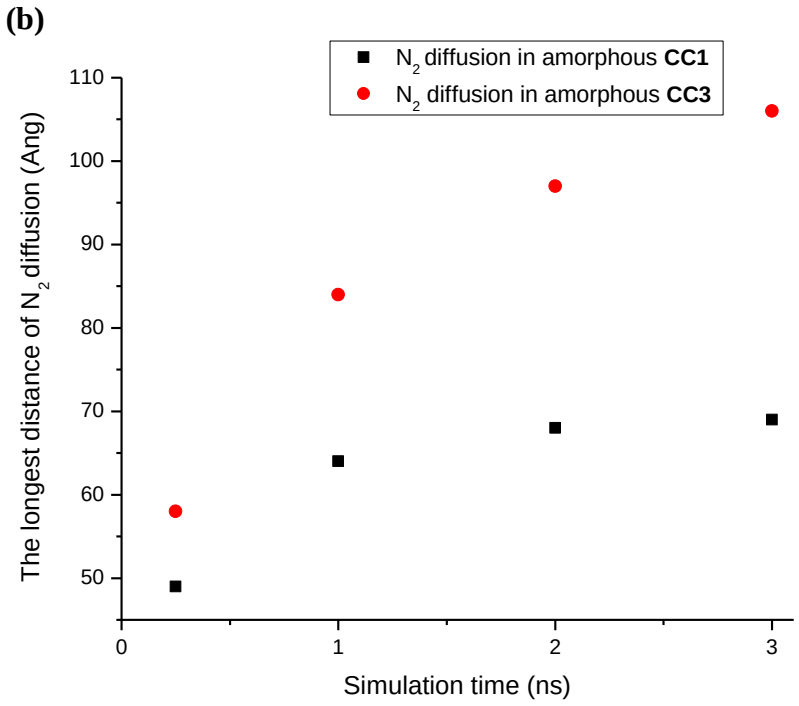

Figure 24. (a) The 20 N_2 molecules diffusion trajectories in amorphous **CC1** and **CC3** during 0.25 ns, 1 ns, 2 ns and 3 ns simulation time respectively. (b) The longest distance of N_2 molecules diffusion is plotted at each simulation time.

6.10 Network topological analysis

The analysis below attempts to map a diffusing connection between a pair of cage molecules for gas hopping in amorphous **CC1** and **CC3**. A PERL script was used to analyse gas hopping 'routes'. Like driving a vehicle on a road, **M**, **A** and **B** roads are introduced to classify the hopping. The motorways can clearly demonstrate the connected cage molecules for gas diffusion. The hopping network can be classified by the number of gas hops that occurred between two cages. We represent connection by an **M** motorway when the hopping number is above 20 over a 10 ns simulation. An **A** road is the one with hopping number ranging from 6 to 19. The hopping number for a **B** road is no more than 5. Figure 25 demonstrates the **M**, **A** and **B** motorways for N_2 and H_2 hopping in amorphous **CC3** respectively. The cage centre of mass was used to represent the cage molecule in the models. It should be noted that the connecting lines do not represent the diffusion pathways of gas molecules.

For N_2 diffusion in amorphous **CC3** in Figure 25 (a), cage No. 15 and cage No.25 were involved in a **M** motorway. The hopping number for these two cages was 479 during a 10 ns MD simulation which indicated that the majority of cage to cage hopping occurred in this area. A solvent accessible surface area of amorphous **CC3** using a N_2 probe radius of 1.82 Å is shown in Figure 26(a), and a pore channel existed between cage 15 (coloured as pink) and cage 25 (coloured as green). The extrinsic pore channel fully connected with the intrinsic voids in cage 25 as shown, but does not connect with cage 15 intrinsic voids in the static structure snapshot. Following the N_2 diffusion trajectory (red dots) in Figure 26 (b), it was observed N_2 molecule travelled along a channel from cage 25 to cage 15. The connection between the channel and cage 15 would be expected to form during simulation due to cooperative diffusion, as a result of the cage dynamic motion. No **A** road contributed to N_2 hopping in amorphous **CC3**.

In the case of H_2 diffusion in amorphous **CC3**, five **M** motorways were shown in Figure 25(d). The cage to cage connections occurred between cage 5 and cage 28, cage 15 and cage 25, cage 16 and cage 35, cage 19 and cage 23, cage 27 and cage 28, respectively. As solvent accessible surface areas using a H_2 probe shown in Figure 26(c), the hopping between these cages is attributed to the pore connectivity. A more complex **B** road network was displayed for H_2 hopping and all the cage molecules were involved which corresponded to interconnected pore structure.

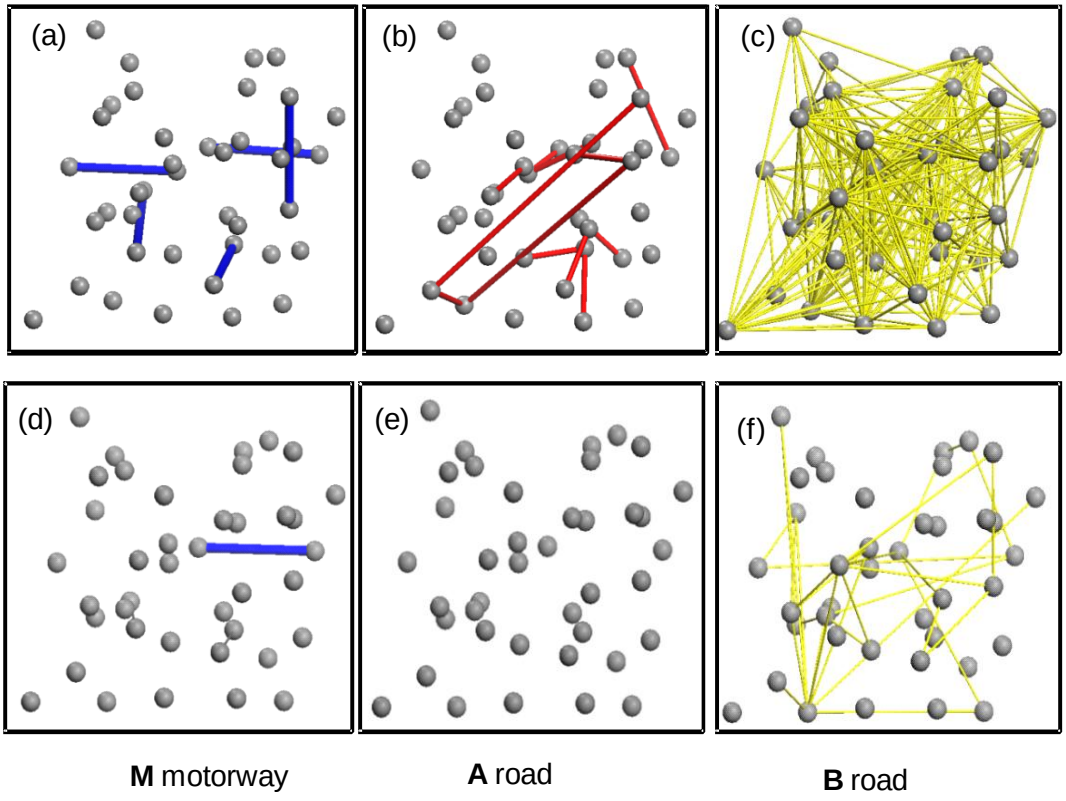

Figure 25. (a-c) M motorway, A and B roads for N_2 in amorphous **CC3**. (d-f) M motorway, A and B roads for H_2 in amorphous **CC3**.

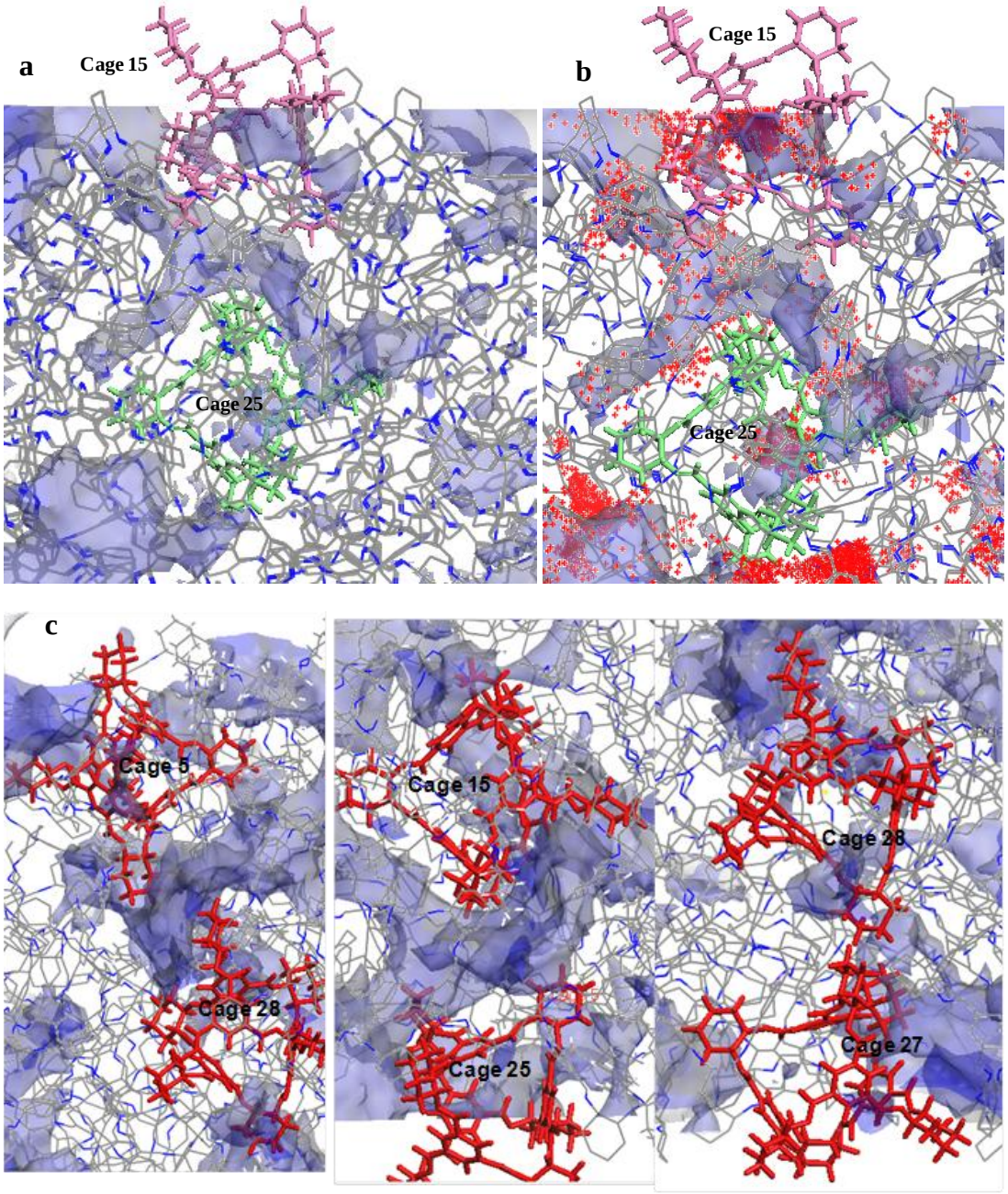

Figure 26. (a) A pore channel connecting cage 15 (pink one) and cage 25 (green one) for M motorway, N_2 diffusion in amorphous **CC3**. Solvent accessible surface areas generated using a N_2 probe radius of 1.82 Å. (b) N_2 trajectory following the pore channel hop between these two cage molecules. (c) Pore channels connecting cages for M motorway, H_2 diffusion in amorphous **CC3**. Solvent accessible surface areas generated using a H_2 probe radius of 1.42 Å.

6.11 Conclusions

In this study, we designed a simulation methodology for packing amorphous porous organic cages without feeding in target experimental density. The good agreement between structural properties of simulated samples and experimental data suggests that the method generates reliable structural models and represent bulk materials that can enable further characterisations. A small variation in physical properties is observed among the simulated samples attributed to the nature of amorphous materials. We correlate the dynamic information from the gas diffusion trajectories, hopping and self-diffusivities to rationalize gas selectivity in amorphous **CC1** and **CC3**. The simulation results reveal that N_2 diffusion is restricted in amorphous **CC1**, but H_2 can diffuse through the whole system which is corresponding to H_2/N_2 gas selectivity of 12 in the experiment. Furthermore, N_2 and H_2 diffusion in amorphous **CC3** is faster than **CC1** due to a larger accessible pore volume. The diffusion trajectories and hopping analysis show that amorphous **CC3** are porous to both H_2 and N_2.

We emphasize that the simulations provide the detailed information on the microscopic structures in these amorphous materials, including gas hopping, accumulative cage occupancy by gas molecules, residential times, and diffusion pathways, which can not be achieved by the experimental techniques. We also obtain self-diffusivities of H_2 and N_2 in amorphous **CC1** and **CC3** respectively which verify dynamic diffusion and experimental observations. The MD simulations were carried out with different structural samples to provide statistical data for predicting properties of amorphous materials. This methodology will be applicable to apply to other classes of molecules structure generation and prediction of gas diffusion properties.

6.12 Chapter acknowledgements

In this chapter, I would like to thank Andy and Abbie for their supervision and suggestions on my work. Dan Holden designed the Cage Specific Force Field (CSFF) for this work. Kim Jelfs wrote up all PERL scripts for gas hopping analysis. Tom Hasell carried out the experiments for amorphous **CC1** and **CC3**.

6.13 References

1. (a) Jiang, S.; Jones, J. T. A.; Hasell, T.; Blythe, C. E.; Adams, D. J.; Trewin, A.; Cooper, A. I., Porous organic molecular solids by dynamic covalent scrambling. *Nat. Commun.* **2011,** *2*, 207; (b) Hasell, T.; Chong, S. Y.; Jelfs, K. E.; Adams, D. J.; Cooper, A. I., Porous Organic Cage Nanocrystals by Solution Mixing. *J. Am. Chem. Soc.* **2011,** *134* (1), 588-598.
2. (a) Duren, T.; Bae, Y.-S.; Snurr, R. Q., Using molecular simulation to characterise metal-organic frameworks for adsorption applications. *Chem. Soc. Rev.* **2009,** *38* (5), 1237-1247; (b) Getman, R. B.; Bae, Y.-S.; Wilmer, C. E.; Snurr, R. Q., Review and Analysis of Molecular Simulations of Methane, Hydrogen, and Acetylene Storage in Metal–Organic Frameworks. *Chem. Rev.* **2011,** *112* (2), 703-723.
3. (a) Krishna, R., Diffusion in porous crystalline materials. *Chem. Soc. Rev.* **2012,** *41* (8), 3099-3118; (b) Tian, J.; Thallapally, P. K.; McGrail, B. P., Porous organic molecular materials. *CrystEngComm* **2012,** *14* (6), 1909-1919.
4. (a) Heuchel, M.; Fritsch, D.; Budd, P. M.; McKeown, N. B.; Hofmann, D., Atomistic packing model and free volume distribution of a polymer with intrinsic microporosity (PIM-1). *J. Membr. Sci.* **2008,** *318* (1–2), 84-99; (b) Hofmann, D.; Fritz, L.; Ulbrich, J.; Schepers, C.; Böhning, M., Detailed-atomistic molecular modeling of small molecule diffusion and solution processes in polymeric membrane materials. *Macromol. Theory Simul.* **2000,** *9* (6), 293-327; (c) Hofmann, D.; Heuchel, M.; Yampolskii, Y.; Khotimskii, V.; Shantarovich, V., Free Volume Distributions in Ultrahigh and Lower Free Volume Polymers: Comparison between Molecular Modeling and Positron Lifetime Studies. *Macromolecules* **2002,** *35* (6), 2129-2140.
5. Lim, S. Y.; Tsotsis, T. T.; Sahimi, M., Molecular simulation of diffusion and sorption of gases in an amorphous polymer. *J. Chem. Phys.* **2003,** *119* (1), 496-504.
6. Curco, D.; Aleman, C., Simulation of dense amorphous polymers by generating representative atomistic models. *J. Chem. Phys.* **2003,** *119* (5), 2915-2922.
7. Budd, P. M.; Ghanem, B. S.; Makhseed, S.; McKeown, N. B.; Msayib, K. J.; Tattershall, C. E., Polymers of intrinsic microporosity (PIMs): robust, solution-processable, organic nanoporous materials. *Chem. Commun.* **2004,** (2), 230-231.
8. Lee, J.-Y.; Wood, C. D.; Bradshaw, D.; Rosseinsky, M. J.; Cooper, A. I., Hydrogen adsorption in microporous hypercrosslinked polymers. *Chem. Commun.* **2006,** (25), 2670-2672.
9. Cooper, A. I., Conjugated Microporous Polymers. *Adv. Mater.* **2009,** *21* (12), 1291-1295.
10. Trewin, A.; Willock, D. J.; Cooper, A. I., Atomistic Simulation of Micropore Structure, Surface Area, and Gas Sorption Properties for Amorphous Microporous Polymer Networks. *J. Phys. Chem. C* **2008,** *112* (51), 20549-20559.
11. Abbott, L. J.; Colina, C. M., Atomistic Structure Generation and Gas Adsorption Simulations of Microporous Polymer Networks. *Macromolecules* **2011,** *44* (11), 4511-4519.

12. Larsen, G. S.; Lin, P.; Hart, K. E.; Colina, C. M., Molecular Simulations of PIM-1-like Polymers of Intrinsic Microporosity. *Macromolecules* **2011,** *44* (17), 6944-6951.
13. (a) Krishna, R.; van Baten, J. M., Describing Mixture Diffusion in Microporous Materials under Conditions of Pore Saturation. *J. Phys. Chem. C* **2010,** *114* (26), 11557-11563; (b) Krishna, R., Describing the Diffusion of Guest Molecules Inside Porous Structures. *J. Phys. Chem. C* **2009,** *113* (46), 19756-19781.
14. Alavi, S.; Afagh, N. A.; Ripmeester, J. A.; Thompson, D. L., Molecular Dynamics Simulations of p-tert-Butylcalix[4]arene with Small Guest Molecules. *Chem. Eur. J.* **2006,** *12* (20), 5231-5237.
15. Alavi, S.; Woo, T. K.; Sirjoosingh, A.; Lang, S.; Moudrakovski, I.; Ripmeester, J. A., Hydrogen Adsorption and Diffusion in p-tert-Butylcalix[4]arene: An Experimental and Molecular Simulation Study. *Chem. Eur. J.* **2010,** *16* (38), 11689-11696.
16. El-Barghouthi, M. I.; Assaf, K. I.; Rawashdeh, A. M. M., Molecular Dynamics of Methyl Viologen-Cucurbit[n]uril Complexes in Aqueous Solution. *J. Chem. Theory Comput.* **2010,** *6* (4), 984-992.
17. (a) Bharadwaj, R. K.; Boyd, R. H., Small molecule penetrant diffusion in aromatic polyesters: a molecular dynamics simulation study. *Polymer* **1999,** *40* (15), 4229-4236; (b) Pavel, D.; Shanks, R., Molecular dynamics simulation of diffusion of O_2 and CO_2 in amorphous poly(ethylene terephthalate) and related aromatic polyesters. *Polymer* **2003,** *44* (21), 6713-6724; (c) Seong Y. Lim, T. T. T., and Muhammad Sahimi, Molecular simulation of diffusion and sorption of gases in an amorphous polymer. *J. Chem. Phys.* **2003,** *119* (1).
18. Seong Y. Lim, T. T. T., and Muhammad Sahimi, Molecular simulation of diffusion and sorption of gases in an amorphous polymer *J. Chem. Phys.* **2003,** *119* (1), 9.
19. (a) Meunier, M., Diffusion coefficients of small gas molecules in amorphous cis-1,4-polybutadiene estimated by molecular dynamics simulations. *J. Chem. Phys.* **2005,** *123* (13), 134906-7; (b) Charati, S. G.; Stern, S. A., Diffusion of Gases in Silicone Polymers: Molecular Dynamics Simulations. *Macromolecules* **1998,** *31* (16), 5529-5535.
20. Jones, J. T. A.; Holden, D.; Mitra, T.; Hasell, T.; Adams, D. J.; Jelfs, K. E.; Trewin, A.; Willock, D. J.; Day, G. M.; Bacsa, J.; Steiner, A.; Cooper, A. I., On–Off Porosity Switching in a Molecular Organic Solid. *Angew. Chem. Int. Ed.* **2011,** *50* (3), 749-753.
21. Daniel Holden, K. E. J., Andrew I. Cooper, Abbie Trewin, and David J. Willock, A Bespoke Force Field for Simulating the Molecular Dynamics of Porous Organic Cages. *Journal Phys Chem C* **2012**. (**DOI:** 10.1021/jp305129w)
22. Sun, H., Ab initio calculations and force field development for computer simulation of polysilanes. *Macromolecules* **1995,** *28* (3), 701-712.
23. M. J. Frisch, G. W. T., H. B. Schlegel, G. E. Scuseria, M. A. Robb, J. R. Cheeseman, G. Scalmani, V. Barone, B. Mennucci, G. A. Petersson, H. Nakatsuji, M. Caricato, X. Li, H. P. Hratchian, A. F. Izmaylov, J. Bloino, G. Zheng, J. L.

Sonnenberg, M. Hada, M. Ehara, K. Toyota, R. Fukuda, J. Hasegawa, M. Ishida, T. Nakajima, Y. Honda, O. Kitao, H. Nakai, T. Vreven, J. A. Montgomery, Jr., J. E. Peralta, F. Ogliaro, M. Bearpark, J. J. Heyd, E. Brothers, K. N. Kudin, V. N. Staroverov, R. Kobayashi, J. Normand, K. Raghavachari, A. Rendell, J. C. Burant, S. S. Iyengar, J. Tomasi, M. Cossi, N. Rega, J. M. Millam, M. Klene, J. E. Knox, J. B. Cross, V. Bakken, C. Adamo, J. Jaramillo, R. Gomperts, R. E. Stratmann, O. Yazyev, A. J. Austin, R. Cammi, C. Pomelli, J. W. Ochterski, R. L. Martin, K. Morokuma, V. G. Zakrzewski, G. A. Voth, P. Salvador, J. J. Dannenberg, S. Dapprich, A. D. Daniels, Ö. Farkas, J. B. Foresman, J. V. Ortiz, J. Cioslowski, and D. J. Fox, Gaussian, Inc., Wallingford CT, 2009.

24. Smith, W.; Yong, C. W.; Rodger, P. M., DL_POLY: Application to molecular simulation. *Mol. Simul.* **2002,** *28* (5), 385-471.

25. Hockney, R. W., The potential calculation and some applications. *Methods in Computational Physics* **1970,** *9*, 135-211.

26. Rappe, A. K.; Casewit, C. J.; Colwell, K. S.; Goddard, W. A.; Skiff, W. M., UFF, a full periodic table force field for molecular mechanics and molecular dynamics simulations. *J. Am. Chem. Soc.* **1992,** *114* (25), 10024-10035.

27. Thijssen, J. M., *Computational Physics*. Cambridge University Press: 2007.

28. Pignataro, B., *Molecules at work*. Wiley-VCH: 2012.

29. Sircar, S., Basic Research Needs for Design of Adsorptive Gas Separation Processes. *Ind. Eng. Chem. Res.* **2006,** *45* (16), 5435-5448.

30. Potoff, J. J.; Siepmann, J. I., Vapor–liquid equilibria of mixtures containing alkanes, carbon dioxide, and nitrogen. *AIChE Journal* **2001,** *47* (7), 1676-1682.

31. Skoulidas, A. I.; Sholl, D. S., Molecular Dynamics Simulations of Self-Diffusivities, Corrected Diffusivities, and Transport Diffusivities of Light Gases in Four Silica Zeolites To Assess Influences of Pore Shape and Connectivity. *J. Phys. Chem. A* **2003,** *107* (47), 10132-10141.

32. (a) Rankin, R. B.; Liu, J.; Kulkarni, A. D.; Johnson, J. K., Adsorption and Diffusion of Light Gases in ZIF-68 and ZIF-70: A Simulation Study. *J. Phys. Chem. C* **2009,** *113* (39), 16906-16914; (b) Skoulidas, A. I.; Sholl, D. S., Self-Diffusion and Transport Diffusion of Light Gases in Metal-Organic Framework Materials Assessed Using Molecular Dynamics Simulations. *J. Phys. Chem. B* **2005,** *109* (33), 15760-15768.

Chapter 7

Conclusions and Future Work

7.1 Conclusions

A porous organic cage molecule (**CC2**) was synthesized from 1,3,5-triformylbenzene and 1,2-propylenediamine in acetonitrile solvent in Chapter 3. The shape-persistent [4+6] imine cage molecule showed unique tetrahedral symmetry with an internal void. Six disordered methyl groups on the cage vertices directed the packing of the cage molecules to form 1D channel. The material demonstrated permanent porosity after desolvation with a BET surface area of 533 $m^2 g^{-1}$ and microporous volume of 0.26 cm^3 g^{-1}. The total N_2 uptake of **CC2** was 7.5 mmol g^{-1}at 77 K, 1 bar. It adsorbed 8.9 mmol g^{-1} H_2 at 77 K and 7 bar which have exceeded reports for other porous organic molecules. The CH_4 sorption capability was 0.95 mmol g^{-1} at 287 K, 1 bar and the CO_2 uptake of **CC2** was 3.0 mmol g^{-1} at 275 K, 1 bar.

A [2+3] 'propeller' cage (**CC6**) was described in Chapter 4. **CC6** was synthesized by the condensation reaction of 1,3,5-tri-(4-formylphenyl) benzene with 1,5-pentanediamine in methanol solvent. The material had an ideal selectivity of 11 for CO_2/N_2 at 300 K, 1 bar. Additionally, it exhibited a H_2/N_2 selectivity of 2.4 at 77 K, 1 bar. The gas selectivity can be rationalized by pore connectivity on the basis of the crystal packing. The Connolly surface of the crystal structure generated using a N_2 probe radius showed a narrow restricted 1D channel without connecting with 'side pore' which indicated a low N_2 uptake. Although the ideal selectivity of [2+3] 'propeller' cage was lower than other literature examples, the absolute uptakes were higher than other [2+3] imine cages. The future challenge would be to design porous organic molecule with both high selectivity and high gas uptake.

The amorphous porous cage molecules were synthesized by three novel methods which were cage-diamine exchange, cage-cage interchange and co-reaction of 1,3,5-triformylbenzene (TFB) with a mixture of both 1,2-ethylenediamine (EDA) and 1,2-cyclohexanediamine (CHDA) as described in Chapter 5. A distribution of products had both EDA-linked and CHDA-linked vertices in a single cage molecules. These molecular species packed together ineffectively, thus creating permanent porosity in the amorphous solid. The H_2/N_2 gas selectivity was observed as a function of the EDA: CHDA ratio on the cage vertices in these amorphous cage materials. Amorphous **CC1**, with all EDA vertices, showed a H_2/N_2 selectivity of 12 at 77 K, 1 bar. Amorphous cage materials with high EDA ratios adsorbed much more H_2 than

N_2. For example, materials from co-reactions with a ratio of EDA and CHDA to be 5: 1 exhibited a H_2/N_2 selectivity of 5. However, amorphous materials with low EDA ratios did not show H_2/N_2 gas selectivity. For example, amorphous **CC3** with all CHDA vertices is highly porous to both H_2 and N_2. The BET surface area of one of these amorphous scrambled cage materials was up to 898 m^2 g^{-1} which has exceeded crystalline porous cage molecules and other porous amorphous molecules.

Molecular simulation has been used to characterize these amorphous porous cage materials in Chapter 6. A methodology has been developed to build simulated structures of amorphous cage materials. The proposed structure generation procedure consists of four steps:

(1) Randomly loading cages at a low density.

(2) Stabilization of the initial configuration using NVE ensemble.

(3) Compression of the system using NPT ensemble.

(4) A geometry optimization for the configuration.

All simulated models were characterized by their porosity with surface areas, densities and microporous volumes. The simulated results show good agreement with available experimental data. When the models were constructed, molecular dynamic simulations were then performed for gas diffusion in these amorphous porous materials. Gas diffusion trajectories, gas hopping analysis and self-diffusivities were carried out to rationalize gas selectivity in amorphous **CC1** and **CC3**. The simulation results revealed that N_2 diffusion was restricted in amorphous **CC1**, but H_2 could diffuse through the whole system for amorphous **CC1** which corresponded to the experimental observation: amorphous **CC1** showed selectively porous to H_2. Furthermore, N_2 and H_2 diffusion in amorphous **CC3** were faster than **CC1** due to a larger accessible pore volume in amorphous **CC3**. The diffusion trajectories and hopping analysis showed that amorphous **CC3** was porous to both H_2 and N_2. The self-diffusivities of H_2 and N_2 in amorphous **CC1** and **CC3** respectively were obtained which verify dynamic diffusion and experimental observations.

7.2 Future work

A family of imine cage molecules has been described incorporating a wide range of functionalities on the cage vertices in the crystalline solid state. It has been shown that the functionalities on the cage vertices or cage topologies have a significant effect on the cage molecular packing and porosities of the materials. In the future, functionalizing imine cage molecule with metal ions would be explored. The sorption properties for cage molecules before and after doping with metals could be investigated using gas sorption isotherms, isosteric heats and binding sites. Electronic or conductive properties could be determined after doping metal ions into cage molecules. Light elements doped porous cage molecules (such as Li and Mg) are expected to enhance H_2 storage capacity. Li ions penetrated in porous organic cages could have potential applications in the field of Li battery.

Initially, **CC1-CC3** cage molecules were used for metal doping reactions and the results showed that these cage molecules could not bind with metals. Additionally, the porous cage molecules with hydroxyl (OH) functional groups were attempted to be synthesized. The motivation of introducing OH functional groups on the cage molecules is to involve binding sites for the metal doping. The starting monomer of 1,3,5-triformylphloroglucinol shown in Figure 1 could be used for future imine cage synthesis. 1,3,5-triformylphloroglucinol can be easily synthesized by one step reaction in a high yield from the literature.

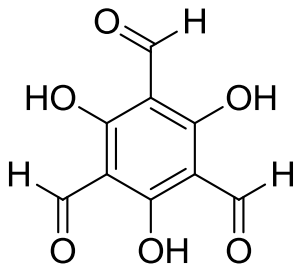

Figure 1. 1,3,5-triformylphloroglucinol for future cage synthesis.

Here, the preliminary results showed that a [2+3] enol-imine cage molecule were prepared by the condensation reaction of 1,3,5-triformylphloroglucinol and 1,2-ethylenediamine in ethanol solvent. The material did not show permanent porosity due to small voids in the cage molecules and packing close between cage molecules. The future reactions will be carried out by choosing various diamines and modifying

reaction conditions in order to form porous [4+6] enol-imine cage molecules. The metal doping reactions could be further investigated using these enol-imine cage molecules.

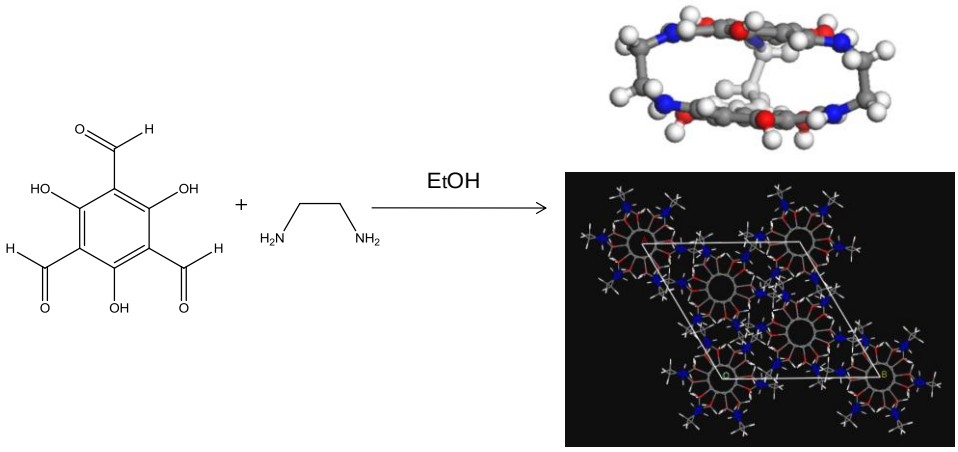

Figure 2. The synthesis of enol-imine cage molecule by the condensation reaction of 1,3,5-triformylphloroglucinol and 1,2-ethylenediamine in ethanol solvent.

For amorphous porous molecules, future work can focus on enhancing porosity by introducing bulkier functionality on the cage vertices, such biphenyl or naphthyl groups by the co-reaction method. It would also be interesting to combine different molecule topologies ([2+3] (**CC6**), [4+6] (**CC1-3**) or [8+12] (**CC7-8**) cage) in an amorphous solid to investigate porosity and gas selectivity. The amorphous cage molecules and polymers (such as soluble PIMs or CMPs) could be co-amorphized in the solid states to form membranes for gas separation. It would be possible to blend amorphous cage molecules with some organic molecules with active sites for the catalysis, fluorescent or photoactive organic molecules for light harvesting, sensing and photocatalysis. More importantly, the simulation methodology for generating amorphous cage models would be used to predict properties of materials before synthesis.